UNIVERSITÀ
DEGLI STUDI
FIRENZE

DOTTORATO DI RICERCA IN FISICA E ASTRONOMIA

CICLO XXX

COORDINATORE Prof. Raffaello D'Alessandro

From dust to planets: high resolution observations of small-scale structures in evolving protoplanetary disks

Settore Scientifico Disciplinare: FIS/05 Astronomia e Astrofisica

Dottoranda
Dott. Greta Guidi

Tutori
Dott. Leonardo Testi

Prof. Alessandro Marconi

Coordinatore
Prof. Raffaello D'Alessandro

Anni 2014 / 2017

Contents

Introduction

The quest for our *cosmic origins* has fascinated mankind across the centuries, but in the past two decades major steps forward have been made in this direction: our knowledge of exoplanetary systems has made significant progresses, due to advances in the detection techniques of planets orbiting nearby stars, and to the raised interest in Young Stellar Objects (YSO). These latter represent the first stages of star formation and their study provides an essential complementary insight on the conditions that could lead to the formation of large solids and eventually planets. This relatively new observational branch was originally developed from ground based infrared and millimeter observations and observations by the Hubble Space Telescope in the 1990s, followed by huge contributions given by space observatories like *Spitzer Space Telescope* (2003 - present day) and *Herschel Space Observatory* (2009 - 2013). Concurrently, the expansion of ground-based radio astronomy lead to the building of improved single dish antennas and multiple arrays ranging from sub-millimeter to centimeter wavelengths.

Protoplanetary disks, often referred to as Class II YSO, are formed due to the conservation of angular momentum during the collapse of a molecular cloud, when the infalling material is channeled through a disk onto the forming central star. At later stages planets are thought to form out of the material in such disks, on timescales of the order of the disk dispersal time ($\sim$1 to 10 Myr). They are extremely complex systems for the multiplicity of processes taking place: gas accretion onto the central star, winds and outflows, photoevaporation, and all the mechanism regulating the evolution of dust such as vertical mixing, dust settling, fragmentation and radial drift, to name a few. Most of the current theoretical models include just limited physics, and are not able to predict the properties of exoplanets that are being measured: this is not just due to the complexity of these systems but also on the lack of knowledge of the disk parameters. Measuring the physical properties of these objects is in fact extremely challenging, but huge progresses have been made in the last few years, to

a large extent thanks to the commissioning of the Atacama Large Millimeter/submillimeter Array (ALMA), a 66 antenna interferometer with baselines spanning up to 15 kilometers and a frequency spectrum going from 31 GHz to 950 GHz (corresponding to wavelengths of 350 μm - 10 mm). Since the start of the operations in 2011 ALMA has provided a large amount of new information as well as astonishing images, literally revolutionizing our view of protoplanetary disks and revealing the process of planet formation while it is occurring, the first emblematic example being the ring system around the star HLTau (ALMA Partnership et al. 2015). Successive ALMA observations of similar objects, showed a large variety of morphologies in the disk images in the sub-millimeter and millimeter range, such as rings and gaps of various extent and location, up to spiral arms. With extensive disks surveys being carried out in several star forming regions, along with the opening of ALMA to large programs since 2016, we are assisting to a substantial advancement in our understanding of disk evolution and planet formation mechanisms.

The processes that regulate dust evolution and growth are crucial for determining the initial conditions leading to the formation of larger bodies: in the widely accepted *core accretion* scenario, the first step towards the formation of rocky cores is the growth of dust grains from sub-micron sizes typical of the interstellar medium into larger aggregates. This critical phase occurs in the dense midplanes of protoplanetary disks, and represents the last directly observable step before the appearance of planetesimals and planets. Several independent observations have shown that once dust is collected in a circumstellar disk it evolves into larger grains and sediments towards the disk midplane (see the review by Testi et al. 2014). The initial mechanism for the growth of solid is direct sticking, as a consequence of low velocity collisions at high densities in turbulent disks. Grain growth is not a straightforward process though, it was realized very early that, as they grow, grains dynamics decouple from the gas and aerodynamical drag becomes a survival problem, leading to the processes of rapid *radial migration*. This process, originally referred to as the *meter size barrier* by Weidenschilling (1977), prevents the growth and survival of millimeter size grains in the outer regions of smooth disks, contrary to direct observations. In the four decades from the original formulation, the detailed theoretical and laboratory investigations of this process have only increased the number of barriers that grains need to overcome to grow in disks, including *fragmentation* and *bouncing* barriers. It is now generally accepted that on top of a smooth size distribution of grains controlled by the *radial drift* and *fragmentation* processes

leading to centimeter size grains in the inner regions of disks (within ~10 AU) and millimeter sizes in the outer disk (beyond 50-100 AU), other *local* processes are required to trap large grains and promote localized growth beyond the barriers and to planetesimal sizes (see reviews by Testi et al. 2014, Johansen et al. 2014).

Thanks to ALMA we can now provide direct observational constraints of these physical processes: the substructures revealed in the dust continuum emission suggest that local mechanisms are leading to dust growth or trapping, and producing inhomogeneities in the dust and gas distributions. My thesis work aims at using new observations at high resolution and sensitivity from ALMA and other complementing facilities to obtain direct insight on the processes driving the evolution of protoplanetary disks and planet formation. Detailed analysis of the thermal emission of the gas and dust in the disk midplane, detected at submillimeter to centimeters wavelengths, can help constraining the disk physical parameters such as mass, density and temperature profiles, as well as the level of growth of the dust particles on their path to the formation of larger bodies. In this thesis I will present the results of this observational study, as well as ongoing projects and the future perspectives in this field.

1 Scientific background

1.1 Building the theory of planet formation

How do planets form? For centuries philosophers, mathematicians and astronomers have been addressing this question, and our modern understanding of this phenomenon is not very different from the hypothesis advanced during the Age of Enlightenment. Since Copernicus' *De revolutionibus orbium coelestium* (1573) and the consequent dismantling of the geocentric view of our Solar System, several scientists such as Johannes Kepler, Tycho Brae, Galileo Galilei, Christiaan Huygens, Isaac Newton and many others contributed with their new theories and observations to a real "astronomical revolution" by the end of 1600. In particular, Newton's formulation of the law of gravitation in 1665 finally gave a mathematical representation to Kepler's laws, which described the orbits of planets in our solar system, but did not indicate the primal cause for such motions (Kepler identified the Sun as responsible for an effect similar to the magnetic force). The elegant solution found by Newton inspired the philosopher Immanuel Kant to theorize a Universe evolving only under the effects of natural laws, attraction and repulsion. In his *Universal Natural History and Theory of Heaven* (1755) Kant describes planets forming from a chaotic nebulae of the constituting elements, by progressive aggregation and then gravitational attraction of the surrounding material. The same hypothesis was perfectioned by Pierre Simon Laplace few years later: his development of infinitesimal calculus and theory of probability, together with the improvements in optical instrumentation allowed him to measure the perturbations in the orbits of planets and satellites, that were hidden to his precursors by observational errors. Laplace thought that the Solar System was in a stable configuration maintained by reciprocal attractions and that it originally had the shape of a fluid, revolving around the forming Sun. He predicted

the progressive settling of the material on a disk, as a consequence of the conservation of momentum, and the formation of concentric rings of vapour, along which planets formed from condensation and then progressively cooled down. This was happening at the end of the XVIII century, when the plenitude of discoveries and results obtained worldwide earned Celestial Mechanics a wide popularity, as well as Astronomy was elected as the queen of all sciences. Later on, due to difficulties in finding an explanation for some aspects of Laplace's theory, such as the formation of a disk or of concentric rings, what is now called the "Kant-Laplace nebular hypothesis" was abandoned for some time. It then gained back popularity in the mid-1900, and was further developed after the first results of infrared surveys in the 70s and 80s confirmed the existence of flattened structures orbiting around young stars (see Section 1.2), to arrive to the current theories of planet formation.

1.1.1 Modern view of planet formation

Our knowledge on the formation of stars and planets rapidly increased in the second half of the XX century, when a larger range of observation (from X to millimeter wavelength) became available from both ground based and space instruments. It was soon discovered that stars originate from cold molecular clouds: if the conditions for gravitational instability are fulfilled, clouds collapse to form a hydrostatic core, while the material infalling from the parental cloud is channeled through a rotating disk and accretes onto the forming protostar (see Section 1.2 for a more detailed discussion of the first stages of star formation). It is now clear that planets must form out of the circumstellar material orbiting around young stars, and accrete the bulk of their gaseous component within a few million years from the initial collapse, as this is the typical timescale for the dispersal of disks (see e.g. Mamajek 2009, Fedele et al. 2010). While the IAU (International Astronomical Union) agreed on a specific definition of "planet" in our Solar System[1], there is no exact definition of exoplanets. The most general description can be summarized as: a large body orbiting around a star whose luminosity does not stem from nuclear fusion. Such definition implies a natural upper limit in mass, given by the minimum temperature required to trigger the nuclear burning of the most easily fused element (Deuterium) in the core, corresponding to about 10^6 Kelvin and translating into a mass of $\sim$13 M_J (where M_J is a Jupiter mass) for a solar-like composition. At higher mass we would be in presence of a *brown dwarf*: an object with mass between $\sim$13

[1] https://www.iau.org/news/pressreleases/detail/iau0603/

and ~80 M_J whose inner temperature will never reach the threshold for hydrogen burning, but is able to sustain Deuterium burning in the early stages of its evolution. A lower limit in mass is not so well defined, but we generally call *dwarf planets* bodies with spherical shape that have not a major dynamical influence on nearby objects. Another interesting class of objects, falling outside the definition given above, are the so called "free-floating planets": objects with formally planetary mass (below $13M_J$) but not gravitationally bound to any star or brown dwarf. Their origin is still not well understood, as they could have been formed either inside protoplanetary disks and then scattered at larger separations by dynamical interactions, or in isolation inside molecular cloud in a similar way as stars.

Regarding the characterization of extrasolar planets, one first distinction can be made between smaller terrestrial planets and gas or ice giant planets, where the first are solid bodies that are able to retain a modest atmosphere, while the latter possess a gas envelope which constitutes a substantial fraction of the total mass. The formation of terrestrial planets is the result of progressive collisions that bring micron-sized dust grains to grow and build larger bodies, eventually reaching planetary sizes. This is thought to be a rather "slow" process that can take up to several million years (Armitage 2013), spanning over 12 magnitudes in size. On the other hand, giant planet formation is not currently explained with a univocal pathway, in fact two qualitatively different mechanisms are invoked: *core accretion* and *gaseous gravitational instability*; an overview of these main scenarios will be presented in this section.

Core accretion

The widely accepted theory of the formation of rocky planets and giant planets with a rocky core is dubbed *core accretion* scenario, and it predicts the aggregation of dust particles in larger bodies, first through direct sticking, then with the help of gravitational attraction after planetesimals (objects with diameter ≥1 Km) are formed, and finally the accretion of gas onto rocky cores. Terrestrial planets are formed when the core does not capture a large amount of gas, usually clearing regions of small dust. Conversely, if a rocky core is formed fast enough to exceed a certain critical mass (typically 10 earth masses) before the gas dispersal, it can give rise to an aerodynamical instability that leads to the rapid accretion of the surrounding gas, resulting in a giant planet.

The core accretion process can be simplified in three main steps (see Figure 1.1), as

described in Beckwith et al. (2000):

- *Sticking and coagulation*: in the earliest stage, particles accrete by direct collisions as they bump into one another, as a consequence of differential velocities in the disk. Aggregates can grow from micron size to meter size in very short timescales ($\sim 10^4 yr$) through a variety of collisional processes (Brownian motions, turbulence, settling, radial migration).

- *Gravitational attraction*: once large (kilometer size) bodies are formed, they can grow exerting gravitational attraction by one-to-one collisions and later by runaway growth, until they reach planetary dimensions.

- *Gas sweeping*: the rocky cores attract the surrounding gas, that accretes onto the surface forming an atmosphere; this process rapidly depletes the remaining gas, either for the dissipation of the disk or by creating a gap in the gaseous disk.

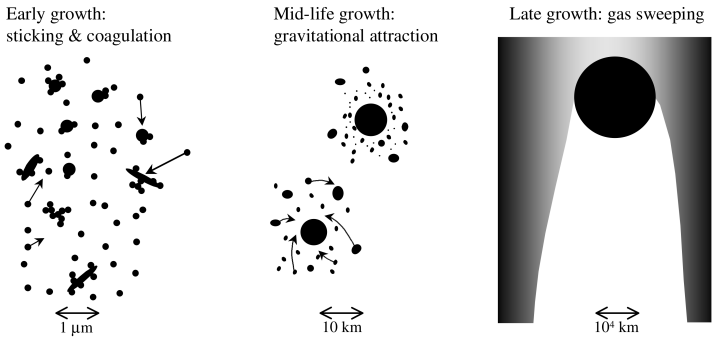

Figure 1.1: Stages of planet formation at growing sizes of the bodies: first steps of coagulation given by collisions, then accretion through a two-body interaction driven by gravitational attraction, finally the sweeping of the remaining gas. (Beckwith et al. 2000).

After the consumption of the available gas reservoir, the accretion attenuates and a long phase of cooling and contraction in quasi-hydrostatic equilibrium begins. The basic condition for a core to retain an atmosphere is for the escape velocity at the surface to be larger than the sound speed in the surrounding gas. Since the latter typically decreases with the distance from the central star, the preferential environment for the formation of gaseous giant results to be in the cold outer regions of disks.

One main weakness of this planet formation theory concerns the formation of km-sized planetesimal from cm-sized aggregates, too small for gravitational attraction to be important, and too big for benefit from direct collision, that might shatter them instead of favouring their

growth. In addition, the rapid inward migration due to aerodynamical friction with the gas component would require fast agglomeration of these large bodies. This problem was first discussed by Weidenschilling (1977) and dubbed *meter-sized barrier*, referring to the characteristic particle size associated with the maximum drift velocity at a orbital radius of 1 au (astronomica unit). This mechanism is discussed in detail in section 1.3.2. Suggested mechanisms that would help avoiding fragmentation are peculiar turbulent structures or vortices that could reduce the relative motion between aggregates; also the growth via condensation that has been identified as an efficient process for the production of cm and dm sized bodies.

Gravitational instability

Gaseous gravitational instability can occur in a protoplanetary disk for high values of the disk-star mass ratio: as a rough indication the global condition for a disk to become unstable can be written as $M_{disk}/M_* \gtrsim h/r$, where h is the disk vertical scale height and r is the radial coordinate. For a typical system around a low mass protostar this corresponds to value of the disk mass greater than ~5-10% of the stellar mass. A more accurate way of quantifying the degree of self-gravitation in a disk is through the Q parameter (Toomre 1964), defined for a keplerian disk as:

$$Q \equiv \frac{c_s \Omega}{\pi G \Sigma} = f \frac{M_{disk}}{M_*} \frac{h}{r} \tag{1.1}$$

where c_s is the sound speed, Ω is the rotational velocity, G is the gravitational constant and Σ is the gas surface density; in the last term of the equation a factor f of the order of the unity is placed before a factor containing h/r, highlighting the dependence from the disk aspect ratio. The condition for instability is fulfilled when Q is lower than a critical value Q_{crit}, typically close to the unity. Equation 1.1 indicates that this likely corresponds to high surface densities, but it also depends on the temperature profile, which strongly affects the h/r ratio. But it is important to notice that when gravitational instability sets on in a disk, the outcome can be twofold: an unstable disk typically generates spiral structures that carry angular momentum outwards, via gravitational torques, while transporting mass inwards. The dissipation of the accretion energy can then result in a heating of a disk, with a consequent rise of the Q parameter and mitigation of the instability, in what appears like a natural stabilizing cycle that brings back the disk in a quasi-stationary state. A different outcome happens when such compensation does not take place and the perturbations caused by the instability can grow and amplify: the result is fragmentation into dense clumps that rapidly collapse to be

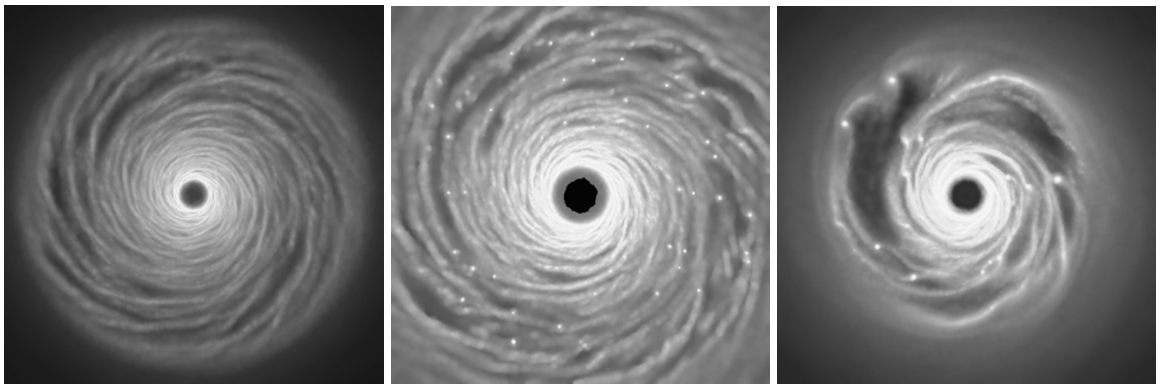

Figure 1.2: Equatorial density structure for a protoplanetary disk with different masses and cooling time, from Rice et al. (2003). *Left box*: Disk with M_{disk}=0.1M_* and cooling time t_{cool}=5Ω^{-1}; there are instabilities at all radii but the disk is in a quasi-stable state. *Central box*: M_{disk}=0.1M_* and t_{cool}=3Ω^{-1}; the disk is highly unstable and fragmentation is taking place, with all the fragments being gravitationally bound. *Right box*: M_{disk}=0.25M_* and cooling time t_{cool}=5Ω^{-1}; there are signs of fragmentation and the most massive fragments are gravitationally bound

potential progenitors of gaseous planets. The condition for the fragmentation of the disk can be expressed in terms of the *cooling time*: if cooling is not efficient, the heating provided by the perturbations generated by gravitational instability can keep the disk in thermal equilibrium. Viceversa, if the cooling timescales are short, gas clumps can cool down and contract rapidly resulting in the fragmentation of the disk. The cooling time depends on the specific cooling mechanism and other parameters like the disk opacity, but it is often expressed in a parametric form as a function of the dynamical timescale, and the critical cooling time is typically of the order of the orbital period, so that the condition for fragmentation has the form $t_{cool} \leq t_{cool,crit} \simeq const \cdot \Omega^{-1}$. As an example, Figure 1.2 shows different outcomes for a gravitationally unstable disk, depending on the initial disk mass and the cooling time.

It is now clear that the main limitation of this scenario comes from the requirement of satisfying both the conditions for gravitational instability and fragmentation: this is more likely verified in the outer regions ($\simeq$ 50-100 au) of very massive disks ($M_{disk} \gtrsim 0.1\ M_*$), therefore at the upper limit of the disk masses inferred from millimeter observation of the dust component (see Williams and Cieza 2011). It should be noted however that the estimates of the total disk masses still suffer from high uncertainties, and recent results indicate that the gas-to-dust ratio may be variable among disks and across disks themselves (e.g. Ansdell et al. 2016, Isella et al. 2016, Miotello et al. 2017, Long et al. 2017), with respect to the constant value of 100 commonly adopted to convert the dust mass into total mass. It is also interesting to notice that from a simple dimensional calculation the characteristic planetary mass that can be formed via gravitational instability in a disk around a solar-like star is

around 8 M_J (Armitage 2013), which is also at the end of the planetary mass function that we observe in extrasolar systems. For a detailed review on the topic of gravitational instabilities in protoplanetary disks we refer to Kratter and Lodato (2016).

1.1.2 Constraints from observations

Thanks to the advance in the detection techniques of planets orbiting nearby stars, in the last twenty years the available information on extrasolar planets has grown remarkably. The first planetary system was discovered around the millisecond-pulsar PSR1257+12 by Wolszczan and Frail (1992), although what is often remembered as the first exoplanet is 51 Pegasi b, a Jupiter-like planet detected with the radial velocity method, and first announced in Florence at the Ninth Cambridge Workshop on "Cool Stars, Stellar Systems and the Sun" by Michel Mayor in 1995 (Mayor and Queloz 1995). To this day the number of confirmed exoplanet is around 3500[2], and more than 4000 additional candidates have been found by the recent NASA Kepler missions.

[2]source: Nasa Exoplanets Archive, http://exoplanetarchive.ipac.caltech.edu

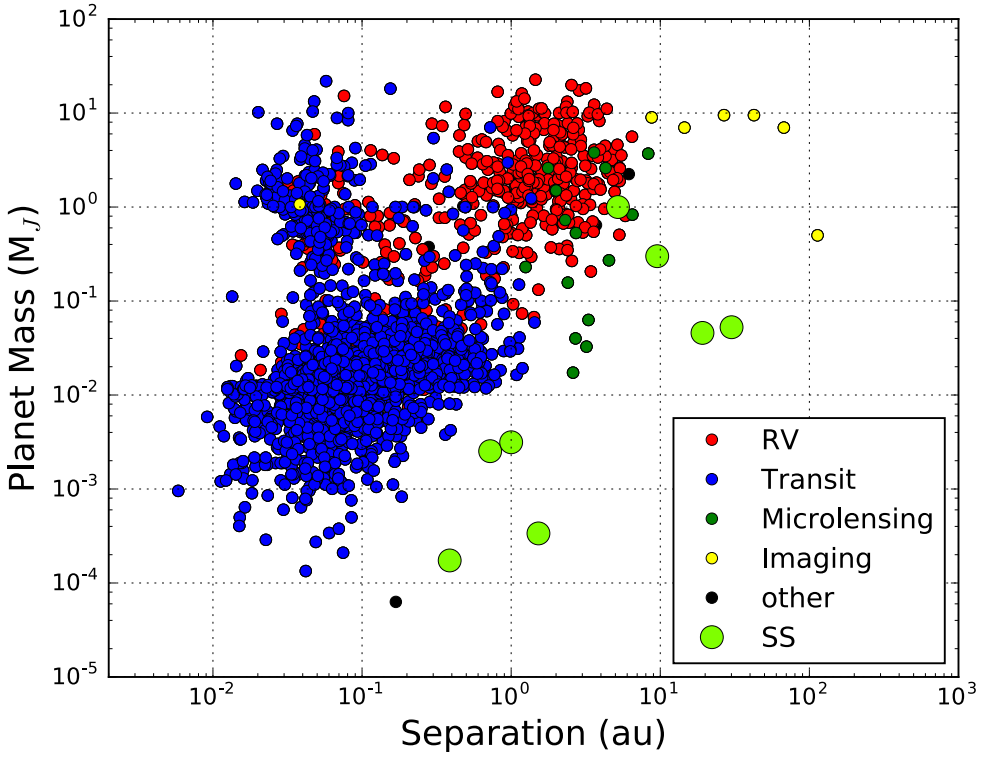

Figure 1.3: Planet mass in function of the orbital separation for 2950 confirmed exoplanets, data taken from *exoplanets.org*. The bigger green dots are drawn at the position of the planets in our Solar System.

The bulk of the known exoplanets have been discovered with the techniques of radial velocities and transits, while fewer detections have been made through astrometry, microlensing and direct imaging. The radial velocity method infers the presence of an orbiting planet by its dynamical interaction with the parent star, measuring the Doppler shift of absorption lines in the spectrum of the stellar photosphere, that reflects the radial component of its motion around the center of mass. Astrometric measurements of the stellar reflex motion in the plane of the sky can similarly reveal the presence of a companion. Still, no exoplanets discovered with this method have been confirmed; new high precision astrometry measurements taken with the GAIA satellite, launched by ESA in 2013, may be transforming this field by discovering tens of thousands of new exoplanets (e.g. Perryman et al. 2014). The transit method relies on high precision photometry that can detect the periodic variation in the stellar brightness caused by the planetary transits across the line of sight between the star and the observer. Gravitational microlensing events happen when the light from a distant source star is deflected by the gravity of a lens-star along the same line of sight from the observer; when a planet is orbiting the lens-star, its gravity can introduce an additional perturbation to the light curve. Finally, direct imaging can reveal planetary companions spatially separated from the host stars from their thermal emission, that typically peaks in the near infrared regime.

Figure 1.3 shows the planetary mass in function of the separation for the known exoplanets to this day: the plot is color-coded based on the discovering method, so that we can note that the different techniques are to a good extent complementary in covering different regions of the parameter space. Still a large fraction of planetary masses and orbital radii are outside the detection limits of the available instruments, and an architecture similar to our Solar System would still be challenging to detect.

Despite these selection effects, we can already point out some interesting features in the planet demographics outside our solar system. One first considerations is that there is striking evidence that planets are ubiquitous in our Galaxy. The statistics on exoplanets are continuously updated by new discoveries, but some interesting correlations have been found, like the increasing frequency of giant planets around stars with higher metallicities (Fischer and Valenti 2005). This relation is qualitatively consistent with the core accretion scenario previously described in this section, as a disk with heavy elements would form faster a more massive planetesimal disk, growing rocky cores of several Earth masses prior to the gas

depletion (Ida and Lin 2004).

Many interesting results are currently found analyzing the datasets from the Kepler[3] mission: its new detections have populated a region of the parameter space that was previously largely unexplored, with 85% of the candidates having radii smaller than Neptune ($R_{Nept} \simeq 4R_{Earth}$) and the vast majority having an orbital period shorter than 100 days. These sub-Neptune planets then appears to be the most common type in our Galaxy, with giant planets being orders of magnitude less numerous in the Kepler sample. As for Earth-like planets (commonly defined as the ones with $R \leq 1.25\ R_\oplus$), they are found in significant number in the Kepler sample, but they show either close orbits (within the orbit of Mercury) or are revolving around stars considerably less massive than the Sun (see Batalha 2014). The selection effect towards smaller separations is unavoidable, because of the easier transit probability at smaller orbital radii; and if extrapolating from the Kepler statistic to larger orbits, it appears that Earth-sized planets are common, but not ubiquitous. Another recent analysis of the Kepler dataset highlighted an intrinsic bimodal distribution in the size of small planets, with two separate populations centered at 1.3 $R_\oplus$ and 2.4 $R_\oplus$ respectively (Fulton et al. 2017). The gap at intermediate sizes, with very few detections of planets with R between 1.5 and 2 $R_\oplus$, could reflect the transition between rocky planets with a thin atmospheres, and cores with gas rich envelopes.

Summarizing, the sample of exoplanets discovered so far revealed a strong level of diversity in extrasolar systems, indicating that our Solar System is not the typical outcome of planet formation in our Galaxy. The current statistics are still not free from observational biases, and it is still hard to measure with high precision fundamental parameters of the known planets like their composition or mass. Ultimately, one of the main obstacles in determining the main formation pathways relies in the fact that we are only able to observe the final architecture of exoplanetary systems, which is the result of a long-lasting dynamical interaction with the disk and with other companions, and can lead to strong modification in the planet orbital parameters, as we think is the case for the giant planets in our Solar System. It is therefore fundamental to study the early phases of planet formation, when large bodies are building in circumstellar disks around young stars, to have a direct insight on the preferential

[3]Kepler is a satellite equipped with 0.95 m mirror, launched by NASA in 2009 and designed with the purpose of determining the frequency of Earth-like planets in the habitable zone (the region where a rocky planet can maintain liquid water on its surface) of Sun-like stars. The satellite has been monitoring simultaneously more than 190 000 stars while orbiting around the Sun for 4 years, looking for periodic signatures in the stellar light curves due to transit of companions.

locations and conditions in which planets are formed.

1.2 Protoplanetary disks

As introduced earlier in this chapter, circumstellar disks are the natural outcome of gravitational collapse in cold molecular clouds. The initial phases of the collapse are rather quick, and from molecular gas, characterized by rather low densities (n$\sim 10^5$ cm^{-3}), stellar densities of the order of $\sim 10^{24}$ cm^{-3} are reached in the central core on timescales of about 10^4-10^5 years. As primordial clouds have already an initial rotation (see e.g. Goodman et al. 1993), the diffuse gas possess a considerable initial angular momentum which is too high to be transferred efficiently to the external medium, and the infalling material from the large initial cloud lands first on a disk rather then directly on the protostar. Once the material has settled in a disk, its specific angular momentum increases with the distance from the star, and it has to be lost or redistributed in order to accrete onto the forming star. This process requires timescales that are much larger than the dynamical timescale, so that the disk can be consider as a statical structure in quasi-equilibrium (Armitage 2013). Understanding how the angular momentum is lost is one of the big open issues on star formation. The first analytical model that described the collapse of a spherical cloud and predicted the formation of a disk was done by Shu (1977), but the first evidence of the presence of flattened structures around young stars was obtained indirectly from the analysis of their spectral energy distribution (SED) at infrared wavelengths. It is worth noticing that until ~40 years ago, infrared surveys could not compete in terms of quality and detail with the optical counterparts. The key turning point was the technological advance in infrared astronomy occurred in the 80s of the last century: the development of solid state NIR (near-infrared) detectors and the launch of IR satellites like IRAS (1983) lead to several important findings. One of those was the discovery of embedded clusters, gravitationally bound aggregates of $\gtrsim$100 stars that suffer from high extinction from the surrounding molecular gas and thus are difficult to detect at optical wavelengths; following studies led then to the current belief that all stars are born within clusters or association (Stahler and Palla 2005). As anticipated above another important results was the discovery and subsequent classification of Young Stellar Objects (YSO): the infrared excess on top of the black body emission from the stellar photosphere of pre-main sequence stars revealed the presence of circumstellar material, and in particular the

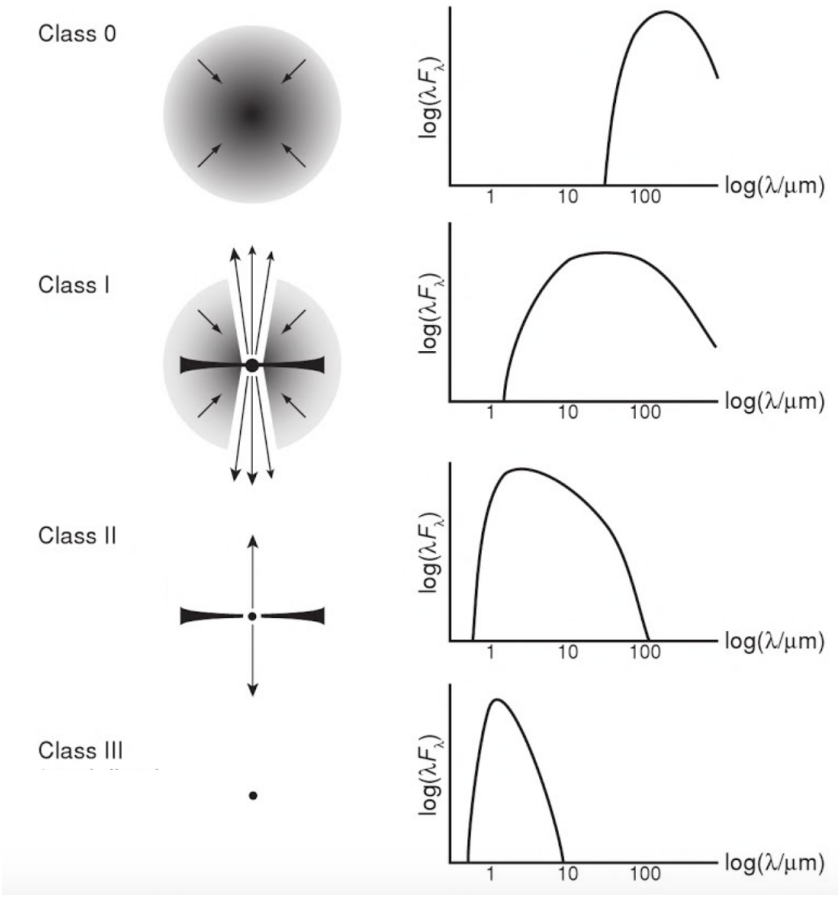

Figure 1.4: Classification scheme of Young Stellar Objects, with the different stages of evolution and corresponding SED. Adapted from Armitage (2013)

different shape of the infrared SED was related to different classes of objects by Lada and Wilking (1984). A formal classification was proposed later by Lada (1987), with a quantitative criteria based on the slope of the SED between ∼2 - 25 μm: depending on the value of the spectral index $\alpha = \frac{dlog(\lambda F_\lambda)}{dlog(\lambda)}$, three different classes of young stellar objects were identified. This empirical classification was intended to reproduce different evolutionary stages, as shown in the scheme of Figure 1.4, although the correspondence could not always be exact, due to observational biases like extinction, inclination of the disk and other effects that could lead to misinterpretations. An outline of the main classes and corresponding evolutionary

stage is given below, the range of values of the spectral index has been slightly modified in the years by different observers, we report here typical values for the classification scheme:

- **Class I** $0 \leq \alpha \leq -0.3$

  When the mass of the accreting protostar exceeds the one of the initial hydrostatic core, the Class I stage begins. A falling envelope is present, that reprocesses the radiation from the star and the already formed disk. Outflows and jets are often detected in association with these objects, with velocities of hundreds of km/s and launching points close to the star.

- **Class II** $-1.6 \leq \alpha \leq -0.3$

  At this stage the stellar contribution is visible at optical wavelengths, the envelope has dissipated and a (partially) optically thin disk of gas and dust is left. UV excess is sometimes detected due to hotspots on the surface of the star due to the accreting gas.

- **Class III** $-3 \leq \alpha \leq -1.6$

  Pre-main sequence stars with faint or no signatures of the presence of primordial material, they can be surrounded by *debris disks* of "second generation" dust generated by collisions of massive bodies

A fourth class was introduced later on, after the development of new instruments operating in the sub-millimeter range:

- **Class 0**

  The less evolved objects formed after the start of the protostellar collapse: the stellar core is still completely embedded in the envelope, so that it is not detectable at NIR wavelengths. Recent observations showed the presence of a rotational support (i.e. a disk) already in this early phase (e.g. Jørgensen et al. 2009, Tobin et al. 2012)

As this thesis work focuses on Class II objects, or *protoplanetary disks*, we are going to discuss in more details some of the processes involved with this evolutionary stage.

1.2.1 Disk structure and dynamics

During the protostellar collapse, viscous stresses and gravitational torques are thought to transport the angular momentum towards the external regions, so while most of the disk material falls inward accreting the protostar, part of it moves outward, absorbing all the

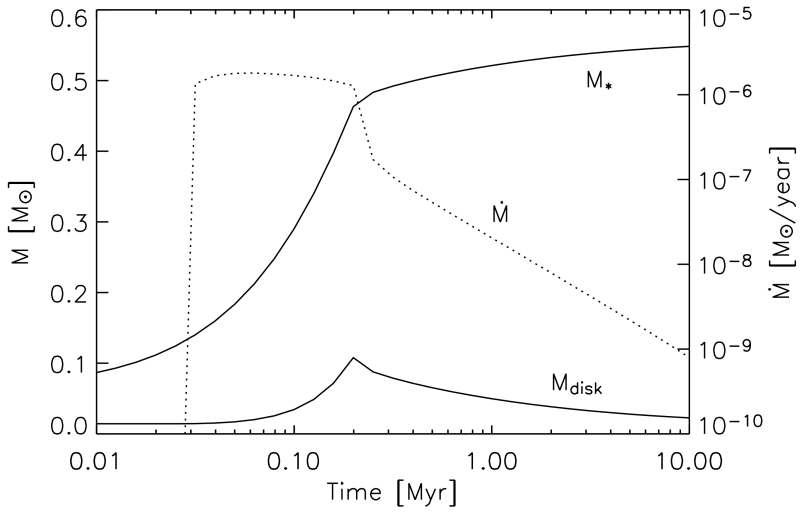

Figure 1.5: Evolution of the star and disk parameters with time during the collapse. The upper solid line represents the stellar mass, the lower solid line is the disk mass, the dotted line is the accretion rate of the material falling in the disk, with the first jump corresponding to the time of formation of the disk (Dullemond et al. 2007).

angular momentum. The collapse usually lasts $\sim 10^5$ years, with accretion rates going from high values of $10^{-5} - 10^{-6} M_\odot/yr$ to $10^{-7} - 10^{-9} M_\odot/yr$ in the final stages. In Figure 1.5 the evolution of the star and disk masses are shown from the beginning of the collapse. The viscosity required for the disk accretion, especially after the matter finished the infall on the disk, is thought to come from turbulence and magnetic stresses: magnetorotational instability (MRI) is the widely accepted mechanism to guide the turbulence and the angular momentum transportation outward. Other non-magnetical sources of anomalous viscosity have been suggested, since in the cold dusty disk the ionization level is usually too low for the magnetic field to be efficiently coupled with the gas, so that the MRI should be inhibited in most disks, but the matter is still under discussion. In order to model the disk without entering in the complex details of the viscosity problem, a simplified model commonly known as *α prescription*, has been proposed (*Shakura and Sunyaev*, 1973): the average viscosity is expressed as

$$\nu = \alpha H_p c_s \tag{1.2}$$

where H_p is the scale height of the pressure and c_s is the isothermal speed of sound, both evaluated in the disk midplane where we have most of the mass. This way the uncertainties coming from the origin of the viscosity are included in the α parameter. The surface density of a steady disk (with constant accreting rate) at distances much bigger then the disk inner

radius, can be written as $\Sigma \sim \frac{\dot{M}}{3\pi\nu}$, and from $H_p = \frac{c_s}{\Omega_k}$ we obtain

$$\Sigma(r \gg r_{int}) = K\frac{\dot{M}}{r^{3/2}\alpha T_c(r)} \tag{1.3}$$

where T_c is the midplane temperature and K a constant equal to $\sqrt{GM_*}\mu m_p/3\pi k$, with μ the mean molecular weight in unity of the proton mass m_p, k is Boltzmann's constant and M_* is the stellar mass. Note that disks are not in a proper steady state, as they evolve under the effect of viscosity and accretion, the first causing a mass loss onto the star and a redistribution of the angular momentum towards the outer regions, resulting in an expansion of the disk; the second causing mass loss through a photoevaporative wind (see paragraph 1.2.4). However, the timescales for the dispersal of the disk through viscous evolution ($\sim 10^8$ yr) are much larger then the average observed disk lifetimes ($\sim 10^6$ yr), allowing to model disks as steady structures. Viscous timescales depend on the radius as $t_{vis} \simeq \frac{r^2}{\nu}$, that for a irradiation-dominated disk becomes $t_{vis} \propto r$: the outer regions evolve more slowly and remain with most of the mass, constantly supplying material to the inner regions.

1.2.2 Vertical Structure

After determining the accretion rate and surface density radial profiles, we want some information about the vertical structure of the disk. For a given surface density $\Sigma(r)$ and gas temperature $T_{gas}(r, z)$, where z is the vertical coordinate, we can obtain the vertical density from the hydrostatic equilibrium

$$\frac{dP}{dz} = -\rho\Omega_k^2 z \tag{1.4}$$

with Ω_k the keplerian velocity ($\Omega_k^2 = \frac{GM}{r^3}$). The main challenge is to evaluate the temperature distribution: the gas affects the structure and the mass of the disk, but the opacity is given by the dust, thus most of the models assume that the gas temperature is equal to the dust temperature, to apply the radiative transfer equation to the dust continuum.

Once determined the temperature profile, we can compute the Spectral Energy Distribution: the thermal emission in a dusty disk model is separated in three regions of wavelength (see Figure 1.6): the most of the energy is emitted in the range $1.5\mu m - 100\mu m$, depending on the maximum and minimum temperature of the dust, and it is called the *Energetic Domain* of the SED. At shorter wavelengths we have the *Wien Domain* and at longer the *Rayleigh-Jeans Domain*. A number of models have been suggested to fit the energy distribution, from

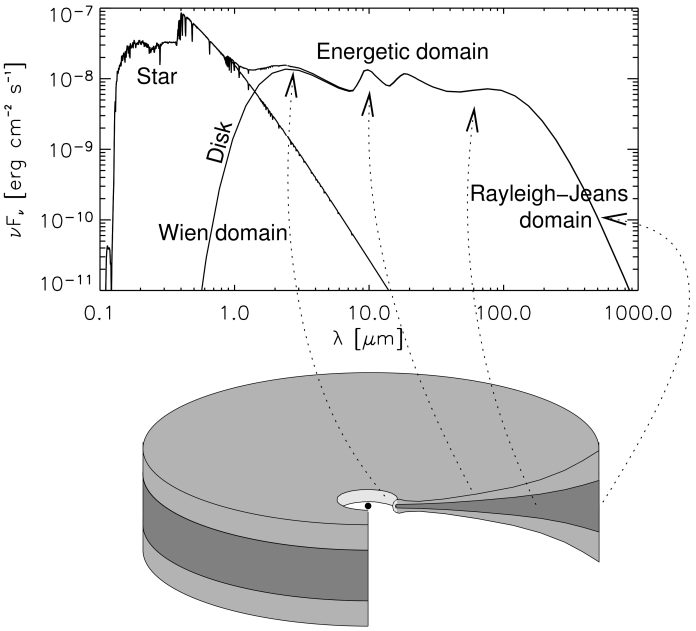

Figure 1.6: Spectral energy distribution for a flared protoplanetary disk. The near-infrared bump comes from the inner ring of dust, the IR feature originates from smaller grains in the superficial layers (the strong increase at $10\mu m$ is due to small silicate grains), the underlying continuum comes from the colder dust in the midplane, with the emission at longer sub-mm and mm wavelengths mostly coming from the outer regions of the disk (Dullemond et al. 2007).

a perfectly flat disk (Adams et al. 1987, Friedjung 1985), to a steady accretion disk heated by viscous dissipation (Hillenbrand et al. 1992, Bell et al. 1997), but none of these models managed to reproduce the observations. A more successful explanation of disk's spectra, especially the strong emission in the far-IR region, was found in a *flaring* geometry of the disks: the ″bowl-shaped″ structure allows the radiation to reach the outer radii of the disk, hence increasing the infrared emission (Kenyon and Hartmann 1987). The irradiation angle, under which the star illuminates the disk, is given for such a disk by

$$\varphi = 0.4\frac{r_*}{r} + r\frac{d(H_s/r)}{dr} \tag{1.5}$$

with H_s the height on the midplane where the disk becomes optically thick to the radiation coming from the star. The effective temperature T_{eff} of the disk is determined through the energy balance, between the incoming flux $\phi = \frac{1/2\varphi L_*}{4\pi r^2}$ and dust black-body emission $B = \sigma T_{eff}^4$ (this holds for an irradiation-dominated disk where we can neglet the energy from viscous dissipation). T_{eff} will be dependent on the disk shape through H_s.

We can notice that for an irradiation-dominated disk (flat or flared) the surface temperature is generally higher than the inside temperature, since the grains on the surface are directly hit by the stellar radiation, while the inner regions only receive the infrared radiation

emitted by the dust in the higher layers. These latter have a low vertical optical depth, due to the small irradiation angle φ, thus they emit an optically thin radiation at a temperature higher than the disk effective temperature, resulting in dust features in emission in the near-infrared. This is observed in almost all the T-Tauri (low-mass variable pre-sequence stars) and Herbig Ae/Be star spectra, indicating that these objects generally have an irradiation-dominated disk.

A number of models have been developed to reproduce the spectral energy distribution of accretion disks, e.g. the 1+1D model (D'Alessio et al. 1998), or the two-layer model (Chiang and Goldreich 1997). They describe fairly well the spectral emission, in particular of T-Tauri stars, but they tend to overproduce the emission in the far-IR range, and they overpredict the fraction of observed edge-on disks. A solution to this discrepancy has been found with the introduction of *dust sedimentation*: in the models this translates in a reduction of the disk surface height, and corresponding simulations well reproduce the SED in the infrared range, confirming the dust settling hypothesis. The comparison of the infrared and sub-mm emission of the spectra (see Fig.1.6) suggests a bi-modal grain size distribution: small (micrometer-sized) grains in the surface layers are needed to explain the IR emission, while millimeter-sized grains near the colder midplane well fit the sub-mm and mm spectral slope. The inner part of the disk is dust free due to sublimation, yet if the central gas infalling on the star is optically thin, the first ring of dust is efficiently heated by the star and results much hotter than the rest of the dust in the disk. This inner rim is likely to produce the ″bump″ in the infrared emission observed for almost all Herbig Ae/Be stars (Figure 1.6), that seems to correspond to a black-body emission at 1500K, the dust sublimation temperature (Isella and Natta 2005).

As protoplanetary disks evolve, the dust grains grow from sub-micron size to centimeter size and reduce the optical thickness of the disk, hence young thick disks are destined to become thin, and eventually debris disks when all the gas is disappeared. Observing the transitional phase where the disk has become optically thin but still has a considerable amount of gas could be profitable, in particular estimating the mass of such transitional disk can give information about the timescales of planet formation. Models of the structure and evolution of protoplanetary disk are reviewed thoroughly in Dullemond et al. (2007).

1.2.3 Gas Temperature

In the models described so far the gas temperature is assumed equal to the dust temperature, but that is likely verified only in the deep layers where the disk is optically thick; at the low densities of the disk surface, the gas is decoupled from the dust and has its own characteristic temperature. Although more difficult to observe than the dust, knowing the gas structure is crucial, since the gas predominates the mass of the disk, regulates the dust dynamic and settling, and the timescales of its depletion in the disk are decisive in determining whether giant gaseous planets will form in the system. Therefore, a model to describe the gas chemistry and temperature is necessary; that requires a notable effort, given the deep bond between the heating/cooling processes and the molecular abundances, and consequently the temperature. The simplest models are stationary, i.e. they assume hydrostatic, thermic and chemical equilibrium, which can reasonably hold in the superficial layers of the disk. These regions are thought to be similar to PDRs (Photon Dominated Regions Tielens and Hollenbach 1985), the gas temperature is generally higher then the dust temperature, it is prevalently constituted by ions and atoms, but at large radii the UV radiation from the star is less penetrating and the gas becomes molecular. In the energy balance the major roles are played by UV and X stellar radiation and by the photoelectric heating, induced by far-ultraviolet radiation on dust grains or PAH (Polycyclic Aromatic Hydrocarbon) molecules, which release energetic electrons and heat the gas.

1.2.4 Dispersal of the disk

As discussed in the previous section protoplanetary disks are thought to evolve in consequence of the radial exchange of angular momentum due to viscous stresses, caused by turbulence (and possibly magnetic torques) in the disk. Writing the characteristic viscous timescale as a function of the orbital velocity Ω: $t_\nu = \frac{1}{\alpha\Omega}\left(\frac{H}{R}\right)^{-2}$ shows that it can be estimated to thousands of orbital periods, assuming the commonly adopted value of 0.01 for the turbulence parameter α, corresponding to million years in the outer disk ($\geq$ 100 au) (Alexander et al. 2014). Since protoplanetary disks are observed to live only a few viscous timescales at most, some other mechanism should play a major role in accelerating the dispersal of the disk. Furthermore, this process has to be very efficient, as the signatures of the presence of the disk and of accretion onto the star seem to disappear at the same time, indicating that the

disk clearing should take place simultaneously at all radii (see e.g. Andrews and Williams 2005). In particular, statistical estimates indicates that the dispersal timescale is about 10 times shorter with respect to the disk lifetime, effectively removing the disk material in about 10^5 years.

Various processes have been considered as dispersal mechanisms: close binaries or encounters in dense star clusters can affect the disk evolution, but dominate only for a small fraction of the disk population. Magnetically-launched jets and outflows are commonly detected in the early phases of the disk lifetime, but the related mass flows are found to be a small fraction of the accretion rate in Class II objects. Also planet formation does not appear to be an important driver of the disk dispersal, as observations suggest that typically extrasolar planet account for less than 1% of the initial disk mass (see Alexander et al. 2014, and references therein). It is now widely accepted that while viscous accretion dominates disk evolution at the early stages (see Figure 1.5), disk winds drive the final dispersal of the disk (see the review by Ercolano and Pascucci 2017). Specifically, *photoevaporation* is thought to be the dominant mechanisms for gas removal at large radii: high energy radiation from the central star can bring the gas temperature to high values, up to 10^4 K in the surface layers of the disk, and about 100-500 K in deeper regions. This results in a pressure gradient that gives rise to a hydrodynamic expansion and subsequent dispersion of the gas in the external medium. Such process is efficient where the thermal pressure wins over the stellar gravitational field, driving the material to flow from the surface in the form of pressure-driven winds: depending on the mechanism driving the wind this would happen e.g. at small radii (~1-5 au) for X-ray driven winds, or large radii for UV winds. Theoretical models predict mass loss rates of the order of 10^{-10} - 10^{-8} $M_\odot$/yr for photoevaporative winds, these are consistent with the values inferred form observations. Slow magnetically driven winds can also possibly play a significant role, extracting mass and angular momentum from the disk, but the corresponding mass loss rates still remain quite uncertain. The disk dispersal process clearly influences the disk evolution, shorting its lifetime with respect to a purely viscous evolution and creating gaps in the inner regions or truncation in the outer parts (due to photoevaporation by nearby massive stars). It also strongly affects planet formation: the gas loss can penalize the growth of planetary envelopes, or prevent the formation of gas giants if the gas disappears too soon from the disk; it also influences planet disk interaction, slowing down inward migration; this effect should be potentially more significant for low mass

planets, but it remains unexplored by the models. On the other hand, since winds remove preferentially dust-poor material, they can enhance the dust to gas ratio, with the effects of enhancing the the disk in heavy elements and possibly trigger gravitational instabilities.

1.3 Measuring grain growth

Evolution of dust in protoplanetary disks puts the grounds for planet formation: dust grains are thought to grow from the sub-micrometer size of the interstellar matter to larger millimeter and centimeter aggregates, allowing the formation of planetesimal and eventually planets. This process is not yet fully understood, mostly because we are not able to observe directly beyond the formation of mm-cm sized particles, before arriving to planetary sized bodies that can be individually observed. In any case, the knowledge of dust properties is definitely important for understanding the disk features, for instance the opacity of the dust is indispensable for solving the radiative transfer in the disk and thus determining the solid mass. The dust in the pre-stellar cold molecular clouds is similar to the one found in the diffuse interstellar medium (ISM), that is a mixture of silicates and carbons with dimension from 100 Å to 0.2 μm, plus smaller carbonaceous grains and PAH.

Several independent observations, from optical and near-infrared imaging, to mid-infrared spectroscopy and millimeter interferometry, have proven that once dust is collected in a circumstellar disk, it evolves into larger grains and sediment towards the disk midplane. This section presents an overview of the main processes involved in the dynamics and growth of dust grains, mainly based on the reviews by Testi et al. (2014) and Natta et al. (2007), to which we refer for an exhaustive discussion.

1.3.1 Dust Transport

Dust particles in disks do not follow a purely keplerian orbit, as their motion is affected by a serie of forces (see the sketch in Fig. 1.7): *drag forces*, arising from a friction between grains and gas, act in the opposite direction of the dust motion and tend to decelerate dust particles. Particles that are larger then the free-main-path of the molecules are said to be in the Stoke's drag regime, (the drag force increase linearly with the particle's size), and the timescale of the deceleration can be expressed by the stopping time $\tau_s = mv/F_{drag}$ where m and v are the

particle's mass and velocity, while the Stoke's number

$$St = \Omega_K \tau_s \tag{1.6}$$

is an useful parameter that describes the aerodynamic behavior of the particles (the same Stoke's number corresponds to the same behavior).

The slight velocity differences between gas (in equilibrium among gravitational, centrifugal and pressure forces) and dust (only affected by gravitational and centrifugal forces) leads to a deceleration of the dust particles, that loses angular momentum and spirals towards the central star. This variation is however very small compared to the orbital velocity, and it depends on the particle's size. The drift velocity towards regions of higher pressure is

$$u_{drift} = \frac{1}{St + St^{-1}(1+\epsilon)^2} \frac{c_s^2}{V_K} \frac{\partial lnP}{\partial lnr} \tag{1.7}$$

where ϵ is the dust-to-gas ratio, $c_s = \sqrt{k_B T/\mu_p}$ the isothermal speed of sound, V_K the Keplerian velocity and P the pressure of the gas. As a consequence we should have observational evidence of particles rapidly drifting to the central regions; non necessarily fall into the star but maybe pile up at some central location. However, the observed population of large grains in the outer disk suggests that there must be other processes counteracting the radial drift, in particular from Eq. 1.7 we see the radial drift can be stopped by locally reversing the pressure gradient.

Two interesting processes that can oppose to radial drift are *advection* and *mixing*: the first is the result of a viscous evolution of the gas that leads to a drag of dust particles in the direction of radial gas motion, as long as they are coupled with the gas, the resulting drag velocity is

$$u_{r,drag} = \frac{u_{r,gas}}{1 + St^2} \tag{1.8}$$

that shows that only small particles, with $St < 1$ are coupled with the gas and thus resent of this force. A positive velocity of the gas in regions of the midplane could hence allow outward transport of the dust. The mixing is instead due to the turbulent motion of the gas, and it is related as well to the efficient coupling between gas and dust. In any case these two mechanisms are not strong enough to overcome the radial drift induced by the pressure gradient. The vertical motion of dust particles is affected by gas drag forces, again they act more effectively on small sized particles ($St < 1$), that are hence damped respect to the gas flow. Their settling velocity results $v_{settl} = St\Omega_K z$, increasing with the size and the

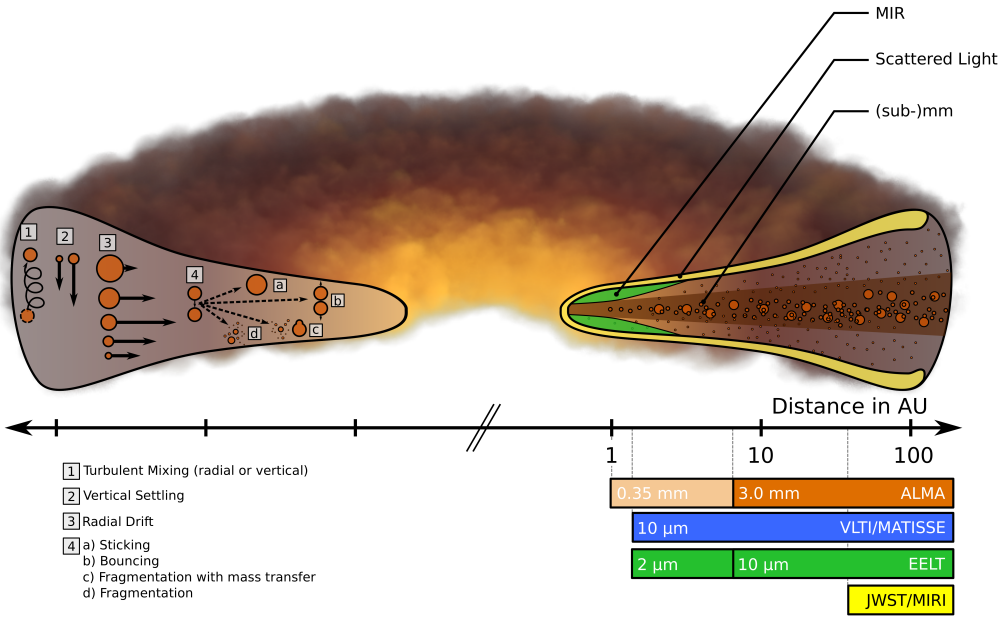

Figure 1.7: Cross-section of a protoplanetary disk, with an illustration of dust evolution, transport processes and observational constraints. On the left: principal dust transport mechanisms and types of collision (the length of the arrows are proportional to the velocities). On the right: different dust population in the various regions of the disk, with corresponding observing techniques. The horizontal axis shows the logarithmic distance from the central stars, the bars on the right hand side show the maximum angular resolution of recent or upcoming facilities, coloured as the regions they could most likely unveil in the near star forming regions (from Testi et al. 2014).

height on the midplane. An effect opposing to vertical settling is turbulent mixing, so the dust vertical structure can be derived imposing the equilibrium between mixing and settling effects. The settling mechanism could lead to a rapid growth in the midplane, yet still leaving a population of small particles in the surface layers, supplied with small fragment resulting from collisions between grains.

An intriguing scenario that could slow down or halt radial drift is the formation of massive planets: when it is massive enough, a planet can open a gap in the gas surface density as a consequence of its gravitational perturbation on the disk material, and trap dust particles in the outer edge of the gap (e.g. Rice et al. 2006).

1.3.2 Growth Processes

The aforementioned mechanisms acting on disk particles give rise to a series of differential velocities between grains, in both vertical and radial direction, that lead to collisions and hence possible growth. The most general mechanism for dust growth is direct sticking, as densities in protoplanetary disks are high enough for this type of coagulation to be important

over the disk lifetime. The growth process depends on a number of parameters like frequency of collisions, grain composition and porosity, impact parameter, impact velocity, and size distribution of the basic components, called *monomers*. The relative velocities increase with the size difference, since particles with the same Stoke's number have practically the same velocities (at least the component due to systematic motions). Additional random motions that can affect differently particles with the same St are *Brownian motions* and *turbulent motion*, this latter much more complicated to predict and model. An alternative mechanism of growth without collision is *condensation*: material in the gas phase can condensate on the surface of dust particles. However the growth of large particles through this process is still doubtful, since there is usually not enough material in the gaseous state to accrete efficiently every microscopic grain, additionally condensation would happen preferentially on the small grains (they dominate the surface area of the dust population), consuming there all the gaseous material. Of course also the opposite effect can take place: sublimation of mantles and solid material can lead to the destruction of dust grains.

Constraining the collisional outcome in function of dust parameters is crucial for the development of dust evolution models; this has been partly accomplished by laboratory experiments conducted in microgravity in the past two decades. We can distinguish three main types of collisional interactions:

1. **Direct collisional sticking**: in the dense regions not too close to the central star particles are thought to be affected mainly by van der Waals attractive forces, such that after a collision, if the kinetic energy is efficiently dissipated, they tend to stick together. The maximum velocity threshold above which grains can stick diminishes at increasing size (e.g. silicate grains of $\sim 1\mu m$ can stick to one another if they collide at $v \lesssim 1m/s$), but it is also influenced by the composition and porosity (water-ice particles are favourite since they have a higher surface energy). From laboratory experiments on sub-mm aggregates with high porosity, a mass dependent threshold velocity was derived as $v \propto m^{-3/4}$. The ″Hit and Stick″ process is considered dominant in the first stages of growth, at first favouring the production of fluffy aggregates, later reaching a compaction stage as larger grains collide and rearrange their internal structure.

2. **Fragmentation**: when the collisional energy is sufficiently high, particles of similar size break up and the remaining mass decreases with the increase of the initial mass of the colliding aggregates.

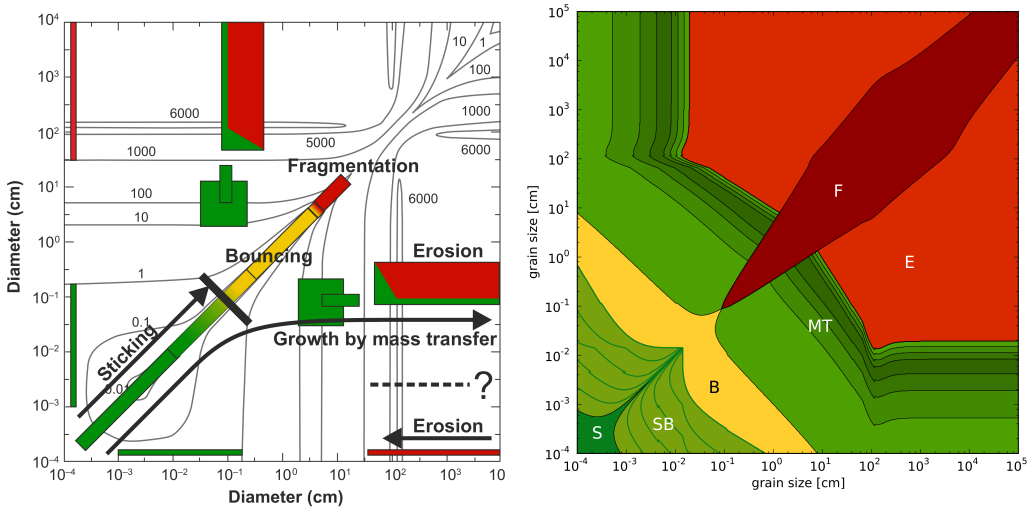

Figure 1.8: Visual representation of collisions outcomes in protoplanetary disks, from Testi et al. (2014). *On the left*: the axis indicate the aggregates' diameter in cm, with the lines corresponding to collision velocities in cm/s between non-fractal agglomerates, based on the model by Weidenschilling and Cuzzi (1993). The coloured boxes denote the regions explored by laboratory experiments: green represents sticking or mass transfer, yellow represents bouncing, red fragmentation or erosion. A possible path to the formation of planetesimals avoiding the bouncing barrier is outlined by the arrow ″Growth by mass transfer″. *On the right*: the collision outcomes on the entire parameter space derived by interpolating the experimental results, referred to silicate grains.

3. **Bouncing**: above the threshold for direct sticking and below fragmentation, aggregates can bounce off one another. Bouncing does not lead to a mass gain so the growth is limited by this so called ″bouncing barrier″. In addiction, bouncing causes a compression of the aggregates that hence decrease their porosity.

In Figure 1.8 a representation of the possible outcomes of dust collisions, as resulting from laboratory experiments. It appears that the bouncing barrier could be bypassed by growth by mass transfer: at velocity near the fragmentation threshold collisions between small and large aggregates can lead to a considerable mass transfer from the small to the large object. These consideration, as well as most of the experiments, are referred to silicate grains and do not apply for instance to icy particles, for which it was found there is no bouncing barrier for dimension of about $0.1\mu m$, such that icy planetesimals can form by direct collision.

The growth by mass transfer can go on as long as the size and velocity of the smaller aggregate is below a threshold curve, and can lead to formation of planetesimals. But there is also an inferior limit, since when growing aggregates are continuously bombarded by micrometer-sized particles, they can experience erosion. Many efforts have been made to develop dust growth models, mostly recurring to strong simplifications and use of average values or single size models, because of the large number of parameters and the wide range

they cover. Most of the studies agree in identifying the first stages of growth with direct sticking, than as the particles sizes and velocities increase, the outcomes are shifted towards bouncing and compaction, to arrive at a population of similar-sized aggregated which further growth is prevented (bouncing barrier). Even without considering bouncing, a size threshold is encountered due to fragmentation, related to particle parameters as (from Birnstiel et al. 2012):

$$a_{frag} \simeq \frac{2}{3\pi} \frac{\Sigma_{gas}}{\rho_s \alpha_t} \frac{u_{frag}^2}{c_s^2} \tag{1.9}$$

where Σ_{gas} is the gas surface density, ρ_s the dust grains' density and u_{frag} the fragmentation threshold velocity from lab experiments. So if fragmentation limits further growth, a steady state is expected, where growth and shattering balance each other. More detailed dust evolution models (e.g. Brauer et al. 2008) showed that collisional formation of planetesimals can be strongly obstructed by radial drift and grain shattering collisions, but dust particles can accumulate in *pressure bumps* and form larger bodies as long as there is a low level of turbulence. Another barrier that can hinder the formation of large aggregates is the *radial drift barrier*, since this mechanism removes preferentially particles larger than a particular size (see Paragraph 1.3.1). The size limit set by drift can be evaluated where the growth timescale ($t_{grow} = a/\dot{a}$) exceeds the drift timescale ($t_{drift} = r/u_{drift}$), approximately

$$a_{drift} \simeq 0.35 \frac{\Sigma_{gas}}{\rho_s} \frac{V_K^2}{c_s^2} \left| \frac{dlnP}{dlnr} \right|^{-1} \tag{1.10}$$

If most of the dust mass is contained in large grains, the drift velocity can be estimated by $u_{drift}(a_{max}(r))$. Simulations suggest that extremely porous grains can however overcome this barrier thanks to their increased collisional cross section.

1.3.3 Snowlines and Grain Growth

The *snowline* in a gas disk is normally defined as the distance from the central star beyond which the water ice is stable against evaporation; in our Solar System for instance this happens at about 2.7 au at a temperature of 170 K (Hayashi 1981). Snowlines can be also referred to other molecules, the carbon monoxide CO is of particular interest in protoplanetary disks since it is the second most abundant molecule, after H_2, and a good tracer of the gas, with its several rotational emission line easily observable in the sub millimeter and millimeter range. As described earlier in this chapter, disks have a vertical temperature and pressure gradients,

due to the dust opacity that absorbs and reprocesses part of the stellar radiation, preventing the direct illumination of the deeper layers. As a consequence we will have a *radial* ice line, separating the inner part of the disk from the colder regions farther from the star, and a *atmospheric* ice line, separating the disk's hot atmosphere from the midplane. These are the sites where ice particles moving with the turbulent gas from colder regions sublimate and pass to the gaseous phase; or viceversa gaseous particles diffuse across the snowlines into condensation regions and they condense onto dust grains. This latter is an extremely interesting mechanism for large grains and planet formation, since it could explain the overcoming of growth barriers in circumstellar disks; we will go into this in the next section.

According to Ros and Johansen (2013) dust grains that are migrating inward across a snowline in protoplanetary disks will lose part of their icy mantles, but cycles of sublimation and condensation will lead to an efficient growth and trapping near the snowline regions. In fact, small particles are coupled to the gas and hence moving on random paths due to turbulence, so a significant fraction stays in the condensation region, growing or accreting onto dust grains. Simplified numerical models of homogeneous water ice particles predict that in moderately turbulent disks ($\alpha \sim 10^{-2}$) particles grow up to decimeter size in a time of few thousand orbits. Particles can grow via condensation also in dead zones (low turbulence regions where MRI does not operate), but more slowly. The most significant growth happens near the radial snowline, but an efficient radial mixing supplies even distant regions of the disk midplane with large grains. The atmospheric ice line, directly heated by stellar radiation, does not contribute much on grain growth (reaching sizes of $\sim 10\mu m$), so we will focus mainly on the radial snowline. This condensation mechanism does not only apply to water vapor, but also other volatile molecules (the most important in disks are NH_3, CH_4, CO and N_2). Lab experiments of low velocities collisions between ice pebbles showed that particles with a frost superficial layer have an increased stickyness with respect to bare silicate grains, and for higher velocities (1-100 m/s) a mechanism of collisional fusion has been suggested, where the ice particles undergo a change of phase during the collision (Wettlaufer 2010). The limitations of these models are due to a number of approximations, like neglecting gas accretion onto the central star and the change of snowline position over time (which is reasonable, since the corresponding timescales are slower then the ones for condensation), the modeling of particles only composed by water ice (generally they are thought to have rocky cores covered by icy mantles), neglecting the collision between grains, and other assump-

tions on the disk turbulence and vertical/radial transport. The results of this modeling is that ice condensation is an efficient way to form centimeter and decimeter-sized particles; this process does not suffer from bouncing and radial drift barrier and can thus be a crucial mode of growth in protoplanetary disks.

1.3.4 Observational Probes of Grain Growth in Disks

Grain growth is expected to happen not only in the disk but also in the stages before the disk formation, in the dense regions of molecular cloud cores. In particular, they could reach several micron sizes in $\sim 1 Myr$ at densities of the order of $10^5 cm^{-3}$, or even hundreds of micron at higher densities. Recent studies of dust properties in protostellar envelopes and young disks indicate possible evidence of formation of large grains (even up the few millimeters sized) during the disks formation stages, in the infalling envelopes (e.g. Miotello et al. 2014).

Observations in the near and medium infrared are thought to trace the dust on the outer surfaces of the disks, where products of grain growth modified by dust transport processes are present, precisely the surface layers and the inner dust rim. These regions are not the places where larger grains are expected to be found, since the major part of dust growth happens in the regions of higher densities, i.e. the disk midplane. However, since the timescales for vertical mixing are shorter then the ones for radial transport, a correlation between surface and midplane grains at the same distance from the star is expected. The tracers of dust particles in these surfaces are given by scattered light and dust emission features in the optical and near-infrared regime. Images at such wavelengths can reach a resolution up to 10-20 au, scattered light becomes redder and more isotropic as grains grow (in the range 0.01-10 μm) and information about grain dimensions can be obtained from the intensity and angular dependence of scattered light. Model fitting of these images at multiple wavelengths indicate a stratification, with smaller grains in the atmosphere and larger grains settled more deep, in agreement with model predictions.

The denser regions of the midplane can be investigated at (sub)millimeter and centimeter wavelengths, where the dust emission is more optically thin. These kind of observations are our only tool to probe grain evolution in this region, where most of the solid mass is confined and also planetesimal and planets are thought to form. But how do we relate the grain dimension with the observables? The thermal emission from warm dust is controlled

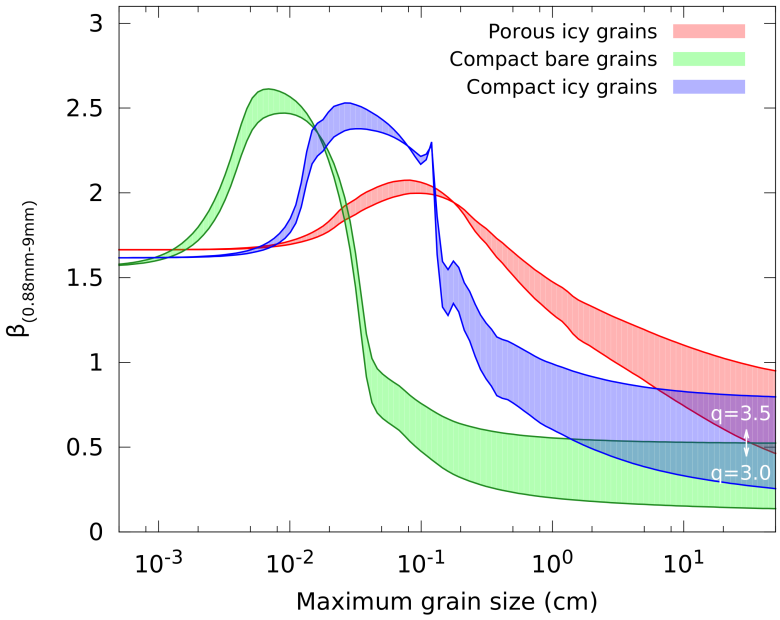

Figure 1.9: Opacity spectral index calculated in the wavelength range 0.88 mm-9 mm in function of grains' maximum size, for a size distribution of $dN = n(a)^{-q}da$. The minimum size is set to 0.01 μm and different colours correspond to grains of different composition and porosity (Testi et al. 2014).

by the dust opacity κ_ν, at millimeter wavelengths this can be related to the frequency of the radiation as (Beckwith et al. 1990)

$$\kappa_\nu = \nu^\beta, \tag{1.11}$$

where β is sensitive to the maximum size of grains a_{max}, but also on other dust morphological parameters, and especially on the grain size distribution $dN = n(a)^{-q}da$, where a is the particle dimension (from Natta et al. 2007).

Natta and Testi (2004) derived the main result that dust grains of 1 mm size or larger give rise to an opacity spectral index β lower than the unity (see Figure 1.9). This is due to the fact that solids with a size much larger then the observation wavelength do not absorb or emit radiation efficiently, thus they are characterized by a lower value of β. The frequency dependence of an optically thin emission at a given temperature in the Rayleigh-Jeans approximation ($F_\nu \propto \nu_{mm}^\alpha$) can be related directly with the opacity spectral index β as $\beta = \alpha_{mm} - 2$. This simplified method has of course a series of limitations and uncertainties, like neglecting possible optically thick regions associated with local overdensities; or the Rayleigh-Jeans regime assumption, that could be no longer accurate in the outer disk where temperatures reach 15-20 K. These approximations can lead to an underestimate of β and hence incorrect predictions on grain sizes. In addiction there can be contaminations by other

sources to the dust continuum emission, e.g. gas in the stellar chromosphere or in the winds and jets. What is done to resolve this uncertainties is to combine the (sub) mm observations with observations at longer wavelengths that can probe the gas emission, and extrapolate the contaminating flux at the frequencies of interest (see e.g. Section 4, Guidi et al. 2016). Taking into account that thermal free free and non-thermal emission from ionized gas in the stellar winds vary on various timescales, almost simultaneous observation should be carried out in order to measure a more correct gas flux.

Many studies relying on multi-wavelength sub-mm photometry have been conducted in star forming regions, at first especially in the northern hemisphere complexes of Taurus-Auriga and Ophiuchus, rich of pre main sequence young stars. The main result of these surveys was the evidence of large aggregates in several bright disks, but no correlation between grain size (α index) and stellar age was found so far (Natta et al. 2007, Ricci et al. 2012). The higher angular resolution of the observations in the past few years confirmed the presence of dust grains at least 1 mm sized in the outer regions. However, a number of disks with low millimeter flux and low spectral index suggests a population of large grains but also a low mass disk, that remains difficult to explain with models, since disks with low surface density hardly grow large aggregates (see equations 1.9 and 1.7). So one would expect that radial drift and fragmentation efficiently remove large grains in low fluxes disks over a few Myr, resulting in a steep increase of α, but this is not what is observed. Hence, the radial drift of large grains must be slowed down by some mechanism, two suggested hypothesis are: local pressure maxima due to inhomogeneities in the disk could trap dust particles, or large grains could be injected very early in the outer part of the disk, and not migrate efficiently because of the weak coupling with the gas.

Resolved images at millimeter/radio wavelengths, with their high sensitivity to cool gas and ability to resolve dust continuum in a wide range of angular scales, can provide a variety of observational probes of models physical predictions. Radial variations of dust properties in the disk can be mapped by inferring the spacial dependence of the spectral index β at different distances from the star from multi-wavelength observation of the dust continuum. Both initial studies with limited wavelength ranges of resolved continuum, and more recent works extended to longer (up to cm) wavelengths conclude that a constant value of β with the radial distance does not well fit the observed spectral profiles, while a better consistency comes from a spectral index increasing with radius (e.g. Pérez et al. 2015, Tazzari et al.

2016). Interferometric measurements agree that a general recurring feature of young disks is the anti-correlation between the size of the dust emission region and the observing wavelength. This feature is consistent with models predictions of larger particles (emitting more efficiently at longer wavelengths) concentrated at smaller radii of the disk, under the action of radial drift.

1.4 Observing disks in the high resolution era: the ALMA revolution

Since the development of the first sensitive detectors at infrared and millimeter wavelengths, huge progresses have been made in the study of young stellar objects in the last ~40 years. Early statistical studies at infrared wavelengths were realized with the IRAS satellite in the late 1980s (Taurus-Auriga, Myers et al., 1987; Lynds 1641, Strom et al., 1989). as well as single-dish millimeter surveys (Taurus-Auriga, Beckwith et al., 1990; Ophiuchus, André and Montmerle, 1994). Furthermore, early measurements of the integrated opacity spectral index from multi-wavelengths observations at (sub-)/millimeter wavelengths already indicated the presence of large grains in protoplanetary disks (Weintraub et al. 1989).

The bulk of the available datasets on disks and young stellar objects had significant contributions from the *Spitzer* and *Herschel* infrared observatories, and from the interferometers working in the sub-mm to centimeter range like the SMA, VLA and ALMA (see Sections 2.6 for details on the last two instruments). A growing number of young star forming regions is being studied with increasing detail: recently, the extraordinary ALMA sensitivity allowed to detect Class II objects at a high level of completeness in Lupus (Ansdell et al. 2016), Chamaeleon I (Pascucci et al. 2016), Upper Sco (Barenfeld et al. 2016), σ Orionis (Ansdell et al. 2017), at a spatial resolution as good as ~0.3″. This contributed to outline the first age-dependent statistical studies: Pascucci et al. (2016) found that the disk dust masses in the younger regions (1-3 Myr) is 3 times higher with respect to the older (5-10 Myr) association; and the relation between the dust mass and the stellar mass (M_{dust}/M_{star}) appears to get steeper with age, similarly to what found by Ansdell et al. (2017), possibly being related to the efficiency of radial drift in disks around lower mass stars.

In addition to that, a few nearby systems were imaged with particular detail by ALMA, revealing a variety of small scale (< 20 AU) structures in several protoplanetary disks sur-

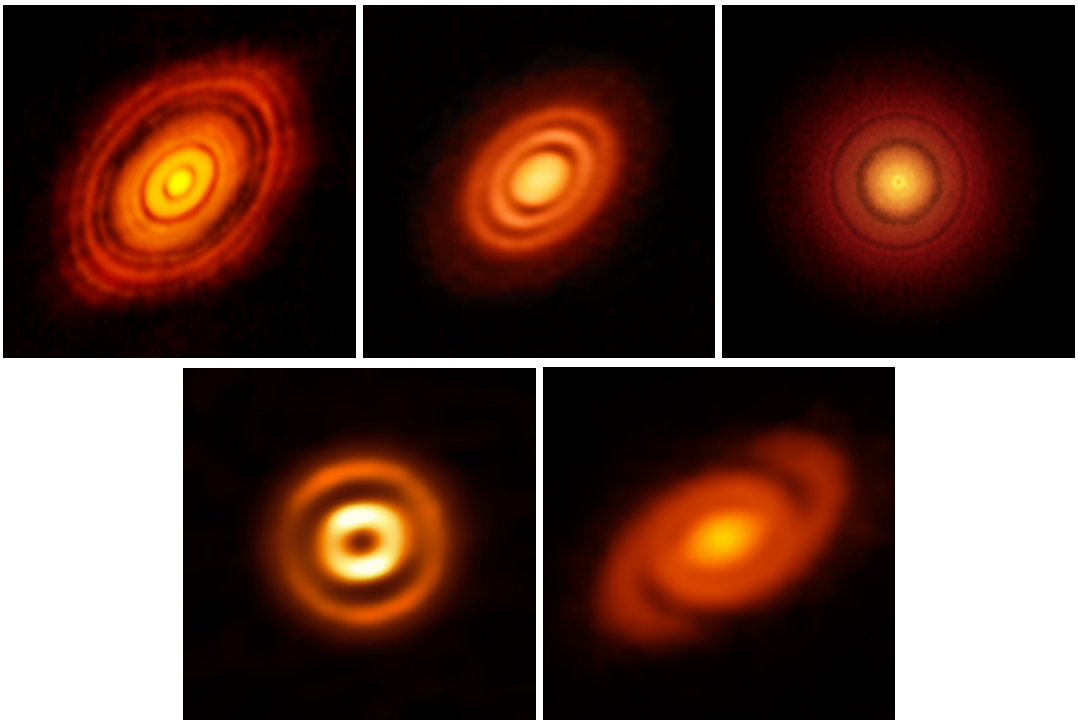

Figure 1.10: Gallery of some of the most well known disks showing features in the dust continuum in ALMA images, from the top left: HL Tau (ALMA Partnership et al. 2015), HD 163296 (Isella et al. 2016), TW Hya (Andrews et al. 2016), HD 169142 (Fedele et al. 2017), Elias 2-27 (Pérez et al. 2016)

rounding low- and intermediate-mass stars, the first emblematic example being the ring system around the star HLTau (ALMA Partnership et al. 2015). The origin of the rings and spiral structures is currently under debate: the most engaging scenario involves massive planets causing dynamical perturbations in these young systems, but other mechanisms such as gravitational instability, vortices, star-disk interaction, condensation fronts or disk chemistry are being considered.

In this framework I focused my PhD work on the observational study of protoplanetary disks at high angular resolution, with the goal of gaining a better understanding of the processes driving dust growth and evolution, and ultimately getting an insight on the planet formation processes. In Part I of this thesis I will describe the observational techniques and reduction tools used for the analysis; Part II consists of the scientific results that have been published in refereed journals, or in the process of being submitted; Part III draws the conclusions of the three-year PhD work and delineates the future prospects for the continuation of the study.

Part I

Observational techniques

2 Radio interferometry

My thesis work is based for the most part on the analysis of interferometric observations in the sub-millimeter and millimeter range. In this chapter I will go through the fundamentals of radio interferometry and the reduction techniques used for producing science datasets.

2.1 Radio Antennas

A radio antenna is a device that collects and detects electromagnetic radiation from a certain direction, and area, in the sky. Since photons are hard to detect singularly at radio wavelengths due to their low energy, a photon-counting receiver is not an option in this case. The electromagnetic waves are detected through the voltage induced by the incoming electric field in a conductor.

For low frequencies ($\lambda \simeq 1$ m) a simple wire antenna can be used: the *Hertz dipole* is simply a concentration of equal and opposite charges, electrically connected and at distance l from each other (see Figure 2.1). The length of the dipole must be $\leq$ the wavelength λ of the incoming radiation, and the device is only sensitive to one polarization, since the current is induced by the field parallel to the dipole length.

In a *Horn Antenna*, from a relatively wide aperture (circular or rectangular) the radiation is collected and converged towards a narrow part, or *horn*, through the metal cavity that functions like a waveguide; then it is converted into current by means of a coaxial cable. It has the advantages of being extremely broadband and having minimal sidelobes (see Paragraph 2.3), so that the thermal noise from the ground is very small. A famous horn antenna is the one at Bell Laboratories in New Jersey used by A. Penzias and R. Wilson when they first detected the Cosmic Microwave Background in 1964 (see Figure 2.2).

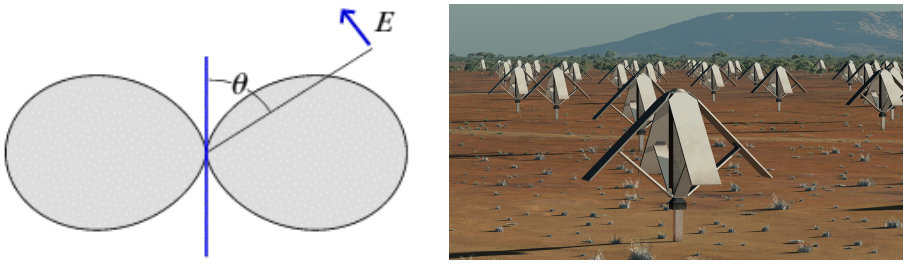

Figure 2.1: On the left: sketch of a Hertz dipole. In grey the Power Pattern lobes (representing the sensitivity in function of direction), with θ the angle between the dipole length and the direction of propagation of the radiation. On the right: a phased array of simple dipole antennas for the low-frequency range (about 50 to 350 MHz). *Credits SKA Organisation/TDP/DRAO/Swinburne Astronomy Productions*

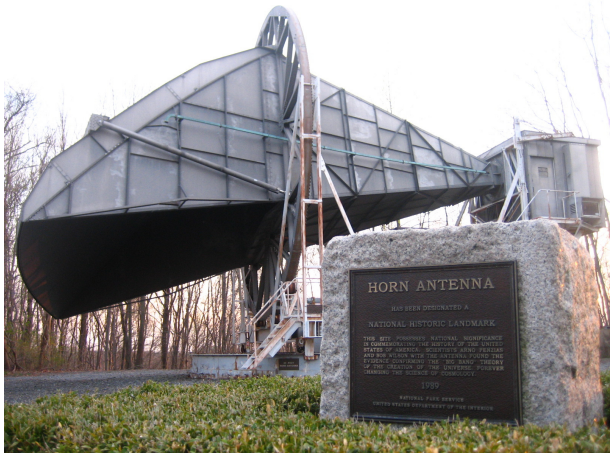

Figure 2.2: The horn antenna at Bell Telephone Laboratories in Holmdel, New Jersey, where Penzias and Wilson first detected the Cosmic Microwave Background radiation in 1964. A rotation axis allows the horn to point different direction in the sky.

The most commonly used antenna is the *Parabolic reflector*: the functioning is similar to the optical telescopes, a primary mirror concentrates the radiation into a focus where is placed a secondary mirror or, in the case of Prime Focus antennas, directly the receiver. The structure of the parabola does not need to be continuous but can be ″gridded″: a manufacturing with precision of 1/10 of the observing wavelength is generally enough to guarantee a good reflection of the signal. Antenna configurations can be, similarly to optical telescopes, Cassegrain, Gregorian, Nasmyth, sometimes with a off-axis geometry (see Figure 2.3), which has the advantage of a more uniform illumination but makes more difficult the shaping of the main reflector, that is no longer simmetric.

Figure 2.3: On the left: a Prime Focus 45-meters antenna of the GMRT (Giant Meterwave Radio Telescope), near Narayangaon town, India. On the right: the Green Bank Telescope (West Virginia, USA), an off-axis gregorian paraboloid of 100m diameter, the world's largest fully steerable telescope.

2.2 Some basic definitions

Before entering into the details of interferometry we recall here some basic equations.

The *Intensity* or *Brightness* of a black body at a temperature of T and at frequency ν is given by the Planck function:

$$I_\nu(T) = \frac{2h\nu^3}{c^2}\frac{1}{e^{h\nu/kT}-1} \tag{2.1}$$

Since at radio wavelengths generally $h\nu \ll kT$, the classical limit of Planck's law (the Planck's constant does not appear) can be adopted:

$$I_\nu(T) = \frac{2\nu^2}{c^2}kT \tag{2.2}$$

this is called the *Rayleigh-Jeans law*, and rewriting the condition as $\nu/[GHz] \ll 21 \quad T/[K]$ we can infere that it holds for thermal radio sources, except maybe some cold regions in the sub-millimeter range.

An important implication of this approximation is that the brightness and the termodynamical temperature are strictly proportional, so it is common in radio astronomy to measure the intensity of an extended source in terms of *brightness temperature* T_B.

$$T_B = \frac{\lambda^2}{2k}I_\nu(T) \tag{2.3}$$

that is the temperature af a black body that emits the same brightness of the observed source. We introduce the *flux density* S_ν as the integral of the intensity over the solid angle subtended by the source:

$$S_\nu = \int_{source} I_\nu d\Omega = \frac{2k}{\lambda^2}T_B\Omega_s \tag{2.4}$$

It depends on the distance of the emitting source from the observer as d^{-2}, so it is not an intrinsic property of an object like Luminosity. Radio telescopes often measure the flux density, and we can describe it by means of instrumental quantities as

$$S_\nu = 2\frac{P}{\eta A d\nu} \tag{2.5}$$

where P is the power received in the frequency range $d\nu$ from a collecting area A with efficiency η (see Paragraph 2.3). The factor 2 is due to the fact that usually the power is measured in a single polarization channel, so the value is duplicated under the assumption that the same power would be given by the other polarization component. S_ν is measured in units of $W\ m^{-2}\ Hz^{-1}$, but since radio sources have very small flux densities, a special astronomical unit is conventionally used: the Jansky (Jy) is defined as

$$1Jy = 10^{-26}Wm^{-2}Hz^{-1} = 10^{-23}ergs^{-1}cm^{-2}Hz^{-1}. \tag{2.6}$$

Spectral distribution of different types of radio sources are represented in Figure 2.4; the different trends of thermal and non-thermal emitters are clearly visible: at these wavelengths the majority are non-thermal emitters with typical increasing intensity at lower frequencies, while examples of black body radiation are the quiet Sun, the Moon, and the Orion A HII region (only at lower frequencies).

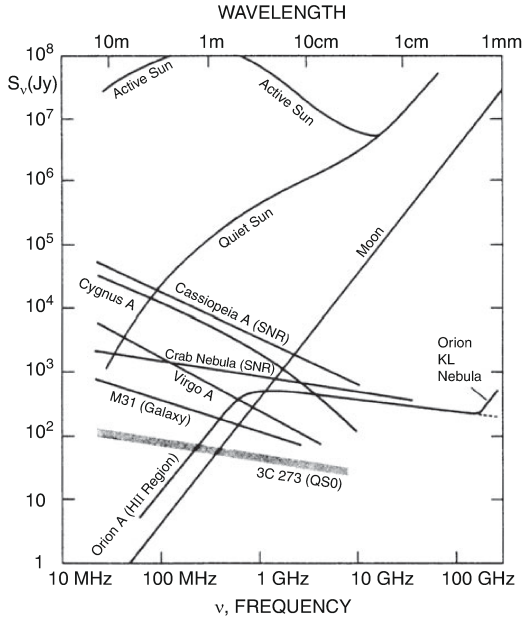

Figure 2.4: Spectral distribution of various radio sources (from Wilson et al. 2013).

2.3 Antenna parameters

The normalized **Power Pattern**, or Beam Pattern, describes the normalized response of an antenna to radiation, as a function of the spherical coordinates θ (latitude) and ϕ (longitude):

$$P_n(\theta, \phi) = \frac{P(\theta, \phi)}{P_{max}} \tag{2.7}$$

where P(θ, ϕ) is the power received by the antenna from the direction (θ, ϕ). Thanks to the Reciprocity Theorem, that states that the properties of a receiving antenna are the same when it is used as a transmitter, we can describe the functioning of antennas when they work in transmission, which sometimes results in a better comprehension. If the antenna was broadcasting, instead of receiving, the power would not be emitted in a perfectly parallel beam, but into a cone of some angle width, this because of the effects of diffraction arising from the finite dimension of the antenna (a graphical representation is given in Figure 2.5).

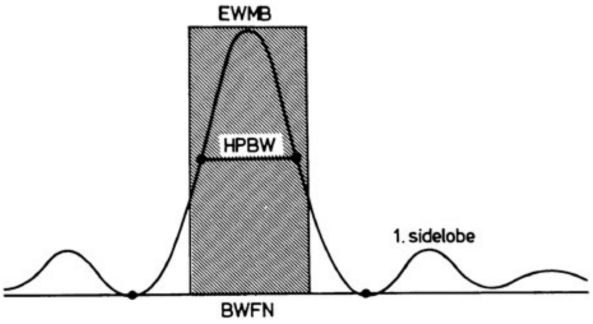

Figure 2.5: The telescope beamwidth with the common notation of one-dimensional power patterns: the HPBW (*Half Power Beam Width*), the EWMB (*Equivalent Width of the Main Beam*) is defined as $\sqrt{12\Omega_{MB}/\pi}$, the BWFN (*Beam Width between First Nulls*) is indicated by the two dots on the zero line (Wilson et al. 2013).

The **Beam solid angle** is expressed by

$$\Omega_A = \int_{4\pi} \int P_n(\theta, \phi) d\Omega = \int_0^{2\pi} \int_0^{\pi} P_n(\theta, \phi) sin\theta d\theta d\phi \tag{2.8}$$

An ideal antenna should have P_n=1 inside Ω_A and P_n=0 elsewhere, but real antennas usually present power pattern with larger values in a certain range of angles then for the rest of the sphere: this range is called the **Main Beam** or main lobe, while the remainder are the *side lobes* or back lobes. The **Main beam solid angle** is defined as

$$\Omega_{MB} = \int_{mb} \int P_n(\theta, \phi) d\Omega \tag{2.9}$$

Hence the quality of one antennas changes depending on how well the power pattern is concentrated in the main beam; one useful parameter is the **Main beam efficiency**

$$\eta_B = \frac{\Omega_{MB}}{\Omega_A} \tag{2.10}$$

that is an indicator of the fraction of the power contained in the main beam, and it is independent from of the angular size of the main beam itself. The angular extent of the main beam is measured with an equivalent indicator: the HPBW (*Half Power Beam Width*), also referred to as the *full width half power* (FWHP), which is the angle between the points of the main beam where the power pattern has half of the maximum value.

2.4 Principles of Interferometry

A central issue in observational astronomy is the quest for angular resolution: the theoretical resolving power of a telescope, ignoring the effects of the atmosphere, depends on the size of its aperture and on the wavelength we are observing, according to the *Rayleigh criterion*

$$\theta = 1.22\frac{\lambda}{D} \tag{2.11}$$

where D is the diameter of the circular aperture, and θ is the minimum angle under which two distinct sources can be distinguished; for radio antennas it is comparable to the angular size of the main beam. Reaching resolutions of fractions of arcseconds like in optical regime would require, for millimeter wavelengths, radio antennas with inconceivably large apertures: e.g. to have a resolution of $0\farcs1$ at 1 mm we would need a ∼2 km antenna. As a comparison we can notice that the resolution of Effelsberg 100 meters antenna at cm wavelengths (∼20″at 1 cm) is comparable to the human eye in the visible range.

Until recently the largest single-dish telescope on Earth was Arecibo, with its 305 meters spherical reflector constructed inside a natural depression in the island of Porto Rico. It has been overcome in 2016 by the FAST telescope, an also not orientable spherical reflector built in a karst depression in the Guizhou province (south of China) and with an aperture of 500 meters in diameter. The largest orientable antenna are Effelsberg, in Germany and the Green Bank Telescope in West Virginia, with reflectors of 100 meters diameters. Building much bigger antennas would be difficult and beyond the limits of current technology. The solution that is world widely adopted is interferometry: combining the signals of several telescopes viewing the same source at the same time, and making use of the Earth's rotation, allows to

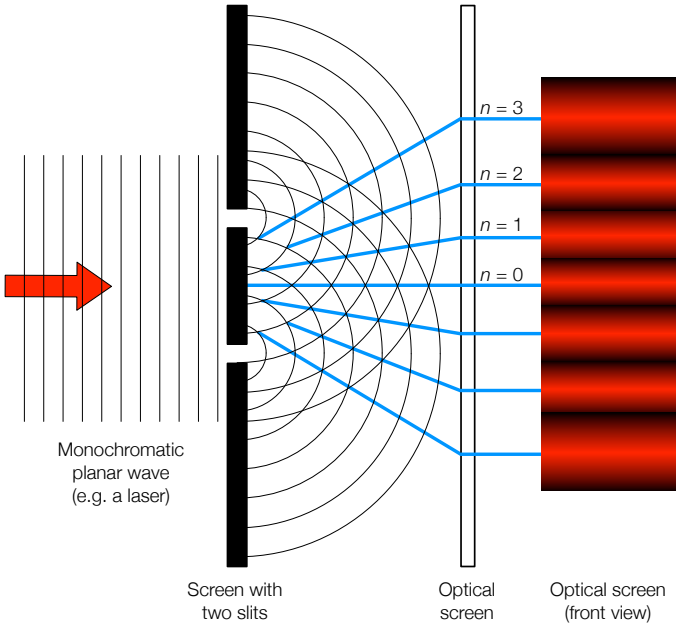

Figure 2.6: Representation of Young's double slit experiment. Credits: Northumbria University 2014-17

reach considerably higher resolutions. Interferometry can be better exploited in radio rather than in the optical range, since atmospheric turbulence has a very small effect on radio waves being the wavelengths larger then the typical turbulence cells, so the wavefronts coherence can be preserved even for wide separations between the telescopes. This technique is based on the interference of electromagnetic waves, as showed in the famous double slit experiment by Thomas Young: when a coherent light source illuminates a plate with two parallel slits separated by a distance d, the wavefronts emerging from the slits produce an interference pattern on a screen placed behind the plate at a distance D (Fig. 2.6).

Under the assumption of $d \ll D$ (the distance of the screen is much larger then the slits separation), the difference in path that the two rays cover when travelling from the plate to the screen result in a phase difference, at an angle θ, of $\phi = kdsin\theta$, where k is the wave number $k = \frac{2\pi}{\lambda}$. When this phase difference is a multiple of π, or in other words, when the difference in path is an integer number of wavelengths, the two waves produce a constructive interference

$$dsin(\theta) = m\lambda \qquad m = 0, 1, 2, ... \tag{2.12}$$

and we see a bright line on the screen. Otherwise, the condition for a destructive interference, that products a minimum (a dark line) in the fringe pattern, is:

$$dsin(\theta) = (m + \frac{1}{2})\lambda \qquad m = 0, 1, 2, ... \tag{2.13}$$

For small angles we can use the approximation $sin\theta \sim \theta$ and the angular distance between consecutive constructive interference is

$$\theta \sim \frac{\lambda}{d} \tag{2.14}$$

that last equation represents the angular resolution of a two-element interferometer: instead of the aperture diameter we have now the distance between the two antenna as a denominator, that means that increasing the separation between the antennas we can increase the resolution of our observations.

2.4.1 The Heterodyne Interferometer

A first clarification between two different kinds of radiometers is needed: **incoherent radiometers** do not preserve the phase and work as direct detection systems. The most common type are *bolometers*, and they make use of the variation of the resistance R of a material with its temperature: when radiation is absorbed the temperature varies and this changes the measure of the intensity of the incident field. Being basically very sensitive thermometers, they have no specific frequency or polarization response and are used in the millimeter and sub-mm range.

In radio interferometers both the amplitude and the phase of the radiation must be preserved, therefore only **coherent radiometers** (commonly *heterodyne* or *superheterodyne* systems) are used: in such systems the frequency of the input is translated to another (usually lower) frequency before processing, the phase of the received wave is preserved and they are sensitive to the single polarization.

The simplest radio interferometer consists of two antennas A_1 and A_2 separated by a distance **B**, called *baseline*, and pointing a distant source in the direction **s** (see Figure 2.7). A plane electromagnetic wave induces the voltage V_1 at the output of the antenna A_1

$$V_1 \propto Ee^{i\omega t} \tag{2.15}$$

while at the output of A_2 we have

$$V_2 \propto Ee^{i\omega(t-\tau_g)} \tag{2.16}$$

where τ_g is the *geometric delay* caused by the difference in path $\mathbf{B}\cdot\mathbf{s}$ to reach the two antennas, that depends on the orientation of the baseline respect to the waves propagation:

$$\tau_g = \frac{\mathbf{B}\cdot\mathbf{s}}{c} \tag{2.17}$$

with **B** representing the baseline vector, directed from antenna A_1 to A_2 and c the speed of light.

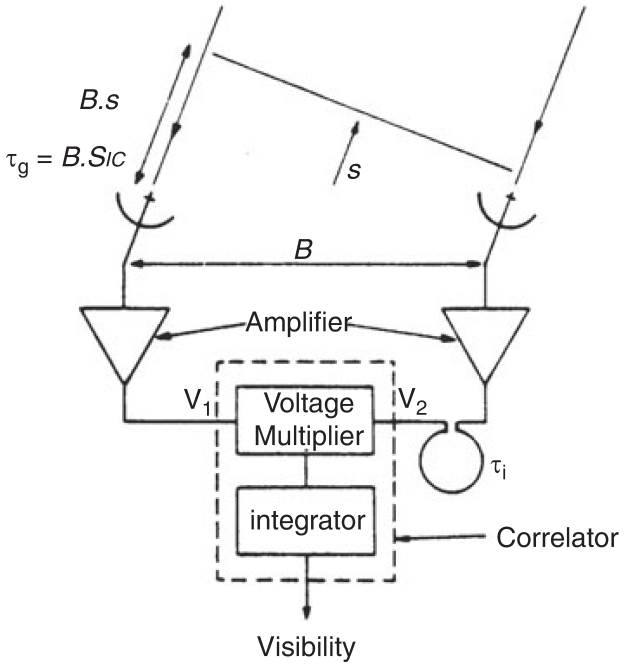

Figure 2.7: Schematic diagram of a two element interferometer Wilson et al. (2013)

The signal coming from each antenna is combined with another strong monochromatic signal of a Local Oscillator (LO), in a way that the resulting frequency is more easily amplified for further processing. The device that performs this frequency shift is the *mixer*, an essential part of heterodyne receivers; this process can bring additional noise but the information contained in the original signal should not be changed. The mixer superimposes the two signal to produce an output like

$$I(t) = a_0 + a_1(V(t) + V_{LO}(t)) + a_2(V(t) + V_{LO}(t))^2 + a_3(V(t) + V_{LO})^3 + ...$$

Inserting a filter at the output of the mixer allows to select only the ν such that

$$\nu_{IF} - \frac{\Delta\nu}{2} \leq |\nu - \nu_{LO}| \leq \nu_{IF} + \frac{\Delta\nu}{2} \tag{2.18}$$

where ν_{IF} is an Intermediate Frequency, significantly different from the original radio frequency. After mixing and filtering, the original signal is shifted to a frequency $\nu - \nu_{LO}$ or $\nu_{LO} - \nu$, it is proportional to the original electric field E and to the voltage of the local oscillator Q; the phase may be shifted by a constant value becoming $\phi - \phi_{LO}$ or $\phi_{LO} - \phi$. In other

words the output of the receiver is

$$\begin{cases} I(t) \propto EQe^{i[2\pi(\nu-\nu_{LO})t+\phi-\phi_{LO}]} \\ or \\ I(t) \propto EQe^{i[2\pi(\nu_{LO}-\nu)t-\phi+\phi_{LO}]} \end{cases}$$

where the other components resulting from the superimposition of the two signals are blocked by the bandpass filter. A mixer that accepts simultaneously frequencies higher and lower than the local oscillator frequency is called Double Side Band (DSB) receiver: the two ranges are called Upper Side Band and Lower Side Band (see Fig. 2.8) and the receiver cannot a priori distinguish between them.

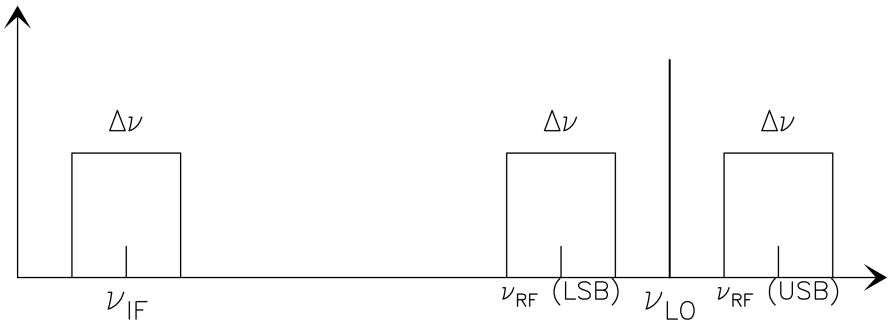

Figure 2.8: Relation between the original radio frequency (ν_{RF}), the intermediate frequency (ν_{IF}) and the local oscillator frequency (ν_{LO}) in an heterodyne system. The intervals of frequency on the sides of ν_{LO} are the Lower Side Band (LSB) and the Upper Side Band (USB). Credits: Stèfane Guilloteau, “Millimeter Interferometers" in IRAM Millimeter Interferometry Summer School, 1998

The output IF signals are amplified, then combined together and time-averaged into a *correlator* (Fig. 2.7). The output voltage of each antenna is composed by the source signal (V_S) and the noise of the receiver (V_R), so

$$V_1 = V_S + V_{R1} \qquad V_2 = V_S + V_{R2} \tag{2.19}$$

These signal can be combined in different ways: in *adding* interferometers the squared sum of the signal is evaluated:

$$\langle (V_1 + V_2)^2 \rangle = \langle V_{R1}^2 \rangle + \langle V_{R2}^2 \rangle + 4\langle V_S^2 \rangle \tag{2.20}$$

where the mixed products like $V_{R1} \cdot V_{R2}$ do not correlate and can be set to zero. Here we can notice that the noise from the two receiver is included in the output, so the source signal is ″buried″ in the total output; a consequence is that in presence of fluctuating gains of the receivers, it is difficult to evaluate the original signal.

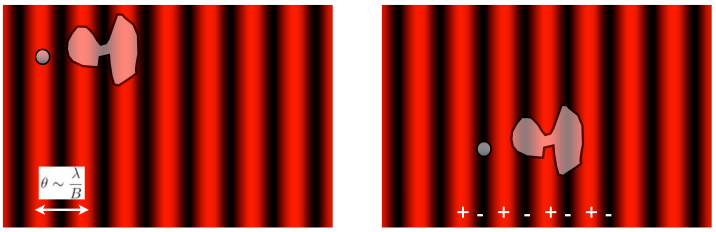

Figure 2.9: Simplified representation of a fixed 2 elements interferometer east-west oriented: as the sources move with the rotation of the Earth, the complex output of the interferometric system will vary depending on the alignment between the structures and the fringes at a given time. In the figure the small source is not resolved since it is smaller that the difference between two positive (or negative) fringes, while the larger irregular source is resolved (from Garrett, M., Course o Radio Astronomy (2013), Netherlands Institute for Radio Astronomy)

But if we multiply the signals instead of adding them, we obtain

$$\langle (V_1 \cdot V_2) \rangle = \langle V_{R1} V_S + V_{R1} V_{R2} + V_S V_{R2} + V_S^2 \rangle = \langle V_S^2 \rangle \tag{2.21}$$

where the simplification is performed by setting to zero the uncorrelated terms. In this case the output is restricted to the source signal, and we are in presence of a *multiplying* interferometer. The correlator is called a *cross-correlator* and it is used in the majority of modern radio interferometers.

Therefore, the output of the *correlator* is

$$R(\tau) \propto E^2 e^{iw\tau} \tag{2.22}$$

it varies periodically with the delay τ, that can be identified with the difference between the geometrical delay τ_g and the instrumental delay τ_i

$$\tau = \tau_g - \tau_i \tag{2.23}$$

As τ slowly varies because of the Earth's rotation (the pointing direction $\mathbf{s}$ of the telescopes changes as the antennas track the source in the sky), the direction of the constructive/destructive interferences scan the source in the sky and we will measure *interference fringes* as a function of time (see Figure 2.9). If the size of the source is bigger than the distance between two adjacent positive or negative fringes, it becomes *resolved out* and the response of the interferometer remains the same as the source moves across the sky. For the imaging of these larger structures short baselines are required; on the other hand, long baselines are necessaries to measure small sized sources. To evaluate if an object is resolved, we define the *fringe visibility* V_M as the ratio

$$V_M = \frac{I_{max} - I_{min}}{I_{max} + I_{min}} \tag{2.24}$$

with I_{max} and I_{min} the maximum and the minimum of the intensity of the resulting image. The fringe visibility is equal to 1 if we are observing a point-like source, and we are able to see the zero intensity of the destructive interferences (dark fringes); otherwise if the visibility is less than the unit, the object is said to be resolved (see Figure 2.10).

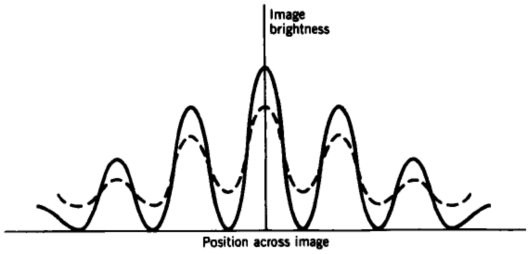

Figure 2.10: The intensity of an image as a function of the angle from the center, in a direction parallel to the spacing between the antennas. The solid line shows the profile for a point-like source with fringe visibility V_M equal to 1; the dashed line represents a partially resolved star with V_M=0.5. Thompson et al. (2001)

It is possible to express the visibility as a function of the aperture separation (baseline) and other measurable quantities: we can notice that for a source of brightness $I_\nu(\mathbf{s})$, the power received per bandwidth $d\nu$ from the element of solid angle $d\Omega$ is $A(\mathbf{s})I_\nu(\mathbf{s})d\Omega d\nu$, where $A(\mathbf{s})$ is the effective collecting area in the direction $\mathbf{s}$, and we will assume it is the same for each antenna. The total response of the interferometer is obtained by integrating over the solid angle covering the source S:

$$R(\mathbf{B}) = \int_\Omega \int A(s) I_{\nu(\mathbf{s}} exp\left[i2\pi\nu\left(\frac{1}{c}\mathbf{B}\cdot\mathbf{s} - \tau_i\right)\right] d\Omega d\nu \tag{2.25}$$

The function $R(\mathbf{B})$ is called *Visibility Function*, and the main challenge of interferometry is to retrieve the best representation of I_ν from $R(\mathbf{B})$ in presence of errors.

In this description we are undertaking two main assumptions: first, the incoming radiation is a plane wave, so we receive plane and parallel wavefronts perpendicular to the direction of propagation (the source we are observing is in the *far field* of the telescope). Second, the source must be spatially incoherent, that is, the waveforms radiated from different angular elements $d\Omega$ are uncorrelated (i.e. independent).

So far we have considered a monochromatic radiation, but what we really detect is a sum of waves of slightly different frequencies that are included in the bandwidth $\Delta\nu$ of the receiver: while the geometrical delay $\tau_g = \mathbf{B}\cdot\mathbf{s}/c$ is independent from the frequency, the same may not be true for the instrumental delay τ_i. Furthermore, a certain range of wavelengths in the incoming radiation will cause a spread in the number of λ that covers the path

difference $\mathbf{B} \cdot \mathbf{s}$ between the two antennas: if this $\Delta\lambda$ becomes closer to λ, there will be no longer a well-defined phase difference between the two signals and the fringe will disappear. What is done to prevent the washing-out of the fringes is adjusting τ_i by inserting a delay between the antennas, in a way that the total delay $\tau = \tau_g - \tau_i$ is zero in the center of the band; this way, the two path lengths from the source to the multiplier are nearly equal. In the first interferometers this was done by switching the length of cables in the system, today the signal is digitalized after the conversion to the intermediate frequency, and then it passes trough a digital shift register. This adjustment is equivalent to centering the response of the interferometer in the central fringe in Young's double slit experiment, and it is referred to as *fringe stopping*.

2.4.2 A coordinate system for interferometry

The first step for determining the brightness I_ν from the Visibility function is to choose a convenient coordinate system. First we write the unit vector $\mathbf{s}$, pointing toward a chosen origin, as

$$\mathbf{s} = s_0 + \sigma \qquad |\sigma| = 1 \tag{2.26}$$

where s_0 is a position close to the center of the region of investigation. Substituting in eq.(2.25) we obtain

$$R(\mathbf{B}) = exp\left[iw\left(\frac{1}{c}B \cdot s_0 - \tau_i\right)\right] d\nu \int_S \int A(\sigma)I(\sigma)exp\left(i\frac{w}{c}\mathbf{B} \cdot \sigma\right) d\sigma \tag{2.27}$$

where the first exponential defines the phase of $R(\mathbf{B})$ in the center of the image, and the integral is the *visibility* V:

$$V(\mathbf{B}) = \int_S \int A(\sigma)I(\sigma)exp\left(i\frac{w}{c}\mathbf{B} \cdot \sigma\right) d\sigma \tag{2.28}$$

Remembering that the phases of the correlated signals are set to have a zero delay in the center of the image, we can see that the visibility V is referred to this position. We now specify the baseline vector $\mathbf{B}$ in a new coordinate system (u, v, w), such that

$$\frac{w}{2\pi c}\mathbf{B} = (u, v, w) \tag{2.29}$$

where w in chosen in the direction of the source s_0, u points in the local east direction and v in the north direction; the three coordinates are expresses in units of wavelength $\lambda = 2\pi c/\omega$.

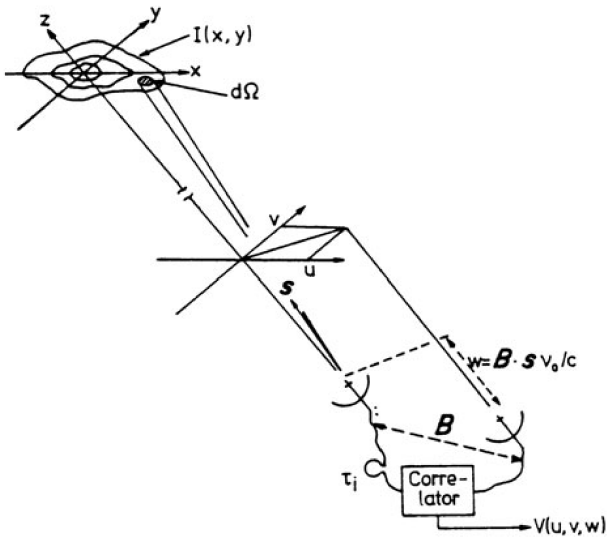

Figure 2.11: A representation of the geometry and coordinates for interferometric observations. Wilson et al. (2013)

The vector $\sigma = (x, y, z)$ is defined in cartesian coordinates, where xy plane is a projection of the celestial sphere into a tangent plane, with tangent point and origin defined by s_0; the position in the sky is defined by the direction cosines x, y and z with respect to the u, v and z axis (Figure 2.11). The relations between these sets of coordinates are

$$\begin{cases} \nu\mathbf{B}\cdot\mathbf{s}/c = ux + vy + wz \\ \nu\mathbf{B}\cdot s_0/c = w \\ z = \sqrt{1-x^2-y^2} \\ and \\ d\Omega = \frac{dxdy}{z} = \frac{dxdy}{\sqrt{1-x^2-y^2}} \end{cases}$$

Expressing the visibility in Fourier-space coordinates we have

$$V(u,v,w) = \int_{-\infty}^{\infty}\int_{-\infty}^{\infty} A(x,y)I(x,y)exp\left[i2\pi(ux+vy+w\sqrt{1-x^2-y^2})\right]\frac{dxdy}{\sqrt{1-x^2-y^2}} \quad (2.30)$$

with the integrals extremes are set to ∞ under the assumption that $A(x, y) = 0$ outside the primary beam of the telescope.

This expression resembles a two dimensional Fourier integral, if it wasn't for the factor $w\sqrt{1-x^2-y^2}$; but if the region of the sky to be mapped is sufficiently small then $\sqrt{1-x^2-y^2} \cong const \cong 1$, and 2.30 becomes

$$V(u,v,w)e^{-i2\pi w} = \int_{-\infty}^{\infty}\int_{-\infty}^{\infty} A(x,y)I(x,y)e^{i2\pi(ux+vy)}dxdy \quad (2.31)$$

The factor $e^{-i2\pi w}$ is the phase correction to apply to the observed V to measure the visibility in the uv plane ($w = 0$):

$$V(u, v, w)e^{-i2\pi w} = V(u, v, 0) \tag{2.32}$$

Sobstituting in (2.31) and performing the inverse Fourier transform we obtain

$$I'(x, y) = A(x, y)I(x, y) = \int_{-\infty}^{\infty} V(u, v, 0)e^{-i2\pi(ux+vy)}dxdy \tag{2.33}$$

where $I'(x, y)$ is the brightness distribution on the sky $I(x, y)$ modified by the primary beam shape A(x,y) of the individual antennas (we had taken before the assumption of the two antennas having the same effective collecting area $A(\mathbf{s})$). The u, v plane is often referred to as the *Fourier plane* or *pupil plane*, the (u, v) values are often expressed in units of the observing wavelength λ; their Fourier transform pairs are in units of radians and since they define the image, the x, y plane is called the *image plane*. The (u, v) coordinates represent the Fourier components of the sky brightness, hence the interferometer acts as a linear filter in the Fourier space, selecting some of the Fourier components depending on the array configuration. Since we need to reconstruct the sky brightness from the visibilities, this filtering affects the image fidelity (see Sect. 2.5).

A crucial parameter in interferometric observations is the *uv coverage*: when the antennas are pointing a target in the sky, they measure the visibility function in a point (u,v) of the plane; as the Earth rotates and the telescope keeps tracking the source, the projected baseline changes, and after 24 hours of observations it draws an ellipse in the uv plane.

If we have more than two elements in our interferometer and they are placed at different mutual distances, the uv coverage is improved since different baselines correspond to different *uv-distances* (the distance from the origin of the uv coordinates system); a simplified scheme of the uv coverage of a three element interferometer is given in Figure 2.12.

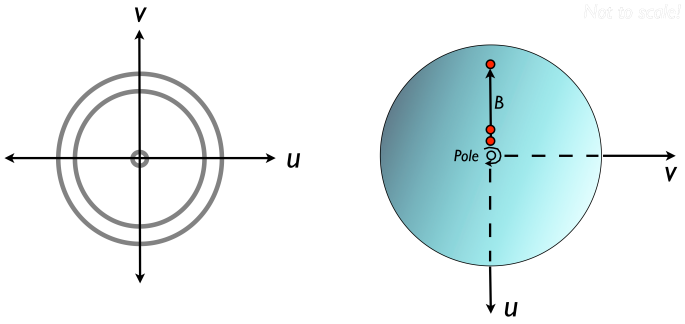

Figure 2.12: Sampling of the uv plane for 3 antennas defining 3 different baselines, seen by a source located at the Pole: as the Earth rotates, the projection of the baseline vectors doesn't change but their direction does, thus the baselines trace a circle in the uv plane.

It is worth noticing the fact that the visibility V(u,v) is equal to its complex conjugate V*(u,v): the orientation of the baseline formed by two antennas clearly repeats (with only the phase reversed) after half a rotation of the Earth; that means that after 12 hours observation no new information is obtained if we keep tracking the source for a complete rotation.

We call **Visibilities** the measurements we collect as we scan portions of the u, v plane, and they consist of the values of amplitude and phase of the correlator output for each baseline, at a given time. Of course the observation time on the sources is usually much less than 24h, so we cover only arcs of ellipses in the uv plane: the ensemble of such (portions of) ellipses is the *uv* coverage. An example is given in Figure 2.13, with a *uv* plane sampling of the VLA interferometer for different declinations of the source and different integration times.

The antenna configurations in a radio telescope are chosen to cover the uv plane as much as possible: the more the uv plane is filled, the higher will be the quality and fidelity of the final images.

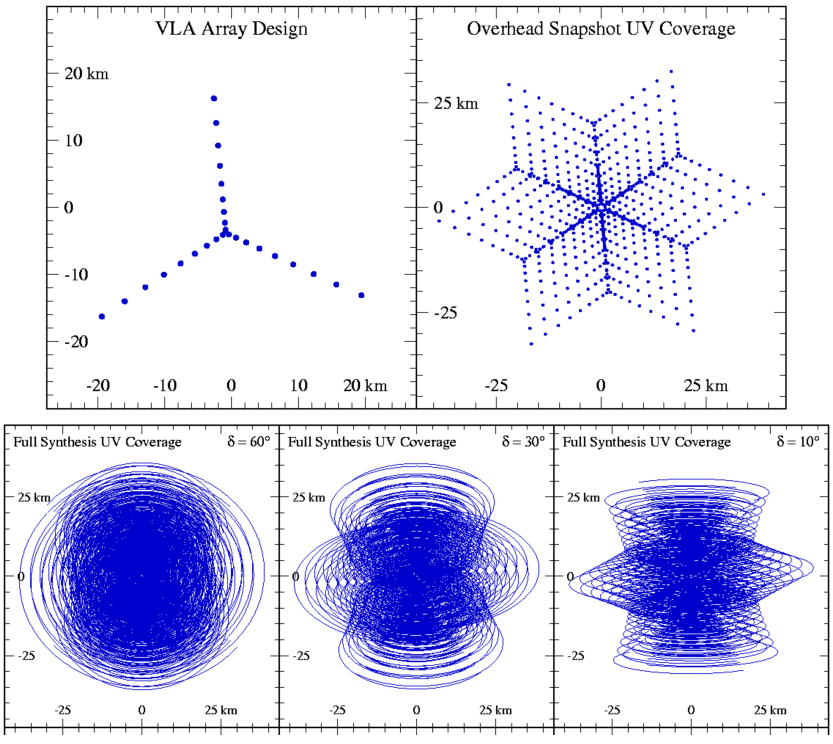

Figure 2.13: Above: antenna positions of the A-array (maximum baseline of 36 Km) of the Very Large Array in New Mexico (left), and the uv coverage for a single scan, showing the instantaneous location of the baselines in the uv plane (right).
Below: full synthesis (or *full track*, meaning that the measurements of the target are extended for a few hours) VLA observation for sources at different declinations.

2.5 Aperture Synthesis

Aperture Synthesis is the standard method used to produce high resolution images by combining a number of independent visibility measurements. The imaging process consists in determining as best as possible the sky brightness distribution $I_\nu(x, y)$ that appears in equation 2.31. This process is not straightforward since the response of the interferometer is affected by some limitations: there is a limit to the angular resolution given by the maximum values of (u, v); also the minimum spacing between two antennas will set a minimum u, v distance in our mapping. Finally the limited coverage of the uv plane due to the missing (u, v) component, or spacial frequencies, gives rise to a worse estimate of the image. Another issue derives from the fact that instrumental noise and the atmospheric variations corrupt our measured visibilities, that therefore need to be adjusted, or *calibrated*, to retrieve their true values.

2.5.1 Gridding *uv* Data

Even for small data sets, the calculation of an image from the (u, v) data is quite time consuming; for this reason the observational data in the u, v plane must be arranged in a computationally optimized way. The method that is generally used to to speed the calculations for the inverting of Eq. (2.31) is the Fast Fourier Transform algorithm (FFT): for it to be efficient, the visibilities must be placed in a regular grid. Since the observation hardly lie in such regular patterns, an interpolation scheme has to be used, and the best way to carry it out is through a convolution procedure. The *gridded visibility function* can be represented as

$$V''(u, v) = III(u, v)G(u, v) \otimes V'(u, v) \tag{2.34}$$

where $V'(u, v)$ is the measured function, $G(u, v)$ is a convolving function, $\otimes$ is the convolution operator, so that an interpolated function $V''(u, v)$ is defined for every (u,v). III is the Sha function

$$III(u, v) = \Delta u \Delta v \sum_{j,k=-\infty}^{\infty} \delta(u - j\Delta u)\delta(v - k\Delta v) \tag{2.35}$$

defining a grid with cells of size Δu and Δv. Substituting this new interpolated visibility to V(u,v,0) in Eq. (2.33), recalling that the Fourier transform of the Sha function is another Sha function but with cell size $1/\Delta u$ and $1/\Delta v$, and applying the Convolution Theorem (which

states that the Fourier transform of a product of functions is the convolution of their Fourier transforms) to Eq. (2.34), we have that the intensity distribution is given by

$$I(x, y) = III(x, y) \otimes [g(x, y)I'(x, y)] \tag{2.36}$$

where g(x,y), the Fourier transform of G(u,v), is the *grading function* that gives rise to the beam G(u,v). From this relation we can observe that if the grading function $g(x, y)$ is not equal to zero outside the image area, which usually happens for most practical convolving functions, radiation from outside this region can be *aliased*, or ′folded back′ into the image, so this overlapping leads obviously to a loss of information. Undersampling and truncated sampling at the limits of the u, v coverage are the main causes of aliasing.

The best ways to avoid these kind of issues are: making a image large enough so that we don't risk to have sources of interest near the edges, do not undersample the observational data, and use a convolution function $G(u, v)$ whose Fourier transform $g(x, y)$ drops very fast beyond the limits of the image. This last condition would require convolution functions that are not highly confined in the u, v plane, but that would imply an increase in the computing time. A compromise between these two limitation leads to a limited choice of G functions: typically a *pillbox* function (G = 1 for $u^2 + v^2 \leqq u^2_{max}$, G=0 otherwise), a truncated exponential, a truncated *sinc* function, or other combinations of the preceedings.

2.5.2 Dirty Map and Dirty Beam

Considered that our observations lead to a discrete distribution of the visibilities, we will look on a version of (2.33) involving a summation instead of an integral, and define the image resulting from a discrete Fourier transform as the **Dirty Image**:

$$I_D(x, y) = \sum_k w(u_k, v_k)V(u_k, v_k)e^{-i2\pi(u_k x + v_k y)} \tag{2.37}$$

where $w(u, v)$ is a weighting function, used to compensate the partial coverage of the u, v plane by assigning variable weights to each grid cell after the gridding process. The most common choices are

$$\begin{cases} w(u_k, v_k) = 1, & \text{Natural Weighting} \\ w(u_k, v_k) = \frac{1}{N_s(k)} & \text{Uniform Weighting} \end{cases}$$

where $N_s(k)$ is the number of data points within a symmetric region of the (u,v) plane of characteristic width s, centered on the k^{th} point. *Natural weighting* treats all points the same and

gives the best signal-to-noise for detecting weak sources, but it emphasize the data relative to short u, v distances and thus produces a bigger beam, meaning a lower angular resolution. On the opposite, *Uniform weighting* gives more weight to long baselines resulting in a smaller beam, the drawbacks being increased inner sidelobes and an inevitable loss of sensitivity. But these are only extreme cases, what is usually done is choosing an intermediate weighting, a *robust weighting*, that combines the advantages of the Natural and Uniform weighting, by increasing the resolution and lowering the sidelobes without degrading too much the signal-to-noise of the image.

The dirty image, or dirty map, $I_D(x, y)$ is not a fine representation of $I'(x, y)$, but they are related by

$$I_D(x, y) = P_D(x, y) \otimes I'(x, y) \tag{2.38}$$

where $P_D(x, y)$ is called the **Dirty Beam**, that is the response of the system to a point source:

$$P_D = \sum_k w(u_k, v_k) e^{-i2\pi(u_k x + v_k y)} \tag{2.39}$$

it is the equivalent of the *point spread function* in optical observations, and can be understood as a transfer function that distorts the image.

Summarizing what described above: after performing an inverse Fourier transform on our visibility data to obtain a Dirty Image, a deconvolution is required to retrieve the brightness distribution (modified by the interferometer primary beam A(x,y)) $I'(x, y)$. Deconvolution is alway a non-linear process, and it is necessary to formulate a series of hypothesis and constraints to help selecting plausible solutions; we will get into more details in the next paragraph.

2.5.3 The CLEAN Method

The CLEAN algorithm, conceived by J. Högbom in 1974, is the standard method used to derive the solution of the convolution in Eq. 2.38, and it relies on the assumption that the radio source we want to image is an ensemble of a finite number of point sources in an empty background. The position and strength of these point sources is found with an iterative approach, and the final deconvolved image results in a sum of these point components convolved with

a CLEAN beam, usually Gaussian. A simple scheme of the algorithm can be summed up in the following steps:

1. Make the dirty map, and find the strength and position of the brightest point.

2. Subtract from the dirty image, at the position of the peak, some scaled fraction (e.g. 10%) of the dirty beam and store the position and intensity in a model as a ″CLEAN component″.

3. Go back to point 1: find the strongest source in the new dirty map, unless the peak is below some threshold specified by the user, or the number of iteration N_iter is too large than some specified value; the goal is to remain only with noise left in the map.

4. Take all the CLEAN components, add back the residual noise left in the dirty image, and convolve them with a properly chosen CLEAN beam (usually a Gaussian fitted to the central lobe of the dirty beam).

Using a mathematical representation, the CLEAN iterations aim to determine the intensities $A_i(x, y)$ such that

$$I''(x, y) = \sum_i A_i P_D(x - x_i, y - y_i) + I_\varepsilon(x, y) \tag{2.40}$$

where I'' is the dirty map obtain by the Fourier inversion of the visibility function, P_D is the dirty beam, and I_ε is the residual brightness distribution after the decomposition. The summation is taken over a finite number i of point sources. We can say to have performed a good CLEAN if I_ε is of the order of the noise in the measured intensity, as mentioned in point 3.

Several modification to the original algorithm have been made (e.g. *Clark*, *Cotton and Shwab*) to reduce the computing time; however the validity of this method and its capability to produce realistic images is still an open question, related to the non uniqueness and instability of the solutions (when more visibilities are added, the solutions change drastically), this is related to the non-linearity of the operation.

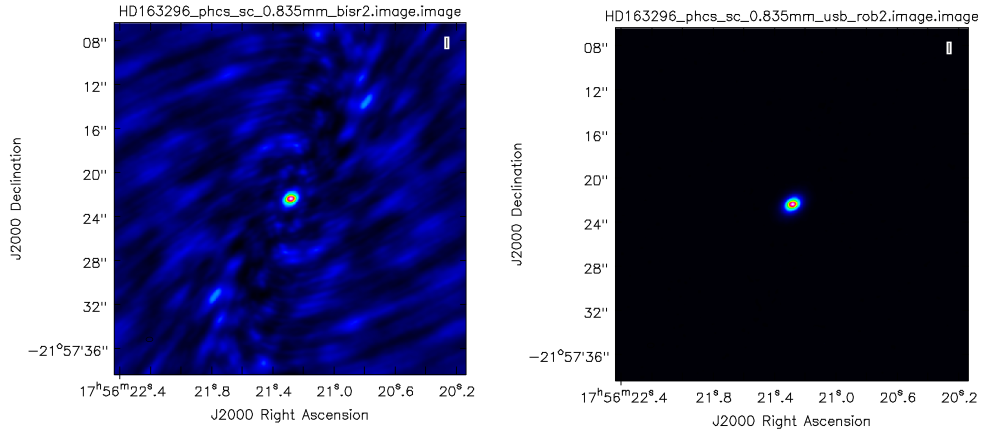

Figure 2.14: Dirty map (on the left) and CLEANed map (on the right) of ALMA Band 7 observations of HD163296 protoplanetary disk (see Chapter 4). The artifacts in the dirty map are related to the incomplete uv coverage, and they are abundantly reduced in the final image after a few thousand iterations.

2.6 The *Atacama Large Millimeter Array*

2.6.1 The ALMA Project

ALMA (the Atacama Large Millimeter/submillimeter Array) is one of the largest ground-based international astronomy projects, and will be the major facility for millimeter and submillimeter observations for the years to come. It consists in a complete astronomical imaging and spectroscopic instrument for the millimeter/submillimeter regime, providing capabilities and wavelength coverage that complement those of other similar telescopes of this epoch, such as the Very Large Array (VLA), James Webb Space Telescope (JWST), the optical/infrared 39m-class telescopes (TMT, E-ELT, etc...), and the Square Kilometer Array (SKA). In particular, ALMA is now filling a scientific gap by providing a sensitive, high-resolution probe of the cold gas and dust properties of star-forming region in our Galaxy, other galaxies, and in protoplanetary disks, which are otherwise obscured at shorter wavelengths.

The first idea in Europe, United States and Japan to build a new generation of millimeter interferometer goes back to the 1990's, and it was soon realized that such an ambitious project needed a joint collaboration to be realized. From the first resolution between ESO (European Southern Observatory) and NRAO (National Radio Astronomy Observatory) to pursue a common project in 1997, many efforts have been done for the organization and discussion of the details, then in 2002 the choice of a plateau at 5000m in Chile as the location,

and finally in 2004 an agreement between ESO, the NSF (National Science Foundation), and NINS (the National Institutes for Natural Sciences, Japan) concerning the construction of the enhanced Atacama Large Millimeter/submillimeter Array was signed. The final project was decided to be cost-shared in 37.5% / 37.5% / 25% between North America, Europe, and Japan, respectively; with the observing time assigned accordingly to these percentages, after subtracting a 10% share for Chile. In 2003 the construction begins and the first prototype antenna is tested at the ALMA Test Facility (ATF) site in New Mexico, in 2007 the first antenna arrives in Chile, in October 2011 ALMA opens his eyes: the Cycle 0 Early Science observations starts with 16 antennas; and finally in 2013 the ALMA inauguration.

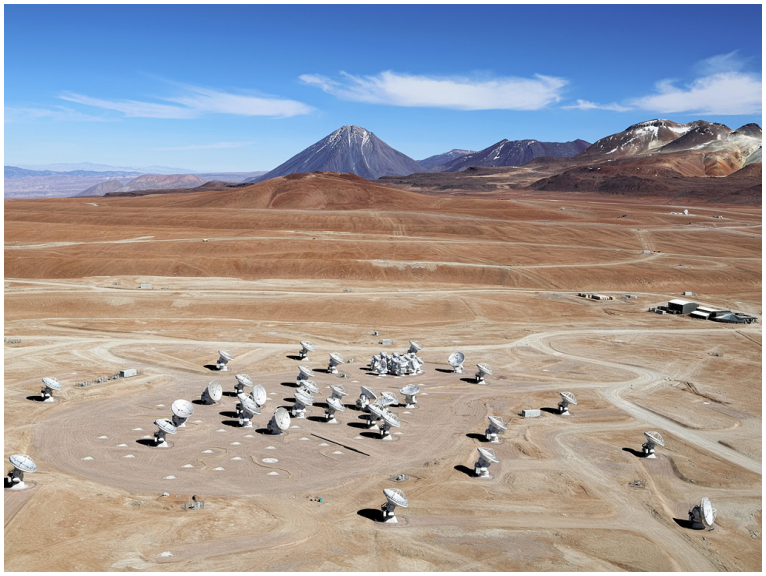

Figure 2.15: Aerial view of the Chajnantor Plateau, located at an altitude of 5000 meters in the Chilean Andes, where ALMA antennas is located. The large antennas have a diameter of 12 meters, while 12 smaller antennas with a diameter of 7 meters make up the ALMA Compact Array (ACA). On the horizon, the main peaks from right to left are Cerro Chajnantor, Cerro Toco, and Juriques. This photo was taken in December 2012, four months prior to the ALMA inauguration. Courtesy of ALMA (ESO/NAOJ/NRAO).

2.6.2 Observing with ALMA

ALMA has an unique location: the Chajnantor plateau in the Chilean Andes, at 5000 meters altitude and -23°latitude, presents an extremely dry and stable environment, and its wide plateau allows the positioning of the antennas over a region of about 16Km extension. The complete ALMA array consists of 66 high precision antennas: 50 antennas of 12 meters diameter, which can provide a very high angular resolution and sensitivity, and the so-called ALMA Compact Array (ACA), formed by 4 antennas with a 12 meters diameter and 12 an-

tennas with a 7 meters diameter, designed for extended structures (Figure 2.15). The antennas can be moved by means of heavy haulers to change the baselines distribution, obtaining more extended or more compact arrays depending on the science purpose.

The frequency spectrum covered by ALMA goes from 31 GHz to 950 GHz, with 10 spectral band available in this range (Figure 2.16). The top spatial resolution reached by ALMA is 5 milli-arcseconds at 900 GHz (better than the VLA and HST) and about 40 milli-arcsecond at 100 Hz, and the top velocity resolution is better than 0.05 km/s. The scientific fields that can benefit from this facility are several, however the main goals that drove the ALMA project are: the ability to detect spectral lime emissions from CO or CII from a galaxy at a redshift $z \simeq 3$ in 24 hours; the ability to image the gas kinematics in protostars and protoplanetary disks at small distances from the Sun ($\sim$ 150 pc); the capability to provide high dynamic range images at sub-mm wavelengths with resolutions of 0.1 arcseconds.

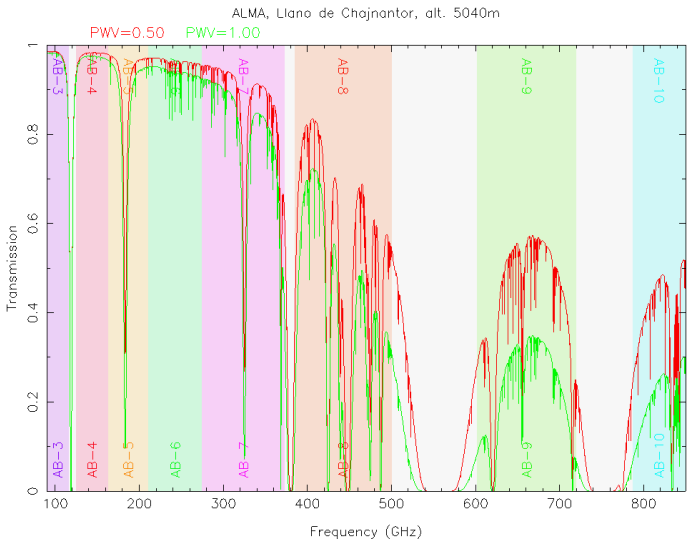

Figure 2.16: Athmospheric transmission between 90 and 900 GHz, for typical values of precipitable water vapor (0.5 and 1 mm) on Llano de Chajnantor. The vertical coloured columns represent the ALMA bands. The plot has been generated in the ALMA Science Portal (under *Home* → *About* → *Atmosphere Model*).

The Field of View (FOV) of the observations is given by the FWHP of the antenna primary beam, thus it is independent from the array configuration. At 300 GHz ($\sim$1 mm) the FOV is about 21 arcseconds; if a region larger then the main beam needs to be imaged, the mosaicking technique is necessary. The ALMA observations are conducted in Service Mode (by ALMA staff) with flexible scheduling, they are carried out 24 hours per day, apart from maintenance periods, and they are executed in the form of Scheduling Blocks (SBs), which contain all the necessary information to execute the observation. The output for astronomers

include calibrated data and processed images.

The observations are available in dual polarization (XX and YY) for a better sensitivity, or in single polarization mode (XX or YY) for a better spectral resolution; starting from Cycle 3, observations of the XY and YX components make possible to measure linear polarization.

2.7 The *Very Large Array*

Figure 2.17: The 25-meters antenna of VLA (Socorro, New Mexico) in their Y-shape array. Courtesy of NRAO/AUI.

The VLA (now called the Karl G. Jansky-Very Large Array) is one of the worlds's majors radio telescope, is situated in the Plains of San Agustin, west of Socorro (New Mexico), and consists of 27 antennas of 25 meters diameter, providing 351 individual baselines in the Y-configuration (see Figure 2.17). Working in interferometric mode, it can reach a resolution equal to a 36 Km aperture, and a collecting area of a 130 meters dish in diameter. The Y-shaped array can be arranged in four different configuration: A, B, C or D, corresponding to a maximum antenna separation of 36.4 Km, 11.1 Km, 3.4 Km and 1 Km respectively. The telescopes are switched between these configuration approximately every four month. The VLA resolution depends on the array configuration, for the maximum available frequency (43GHz) it gives a resolution of 0.04 arcseconds; the angular resolution and other parameters of the different VLA bands are reported in Figure 2.18.

The Expanded Very Large Array (EVLA) was a project aimed at the improvement of the

Receivers Available at the VLA								
	4 Band	**P Band**	**L Band**	**C Band**	**X Band**	**U Band**	**K Band**	**Q Band**
Frequency (GHz)	0.073-0.0745	0.30-0.34	1.34-1.73	4.5-5.0	8.0-8.8	14.4-15.4	22-24	40-50
Wavelength (cm)	400	90	20	6	3.6	2	1.3	0.7
Primary beam (arcmin)	600	150	30	9	5.4	3	2	1
Highest resolution (arcsec)	24.0	6.0	1.4	0.4	0.24	0.14	0.08	0.05
System Temp	1000-10,000.K	150-180.K	37-75.K	44.K	34.K	110.K	50-190.K	90-140.K

Figure 2.18: VLA parameters for the eight different observational bandwidth. Courtesy of NRAO.

already existing Very Large Array (VLA), in terms of increased sensitivity, resolution and imaging capability. It has been designed to improve by a factor of 10 or more the capabilities of VLA, its major specifics are: an angular resolution of 10 milliarcseconds (at 23 GHz), a sensitivity of less then 1 microJy (in the range 1-40 GHz), a frequency resolution from 0.1 Hz to 1 MHz, with a minimum of 16 384 spectral channels; a spatial dynamic range greater than 10^6, frequency dynamic range greater than 10^5, and an image field of view of 10^9 pixels. To achieve these goals, new receivers with higher frequency range have been mounted, two new bands (Ka and S) and much wider bandwidth have been added finally a new compact configuration ('E') has been introduced , for low brightness wide-field mosaicking capability. Some examples of the science goals that inspired the EVLA project are: obtain the highest resolution of high redshift galaxies, resolve the center of quasars and the dusty cores of galaxies, analyze Novae expansion, and provide AU-scale images of massive star formation. Concluding, VLA produces similar sensitivity and resolution as ALMA, but at centimeters wavelengths, so they can be considered to a great extent complementary instruments.

3 High contrast imaging

Direct imaging is an observing technique used for the detection of exoplanets from their thermal emission (see Section 1.1.1). This method is potentially very powerful, as a direct detection permits a spectroscopic and photometric characterization of the planetary companions, but also is sensible to a wide range of planet-star separations (≥5 au), respect to other methods such as radial velocities, transits or microlensing (see the review by Fischer et al. 2014). However, separating the light of the planet from the much brighter central star constitutes an arduous technical challenge: in order to reach the necessary high performances, a combination of optical solutions and post-processing of the data must be applied. In this Chapter I will give an overview of the instruments and the reduction techniques that are employed in this field, with a particular attention to the NIRC2 detector mounted at the Keck telescope, which I have used for my thesis work.

3.1 Instrumentation

The main issue in the direct imaging of exoplanets is removing the light from the central star: even in absence of atmospheric turbulence and even considering ideal optical components, a point source creates a diffraction pattern on the detector, due to the finite aperture of the telescope and the internal optical elements. A circular aperture generates a series of bright and dark rings, where most of the light ends in the central bright maximum (or *Airy disk*, see Figure 3.1). In order to remove this diffraction pattern that could hide a possible planetary emission, coronographic masks are used to block the light of the on-axis star. A broad range of different coronographs have been developed over the years, starting from simple occulting elements to modern phase masks (see Section 3.1.1). These devices can remove diffraction

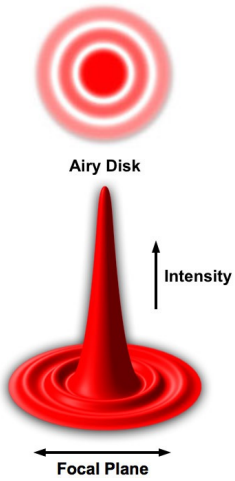

Figure 3.1: Diffraction figure from a circular aperture, the major fraction of the light from the point source is concentrated in the first maximum (Airy disk). Adapted from *Carl Zeiss Microscopy Online Campus*.

down to a level of several orders of magnitude ($\gtrsim 10^{-4}$) of the central peak emission, beyond a minimum separation from the central star called Inner Working Angle (IWA), typically of the order of 2-4λ/D where λ is the observing wavelength and D is the aperture diameter of the telescope.

Another important effect is due to atmospheric turbulence : this causes diffraction of the incoming light, that can be partially removed with adaptive optics (AO), a technique that allows to rapidly correct for wavefront variations employing deformable mirrors. The perturbations in the wavefront caused by the atmosphere are larger at shorter wavelengths, due to the higher variations of the refractive index in the turbulent layers, so that the best results in imaging from ground based observatories are reached at near-infrared wavelengths. In particular, 8-10 meters large telescopes become diffraction limited at ~15-20 μm, depending on the site. A quantity that is often used to evaluate the performances of an AO system is called *Strehl ratio*, defined as the ratio between the peak intensity of the measured point spread function (PSF) and the one of the theoretical PSF: typical values are around 0.4-0.8 in the K band (1.9-2.4μm) by well performing AO systems. Another complication is given by static or quasi-static wavefront errors, generated by the optical elements internal to the telescope, which cause a pattern of diffraction elements, or *speckles*, that can be easily confused with signals from a point source; a partial correction for this effect is achieved in the post-processing of the data (see Section 3.2).

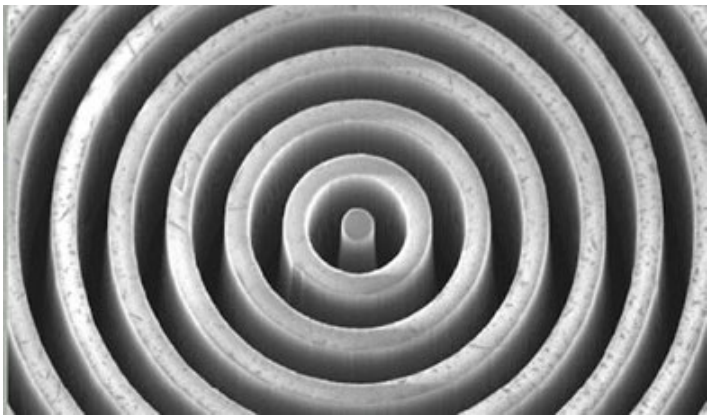

Figure 3.2: Keck L-band vortex made from sub-wavelength gratings etched into a synthetic diamond substrate, the picture covers a sector about 20μm wide in the horizontal direction. Credits: W. M. Keck Observatory

3.1.1 The vortex coronograph at Keck/NIRC2

NIRC-2 (Near InfraRed Camera) is a near-infrared detector mounted on the Keck telescope, on the summit of Mauna Kea, in the Big Island of Hawai'i. NIRC-2 operates from 1μm to 5μm, taking full advantage of the Keck adaptive optic system. Three different cameras are available for imaging, with the smaller pixel scale being 0.″01 and resulting in a 10x10 arcseconds field of view. On March, 2015 two vortex masks optimized to work in the L' band were installed on NIRC2 as a result of a collaboration between JPL (Jet Propulsion Laboratory), CIT (California Institute of Technology), the European VORTEX group and W.M. Keck Observatory (WMKO). The vortex coronographic approach is a recent technique, originally proposed by Mawet et al. (2005), that aims at combining high transmission and small inner working angles for the high resolution imaging of faint sources around bright objects, such as exoplanets orbiting their parent star. It consists of a focal plane microcomponent, made up of a circular grid with sub-wavelength spaced grooves (see Figure 3.2), complemented by a Lyot stop in the pupil plane. The technology for the manufacturing of such subwavelength grating currently allows to produce high quality vortex masks for wavelengths as short as the L' band (~3.7μm, see Vargas Catalán et al. 2016).

The significant advantage of this technique is to minimize the suppression of the signal at small distances from the central object (which is the main weakness of classical amplitude masks due to their physical extent), achieving inner working angles $\simeq \lambda$/D (see Serabyn et al. 2017, and references therein). Another important parameter that describes the performances of a coronograph is the *contrast*, given by the ratio of the residual off-axis starlight to the peak

of the on-axis stellar PSF. Optimal performances were registered during the observations of the benchmark target HR8799 with NIRC2 and the vortex coronograph: after ∼2 hours integration a contrast of 10^{-4} (corresponding to 10 magnitudes) at a 5σ level was reached at a $0\farcs3$ separation (*User Manual for the Vortex Coronograph at NIRC2 on Keck II*, WMKO); the excellent image quality is also guaranteed by the good seeing conditions of the Mauna Kea site and the high Strehl ratios $\gtrsim 80\%$ in the L' band achieved by the KeckII AO system. For the processing of the NIRC2/vortex observations, the *python* package VIP (Vortex Imaging Processing) has been developed and made available to the community (Gomez Gonzalez et al. 2017).

3.2 Post-processing

As mentioned earlier in this chapter, the wavefront errors that are not corrected by adaptive optics can be mitigated in the post-processing phase, after the observations. In order to remove effectively the speckle noise, two main procedures need to be applied. First, a separation between the diffraction figures and a potential planetary signal has to be done: this can be achieved with different techniques, such as Angular Differential Imaging (ADI), relying on the rotational diversity of the speckles and the planet, Spectral Differential Imaging (SDI), relying on the wavelength dependence of the speckle pattern, and Reference star Differential imaging (RDI), where a different target star is observed and used to estimate the stellar PSF. A second step consists in building a synthetic PSF the best reproduces the one to be subtracted, making use of an optimization algorithm.

ADI is a powerful PSF calibration technique that is widely used with direct imaging instruments, as it can attenuate the speckle noise by a large factor, reaching a final signal-to-noise up to ∼30 times higher than a classical observing technique (Marois et al. 2006). It takes advantage the intrinsic field of view rotation during the acquisition of image sequences in telescopes with alt-azimuthal mount: when the observations are taken in *vertical* mode, the instrument field derotator is switched off, so the instrument and the telescope optics remain aligned while the field of view rotates following the target on the sky. This way an off-axis signal from a potential companion of the central object will fall at different positions in the detector, whereas the speckle pattern will remain mostly fixed. To obtain a better efficiency with this technique it is desirable to maximize the FOV rotation, which can be

done by observing the target during its passage at the meridian, in fact the rotation rate (in radians per seconds) of the FOV is calculated as (McLean 2008):

$$\omega = \Omega cos(A)\frac{cos(\phi)}{sin(z)} \tag{3.1}$$

where Ω is the sidereal rate (7.2925 x 10^{-5} radians/sec), A is the target azimuth, z the zenith distance and ϕ the latitude of the telescope. A series of frames is thus collected as the target moves across the sky, and the final raw dataset consists in a "cube" of equally integrated frames with different parallactic angle (i.e. the angle between the maximum circle that passes through the object and the zenith, and the hour circle of the object). After the pre calibration (sky/dark subtraction, flat field normalization, bad pixel correction) of the science frames, a final reduced image can be obtained by subtracting the median of all the images from each frame, then combine them together after performing a rotation to align them at the same parallactic angle. To further increase the signal-to-noise and hence the sensitivity to planetary companions, several algorithms that can optimize the PSF subtraction have been proposed; many of these are based on principal component analysis (PCA), which creates an orthogonal basis for the frames, that are linearly combined to model the supplied PSF. The number of modes - or components - can be varied to obtain the best fit to the images PSF: the first mode more generally matches all the images, while the further modes represent higher orders perturbations (Wahhaj et al. 2015).

3.3 Recent results

In the last few years several high contrast imaging systems have been installed on 8-10 meter class ground based telescopes for the direct imaging of exoplanets orbiting young stars (e.g. KeckII/NIRC2, LBTI, Gemini South/GPI, VLT/SPHERE), where the first planetary companion being discovered with this technique was 2MASSW J1207334-393254 (Chauvin et al. 2005). Most of those systems operate in the short NIR wavelengths (1 - 2.5 μm), relying on "extreme" adaptive optics (ExAO). In spite of the higher thermal background, longer infrared wavelengths, such as the L band, have the advantage of higher Strehl ratios and also lower contrasts between the parent star and young Jovian planets (see e.g. Baraffe et al. 2003). Young planets can provide a better detectability, as their higher potential gravitational energy results in a brighter emission in the NIR regime. It is therefore not surprising that several planets have been found in systems with debris disks, a clear signature of young age

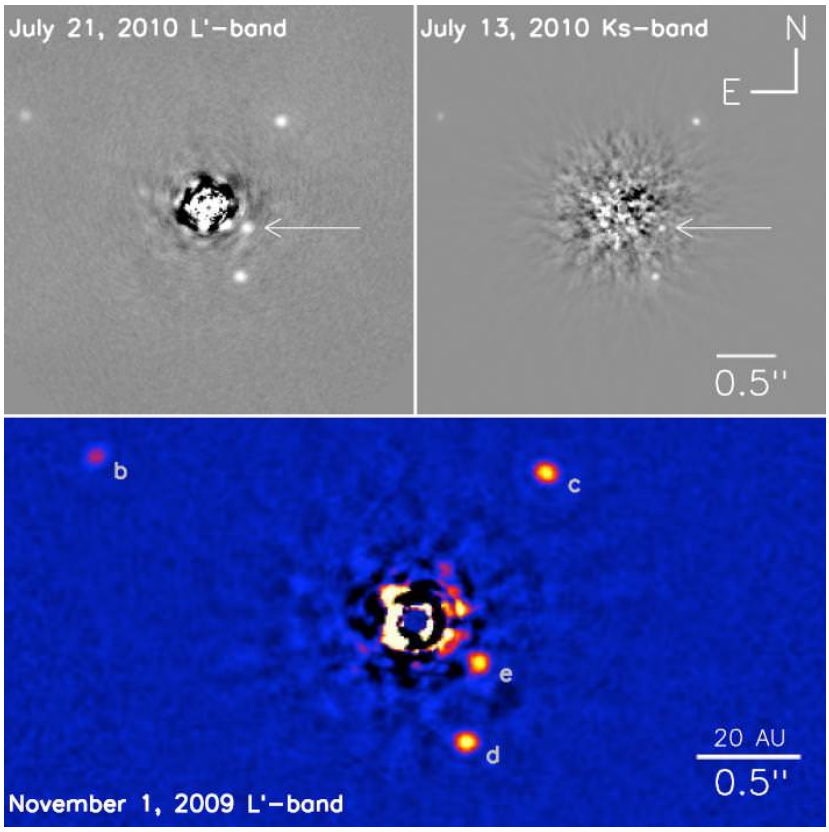

Figure 3.3: Reduced images of HR8799 acquired with KeckII, after ADI processing (from Marois et al. 2010).

of the system: a few example are β Pictoris (Lagrange et al. 2010), HD 95086 (Rameau et al. 2013), Fomalhaut (Kalas et al. 2008), GJ758 (Thalmann et al. 2009), and HD 106906 (Bailey et al. 2014).

A spectacular example is given by the HR8799 system (see Figure 3.3), where four giant planets (with masses between 7 and 10 M_J and orbital semi-major axis up to ~70 au) were discovered using Keck telescope (Marois et al. 2008, 2010). Recently, the search for planets has been pushed to even earlier stages, imaging young protoplanetary disk where protoplanets could be still embedded; this represents an even harder challenge as the scattered light from the disk can mask the light coming from the planet. Preferential targets are disks with large dust/gas cavities (*transitional disks*), so far a few detections have been claimed, but often have been disproven by follow up observations: a candidate has been proposed for HD 169142 (Reggiani et al. 2014, Biller et al. 2014), but successive detection in polarized light suggested the emission was due to scattered light from the disk atmosphere (Ligi et al. 2017); two companions around the transition disk LkCa 15 (Sallum et al. 2015) seem to be confirmed, while a previous detection in HD 100546 has been recently disproved by Rameau et al. (2017) using GPI at Gemini South. Tentative search of planetary com-

panions in non-transition disks that present gaps or other structures in the dust distribution have been attempted (e.g. HL Tau,Testi et al. (2015); TWHya, Ruane et al. (2017)), but with no detections so far. Preliminary results from vortex/NIRC2 observations of the ringed disk around the Herbig Ae star HD 163296, taken in May 2017, are presented in Chapter 6.

Part II

Results

4 Dust properties across the CO snowline in the HD 163296 disk

This Chapter consists of the work published in 2016 in the journal Astronomy&Astrophysics, with the title *Dust properties across the CO snowline in the HD 163296 disk from ALMA and VLA observations* (Guidi et al. 2016).

Abstract

Context: To characterize the mechanisms of planet formation it is crucial to investigate the properties and evolution of protoplanetary disks around young stars, where the initial conditions for the growth of planets are set. The high spatial resolution of Atacama Large Millimeter/submillimeter Array (ALMA) and Karl G. Jansky Very Large Array (VLA) observations now allows the study of radial variations of dust properties in nearby resolved disks and the investigation of the early stages of grain growth in disk midplanes.

Aims: Our goal is to study grain growth in the well-studied disk of the young, intermediate-mass star HD 163296 where dust processing has already been observed and to look for evidence of growth by ice condensation across the CO snowline, which has already been identified in this disk with ALMA.

Methods: Under the hypothesis of optically thin emission, we compare images at different wavelengths from ALMA and VLA to measure the opacity spectral index across the disk and thus the maximum grain size. We also use a Bayesian tool based on a two-layer disk model to fit the observations and constrain the dust surface density. *Results*: The measurements of the opacity spectral index indicate the presence of large grains and pebbles ($\geq$1 cm) in the inner regions of the disk (inside ~50 AU) and smaller grains, consistent with ISM sizes, in the outer disk (beyond 150 AU). Re-analyzing ALMA Band 7 Science Verification data, we find (radially) unresolved excess continuum emission centered near the location of the CO

snowline at ~90 AU.

Conclusion: Our analysis suggests a grain size distribution consistent with an enhanced production of large grains at the CO snowline and consequent transport to the inner regions. Our results combined with the excess in infrared scattered light suggests there is a structure at 90 AU involving the whole vertical extent of the disk. This could be evidence of small scale processing of dust at the CO snowline.

4.1 Introduction

The mechanisms that cause small dust particles to grow into larger bodies and eventually form planets are still not fully understood, in spite of the large laboratory, theoretical, and observational efforts (see the review by Testi et al. 2014). These processes are thought to occur in circumstellar disks around young stars on rather short timescales: infrared surveys show that the number of low mass stars with disks drops dramatically for stars older than 10 Myr (Mamajek 2009, Hernández et al. 2007), suggesting that in order to form large solids before the disk disperses, the growth process has to take place within a few million years. Analysis of dust properties in protostellar envelopes and young circumstellar disks suggests that large grains (even up to few millimeter size) are formed during the disk formation stage in infalling envelopes (Kwon et al. 2009, Miotello et al. 2014); still, substantial growth of dust grains occurs in the cold midplane of protoplanetary disks, where most of the solid mass is confined and planetesimals and planets are thought to form. The recent ALMA results for the young protoplanetary disk surrounding HL Tau suggest that planet formation may indeed occur very early in the disk's lifetime (ALMA Partnership et al. 2015, Dipierro et al. 2015, Tamayo et al. 2015).

The life of a growing dust grain in a protoplanetary disk is not an easy one. It was realized already four decades ago that aerodynamical friction may effectively prevent grain growth (Weidenschilling 1977). The process of rapid radial migration and fragmentation sets an upper limit to the grain sizes as a function of radius and a very rapid evolutionary timescale for dust particles in disks (Brauer et al. 2008, Birnstiel et al. 2012). These theoretical expectations are at odds with direct observations of dust properties in the outer disks from millimeter observations (Ricci et al. 2010, Birnstiel et al. 2010). This is a general result, although some authors have shown that disks with peculiar growth processes (e.g., Laibe 2014, Drążkowska

et al. 2014) or specific dust properties (Okuzumi et al. 2012) may retain large particles more efficiently. To overcome the general inconsistency between models and observations, the most commonly accepted scenarios involve local grain growth and trapping in small regions, with sizes close to or smaller than the local disk scale height (Pinilla et al. 2012b, Testi et al. 2014, Johansen et al. 2014). The regions in the disk midplane that correspond to the snowlines of major volatiles are particularly interesting. These may promote locally efficient grain growth through recondensation across the snowline or by changing the sticking properties of ice-coated grains and, in addition, the local release of volatiles from the ices may induce a local pressure bump that could trap large grains (e.g., Supulver and Lin 2000, Wada et al. 2009, Ros and Johansen 2013, Gundlach and Blum 2015).

The dense regions of disk midplanes can be investigated at submillimeter and millimeter wavelengths, where the dust emission is more optically thin and can now be spatially resolved with present-day facilities, such as the Atacama Large Millimeter/submillimeter Array (ALMA) and the Karl G. Jansky Very Large Array (VLA). These facilities allow us to obtain sensitive and high angular resolution observations of the dust continuum and gas emission lines from protoplanetary disks and therefore study the radial variations of the physical parameters of the disk. Recent results include the study of the dust properties as a function of radius in disks (Guilloteau et al. 2011, Banzatti et al. 2011, Pérez et al. 2012, 2015, Menu et al. 2014, Tazzari et al. 2016, e.g.,), and the clear identification of the CO snowline in nearby disks (Mathews et al. 2013, Qi et al. 2013, 2015), through its effects on DCO^+ and N_2H^+ abundances. It is thus becoming possible to directly investigate the effect of the CO snowline on grain growth observationally. This snowline is thought to be one of the most important after that of water, because the CO abundance in protostellar ices is found to be about 30-40% of H_2O (Öberg et al. 2011). In this work we focus on the Herbig Ae star HD 163296, a bright and isolated object at a distance of 122^{+17}_{-13} parsec (van den Ancker et al. 1998) with a relatively massive disk ($\sim 0.1 M_\odot$: Qi et al. 2011, Isella et al. 2007) and an excellent prototype for gas- and dust-rich protoplanetary disks. An estimated age of 5 Myr was obtained from the comparison between Hipparcos astrometric measurements and pre-main sequence evolutionary models by van den Ancker et al. (1998). The stellar parameters computed by Natta et al. (2004) are $M_* = 2.3 M_\odot$, $L_* = 36 L_\odot$, $T_{eff} = 9500 K$. To study the dust properties in the protoplanetary disk around HD 163296, we re-analyse the ALMA Science Verification observations (de Gregorio-Monsalvo et al. 2013, Mathews et al.

2013, Rosenfeld et al. 2013) and for the first time discuss the continuum emission in Band 6, combined with new VLA observations from the Disks@EVLA collaboration. In §2 we describe the observational data, in §3 we report the main new results of our analysis, in §4 we present the result of our disk modeling, and in §5 we discuss the main implications for grain properties.

4.2 Observations

4.2.1 ALMA observations

The ALMA observations of HD 163296 (also known as MWC 275) were part of the ALMA Science Verification Program 2011.0.000010.SV[1]. Band 6 observations were performed on 2012 June 9, June 23, and July 7 using a set of configurations comprising 20, 21 and 19 antennas, respectively. The total integration time was 3.14 hours (1.4 hours on the science source), the field of view was ∼20 arcseconds and the baselines ranged from 20 to 400 meters, corresponding to spatial scales of 1600 AU to 80 AU at the distance of the object. The flux density calibrator for the three execution blocks were Juno, Neptune, and Mars, while the phase calibrator was J1733-130 and the bandpass calibrator J1924-292. The correlator was set with four spectral windows in dual polarization mode, two spectral windows in the upper side band and two in the lower side band. Two spectral windows, #0 (216.2 - 218 GHz) and #3 (233.1 - 234.9 GHz), were used to observe the line-free continuum with channel widths of 488 kHz; while at higher resolution (244 kHz) spectral window #1 (219.5 - 220.4 GHz) included the $C^{18}O(2-1)$ line at 219.560 GHz and the $^{13}CO(2-1)$ line at 220.398 GHz, and spectral window #2 (230.5 - 231.5 GHz) covered the $CO(2-1)$ line at 230.539 GHz. Imaging of the continuum emission of HD 163296 was performed excluding the above-mentioned lines (see Rosenfeld et al. 2013, Klaassen et al. 2013). Data was calibrated using version 4.1.0 of the Common Astronomy Software Application (CASA), self calibration was applied making use of the line-free channels, and using robust weighting during the CLEAN deconvolution, we were able to reach a resolution of 0.74" × 0.60" with a rms of 0.37 mJy/beam (see Table 4.1).

Band 7 observations were made on 2012 June 9, June 11, and June 22 with the same

[1]The ALMA Science Verification data can be found at: `https://almascience.eso.org/alma-data/science-verification`

antenna configurations as for Band 6. Collectively, the five datasets covered an integration time of 3.9 hours, with 2.3 hours on the science target. The flux density calibrators were Juno and Neptune, while the bandpass and phase calibrators were the same as those used for Band 6. The two spectral windows in the lower side band were #2 (345.56 − 346.03 GHz) and #3 (346.52 − 347.47) with channel widths of 122 and 244 kHz, respectively. The ones in the upper side band were #1 (356.50 − 356.97 GHz) with 122 kHz channel width and #0 (360.11 − 360.23 GHz) at a high spectral resolution of 30.5 kHz; these included the emission lines: CO(3 − 2) at 345.796 GHz (#2), $HCO^+(4-3)$ at 356.734 GHz (#1), $H^{13}CO^+(4-3)$ at 346.998 GHz (#3) and $DCO^+(5-4)$ at 360.160 GHz (#0). A detailed analysis of these spectral lines has been published by Mathews et al. (2013), de Gregorio-Monsalvo et al. (2013), and Rosenfeld et al. (2013). In this work we focus on the imaging of the continuum emission, obtained with the task CLEAN applying a robust weighting with Briggs parameter 0.5 and achieving a synthesized beam of 0.57" × 0.37" and a rms of 0.18 mJy/beam (see Table 4.1).

4.2.2 VLA observations

Observations of HD 163296 were made using the Karl G. Jansky Very Large Array (VLA) of the National Radio Astronomy Observatory[2] as part of the Disks@EVLA project (AC982) in 2011 May and June in the BnA and A configurations. The Ka-band (λ ∼1cm) receivers were used with two 1GHz basebands centered at 30.5 and 37.5GHz, providing projected uv-spacings from 25 to 3,800 kλ. The complex gain was tracked via frequent observations of J1755−2232, and the spectral shape of the complex bandpass was determined through observations of 3C279. The absolute flux density scale was derived from observations of 3C286 (Perley and Butler 2013, e.g.,), and its overall accuracy is estimated to be 10%. The data were calibrated, flagged, and imaged using a modified version of the VLA Calibration Pipeline (see https://science.nrao.edu/facilities/vla/data-processing/pipeline/scripted-pipeline) with CASA. The astrometry reported here corresponds to what was derived from the A configuration data.

In addition, HD 163296 was observed with the C-band (λ ∼6cm) receivers in the DnC configuration in September 2010, in order to evaluate any potential contamination from ion-

[2]The National Radio Astronomy Observatory is a facility of the National Science Foundation operated under cooperative agreement by Associated Universities, Inc.

ized gas at shorter wavelengths. Two 1GHz basebands were centered at 5.3 and 6.3GHz. Complex gain variations were tracked through observations of J1820−2528, and the bandpass and absolute flux density scale was obtained through observations of 3C286. The data were calibrated, flagged, and imaged using the CASA data reduction package. HD 163296 was detected with integrated flux density $F_{5.2\mathrm{cm}} = (410 \pm 57)\mu$Jy.

4.3 Observational results

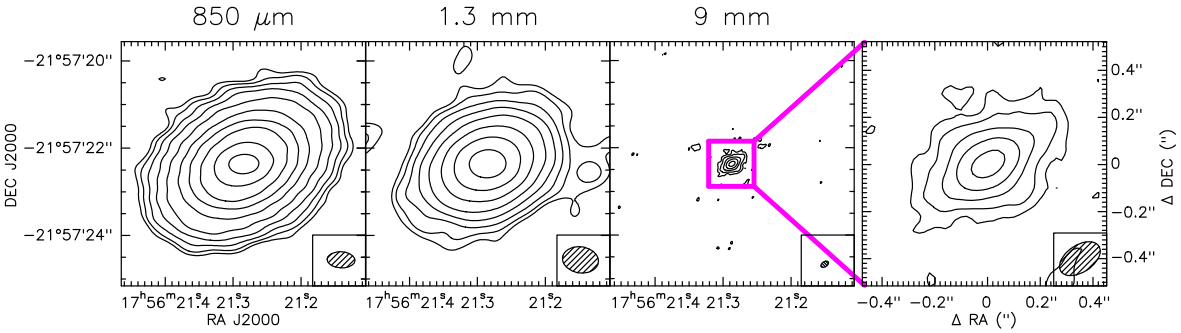

Figure 4.1: Continuum maps at different wavelengths, from the left: 850 μm, 1.3 mm, and 9 mm, the last obtained from the combination of VLA 8.0 mm and 9.8 mm bands. The contour levels correspond to -3 (dashed), 3, 6, 12, 24, 48, 100, 200, 400, 800, 1600 σ. The bottom right of every panel shows the synthesized beam (see Table 4.1).

	λ [mm]	ν [GHz]	F_{int} [Jy]	F_{peak} [Jy/beam]	rms [mJy/beam]	CLEAN beam [FWHM]	Beam P.A. [°]
ALMA B7	0.85	352.9	2.13 ± 0.21	0.44	0.18	$0.57'' \times 0.37''$	86.5
ALMA B6	1.33	225.3	0.60 ± 0.06	0.22	0.37	$0.74'' \times 0.60''$	77.3
VLA Ka	9.00	34.0	$(1.83 \pm 0.02) \cdot 10^{-3}$	$0.847 \cdot 10^{-3}$	0.013	$0.18'' \times 0.11''$	-49.4
VLA Ka	8.00	37.5	$(2.02 \pm 0.2) \cdot 10^{-3}$	$0.928 \cdot 10^{-3}$	0.024	$0.16'' \times 0.10''$	−56.1
VLA Ka	9.83	30.5	$(1.65 \pm 0.2) \cdot 10^{-3}$	$0.806 \cdot 10^{-3}$	0.015	$0.19'' \times 0.12''$	131.5

Table 4.1: Parameters for the deconvolved images displayed in Fig. 5.C.1 and for the images obtained from the single VLA frequencies of 30 and 37 GHz.

4.3.1 Continuum maps

In Figure 5.C.1 we show the continuum intensity maps obtained from the line-free channels at three different wavelengths: ALMA Band 7, ALMA Band 6, and the combination of the two VLA frequency ranges at 30.5 and 37.5 GHz. The parameters of the images are listed in Table 4.1.

In agreement with previous work (de Gregorio-Monsalvo et al. 2013, Natta et al. 2004), we observe more compact emission at longer wavelengths, obtaining at 850 μm a projected radius of ~2.4″ at a three-sigma level, corresponding to about 290 AU, while the outer radius of the emission is ~260 AU at 1.3 mm, and ~40 AU at 8-10 mm. We note that the low signal-to-noise of the VLA data at 8 and 10 mm can lead to underestimating the extent of the emission at these wavelengths, and it is critical to consider the visibility function for a proper analysis of the disk structure. We use 44° for the disk inclination and 133° for the disk position angle (from Qi et al. 2011) and plot the normalized real and imaginary part of the visibilities in Figure 4.2.

These plots show that the real part of the visibilities declines more steeply at the shorter wavelengths (ALMA 850 μm and 1.3 mm) than at longer wavelengths (VLA 8 mm and 9.8 mm), demonstrating that the millimeter wavelength emission is intrinsically considerably more extended than the centimeter wavelength emission (a point source would be a constant 1.0 as a function of uv-distance in this plot). The integrated flux density above the 3σ level at 850 μm is $F_{850\mu m} = 2.13 \pm 0.02$ Jy, similar to the value found by Isella et al. (2007) and de Gregorio-Monsalvo et al. (2013), while in Band 6 we find $F_{1.3mm} = 0.59 \pm 0.06$ Jy. At the longer wavelengths, the flux density decreases by almost 3 orders of magnitude, with $F_{8mm} = 2.0 \pm 0.2$ mJy and $F_{10mm} = 1.6 \pm 0.2$ mJy. We include a calibration error of 10% in the measurements of the flux densities. We find a smoothly decreasing intensity profile at all wavelengths, consistent with the disk temperature and surface density decreasing with radius.

4.3.2 Proper motions

We checked whether the position of the star at the two different epochs of our observations was consistent with the proper motions reported in the literature: applying a gaussian fit with to the images we find that the positions of the peaks fall within the 3σ error ellipse from the predicted position based on the Hipparcos astrometric mission measurements (J1991.25). For the ALMA observations (2012), we used Band 7 data because of its better signal-to-noise, with the peak position of the images obtained from the calibrated dataset before the self-calibration was applied. Figure 4.3 displays the estimated positions of the central star, and the astrometric error for interferometric observations is affected, among other things, by the phase calibration and depends on several factors (weather conditions, the separation

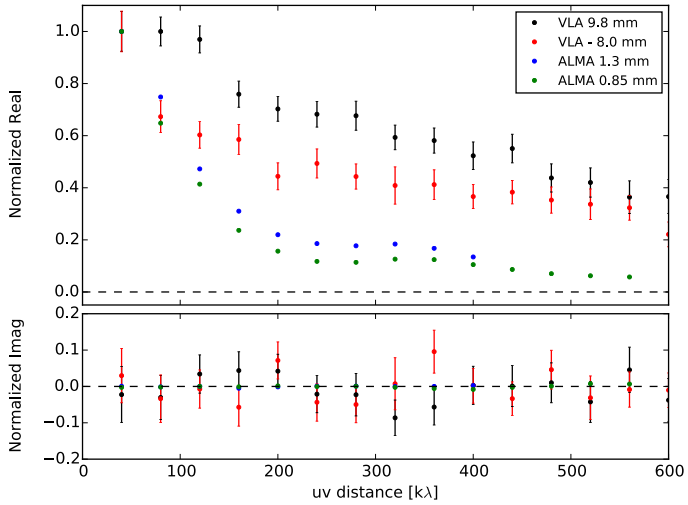

Figure 4.2: Real and imaginary parts of the measured visibilities as a function of uv-distance, deprojected assuming PA=133°, i=44°and bin-averaged every 40 kλ. Visibilities at each wavelength have been normalized by the average value at 40 kλ and error bars display the standard error of the mean, negligible for ALMA observations.

between the target and the calibrator, etc.). We assume here that the absolute astrometry of the ALMA data is 0.1″[3], while for the VLA in A configuration, it is expected to be ∼ 0.02″[4]. The proper motions derived from a least-squares interpolation between our peaks at the two different epochs and the J1991.25 Hipparcos position are consistent with the latest reduction of the Hipparcos data (van Leeuwen 2007) within the errors and are listed in Table 4.2. The main difference we find is in the right ascension, where our best fit would imply a smaller proper motion. Nevertheless, the difference is still well within the uncertainties.

4.3.3 SED and free-free contribution

The integrated flux densities measured within a three-sigma level in our observations and the spectral energy distribution predicted by our model (see Section 4.4) are plotted in Figure 4.4. Our model is consistent with the observed flux densities in the literature (Natta et al. 2004, Isella et al. 2007). At submillimeter and millimeter wavelengths, the continuum emission is due to the dust in the colder regions of the disk midplane, while at centimeter wavelengths the emission may also arise from free electrons in the stellar wind. Since this contribution

[3] https://help.almascience.org/index.php?/Knowledgebase/Article/View/153/6/what-is-the-astrometric-position-accuracy-of-an-alma-observation

[4] https://science.nrao.edu/facilities/vla/docs/manuals/oss/performance/positional-accuracy

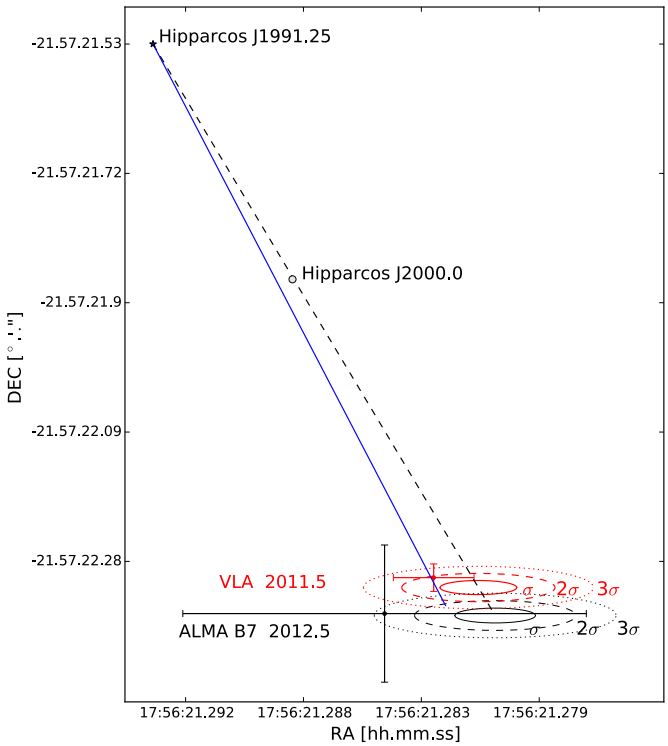

Figure 4.3: Position of HD 163296 at the different observing epochs. The dashed line represents the proper motions from the Hipparcos measurement (J1991.25) to 2012, with respective proper motion error ellipses at 1, 2, and 3 σ from the predicted positions. The black dot indicates our position estimate for the star at epoch 2012.5 based on the peak of the image in Band 7, while the red dot is the peak of the VLA image at 9 mm in 2011.5. The error bars are given by the astrometric accuracy of 0.1 arcsec for ALMA and 0.02 arcsec for VLA. The blue solid line represents the proper motions calculated from a least-squares regression between Hipparcos measurements and the observations.

is thought to come from a region in the inner part of the disk, we examined the longest baselines (≥1500 kλ) in the VLA 8.0 and 9.8 mm observations and we estimate an upper limit of 0.3 mJy for this wind emission, corresponding to the asymptotic value reached at the higher uv-distances by the real part of the visibilities. We fit a power law for the free-free emission by performing a least squares interpolation between our estimates at 8 and 10 mm and other VLA measurements at 3.6 cm (Natta et al. 2004) and 5.2 cm (see Section 4.2). The resulting power law is $F_\nu \propto \nu^{-0.19\pm0.11}$, and is shown in Figure 4.4 (where we plot νF_ν as a function of λ). According to this estimate, the free-free component at wavelengths shorter than 7 mm is negligible (see also Natta et al. 2004).

4.3.4 Excess emission at 850 μm

In Figure 4.5 we show the intensity profile of the image at 850 μm: as the disk is inclined by 44° from the line of sight, the best angular resolution is reached using only the data along the

	RA [$hh:mm:ss$]	DEC [°.′.″]
Hipparcos J1991.25	17:56:21.293	-21.57.21.527
VLA 2011.5	17:56:21.283	-21.57.22.30
ALMA 2012.5	17:56:21.285	-21.57.22.36

	pm-ra [mas/yr]	pm-dec [mas/yr]	error ellipse [$mas\ mas$]
Hipparcos	-7.98	-39.21	[0.94 0.51]
this paper	-6.8	-38.5	[1.0 1.0]

Table 4.2: Coordinates and proper motions of HD 163296. Top table: right ascension and declination of HD 163296 at the different epochs. Bottom table: proper motions with associated error ellipse from Hipparcos measurements and from the least squares interpolation performed in this paper.

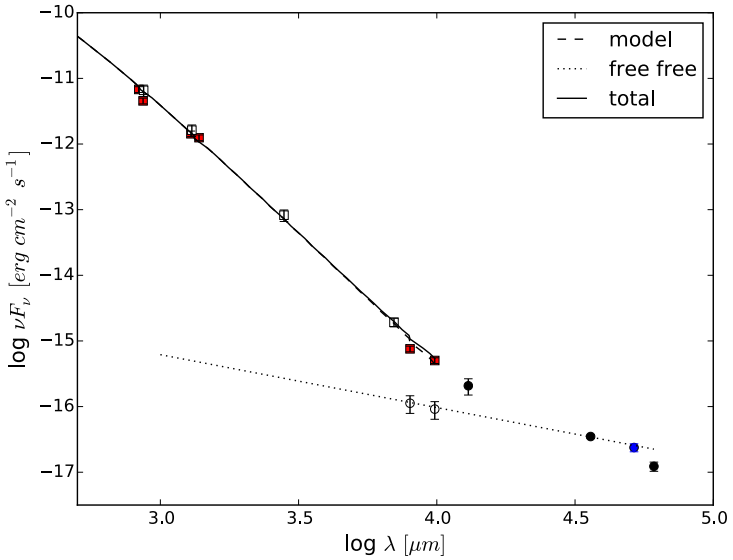

Figure 4.4: HD 163296 spectral energy distribution. Our measurements are represented in red filled squares, the white empty squares are taken from the literature (Isella et al. 2007, Natta et al. 2004), and the longer wavelength measurements used to evaluate the free free contribution are shown with full black circles (Natta et al. 2004) and a blue full circle (Disks@EVLA collaboration). Empty circles show the value of 0.3 mJy for the free free emission estimated in this paper. The dashed curve shows the best fit model from this paper (see Section 4.4), the dotted line is the estimated free-free emission, and the solid line the sum of the two.

projected disk major axis. We considered the pixels inside one beam across the major axis, each point corresponding to a pixel of 0.1 arcsec in the image (the points are therefore not all independent). The vertical spread is due to the shape and position angle of the synthesized beam, and to estimate the error when averaging on bins (Fig. 4.5, second panel) we weighted the points for the number of correlated pixels, i.e., $\sigma = \sqrt{\frac{\frac{1}{M}\Sigma_i(x_i-\mu)^2}{N/M-1}}$, where M is the number of correlated points and N the number of averaged pixels.

A simple analysis of the profiles reveals a bump in the emission between 80 and 150 AU: fitting a simple polynomial to outline a smooth profile does not produce an accurate fit (see Fig. 4.6). The degree of the polynomial was chosen as the lowest degree that would provide a reasonable fit to the intensity profile. To characterize the properties of this bump we fitted a combination of a 3rd degree polynomial plus a gaussian curve to our flux density profile (see Fig. 4.6, right panel): subtracting the polynomial from the data leaves a gaussian-shaped residual (see Fig.4.5, second panel) centered at about (106 ± 4) AU, with a full width at half maximum (FWHM) of (71 ± 18) AU and a peak at (67±29)% of the smooth polynomial profile. An estimate of the maximum spatial extent of the feature can be derived from deconvolving our best fit Gaussian with the synthesized beam (∼0.5″ in Band 7), resulting in an upper limit of ∼40 AU in FWHM. These values depend on the choice of the pixel size of the image and the tolerance we use for the points on the major axis, and thus are useful only for giving a rough estimate of the spatial scale of this unresolved emission excess. An independent analysis of this excess, obtained from modeling the visibilities directly, is shown in Section 4.

The feature cannot be clearly identified in Band 6 intensity profiles: we find an indication of a faint excess in the radial profiles along the disk projected major axis, but its detection depends on the small variation in the position angle and inclination parameters, making its characterization unreliable. This is consistent with the lower angular resolution of the Band 6 SV data: if we image the Band 7 dataset with a restoring beam equal to Band 6 resolution, the feature is diluted and cannot be reliably separated from the smooth disk emission (see Figure 4.7).

Polynomial	a_0 (4.2±0.1)e-01	a_1 (-5.6±0.3)e-03	a_2 (2.7±0.2)e-05	a_3 (-4.8±0.6)e-08
Polynomial + Gaussian	a_0 (4.6±0.2)e-01	a_1 (-7.3±0.9)e-03	a_2 (4.0±0.7)e-05	a_3 (-7.4±1.6)e-8
	α [Jy/beam] (3.4±1.5)e-02	μ [AU] (1.06±0.04)e+02	σ [AU] (3.0±0.8)e+01	

Table 4.3: Best fit parameters of the polynomial fits with associated standard deviations, obtained from the least-square interpolation of the data along the major axis using a 3rd-degree polynomial ($y = a_0 + a_1x + a_2x^2 + a_3x^3$) and a polynomial plus a Gaussian curve ($y = a_0 + a_1x + a_2x^2 + a_3x^3 + \alpha\, exp(-(x-\mu)^2/2\sigma^2)$), where x is in AU and y in Jy/beam.

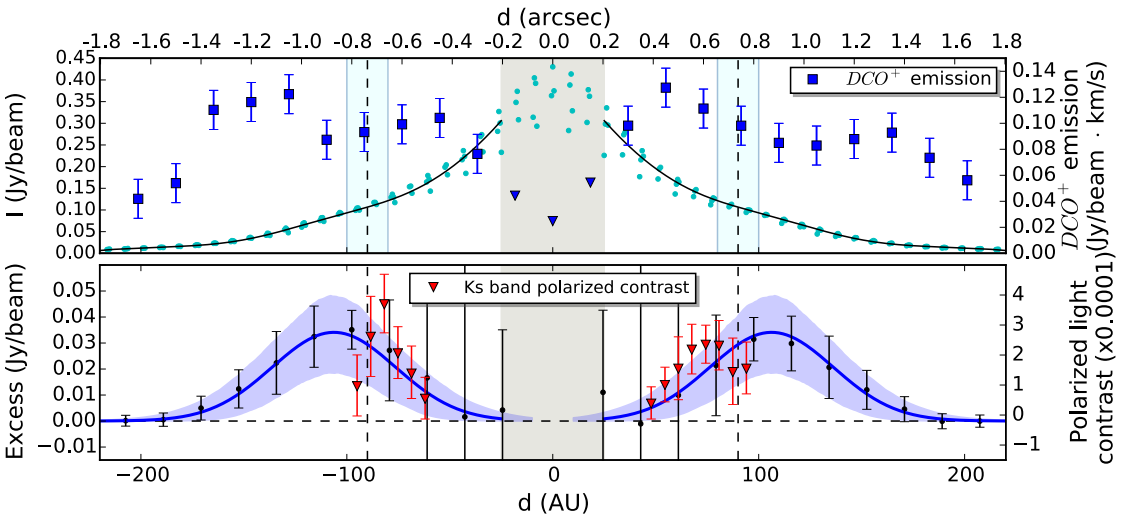

Figure 4.5: *Top panel*: flux density at 850 μm along the disk major axis from SE (left) to NW (right). The solid line represents the fit (polynomial profile + a Gaussian for the excess) performed excluding the inner 0.2 arcsec of the disk (gray shaded area). The vertical dashed line corresponds to the CO snowline at 90 ± 10 AU (from Qi et al. (2015)). DCO^+ emission in blue squares binned by 0.15 arcsec, the blue triangles show the upper limit of DCO^+ emission in the inner 0.2 arcsec region of the disk, where we are limited by resolution. *Bottom panel*: residuals obtained by subtracting the polynomial fit from the data are shown with black dots binned by 0.15 arcseconds. The blue solid line represents the Gaussian that best fits the excess (see Table 4.3), with the shaded area showing the 1σ fit uncertainty. The red triangles are the polarized light contrast in the Ks band (from Garufi et al. 2014, the scale is on the right side vertical axis).

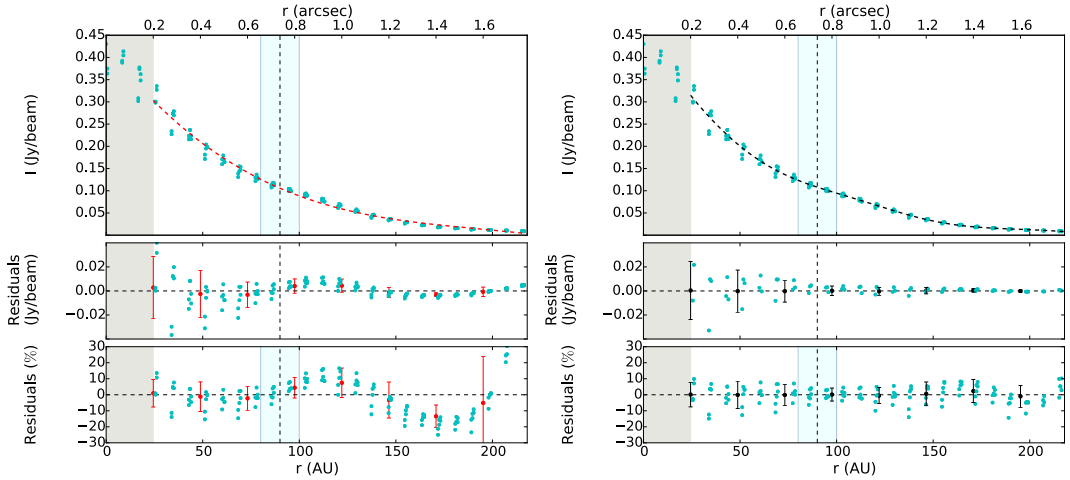

Figure 4.6: *Left:* flux density across the disk major axis with a polynomial fit of degree 3 (dashed line in the upper panel). The second and third panels show the absolute residuals and the percentage residuals respectively. *Right:* the same intensity profile fitted with a 3rd-degreee polynomial plus a Gaussian (see Table 4.3 for the best fit parameters).

4.3.5 DCO^+ emission

We extracted the DCO^+(J = 5−4) emission lines at 360.160 GHz from the ALMA Band 7 observations in order to compare the dust continuum radial profile with a potential molecular

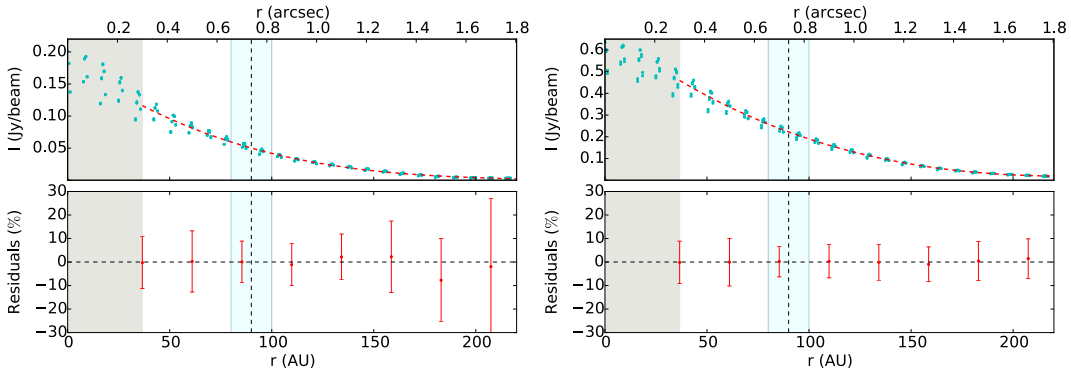

Figure 4.7: *Left:* radial profile at 1.3 mm across the disk major axis, with the dashed curve resulting from the polynomial fit of the data. Bottom panel: absolute residuals with respect to the polynomial interpolation. The excess emission found at 850μm is not visible in Band 6. *Right*: radial profile of the image at 850 μm restored with the same beam as Band 6 (0.74″×0.60″, PA 77.3°).

tracer of the CO snowline (Mathews et al. 2013, see). We used the CASA task "clean" with natural weighting to produce an integrated map of the DCO^+ emission in the velocity range 0.8-10 km/s, and the resulting synthesized beam is $0.62'' \times 0.42''$. We find a ring-like structure, similar to the one reported by Mathews et al. (2013), with a central radius of ~110 AU and a total extent of the DCO^+ emission (detected at greater than 3σ) of 200 AU in radius. In Fig. 4.5 (top panel), we show the radial profile of the integrated DCO^+ emission along the disk projected major axis: we note a symmetry between the southeast and the northwest directions, both displaying a double peak at a distance of ~60 AU and ~140 AU from the central star. We also point out that the minimum between the two peaks on both sides appears to fall at the position of the excess in the continuum emission at 850 μm (~110 AU). The signal-to-noise ratio of the DCO^+ image is very low, so this result is very tentative and should be verified with higher sensitivity observations.

4.3.6 Spectral index profiles

The dust opacity at millimeter and submillimeter wavelengths is usually approximated by a power law, $\kappa_\nu \propto \nu^\beta$ (Hildebrand 1983, e.g.,). The emission properties depend on the details of the composition, geometry, and size distribution of dust grains, most of which are very difficult to constrain. A general conclusion, however, is that in the conditions expected for dust in the densest regions of cores and disks, larger grain sizes correspond to lower values of the β index (Miyake and Nakagawa 1993, Stognienko et al. 1995, Natta and Testi 2004, Draine 2006, e.g.,). Even though directly connecting a value of β to the detailed properties of

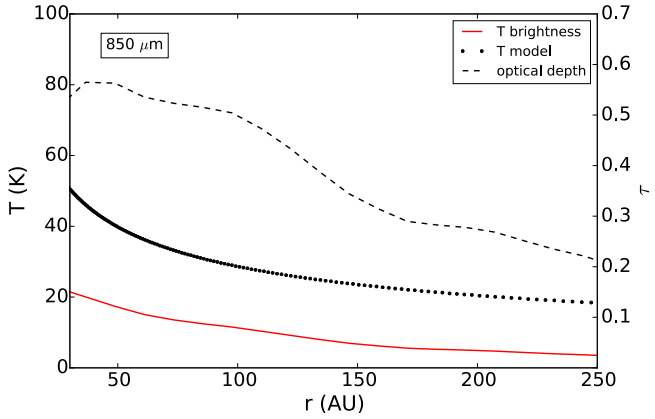

Figure 4.8: Temperature profile of the best fit model (see Sect.4.4) in black dots and brightness temperature from the observations at 850 μm (red solid line) plotted in function of the distance, starting from 30 AU to have a reliable estimate considering the resolution of the observations. On the right axis, the optical depth from the comparison of the two temperatures, plotted as the dashed line.

the dust population is not possible, measurements of β have been successfully used to infer the growth of dust in disks for many years (e.g., Beckwith and Sargent 1991, Wilner et al. 2000, Testi et al. 2001, 2003, Rodmann et al. 2006, Ricci et al. 2010, Kwon et al. 2015).

Previous measurements of the dust opacity power law between 0.87 and 7 mm (Isella et al. 2007) and between 1.3 and 7 mm (Natta et al. 2004) have already shown that grain growth occurs in the disk around HD163296. With the high resolution of ALMA it is now possible to extend these studies and constrain the radial behavior of the opacity spectral index β (see, e.g., Pérez et al. 2012, 2015), not just its average value across the disk. We recall here that the emission from the disk midplane is generally optically thin, and at these wavelengths the Rayleigh-Jeans regime is a good approximation. To verify these assumptions, we compared the brightness temperature derived from our observations with the temperature profile of our best-fit model (see Sect. 4.4), in order to estimate the optical depth τ of the emission as $\tau \simeq -ln(1 - T_b/T_{model})$. We found τ increasing toward the central regions, as expected, with values <0.6 for the emission at 850 μm, and <0.5 for the emission at 1.3 mm outside a inner region of ~30 AU (see Fig. 4.8 for the 850 μm optical depth profile). At longer wavelengths, we estimate a lower optical depth with values of $\tau < 10^{-1}$ at both 8 and 10 mm. The assumption of optically thin continuum emission is therefore consistent with our data, and we expect a linear relation between flux density and dust opacity.

The flux density emitted from a ring dr at a given radius can be written as

$$F_\nu(r) \propto \Sigma(r) \cdot B_\nu(T(r)) \cdot \nu^{\beta(r)}, \tag{4.1}$$

where $T(r)$ and Σ(r) are the midplane temperature and surface density at the distance r from

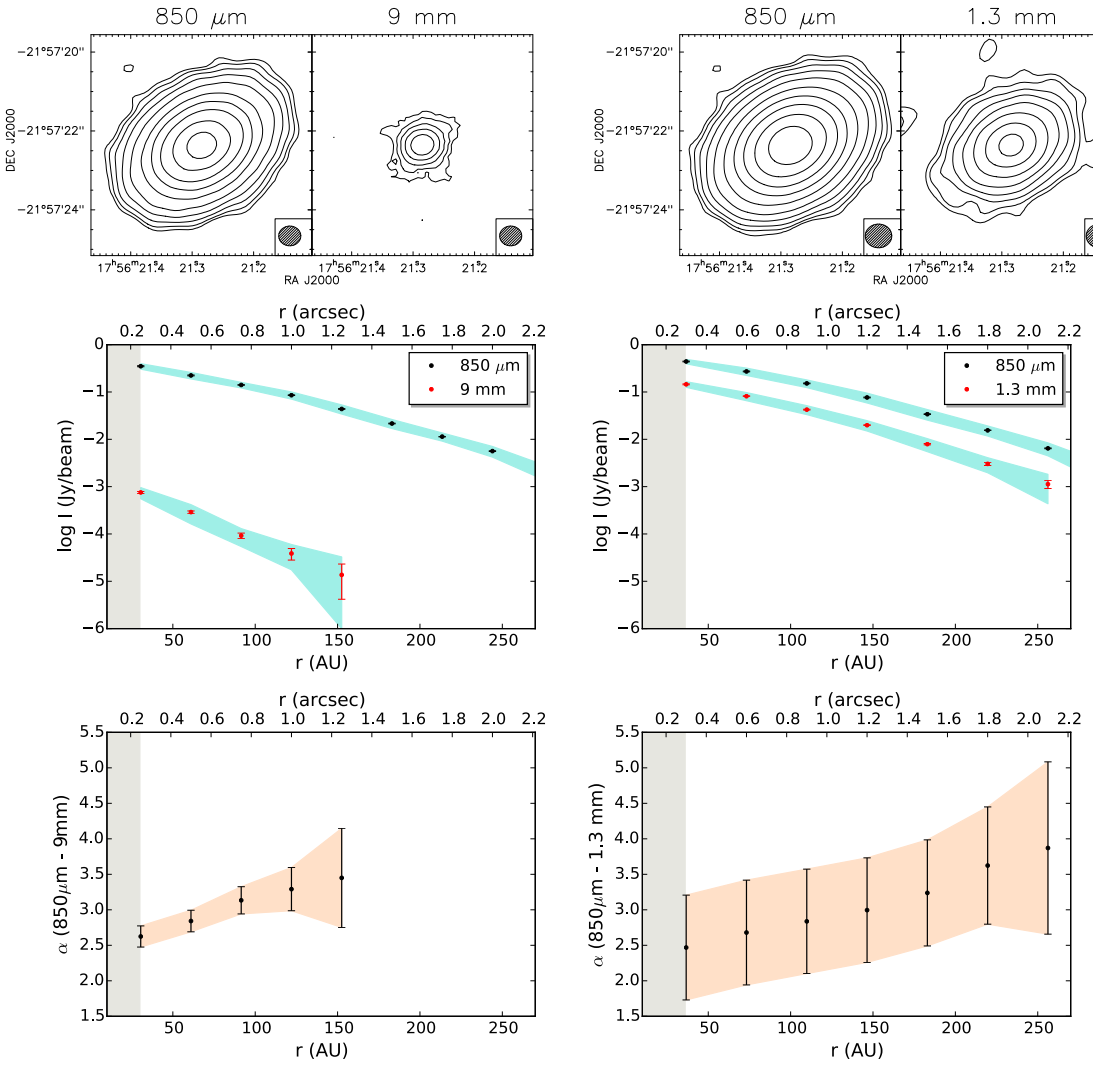

Figure 4.9: *Left*: Flux density maps (top panel) at 850 μm and 9 mm with contour levels at -3 (dashed), 3, 6, 12, 24, 48, 100, 200, 400, 800, and 1600 σ. Disk surface brightness profiles (middle panel) used to compute the spectral index, plotted on a logarithmic scale. The shaded region shows the dispersion of the individual data points in the images, while the error bars show the uncertainty on the mean for each bin. The flux density spectral index (bottom panel) was calculated between 850 μm and 9 mm as a function of radial distance. The profiles were averaged on ellipses of semi major axis r (shown in arcsec and AU in the top and bottom axes, respectively). The shaded region indicates the uncertainty of the measurement, resulting from the noise of the deconvolved images and the systematic calibration uncertainty; the low signal-to-noise ratio in the VLA map dominates the uncertainty on the spectral index determination beyond ~100 AU. *Right*: as above, but for the two ALMA datasets at 850 μm and 1.3 mm.

the star, and B_ν is the Planck function. In the Rayleigh-Jeans regime we therefore have $F_\nu(r) \propto \Sigma(r) \cdot T(r) \cdot \nu^2 \cdot \nu^{\beta(r)}$. Producing matched images (same beam, pixel size and centered on the peak of the emission) at different wavelengths and measuring the ratio of the flux densities as a function of distance from the star allows the spectral index, α (where $F_\nu \propto \nu^\alpha$), to be determined. Then, given the assumptions noted above, the power-law dependence of the dust opacity, β, can be derived as $\beta = \alpha - 2$ and does not depend on temperature or surface

density. As discussed in Sect. 4.3.3, the observation at 8 and 10 mm includes gas emission from the stellar wind that needs to be subtracted to study the dust emissivity. The VLA maps used to compute the spectral index were produced by subtracting a point source at the center of the system with a flux density of 0.3 mJy from the calibrated visibilities (see Sec. 4.3.3).

In the lefthand panel of Figure 4.9 we show the intensity maps at 850 μm and 9 mm with a circular beam of 0.5″, the corresponding averaged radial intensity profiles and the derived α profile. The intensity-averaged values (and consequently the spectral index) are plotted as long as they stay above the 1σ level. We see an increasing trend in the spectral index α from ∼2.5 in the inner regions to ∼3.5 at 150 AU. The profiles are displayed starting from and sampling every half resolution element of the images, corresponding to ∼30 AU; the large error associated with this spectral index profile is dominated by the limited signal-to-noise ratio of the VLA images. With the same procedure we computed the spectral index between the ALMA Band 6 and 7 images, with a matching circular beam of 0.6″, and obtained the profile shown in the righthand panel of Figure 4.9. In this case the profile is sampled every 0.3″ (∼40 AU). In spite of the high signal-to-noise of the ALMA images, the large uncertainties are caused by the small wavelength leverage between the ALMA Band 6 and 7 observations. In propagating the uncertainty on α, we used a 10% calibration error for each flux, which in the case of $\alpha(850\mu m - 1.3mm)$ represents a pessimistic estimate, because the two ALMA observations were carried out with the same phase calibrator and with Neptune as flux calibrator. Within the uncertainties the α profile seems to be consistent with the measurements between 850 μm and 9 mm. The spectral index remains below the value of 3 beyond 50 AU, corresponding to a β<1 under the assumptions mentioned above, this indicates the presence of grains that have grown to at least 1 mm in size (using the dust opacity curves computed by Testi et al. 2014). We find no features in the α (and by implication, β) profiles across the CO snowline, as would be expected for localized grain growth, but it should be noted that the resolution of the spectral index maps is limited by the lower resolution of Band 6 observations (∼0.6″), which would not be sufficient to detect small scale variations of the emission (see Section 4.3.4). We return to the estimate of $\beta(r)$ in Sect. 4.5.

4.4 Modeling results

In Section 4.3.4 we have shown that the surface brightness radial profile for the continuum emission at 850 μm is compatible with having an excess peaked around 110 AU, with deconvolved FWHM $\leq$ 40 AU. To assess the robustness of this result, we performed a direct fit of the interferometric data (i.e., the visibilities) using the fitting scheme described by Tazzari et al. (2016) to which we refer for the analysis details. To estimate the disk thermal emission at 850 μm, we used a classical two layer disk model (Chiang and Goldreich 1997) with refinements by (Dullemond et al. 2001) and a reduced disk flaring that adequately describes the observed far-infrared flux (from Tilling et al. 2012). The resulting vertical scale height for the surface layer at $R > 50$ AU is $h/R \sim 0.08$. Moreover, we assumed a constant dust to gas mass ratio $\zeta = 0.01$ and the following gas surface density profile:

$$\Sigma_g(R) = \Sigma_0 \left(\frac{R}{R_0}\right)^{-\gamma} \exp\left[-\left(\frac{R}{R_c}\right)^{2-\gamma}\right], \tag{4.2}$$

where $R_0 = 10$ AU is a fixed scale length and Σ_0, R_c, and γ are free parameters to be fitted. To compute the disk emission, the dust opacity is calculated using Mie theory (see Trotta et al. 2013, for details of the computation) assuming the same dust composition throughout the disk, given by the following fractional abundances adapted from Pollack et al. (1994): 5.4% astronomical silicates, 20.6% carbonaceaous material, 44% water ice, and 30% vacuum. Furthermore, we assume a power-law grain size distribution $n(a) \propto a^{-q}$ for $a_{\rm min} \leq a \leq a_{\rm max}$, where a is the grain radius. To model the expectation that in the disk midplane there are larger grains than on the surface (Testi et al. 2014), we used different parametrization for the grain size distribution in these two regions: $q = 3.5$, $a_{\rm min} = 10$ nm, $a_{\rm max} = 100\,\mu$m in the surface and $q = 3$, $a_{\rm min} = 10$ nm and $a_{\rm max} = 0.8 * (R/10\ AU)^{-1.025}$mm in the midplane, where this variable maximum grain size is chosen to reproduce the $\beta(R)$ profiles found in Sect. 4.3.6. The modeling methodology is based on a Bayesian approach and employs an affine-invariant Markov Chain Monte Carlo (MCMC) ensemble sampler (Foreman-Mackey et al. 2013) to explore the parameter space and find the best-fit models (Tazzari et al. 2016).

In panel (a) of Figure 4.10 we show the comparison between the observations at 850 μm and the best-fit model (obtained running a MCMC with 500 chains) that corresponds to the following median values: $\gamma = 0.882 \pm 0.002$, $\Sigma_0 = (13.40 \pm 0.03)$ g/cm^2, $R_c = (118.7 \pm 0.2)$ AU. We note that the model with median values also gives the minimum χ^2, with $\chi^2_{\rm red}$ =1.853. The ring-shaped residuals are clearly visible in the righthand plot of panel (a), and this show

that a simple two-layer disk model with a monotonically decreasing surface density (and thus surface brightness) is not sufficient to completely account for the observed flux density profile.

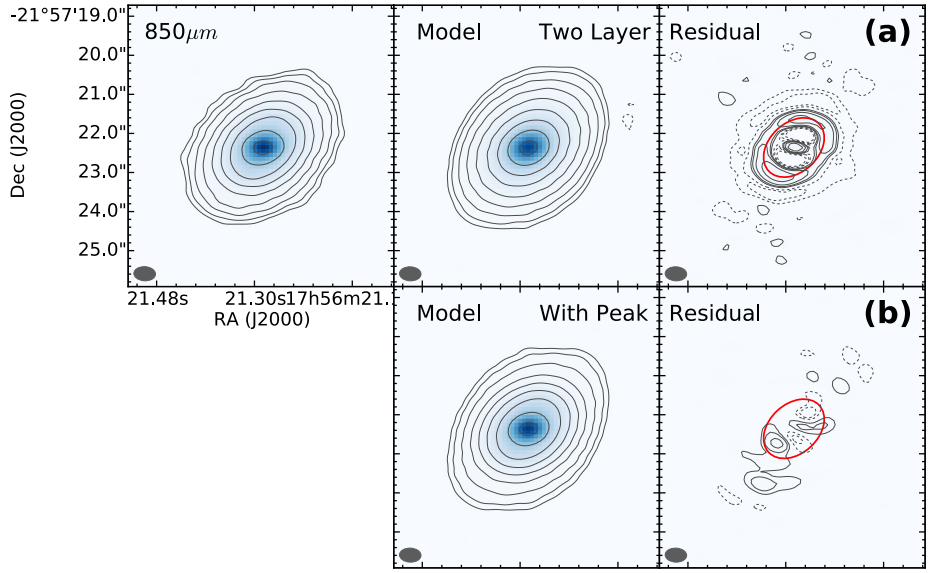

Figure 4.10: Continuum maps at 850μm showing the results of the fits of the visibilities. The top left panel shows the observations, the two panels in the center the best-fit model, and the two panels on the right the residuals. The red solid curve represents the CO snowline at 90 AU. Panel (a): we use a classical two-layer disk model that implements a monotonically decreasing surface brightness. Ring-shaped residuals are clearly visible. Panel (b): we use the two layer disk model with an additional Gaussian peak. We fit the peak location ($R_{\rm p}$ = 96 AU) and width FWHM$_{\rm p}$ = 58 AU. The residuals are substantially reduced. The parameters used for the CLEAN are the same as discussed in Section 4.2, and the contour levels are the same as those used in Figs. 5.C.1 and 4.9.

To assess whether the residuals can be explained by adding a simple ring-like peak or whether they need a more complicated treatment, we performed another fit with a modified version of the two-layer model. This modified two-layer disk model implements an additional ring-like structure in the 850 μm emission, with a disk surface brightness $I'(R)$ as follows:

$$I'(R) = I_{\rm 2L}(R) + I_p I_{\rm 2L}(R_p) \exp\left[-\frac{(R-R_p)^2}{2\sigma_p^2}\right], \tag{4.3}$$

where $I_{\rm 2L}(R)$ is the brightness computed by the classical two layer model, R_p the peak center, σ_p the peak width, and I_p the peak intensity (in units of the brightness in the vicinity of the peak, namely $I_{\rm 2L}(R_p)$). This new model therefore has six free parameters: three of them for the two-layer model (γ, Σ_0, R_c) and another three to define the peak (R_p, σ_p, I_p). We performed the fit with the Tazzari et al. (2016) modeling tool discussed above, with the results shown in panel (b) of Figure 4.10. The best-fit model ($\chi^2_{\rm red}$ =1.830) is described

by $\gamma = 1.32 \pm 0.01$, $\Sigma_0 = (24.6 \pm 0.3)$ g/cm^2, $R_c = (111.3 \pm 0.8)$ AU, which correspond to a radial profile that is slightly steeper than the simple power-law model but has a similar cut-off radius. For the Gaussian peak, we find that is described by $R_p = (96 \pm 1)$ AU, $\sigma_p = (24.9 \pm 0.5)$ AU and $I_p = 128 \pm 20\%$. This modified disk model is able to reproduce the observations with an extremely good agreement, as confirmed by the considerably smaller residuals (right plot of panel (b), Figure 4.10). The midplane temperature is computed at every radius according to the two-layer approximation: in Figure 4.8 (Section 4.3.6) we show the temperature profile of this best-fit model.

In conclusion, the peak inferred from the direct fit of the visibilities is evidence of a ring-like structure centered at 96 AU with a FWHM= $2\sqrt{2\ln 2} \cdot \sigma_p \approx (58 \pm 3)$ AU, compatible with the upper limit resulting from the simple polynomial+Gaussian fitting of the continuum surface brightness in Section 4.3.4.

4.5 Discussion

In Section 4.3 we derived spatially resolved spectral index profiles for the dust emission from the HD 163296 protoplanetary disk and we identified and characterized an unresolved excess 850 μm emission centered at ~110 AU. The presence of this feature has also been confirmed through a detailed modeling of the visibilities in Sect. 4.4. In this section we analyze these results and their possible implications for the growth of grains in the HD 163296 disk.

4.5.1 $\beta(r)$ profiles and grain growth

In Section 4.3.6 we derived the radial distribution of the spectral index as measured combining the ALMA 850 μm image with the ALMA 1.3 mm or the VLA 10 mm images. Under the assumptions of optically thin emission and Rayleigh-Jeans regime, the spectral index profiles can be directly converted into opacity power-law index profiles by subtracting a constant value of 2.0. Our modeling of the disk (Sect. 4.4) and the comparison of the measured brightness temperature with the expected temperature profile from our model (Sect. 4.3.6) confirm that the emission is optically thin throughout the disk, with the exception of the very inner region that is not resolved by the ALMA and VLA observations. On the other hand, the Rayleigh-Jeans approximation is not fully justified in the outer regions of the disk, especially for the ALMA Band 7 data. To estimate the value of the opacity power-law index as a

function of radius we thus used (see Eq. 4.1)

$$\beta(r) = \left[\log\left(\frac{\nu_1}{\nu_2}\right)\right]^{-1} \left[\log\left(\frac{F_{\nu_1}(r)}{F_{\nu_2}(r)}\right) - \log\left(\frac{B_{\nu_1}(T(r))}{B_{\nu_2}(T(r))}\right)\right] \tag{4.4}$$

where $T(r)$ are the temperature profiles derived from our models. In Fig. 4.11 we show the profiles of $\beta(r)$ obtained from Eq. 4.4 using the intensity profiles shown in Fig. 4.9.

Our analysis of the continuum emission at three different frequencies shows in the first place a decreasing spatial extent with increasing wavelength, confirming the presence of dust processing and radial transport in this disk, as already shown by the comparison between the size of the dust and gas disk by de Gregorio-Monsalvo et al. (2013) and confirm and extend the results of Natta et al. (2004, 2007), who showed the presence of large grains in the HD 163296 disk from integrated spectral indices and suggested a possible spectral index variation within the disk.

The $\beta(r)$ profiles are qualitatively consistent with the results of similar analyses performed in other classical smooth disks (Guilloteau et al. 2011, Banzatti et al. 2011, Pérez et al. 2012, 2015, Trotta et al. 2013, Menu et al. 2014, Tazzari et al. 2016), with a significant variation of β throughout the disk ($\Delta\beta > 1$), indicating a maximum grain size a_{max} decreasing with the distance from the star. The ALMA and VLA data provide for the first time the combination of signal-to-noise ratio, angular resolution and image fidelity to successfully perform an analysis in the image plane. Unfortunately, the ALMA Band 6 science verification data do not have the angular resolution to probe the dust properties in a localized region across the CO snowline. Similarly, the VLA data do not have a high enough signal-to-noise ratio at 100 AU and beyond to derive strong constraints in the outer disk.

The conclusion that we can draw from the $\beta(r)$ profiles is that there is convincing evidence of large grains inside the CO snowline, but at ~70 AU resolution the profile appears to be smooth with no features. The data are consistent with significant grain growth throughout the inner 150-200 AU of the disk. As discussed by many authors (see, e.g., Testi et al. 2014, and references therein), deriving a direct constraint on the level of grain growth from the β values is not trivial, because it requires assumptions on the dust structure and composition, which cannot be constrained outside the solar system. Nevertheless, a very broad range of reasonable assumptions on the grains properties imply that β values lower than 1 in the millimeter to centimeter regime can only be produced by grains and pebbles larger than a millimeter in size, and can be significantly larger under reasonable assumptions for grain porosity (Natta and Testi 2004). As an example, if we adopt an educated guess for the grain

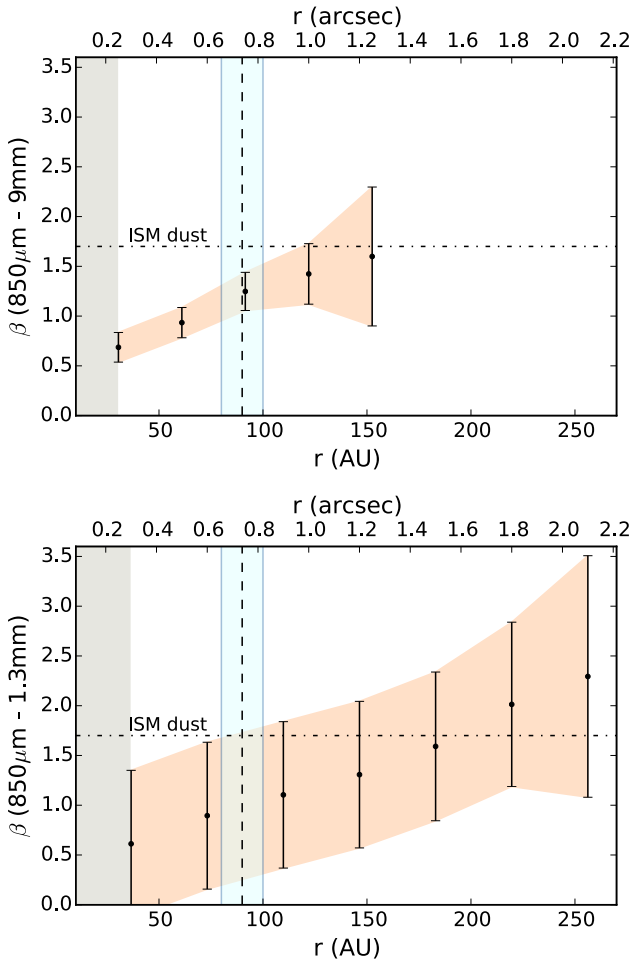

Figure 4.11: Dust opacity power-law index (β) profiles derived using Eq. 4.4. $\beta(r)$ is computed between 850 μm and 9 mm in the top panel and between 850 μm and 1.3 mm in the bottom panel. The uncertainties are propagated from the surface brightness profiles presented in Fig. 4.9. The derived values of $\beta(r)$ in the top panel are dominated by the low signal-to-noise in the VLA image from ~100 AU and are very uncertain beyond this radius. The CO snowline at 90±10 AU from Qi et al. (2015) is pictured as the dashed vertical line.

composition based on the constraints from our own Solar System (e.g., Pollack et al. 1994), combined with a fraction of vacuum of ~50%, we derive maximum grain sizes as large as ~ 1 cm at the CO snowline and even exceeding ~ 10 cm in the inner ~50 AU of the disk (see Fig. 4 of Testi et al. 2014).

4.5.2 The nature of the 850 μm excess

We found an excess emission at 850 μm located at about 105-115 AU from the star with a full width along the disk major axis of $\leq$40 AU. This excess appears to be located very close to the CO snowline at 90 AU as measured by Qi et al. (2015), who resolved the N_2H^+ emission in this disk with ALMA. The N_2H^+ molecule is thought to be a robust tracer of CO

condensation fronts, because of the strong correlation between its abundance and gas phase CO depletion (see also Qi et al. 2013).

An analogous excess ring was found in the images of scattered light from HD 163296 taken with VLT/NACO (Garufi et al. 2014): polarized light images in Ks band displayed a "broken" ring feature with an excess along the major axis between ~0.5 and 1 arcsec, corresponding to 60 and 120 AU, respectively (shown in Figure 4.5, middle panel). The upper limit on the extent of the excess we found corresponds to a total radial extent of $\lesssim$40 AU, while the dimension of the resolved ring found in infrared polarized light by Garufi et al. (2014) measured 0.45″ on the east side and 0.6″ on the west side, corresponding to 60 AU and 73 AU, respectively.

The interpretation of the ring in Ks band polarized contrast given by Garufi et al. (2014) was the effect of self-shadowing of the disk created by a puffed-up inner region, with the outer disk emerging from the shadow at the location of the polarized emission. Garufi et al. (2014) could not exclude other effects that are possibly related to the CO snowline, but could not reach a conclusion as the polarized infrared light is tracing the $\tau \sim 1$ (at 2 μm) surface of the disk atmosphere at much higher altitudes in the disk than the cold midplane where the CO snowline (and the bulk of the disk material) is located.

Our result provides an important contribution, since it shows that the excess is not purely a disk surface feature. The detection of the excess at the two different wavelengths, tracing two different vertical regions of the disk, suggests the presence of a structure that concerns the whole vertical extent of the disk. At millimeter wavelengths we are probing the disk midplane, and the emission is proportional to the surface density, the dust properties, and the temperature profile (see Sect. 4.3.6). In principle any localized change of one (or more) of these properties can explain the excess emission that we find in our images.

The lack of sensitivity or angular resolution in the VLA and ALMA Band 6 data do not allow us to probe the spectral index of the excess detected in Band 7. Future ALMA and/or VLA observations may allow us to probe the presence of large grains at the location of the excess emission. The possibility of large grains at the snowline may also be connected with a local increase in the surface density (or temperature), which could also explain the observed excess.

This is indeed expected from the simulations of grain growth across snowlines (e.g., Ros and Johansen 2013). We note that the effect of snowlines on grain growth is still poorly

understood theoretically and much work is still needed. Recent simulations (Stammler, priv. comm.) show that, as grains maintain the (water) ice mantles across the CO snowline, this does not produce a discontinuity in the coagulation and fragmentation properties. The only effect would be a drop in the mass of solid particles inside the snowline because a fraction of the mantles is released in the gas. Such a variation in the surface density distribution across the snowline may produce an effect similar to the one we observe in the brightness profile and possibly also explain the effects on the disk surface observed in the near infrared.

Another mechanism that has been proposed to explain emission rings near snowlines in disks is sintering (Okuzumi et al. 2015): this process brings icy grains to bond at temperatures close to the sublimation temperature. As a consequence, these aggregates can easily fragment by collisions close to the snowline leading to the accumulation of smaller fragments, which are less affected by radial drift. Clearly more theoretical work is needed before a detailed comparison of our observations with models can be done.

An alternative explanation for this excess emission, which is not connected to the presence of the CO snowline, could be that particles are trapped by zonal flows (Dittrich et al. 2013, e.g.,) or by vortices Such a mechanism has been invoked to explain the presence of annular dust confinement in some transitional disks (e.g., Pérez et al. 2014). Future higher angular resolution mm observations of the dust and gas will allow this possibility to be tested.

4.6 Summary

We have re-analyzed HD 163296 ALMA Science Verification data at 850 μm and 1.3 mm, and VLA data at 8 and 10 mm to study the radial behavior of dust properties in this disk. Our goal was to combine high resolution observations to derive the profile of the dust opacity spectral index, which is ultimately related to the size of grains throughout the disk, and look for evidence of grain growth across the CO snowline.

Our analysis shows, in the first place, more compact emission moving to longer wavelengths, confirming that dust processing and radial migration are taking place in this disk. A significant conclusion is that the dust opacity spectral index varies with radius and decreases toward the center to values $\leq$1, indicating the presence of large grains ($\geq$1 mm) in the inner regions of the disk (inside 100 AU). Our β(r) profiles agree with those found in other resolved disks (Guilloteau et al. 2011, Pérez et al. 2012, 2015, Tazzari et al. 2016, e.g.,).

For this particular source, where a direct measurement of the location of the CO snowline is available, our analysis supports a scenario where the grains outside the snowline have not grown significantly, while the inner disk is populated by large grains. This general distribution would be consistent with an enhanced production of large grains at the CO snowline and subsequent transport to the inner regions. The alternative explanation of a smooth distribution of the grain sizes due to growth and transportation processes unrelated to the CO snowline is also consistent with the observed β(r) profile.

A second important finding is the evidence of an excess in the continuum emission at 850 μm near the location of the CO snowline and approximately at the same position of the excess in Ks band polarized light as found by Garufi et al. (2014). Our finding confirms that the infrared excess emission is not only related to a disk surface layer effect, but also has more profound roots in the disk midplane, which is responsible for the 850 μm emission. The possible causes for this bump could be a local increase in the dust surface density due to dust trapping, for example caused by a local pressure maximum at the location of the snowline (Armitage 2013) or by turbulent eddies that can retain grains in their interior (Klahr and Henning 1997).

It is not clear whether the dust at this location has a different opacity spectral index β with respect to the bulk of the dust, since we lack the spatial resolution and/or sensitivity at 1.3 mm and ~10 mm to clearly detect the excess emission.

To conclusively probe whether this excess is a local change in the dust density and properties due to an effect of the CO snowline or another dust-trapping process, ALMA high resolution and sensitivity observations at mm wavelengths are needed, as well as higher sensitivity VLA measurements. As a future development, with ALMA longer baselines we might be able to resolve the iceline of the most important volatile, H_2O, and investigate the role of snowlines in grain growth more extensively.

5 Unveiling a ringed structure in HD 163296

This Chapter consists of the work published in December 2016 on Physical Review Letters (Isella et al. 2016), with the title *Ringed structure of the HD 163296 disk revealed by ALMA*. The authors of this study were: Isella, Andrea; Guidi, Greta; Testi, Leonardo; Liu, Shangfei; Li, Hui; Li, Shengtai;Weaver, Erik; Boehler, Yann; Carperter, John M.; De Gregorio-Monsalvo, Itziar; Manara, Carlo F.; Natta, Antonella; Pérez, Laura M.; Ricci, Luca; Sargent, Anneila; Tazzari, Marco; Turner, Neal.

My contribution to this work regards the first part of the analysis presented in this paper: in particular, I reduced and calibrated the ALMA dataset, generated the science images and cubes, participated in the analysis of the dust and gas morphology and wrote the section of the text describing the observations.

Abstract

We present Atacama Large Millimeter and sub-millimeter Array (ALMA) observations of the protoplanetary disk around the Herbig Ae star HD 163296 that trace the spatial distribution of millimeter-sized particles and cold molecular gas on spatial scales as small as 25 astronomical units (au). The image of the disk recorded in the 1.3 mm continuum emission reveals three dark concentric rings which indicate the presence of dust depleted gaps at about 60 au, 100 au, and 160 au from the central star. The maps of the ^{12}CO, ^{13}CO, and C^{18}O J=2-1 emission do not show such structures but reveal a change in the slope of the radial intensity profile across the positions of the dark rings in the continuum image. By comparing the observations with theoretical models for the disk emission, we find that the density of CO molecules is reduced inside the middle and outer dust gaps. However, in the inner ring there is no evidence of CO depletion. From the measurements of the dust and gas densities,

we deduce that the gas-to-dust ratio varies across the disk and, in particular, it increases by at least a factor 5 within the inner dust gap compared to adjacent regions of the disk. The depletion of both dust and gas suggests that the middle and outer rings could be due to the gravitational torque exerted by two Saturn-mass planets orbiting at 100 au and 160 au from the star. On the other hand, the inner dust gap could result from dust accumulation at the edge of a Magneto-Rotational instability (MRI) dead zone, or from dust opacity variations at the edge of the CO frost line. Observations of the dust emission at higher angular resolution and of molecules that probe dense gas are required to establish more precisely the origins of the dark rings observed in the HD 163296 disk.

5.1 Introduction

After centuries of speculation about planets orbiting stars other than our Sun, the discovery of an extrasolar planet with Jupiter-like-mass came in 1995 (Mayor and Queloz 1995). To date, the most fruitful methods of planetary searches have been transit and radial velocity surveys (Howard et al. 2010, Mayor et al. 2011), especially *Kepler*'s transit surveys (Borucki et al. 2011). However, the discoveries of more than 2000 exoplanet candidates (Morton et al. 2016), mostly gas giants and super-Earths, have raised even more challenges to understanding such systems. For example, while giant planets are believed to form at 0.1-10 au from the central star (Helled et al. 2014), the newly-discovered orbital radii cover a much broader range, 0.01-100 au. This suggests either a surprisingly large mobility of planets or a fundamental flaw in current planetary formation models.

Recently, the unprecedented angular resolution and sensitivity of Atacama Large Millimeter and sub-millimeter Array (ALMA) observations have led to the discovery of ring-shaped structures in the mm continuum emission from the HL Tau and TW Hya protoplanetary disks (ALMA Partnership et al. 2015, Andrews et al. 2016). While the origin of these structures is still debated, it is likely that they are related to the formation of planets, and hence may provide long-awaited observational constraints on the processes responsible for planetary system assembly and evolution.

A number of explanations for the presence of rings in the continuum emission in protoplanetary disks have been put forward. These include the aggregation of solids at the outer edge of disk regions characterized by low turbulence (e.g., Barge and Sommeria 1995, Klahr

and Henning 1997, Li et al. 2001, Lyra et al. 2008, Lyra and Lin 2013, Fu et al. 2014b), variations in the dust opacity at the frost line of volatile elements (Zhang et al. 2015, Okuzumi et al. 2016), and gravitational perturbations caused by yet unseen giant planets (Bryden et al. 1999). In the first two cases, the observed structures might aid the formation of planetesimals by concentrating solid particles and preventing them from accreting onto the star (Pinilla et al. 2012a, Zhu et al. 2012). In the last case, a circular gap is expected when a forming planet is orbiting in a disk. The orbital radius and mass of the planet can be inferred from the location and shape of this gap (Bryden et al. 1999). For HL Tau, it has been suggested that the observed ringed structure is due to the presence of Saturn mass planets orbiting at several tens of au from the central star (Jin et al. 2016). This implies that giant planets can form on much shorter timescales, and at much larger distances from the central star, than predicted by current planet formation models (Helled et al. 2014).

The initial results of ALMA observations are promising but key questions remain unanswered. In particular it is not clear if ring-like structures are common to all protoplanetary disks. ALMA high angular resolution observations targeted the most luminous disks first, and these may not be representative of the bulk of the disk population. Furthermore, dust continuum images do not probe the distribution of the circumstellar gas and thus cannot distinguish unambiguosly between different formation processes. Addressing such questions will require a multi-pronged approach involving both large continuum surveys of nearby protoplanetary disks with ALMA and in-depth multi-wavelength studies of the most relevant structures revealed.

In this Letter, we report on the structure of the HD 163296 disk as revealed by ALMA observations of the dust continuum emission and also line emission from three isotopologues of carbon monoxide, ^{12}CO, ^{13}CO, and C^{18}O. HD 163296 is a young (5 Myr) intermediate mass (2.3 $M_\odot$) Herbig Ae star located at 122^{+17}_{-13} pc from Earth (van den Ancker et al. 1997). The star is surrounded by a gaseous Keplerian disk with a radius of about 550 au. By contrast, mm-wave continuum emission arising from solid particles is confined within 250 au from the star (Isella et al. 2007, de Gregorio-Monsalvo et al. 2013). Previous ALMA observations showed that the continuum emission has a local maximum at about 90 au (Guidi et al. 2016), suggesting a dusty ring at a distance that corresponds to the frost line for CO molecules (Qi et al. 2015). Recently, we have imaged the HD 163296 disk with ALMA at 0.2″ angular resolution, a factor of 3 higher than previous observations and corresponding to a physical

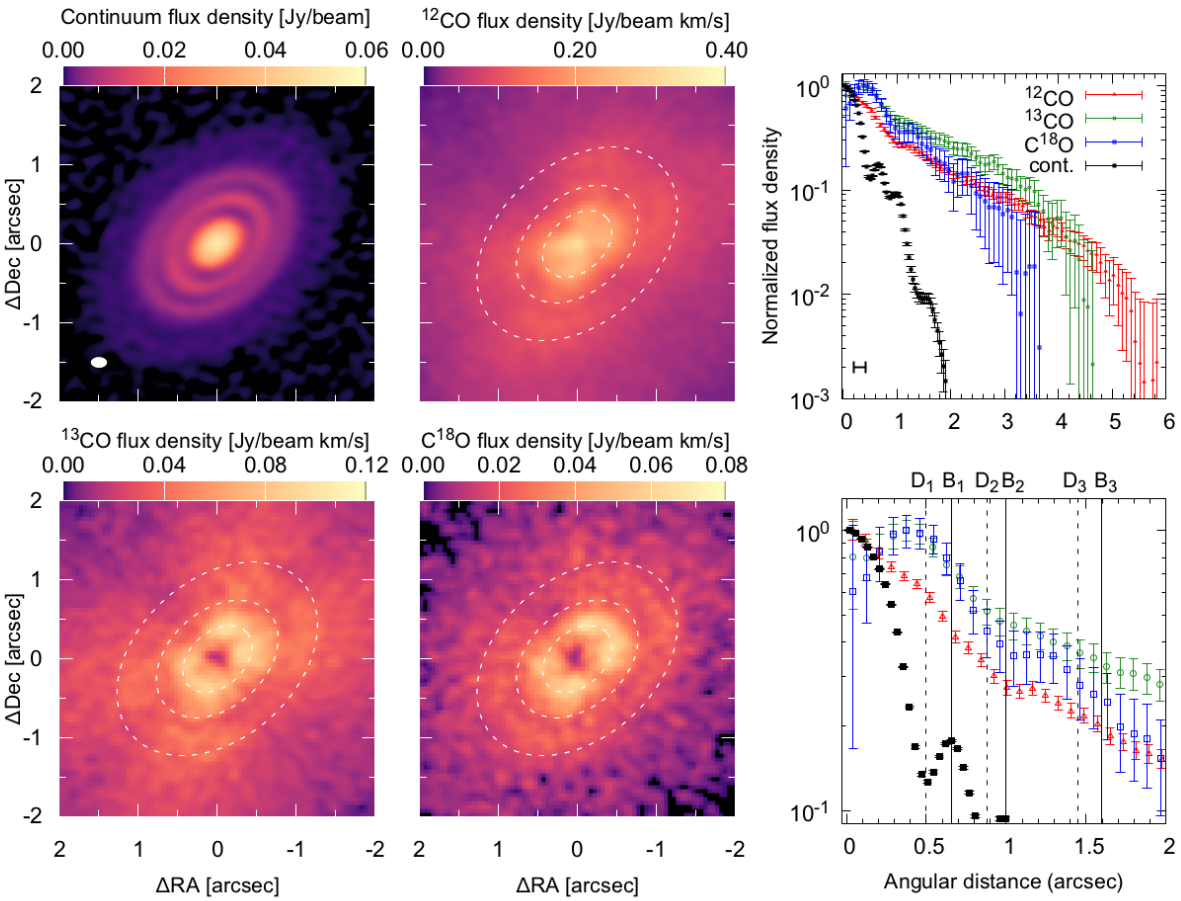

Figure 5.1: ALMA images of the HD 163296 disk emission recorded in 1.3 mm dust continuum (top left), ^{12}CO (top middle), ^{13}CO (bottom left), and C^{18}O (bottom middle) J=2-1 line emission. The angular resolution of the observations, 0.22″×0.14″, is indicated by the filled white ellipse in the continuum image. The dashed ellipses in the CO maps indicate the locations of the dark rings seeing in the continuum map. Azimuthally averaged profiles, normalized to the peak intensities, are shown in the right panels. They are calculated by averaging on elliptical annuli with a position angle of 132°, an eccentricity of 0.7, and a width equal to 1/4 of the angular resolution of the observations. The error bars are calculated by dividing the root mean square noise of the observations (see Table 1 in the Supplemental Material) by the square root of the number of independent beams in each annulus. The vertical lines indicate the position of the dark (D) and bright (B) rings observed in the continuum map. The horizontal bar in the top right panel indicates the angular resolution of the observations.

scale of 25 au at the distance of the star. The observations reveal rings in the dust continuum emission similar to those observed toward HL Tau. They also reveal the morphology of the ^{12}CO, ^{13}CO, and C^{18}O emission on the same angular scales as the continuum. Here we show that the combination of continuum and molecular line observations offers stringent tests for several physical processes related to planet formation and planet-disk interaction.

5.2 Observations

Figure 5.1 shows the images of the HD 163296 continuum emission together with those of the continuum-subtracted, spectrally integrated ^{12}CO, ^{13}CO, and C^{18}O J=2-1 lines. The acquisition and calibration of the data are described in the Supplementary Material. Also displayed are the radial intensity profiles across the disk calculated by averaging the flux density over elliptical annuli characterized by a position angle of 132° and an eccentricity of 0.7 to correct for the disk inclination and orientation Isella et al. (2007), Qi et al. (2015).

The continuum emission is in first approximation centrosymmetric and confined to an angular radius of about 2″ from the central star. It is also characterized by three pairs of low and high luminosity elliptical rings, labeled as (D1, B1), (D2, B2), and (D3, B3), where (D1,B1) and (D3, B3) are the innermost and outermost pairs, respectively. The aspect ratios of the rings correspond to an intrinsically circular disk inclined by 42° with respect to the line of sight; 90° corresponds to an edge-on orientation. The inclination agrees with previous measurements based on CO observations (Isella et al. 2007, Qi et al. 2015). The radial profile of the dust continuum emission decreases by a factor of 1000 within 2″ of the star. The ratios of the continuum intensity for each high/low luminosity ring pair are 1.6 (B1/D1), 1.3 (B2/D2), and 1.08 (B3/D3). In first approximation, the azimuthally averaged profile of the continuum flux density can be modeled by a combination of Gaussian functions, $f(\theta) = g(\theta) - g_1(\theta) - g_2(\theta) - g_3(\theta)$, where $g(\theta) = ae^{-(\theta/b)^2}$ and $g_n(r) = a_n e^{-((\theta-\theta_n)/b_n)^2}$. This profile mimics that of a disk with gaps in the continuum flux density characterized by radius θ_n and width b_n. A nonlinear least-squares Marquardt-Levenberg fit of the observations returns $\theta_1 = (0.44 \pm 0.01)''$, $\theta_2 = (0.81 \pm 0.01)''$, $\theta_3 = (1.13 \pm 0.02)''$, and $b = (0.76 \pm 0.02)''$, $b_1 = (0.23 \pm 0.01)''$, $b_2 = (0.15 \pm 0.01)''$, $b_3 = (0.28 \pm 0.02)''$, with a reduced $\chi^2 \sim 2$. A table with the best fit value of the gaussian modeling is provided in the Supplemental Material.

Molecular emission is detected in all three CO isotopologues, and differs from the continuum in three main aspects. First, the CO intensity maps do not show any prominent ringed structure and, differently from the continuum, their radial profiles cannot be approximated by a simple mathematical function. Second, the ^{13}CO and C^{18}O line intensities have local minima at the center of the disk, while both the continuum and the ^{12}CO line are centrally peaked. We ascribe the ^{13}CO or C^{18}O central minima to an over subtraction of the continuum emission, and not to a physical decrement of the gas density or temperature. This point

is discussed in more details in the Supplemental material. Third, the molecular emission is much more extended and decreases with the orbital radius more slowly than the continuum. In particular, the ^{12}CO emission decreases only to about 15% of its peak value at radius 2″. Zooming into the central disk regions, as in the bottom right panel on Figure 5.1, indicates that only mild changes in the CO emission occurs at the location of the continuum rings. A bump in ^{12}CO emission is observed near D1 and a flattening of the slope of the emission can be seen near B2 for all three isotologues, with the C^{18}O emission increasing slightly between 1″ and 1.2″.

5.3 Data analysis

In this section, we investigate the ringed structure observed in the continuum and the aforementioned morphological differences between continuum and molecular line emission. We do this by modeling the continuum and spectrally integrated line emission maps presented in Figure 1. The analysis of the spectrally resolved line emission will be presented in a future work.

The continuum and line emission of a protoplanetary disks depend on the three dimensional density and temperature distribution of dust and gas, the gas velocity, the dust opacity, the disk inclination, and the distance of the source. In recent years, the HD 163296 disk has been the subject of several studies whose results provide a starting point for our investigation. Following the methodology described in (de Gregorio-Monsalvo et al. 2013) and (Rosenfeld et al. 2013), we describe the surface density of gas and dust as

$$\Sigma(r) = \Sigma_c (r/r_c)^{-\gamma} \exp[-(r/r_c)^{2-\gamma}], \tag{5.1}$$

and the disk temperature as

$$T(r,z) = \begin{cases} T_a(r,z) + [T_m(r) - T_a(r,z)] \left[\cos \dfrac{\pi z}{2 z_q(r)}\right]^{2d(r)}, & \text{if } |z| < z_q(r) \\ T_a(r,z), & \text{otherwise} \end{cases} \tag{5.2}$$

In the latter equation, $T_m(r) = T_{m,0}(r/r_0)^{-q_m}$ and $T_a(r,z) = T_{a,0}(\sqrt{r^2+z^2}/r_0)^{-q_a}$ are the temperature of the disk midplane and surface layer, respectively. The temperatures of these two layers are smoothly connected through the functions $d(r) = d_0(r - r_0) + c$ and $z_q(r) = z_{q,1}(r/r_1)^{q_z} e^{-(r/r_2)^2}$. This rather complex parameterization of the disk temperature mimics the thermal structure of an externally illuminated disk and enable us to generate synthetic

models for the dust and gas emission avoiding calculating the disk temperature using time consuming radiative transfer models.

Using Equation 1 and 2, and the procedure described in the Supplemental Material, we find that the dust emission measured at angular radii less than 0.3″ and lager than 1.8″ is consistent with a dust surface density characterized by $\gamma = 0.1$, $r_c = 90$ au, $\Sigma_c = 0.42$ g cm^{-2}. The low value of γ implies that the dust density within about 90 au from the star scales with the radius approximately as a Gaussian. This result is consistent with the parametric fitting of the dust continuum emission described in the previous section.

Applying the same procedure to the ^{12}CO, ^{13}CO and C^{18}O emission, we find gas surface densities characterized by $\gamma = 0.8$, $r_c = 165$ au, $\Sigma_c(^{12}\mathrm{CO}) = 1.6 \times 10^{-3}$ g cm^{-2}, $\Sigma_c(^{13}\mathrm{CO}) = 2.3 \times 10^{-5}$ g cm^{-2}, and $\Sigma_c(\mathrm{C}^{18}\mathrm{O}) = 2.9 \times 10^{-6}$ g cm^{-2}. Our modeling suggests that (i) the ^{12}CO/^{13}CO and ^{12}CO/C^{13}O density ratios are radially constant, (ii) the CO/dust ratio changes with the orbital radius, and (iii) that the disk thermal structure is characterized by $T_m(r) = 24\mathrm{K}(r/100\mathrm{au})^{-0.5}$ and $T_a(r,z) = 68\mathrm{K}(\sqrt{r^2+z^2}/100\mathrm{au})^{-0.6}$.

However, disk models characterized by a smooth density profile predict too much emission in the region where rings are seen in dust continuum. To correct for this excess, we introduce circular gaps in the dust and gas surface density. Each gap is described by three parameters: the distance between the center of the gap and the star (R), the width of the gap (W), and the ratio between the surface density inside and outside the gap (Δ). We calculate synthetic images for the dust continuum, ^{12}CO, ^{13}CO, and C^{18}O J=2-1 emission for different values of the gap parameters (R, W, Δ), and compare them to the observations. Figure 5.C.5 shows the set of models that better reproduce the observations, while the modeling procedure is described in the Supplemental Material.

The colored area in left panel of Figure 5.C.5 shows the values of the dust surface density compatible with the observations. The dark rings observed in the continuum map are compatible with the presence of three partially dust depleted gaps centered at $R_1 = 60$ au, $R_2 = 100$ au, and $R_3 = 160$ au. Given the finite angular resolution of the observations, there is a degeneracy between the gap width W and dust depletion Δ^d. We find that the narrowest gaps compatible with the observations have widths of $W_1 = 25$ au, $W_2 = 22$ au, and $W_3 = 45$ au. The dust depletion factors inside the gaps are $\Delta^d_1 > 100$, $\Delta^d_2 = 70$, and $\Delta^d_3 = 6$. The widest gaps compatible with the observations have widths of $W_1 = 33$ au, $W_2 = 26$ au, and $W_3 = 55$ au, and depletion factors $\Delta^d_1 = 13$, $\Delta^d_2 = 7$, and $\Delta^d_3 = 3.6$. The dust surface density

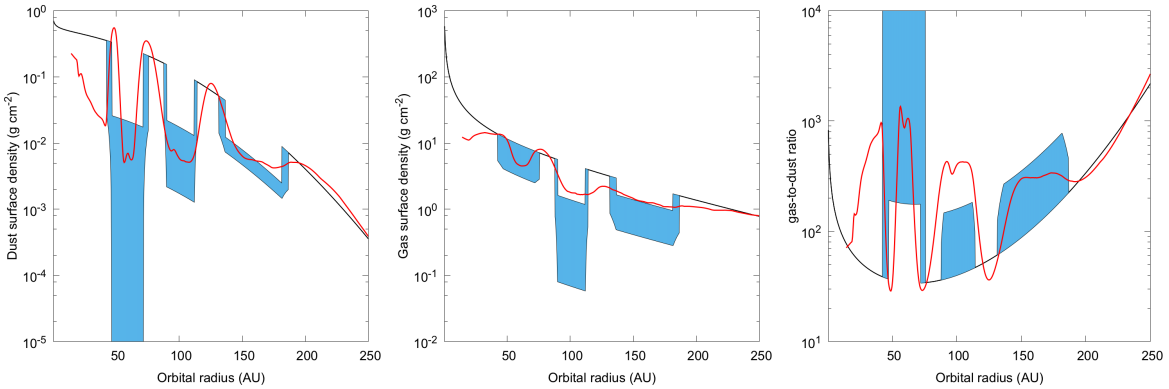

Figure 5.2: Constraints on the dust and gas surface density (left and middle panels, respectively, and on the gas-to-dust ratio (right panel), derived by comparing ALMA observations of the HD163296's disk with synthetic models for the disk emission. The red solid curve indicates the prediction for a disk model perturbed by three planets with masses of 0.1, 0.3, and 0.3 M_J orbiting at 62, 105, and 160 au from the central star.

inside the inner gap is $\lesssim 3 \times 10^{-2}$ g cm^{-2}, while it varies between 3×10^{-3}-3×10^{-2} g cm^{-2} and 4×10^{-3}-7×10^{-3} g cm^{-2} in the middle and outer gaps, respectively. The ratios between the half-width and the radius of the gaps are between 0.21-0.28 for the innermost gap, 0.1-13 for the middle gap, and 0.14-0.17 for the outermost gap.

The central panel of Figure 5.C.5 shows the constraints on the gas (H_2) surface density derived from the CO observations adopting a cosmic molecular abundance $n(^{12}CO/H_2) = 5 \times 10^{-5}$ (Wilson 1999). In our analysis, we assume that the gaps in the dust and CO have the same width and radius, and explore different values for the depletion factor Δ^{CO}. Inside the inner dust gap, we measure Δ_1^{CO} between 0-2.5. This implies that CO molecules are at least 5 times less depleted than the dust. In the middle and outer gaps, we measure Δ_2^{CO} between 3.5-70 and Δ_3^{CO} between 1.8-6, respectively. These latter values are similar to those inferred for the dust.

Finally, the right panel of Figure 5.C.5 shows the gas-to-dust ratio obtained by combining the results for the dust and gas surface density. The gas-to-dust ratio increases from about 40 at 100 au to more than 1000 for $r > 250$ au. The gas-to-dust ratio inside the first dust gap is at least 5 times larger than outside the gap. Such an increase results from the discrepancy between the depletion in dust and CO. Inside the middle and outer dust gaps the gas-to-dust ratio varies by less than a factor of 2. Our model also suggests that the gas-to-dust ratio might increase for $r < 50$ au. However, this result should be taken with caution because both the dust and CO emission inside this radius are optically thick and the corresponding surface densities are affected by a large uncertainty.

5.4 Discussion

To date, the HD 163296 disk is the third system known to host multiple rings in the dust continuum emission, but it is the only one for which we have succeeded in mapping the molecular gas emission at the same angular resolution of the continuum. As mentioned above, such ringed structures are thought to be related to the formation of planets, but it is unclear whether they trace an early stage of planet assembly or whether they result from the interaction with already formed planets. In this section we discuss how measuring the spatial distribution of both gas and dust is key to address this question.

Disk-planet interaction: The interaction between disks and planets is based on the notion that the gravitational field of a planet exerts a tidal torque on the circumstellar material, which allows the transfer of angular momentum between the planet and the disk (see, e.g., Papaloizou et al. 2007). The consequences are twofold: one an hand, the planet is predicted to migrate; on the other hand, the density waves launched by the planet are expected to alter the disk surface density. If the planet gravity exceeds the stellar gravity across the vertical extent of the disk, then the planet opens a circular gap in the disk surface density (Bryden et al. 1999). The radius, width, and level of gas and dust depletion within the gap carry information about the planet and disk properties.

Numerical simulations show that the width W of a gap opened by a planet should depend on the planet mass M_p and orbital radius R_p following the relation

$$W \sim C \times R_p \left(\frac{M_p}{3M_\star}\right)^{1/3}, \tag{5.3}$$

where the proportionality constant C varies between 4-8 (Bryden et al. 1999, Rosotti et al. 2016, Wolf et al. 2007). In the case of HD 163296, the gap widths derived in the previous section would imply planet masses between 0.5-2 M_J for the innermost planet, 0.05-0.3 M_J for the middle planet, and 0.15-0.5 M_J for the outer planet. In addition, the disk viscosity can affect both the gap width and depth (Kanagawa et al. 2016). Various models have predicted that, at equilibrium, the depth of a gap opened by a planet in the gas surface density should depend on the planet mass through the relation (Kanagawa et al. 2015)

$$\frac{M_p}{M_\star} = 5 \times 10^{-4} (\Delta - 1)^{1/2} \left(\frac{h}{0.1}\right)^{5/2} \left(\frac{\alpha}{10^{-3}}\right)^{1/2}, \tag{5.4}$$

where h is the gas disk aspect ratio, Δ is the gas depletion ratio, and α is the Shakura-Sunyaev viscosity parameter (Shakura and Sunyaev 1973). This relation indicates that generally a

lower disk viscosity and aspect ratio would result in a deeper gap for a fixed planet mass.

In the case of HD 163296, we use our disk temperature model derived from the observations to calculate a disk aspect ratio of 0.05 at 60 au, 0.065 at 100 au, and 0.07 at 160 au. By combining Equation 5.3 and Equation 5.4 we estimate the viscosity parameter α. We obtain $\alpha \gtrsim 2\times10^{-2}$ in the inner gap, $10^{-6} < \alpha < 5\times10^{-3}$ in the middle gap, and $10^{-4} < \alpha < 7\times10^{-3}$ in the outer gap. The larger α of the inner gap results from the fact that low or no gas depletion is observed despite a dust gap width that is larger than those of the other two dust gaps. These heuristic considerations work reasonably well for the middle and outer gaps but the inner gap presents additional challenges. The gas-to-dust ratio is the largest for this gap, which for a given planet mass, would require a relatively low viscosity (e.g., Zhu et al. 2012), in contrast to the value derived above. This discrepancy suggests that additional processes might be happening around the first gap, including the possibility of having multiple planets.

To better understand the effect of planet perturbations on the structure of the HD 163296 disk, we have compared the gas and dust surface density derived from ALMA observations with hydrodynamic simulations of the planet-disk interaction. The setup of the simulations is described in the Supplemental Material. The red line in Figure 5.C.5 shows the dust and gas surface density for a disk perturbed by three planets with masses of 0.1 M_J, 0.3 M_J, and 0.3 M_J orbiting at 62 au, 105 au, and 160 au from the star. The surface density profiles were extracted after 2000 orbits of the innermost planet corresponding 7×10^5 yr.

We find that the gas and dust surface density measured across the middle and outer gaps are compatible with perturbations from Saturn mass planets and a disk viscosity parameter $10^{-3} < \alpha < 10^{-2}$. The planets carve rather shallow and axisymmetric gaps in the gas surface density, whereas the gaps in the dust are deeper due to migration of solid particles toward the edges of the gas gaps. As a consequence, the gas-to-dust ratio inside the gaps formed by the planets increases with respect to the surrounding disk regions.

Our simulations show that perturbations from a single planet cannot explain the properties of the inner gap. The width of the gap generated by a 0.1 M_J planet is narrower than that suggested by the observations. A more massive planet would make the gap wider, but the gap would be too depleted in gas. Increasing both the planet mass and the disk viscosity would make the gap wider and shallower, but, a larger viscosity would cause the gas-to-dust ratio inside the gap to drop well below 5. As a possible solution, we argue that the inner gap might be created by multiple planets between 50-70 au. For example, two Saturn mass plan-

ets orbiting around 55 au and 65 au might create a joint gap consistent with the observations though the stability of such a configuration remains to be investigated (see, e.g., Tamayo et al. 2015). However, observations with higher angular resolution would be required to test this hypothesis.

MRI "dead-zone": An ionized Keplerian disk embedded in a weak magnetic field is predicted to be subject to the magneto-rotational instability (MRI, Balbus and Hawley 1991). MRI should generate turbulent motions capable of transporting angular momentum outward, therefore allowing the circumstellar material to accrete onto the star. If the gas ionization varies with the orbital radius, then the mass flow rate throughout the disk is not constant and gas and dust can pile up forming ringed structures.

There are two main transitions in the gas ionization in a disk characterized by a monotonically decreasing surface density. The first happens at a fraction of au from the star where the gas temperature exceed 1000 K and the thermal ionization is strong. The ionized region is predicted to have high turbulence velocities and quickly accrete onto the central star, possibly leading to the formation of a large central hole (Chiang and Murray-Clay 2007). At larger distances the ionization is non-thermal and caused mostly by stellar ultraviolet and X-ray photons and interstellar cosmic rays, which are absorbed over columns of 0.1, 10 and 100 g cm^{-2}, respectively. (Igea and Glassgold 1999, Perez-Becker and Chiang 2011, Umebayashi and Nakano 1981). The ionized regions experience MRI which leads to turbulent speeds that increase with height above the disk midplane in proportion to the Alfven speed, reaching the local sound speed above several disk scale heights (Miller and Stone 2000, Simon et al. 2011). At surface densities above about 10 g cm^{-2}, the disk midplane is expected to be mostly neutral and quiescent. In the outermost disk regions, for $\Sigma < 10$ g cm^2, the disk midplane returns to be partially ionized. The sharp gradient in turbulence, and henceforth in mass flow rate, at the interface between the MRI "dead-zone" and the MRI active midplane is predicted to lead to a pile up of dust and gas, which might appear as an emission ring once observed with ALMA (Flock et al. 2015).

MHD simulations of protoplanetary disks predict that the gas surface density at the outer edge of an MRI dead zone might increase by a factor of a few compared to the surrounding regions (Flock et al. 2015). The increase in gas density creates a gas pressure maxima which might trap dust particles, therefore augmenting the radial variation in the dust surface density. Our measurement of the gas surface density of the HD 163296 disk (central panel

of Figure 5.C.5) indicates that the MRI “dead zone" might extend to about 60-100 au from the central star. This distance is similar to the radius of the first bright continuum ring, suggesting that this process might perhaps be involved in the ring formation. Furthermore, the large gas-to-dust ratio measured inside the inner dust gap would imply low viscosity. This is consistent with the presence of a MRI “dead-zone”. The middle and outer dust gaps at 100 au and 160 au from the star do not seem to be compatible with this scenario though.

Phase transition of volatile elements: The phase transition from solid to gas of molecules such as H_2O and CO is predicted to alter the coagulation and fragmentation properties of dust grains, possibly leading to the accumulation of dust particles in ring-like structures. Dust grains located in the cold regions of protoplanetary disks are expected to be covered by ice mantles, which make them more sticky compared to bare grains and more prone to growth in size as result of collisions. As the size of a dust grain increases, so does the drag caused by the aerodynamic friction with the circumstellar gas. As a result of this process, larger icy grains are predicted to drift inward toward warmer disk regions. Eventually they will cross the frost lines relative to the molecules that form their ice mantles, which will then evaporate. When this happens, the grain size shrinks affecting both its opacity and the gas drag. The combined result is an increase in the dust opacity right behind the frost line, which might result in the formation of bright emission rings in the microwave continuum emission (Banzatti et al. 2015, Zhang et al. 2015).

A second effect of the evaporation of volatile elements from dust grains is described by the so called “sintering" model (Okuzumi et al. 2016) which postulates that the grains are fractal aggregates of smaller particles. Outside each volatile’s frost line, the aggregates are covered by a layer of ice. As inward drifting particles approach the frost line, the ice molecules become mobile and migrate to the necks between the component particles, making rolling and sliding difficult. This reduces the internal degrees of freedom available to take up excess energy when aggregates collide. The aggregates become hard but brittle, and break apart easily in collisions. The smaller fragments drift more slowly, enhancing the dust surface density near the snow line and causing radial variations in the dust opacity (Okuzumi et al. 2016).

In general, the snow lines of H_2O and CO should be the easiest to observed due to the large abundance of these molecules. At the typical densities of protoplanetary disks, water and CO condensate at temperature between 130-150 K and 18-28 K respectively (Qi et al.

2015, Zhang et al. 2015). At the temperatures of the HD 163296 disk (Figure 5.3), the water snow line occurs within 3 au from the star and is not resolved by our observations. Instead, the CO snow line might occur between 40-180 au and might overlap with the ringed structures observed in the continuum.

A key aspect of the sintering and frost line models is that the formation of continuum emission rings by evaporation of volatile elements does not require and might not produce any variation in the gas distribution. Actually, these models require a constant radial inflow of particles which will not happen if the gas density has bumps in the radial direction. Therefore, the depletion of CO molecules measured inside the middle and outer gaps is inconsistent with the evaporation of volatile elements. However, this process might play a role in shaping the disk regions around the innermost dust gap at 59 au, where the CO observations do not show any evidence of gas depletion. Future ALMA observation of molecules capable of tracing denser gas, e.g., HCO+ (Yen et al. 2016), are required to set more stringent constraints on the nature of this inner gap and on the role of the evaporation of volatile elements.

5.5 Conclusions

We have presented ALMA observations of the HD 163296 circumstellar disk that reveal three dark rings in the dust continuum emission. HD 163296 is the third system known to host multiple rings in the dust continuum emission, but it is the only one for which we have succeeded in mapping the molecular gas emission at the same angular resolution of the continuum. By comparing the observations with radiative transfer models, we find that the continuum rings can be explained with the presence of three circular dust depleted gaps with radii of 60 au, 100 au, and 160 au. Furthermore, we find that the density of CO molecules inside the middle and outer dust gaps is also reduced compared to the surrounding regions.

We argue that the morphology of these two gaps is consistent with gravitational perturbations caused by two Saturn-mass planets orbiting at about 100 au and 160 au. Such large orbital radii and the young age of this disk, would imply that giant planets might form much farther away from the central star and much more rapidly than previously thought. Finally, we note that the presented planet configuration might not be unique. A detailed analysis of the HD 163296 ALMA observations in the framework of planet-disk interaction models will

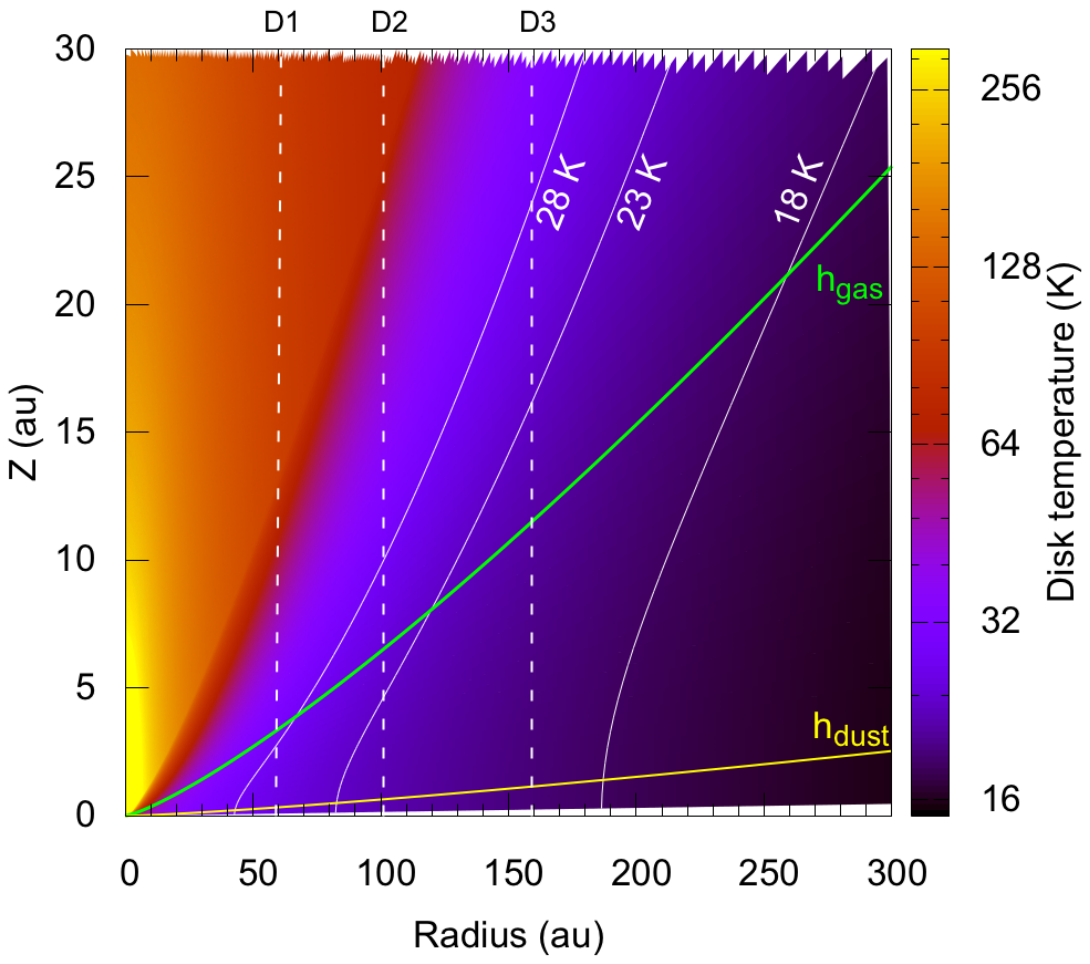

Figure 5.3: Temperature of the HD 163296 disk inferred from the observations of the CO emission. The white solid lines correspond to temperatures of 18 K, 23 K, and 28 K, and indicate the range of condensation temperatures for CO molecules. The vertical dashed line indicate the location of the dust gaps. The green and yellow curves indicate the pressure scale height of gas (h_{gas}) and of large dust grains (h_{dust}), respectively.

be presented in Liu et al. (in preparation).

We do not find any evidence of gas depletion inside the inner dust gap although, due to the large optical depth of the observed CO lines, we cannot rule out the presence of a shallow gas gap. The morphology of the inner dust gap is not well described by perturbations caused by a single planet. Instead we suggest that it might have formed as the result of opacity variations at the outer edge of a MRI "dead-zone" or at the CO frost line.

The results presented in this Letter highlight the importance of imaging protoplanetary disks in both the dust and molecular line emission at high angular resolution. Thanks to the large flux and radial extent, the HD 163296 disk is a perfect target for future ALMA followup

observations. Furthermore, differently from HL Tau, the relative isolation of the HD 163296 disk enables optical and infrared observations to map the morphology of the disk surface and, perhaps, directly detect forming planets.

Supplementary Material

5.A Data acquisition and calibration

HD 163296 was observed by ALMA on 2015 August 5, 8 and 9 at Band 6 using an array configuration that contained 37, 43, and 41 antennas respectively. The projected baselines spanned from 35 m to 1.57 km, resulting in a maximum recoverable size of ∼7″ and an angular resolution of ∼0.2″. J1733-1304 was used to calibrate for bandpass and phase, J1812-2836 was additionally observed every 20 minutes to calibrate the complex gains; Ceres and Titan were used as flux calibrators. The total integration time was ∼4.7 hours, with ∼2.5 hours on the science target.

The correlator was set up to four spectral windows in dual polarization mode, with SPW#1 centered at 231.587 GHz for the continuum (channel width of 15.6 MHz), and three SPWs at high spectral resolution (15.2 kHz, corresponding to 50 m s^{-1} after Henning smoothing): SPW #0 at 230.525 GHz including the CO J=2 - 1 transition, SPW #2 at 220.387 GHz including ^{13}CO J=2 - 1 transition, and SPW #3 at 219.548 GHz including the C^{18}O J=2 - 1 transition. Data were calibrated using the pipelines provided by ALMA, and self calibration was carried out with two rounds of phase calibrations and one of amplitude and phase on the continuum spectral windows of the three execution blocks, then applying the correction tables to both lines and continuum.

The continuum image was generated using the `CLEAN` algorithm in the `CASA` package (version 4.5.0) from the line free channels: we used a pixel size of 0.05″ and a Briggs weighting parameter of -1 to obtain a synthesized beam of 0.22×0.15″ (PA = -88°). After subtracting the continuum in the visibilities space with the task `uvcontsub`, we produced spectral cubes for the three CO lines with a velocity resolution of 50 m s^{-1}.

The angular resolution, rms noise, integrated flux, and peak flux of the dust continuum and spectrally averaged CO maps are listed in Table 5.A.1.

Table 5.A.1: Summary of the continuum and emission line observations. Column 1: name of the observed species and transition. Column 2: reference frequency in GHz. Column 3: spatially integrated flux measured in the continuum (Jy) and in moment 0 of the line emission (Jy km s^{-1}). Column 4: peak flux measured in the continuum (Jy beam^{-1}) and in the moment 0 of line emission (Jy beam^{-1} km s^{-1}). Column 5 and 6: Full Width Half Maximum ($''$) and position angle ($^\circ$) of the synthesized beam. Column 7: robust parameter used for imaging the continuum and line emission. Column 8: root mean square noise measured in the continuum (Jy beam^{-1}) and in the moment 0 line emission (Jy beam^{-1} km s^{-1}).

Species	ν	F_{tot}	F_{peak}	FWHM, PA	rob	noise rms
continuum	231.58797	0.73150	0.0512	0.22×0.15, -89.8	-1	8.9e-5
^{12}CO J=2-1	230.53800	41.054	0.3414	0.22×0.16, -89.8	0	9.0e-3
^{13}CO J=2-1	220.39868	15.529	0.1152	0.23×0.17, -89.4	0	9.4e-3
C^{18}O J=2-1	219.56035	5.463	0.0756	0.24×0.17, -89.6	0	7.4e-3

Table 5.B.1: Best fit values and related 1σ uncertainties of the parametric model of radial profile of the dust continuum emission.

Parameter	Value	Error
a	0.99	±0.01
b	0.76″	±0.02″
a_1	0.55	±0.02
$\theta 1$	0.44″	±0.01″
b_1	0.23″	±0.01″
a_2	0.17	±0.01
θ_2	0.81″	±0.01″
b_2	0.15″	±0.01″
a_3	0.06	± 0.01
θ_3	1.13″	±0.02″
b_3	0.28″	±0.02″

5.B Parametric model of the dust continuum emission

We fit the normalized radial profile of the dust continuum emission with a combination of Gaussian functions, $f(\theta) = g(\theta) - g_1(\theta) - g_2(\theta) - g_3(\theta)$, where $g(\theta) = ae^{-(\theta/b)^2}$ and $g_n(r) = a_n e^{-((\theta-\theta_n)/b_n)^2}$. The values of the best fit parameters are listed in Table 5.B.1, while the comparison between the model and observations is shown in Figure 5.B.1. The best fit parameters and related uncertainties are calculated performing a nonlinear least-squares Marquardt-Levenberg minimization accounting for the errors on the flux measurements.

5.C Disk models and Data analysis

In this section we describe the modeling procedure adopted to analyze ALMA observations. Our main goal is to investigate the nature of ringed structure observed in the continuum

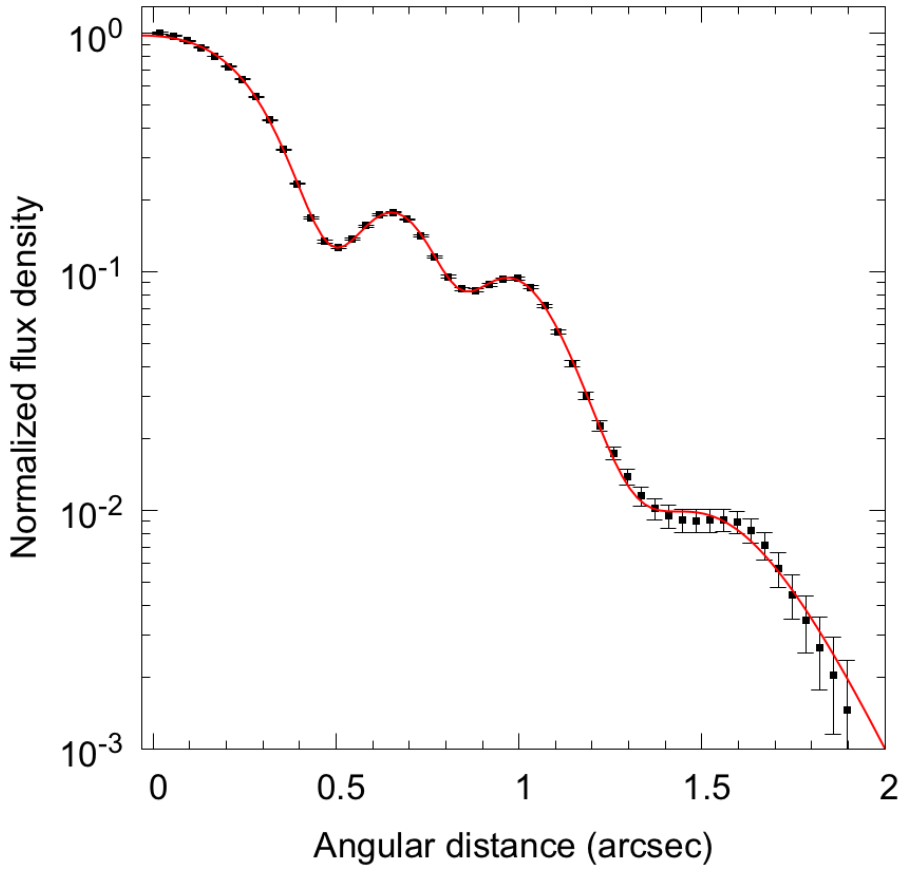

Figure 5.B.1: Comparison between the azimuthally averaged profile of the dust continuum emission (symbols) and a parametric model based on a combination of Gaussian functions.

and the morphological differences between the continuum and the molecular line emission. We do this by comparing the radial profile of the continuum and CO emission with synthetic models for the disk emission. As a caveat, our analysis is performed by exploring the space of model parameters by hand. This choice is dictated by the fact that the large number of model parameters makes an exhaustive exploration of the parameter space extremely time consuming. As a consequence, the disk models presented below should not be considered to provide the best possible match to the observations. Nevertheless, we believe that this approach provides valuable clues to understand the main morphological features of the continuum and line emission. As a second caveat, we limit our analysis to the spectrally integrated map of the molecular emission, and leave the analysis of the gas kinematics to a future paper.

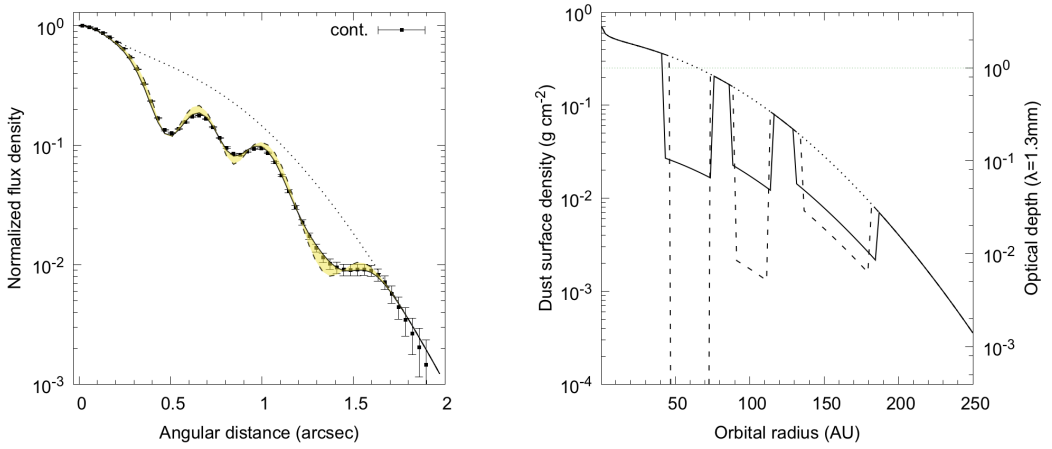

Figure 5.C.1: Physical models for the dust continuum emission. The solid and dashed lines show the intensity (left) and surface density (right) of disk models characterized partially depleted gaps in the radial distribution of dust grains, while the dotted lines correspond to a disk model without gaps. The ringed structure observed in the continuum map is compatible with either narrow and deep gaps or wide and shallow gaps in the surface density profile. The two extreme cases are shown by the dashed and solid line respectively.

5.C.1 Models for the dust emission

We start our analysis by searching for a model for the dust emission capable of reproducing the map of the continuum emission shown in Figure 1 of the main article. This choice is motivated by the fact that while the continuum image is recorded in a line-free region of the spectrum, the molecular line emission is always contaminated by the underlaying continuum. The interplay between line and continuum takes two main forms: first, molecules absorb continuum emission, such that the intensity of the continuum at frequencies covered by molecular lines is lower than the continuum at adjacent line-free wavelengths. This has a strong effect on the appearance of the continuum-subtracted line emission if both line and continuum are optically thick. In this case ($\tau \gg 1$), the intensity of the continuum emission outside the line is proportional to the physical dust temperature T_d, while the intensity at the peak of the line is proportional to the physical gas temperature T_g. This is different from the optically thin case ($\tau \ll 1$), in which the intensity of the continuum+line emission is proportional to $(T_g + T_d) \times \tau$. If $\tau \gg 1$, the line intensity in the continuum-subtracted image is therefore proportional to $T_g - T_d$, and not to T_g as in the optically thin case. Due to the positive vertical temperature gradient of an externally illuminated protoplanetary disk and to the higher opacity of CO molecules compared to dust grains, the layer corresponding to an optical depth of about 1 for the CO emission, i.e., the layer that emits most of the CO

emission, is hotter that the layer emitting the dust continuum ($T_g > T_d$). As a result the CO line is observed in emission on top of the continuum. However, these two temperatures might be quite similar and therefore the continuum subtraction might actually remove a significant fraction of the line emission. For this reason, the interpretation of continuum-subtracted maps of optically thick lines requires caution. A second effect of the interplay between line and continuum emission is that the molecular emission can be absorbed by dust grains if the optical depth of the line is less than that of the dust. This happens if the abundance of the emitting molecule is very low and in the optically thin wings of optically thick lines, such as CO lines.

The interplay between continuum and line emission is complex when the disk emission is spatially resolved, as in the case of HD 163296, and the optical depths of line and continuum emission change with the distance from the star. For example, in the innermost disk regions where both continuum and line emission are optically thick, subtracting the continuum from the line+continuum emission results in underestimating the true line intensity. Moving away from the star, since the optical depth of the continuum drops faster than the optical depth of the line, the effect of the continuum subtraction becomes progressively less important. Finally, in the disk outermost regions where both the line and continuum emission are optically thin, the continuum subtraction returns the true line intensity. As a result of this effect, integrated intensity maps of the continuum subtracted line emission are difficult to interpret. For example, in the case of HD 163296, the over subtraction of the continuum emission in the innermost disk regions leads to a decrement of the ^{13}CO and C^{18}O line emission toward the center of the disk, which might be confused for a chemical or physical effect. We will come back to this point in describing the comparison between models and observations.

We build our disk model upon the recent study of the HD 163296 disk performed by (Rosenfeld et al. 2013, R13 hereafter) and (de Gregorio-Monsalvo et al. 2013), which provide a good description of the ALMA science verification observations of the continuum and ^{12}CO (3-2) and (2-1), ^{13}CO (2-1), and C^{18}O (2-1) line emission observed at a resolution of about 0.6″. These observations have an angular resolution about three times coarser than our new observations and only marginally reveal the presence of substructures in the dust distribution (Guidi et al. 2016).

In brief, the disk surface density and temperature are azimuthally symmetric and depend both on the cylindrical radius r and the distance z from the disk midplane through the Equa-

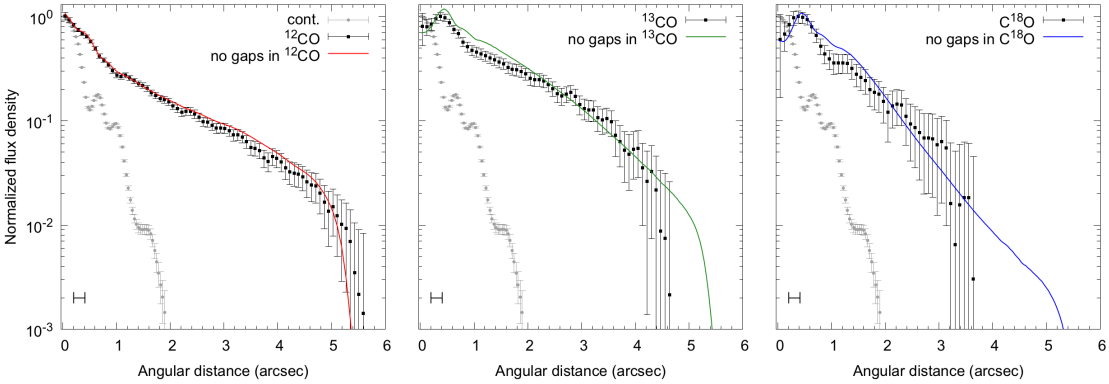

Figure 5.C.2: Comparison between the observations and models for the ^{12}CO (left), ^{13}CO (center), and C^{18}O (right) J=2-1 line emission which do not include any radial gap in the gas density. The solid lines show the radial profile of the CO emission for a disk model characterized by a monotonically decreasing density of CO molecules and a dust surface density with partially depleted gaps as described by the solid curve of the right panel of Figure 2. The radial profile of the dust continuum emission is shown with gray symbols as a reference. The angular resolution of the observations is shown by the horizontal bar on the bottom left of each panel.

tions 1 and 2 in the main paper. The dust surface density is defined between an inner radius of 0.5 AU and an outer radius of 550 AU. The dust density along the direction perpendicular to the disk midplane is calculated by solving the equation of the hydrostatic equilibrium, and assuming that the sub-millimeter grains, i.e., the grains that dominate the opacity at the wavelength of the observations, are settled into a thin disk characterized by a scale height 10 times smaller than that of an hydrostatic equilibrium disk. In order to reproduce the ringed structure observed in the continuum, we carve three circular gaps in the dust density profile. For sake of simplicity, the gaps are rectangular in shape and are described by three parameters: the radius of the center of the gap (R), the full width of the gap (W), and the depth of the gap expressed in units of the non-depleted surface density at the center of the gap (Δ). For each choice of dust surface density, we use the ray tracing module of RADMC-3D (Dullemond 2012) to calculate synthetic images of dust continuum emission assuming a dust opacity at 1.3 mm of 3.95 cm^2 g^{-1}, which corresponds to a typical dust opacity for astronomical grains with a grain size distribution extending up to 1 mm (Isella et al. 2007).

Figure 5.C.1 shows two models that reproduce the continuum map. In both of them, the dust surface density is characterized by $\gamma = 0.1$, $r_c = 90$ au, and $\Sigma_c = 0.42$ g cm^{-2}. The total dust mass integrated between 0.5-550 AU is 6.5×10^{-3} M$_\odot$. This surface density profile has the same γ and mass of that derived by (de Gregorio-Monsalvo et al. 2013) using lower angular resolution data, but a smaller characteristic radius (90 au instead of 125 au).

The uncertainties on γ^d, r_c^d, and the total dust mass appear to be around ±10%. However a statistical exploration of the model parameters, e.g., through a MCMC analysis as in (Isella et al. 2009), is necessary to properly investigate the degeneracies between all the model parameters.

The centers of the three dust depleted gaps are at $R_1 = 60$, $R_2 = 100$, and $R_3 = 160$ AU. Given the finite angular resolution of the observations, there is a degeneracy between the width and the depth the dust gaps, such that we cannot distinguish between deep and narrow or wide and shallow gaps. Two extreme cases are shown by the dashed and solid curves, respectively. The narrowest gaps compatible with the observations have full widths of $W_1 = 25$ AU, $W_2 = 22$ AU, and $W_3 = 45$ AU, and depletion factors of $\Delta_1 > 100$, $\Delta_2 = 70$, and $\Delta_3 = 6$, respectively. The widest gaps have widths of $W_1 = 33$ AU, $W_2 = 26$ AU, and $W_3 = 55$ AU, and depletion factors $\Delta_1 = 13$, $\Delta_2 = 7$, and $\Delta_3 = 3.6$.

5.C.2 Models for the CO emission

Having found a suitable family of models for the dust emission, we now proceed to search for gas emission models able to reproduce the main morphological features of the observed CO emission. In our model, we set the surface densities of ^{12}CO, ^{13}CO, and C^{18}O independently using Equation 1 of the main paper. However, the three CO isotopologues share the same temperature described using Equation 2 of the main paper. The CO density along the vertical direction is then calculated from the surface density and temperature by solving for the equation of the hydrostatic equilibrium. As in R13, we mimic the CO freeze-out by setting the molecular abundance to zero where the gas temperature is less than 19 K. Furthermore, the CO density is reduced by a factor of 10^8 in the disk surface to account for photodissiociation. To calculate the frequency dependent CO emission, we assume that the gas is rotating at Keplerian velocity and that the central star has a mass of 2.3 $M_\odot$.

The CO emission is calculated by using the ray tracing module of RADMC-3D, under the assumption that the CO molecules are in Local Thermodynamic Equilibrium. For each line, we generated synthetic images of the total (line+continuum) and continuum-only emission at 71 velocities between -6 to +6 km/sec. The disk models are inclined by 42° and rotated by 132° to match the orientation of the HD 163296 disk. The same inclination and position angle was used to produce the models for the dust continuum emission discussed above. Continuum-subtracted maps of the CO emission are then obtained by subtracting the line-

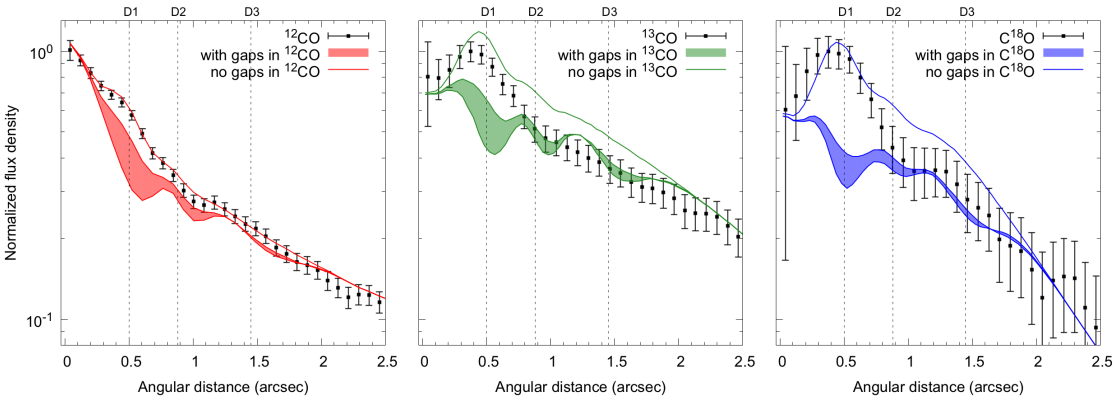

Figure 5.C.3: Comparison between the observations and models for the ^{12}CO (left), ^{13}CO (center), and C^{18}O (right) J=2-1 emission including CO depleted gaps equal to those inferred from the dust emission. The width of the colored lines indicates the intensity range corresponding to the gap models consistent with the continuum emission. The solid lines are as in Figure 4 and show the predicted emission for a disk model without gaps in the CO surface density and gaps in the dust surface density.

free dust continuum emission from the total emission. This latter step is critical to avoid underestimating the line emission in the optically thick disk regions as discussed above. The continuum-subtracted cubes are smoothed at the resolution of the observations, spectrally integrated, and azimuthally averaged following the same procedure adopted to analyze the observations. Since the radial extent of the CO emission measured from the channel maps presented in R13 is smaller than the maximum recoverable scale of our observations, we neglect the effect of the spatial filtering. We tweak by hand the model parameters that control the gas temperature and density until we find a satisfactory fit to the observations. Although this heuristic approach to model fitting has important drawback, it is here justified by the fact that the calculation of a single full model, which includes maps of dust continuum emission as well as spectral cubes of the ^{12}CO, ^{13}CO, and C^{18}O J=2-1 emission, requires several cpu hours.

We start our analysis by noting that the lack of prominent rings in the CO intensity maps either suggests the absence of depleted gaps in the distribution of CO molecules, or, perhaps, that such gaps exist but their observability is hampered by the large optical depth of the line emission. To investigate the first point, we compare the radial profile of the CO emission to a disk model characterized by a monotonically decreasing gas surface density profile without gaps. As for the dust surface density, we adopt the model with narrow gaps described above. We find a good match to the observations using $\gamma = 0.8$ and $r_c = 165$ au for all three CO isotopologues, and $\Sigma_c(^{12}\mathrm{CO}) = 1.6 \times 10^{-3}$ g cm^2, $\Sigma_c(^{13}\mathrm{CO}) = 2.3 \times 10^{-5}$

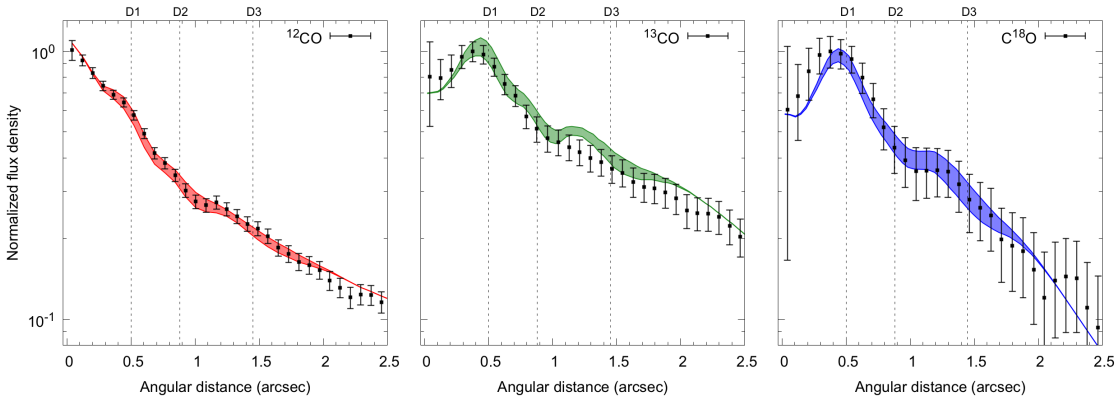

Figure 5.C.4: The solid points are as in Figure 5. The colored regions show the radial profile of the CO emission for disk models in which the CO depletion factor has been tuned to match the observations as discussed in the text.

g cm^2, and $\Sigma_c(C^{18}O) = 2.9 \times 10^{-6}$ g cm^2. The density ratio between CO isotopologues are $^{12}CO/^{13}CO = 70$ and $^{12}CO/C^{18}O = 552$. Our results are in good agreement with (Qi et al. 2011), who found $^{12}CO/^{13}CO = 68 \pm 8$ and $^{12}CO/C^{18}O = 557 \pm 30$. The total mass of ^{12}CO is 2.5×10^{-5} M$_\odot$.

The synthetic intensity profile of this model is shown in Figure 5.C.2. It reproduces remarkably well both the total flux and the radial profile of the ^{12}CO emission but it over predicts the ^{13}CO and $C^{18}O$ emission arising from disk regions between about 0.6″–2″ from the star, which correspond to the location of the middle and outer continuum dark rings. Even if the density and temperature of ^{13}CO and $C^{18}O$ molecules increases toward the center of the disk, our model reproduces the central decrement of the observed emission. As discussed above, this decrement is caused by the over-subtraction of the continuum emission in disk regions where both the CO line and the dust continuum is optically thick. We ran about 200 models for the dust and CO emission changing both the gas density and temperature. We found that the surface densities of ^{12}CO and ^{13}CO are uncertain by about 10-20%, while the uncertainty on the $C^{18}O$ surface density can be as large as 30%.

Our model suggests that most of the ^{12}CO and ^{13}CO emission is optically thick throughout the disk and therefore provides a powerful tool to estimate of the gas temperature. A good fit of the observations is obtained adopting a disk midplane temperature $T_m(r) = 24\text{K}(r/100\text{au})^{-0.5}$ and a disk surface temperature $T_a(r,z) = 68\text{K}(\sqrt{r^2+z^2}/100\text{au})^{-0.6}$. The transition between these two layers is set by the function $\delta(r) = 0.0034 \times (r - 200\text{au}) + 2.5$, and $z_q(r) = 63\text{au}(r/200\text{au})^{1/3} \exp -(r/800\text{au})^2$. The midplane temperature of our model is

about 10% warmer compared to the model discussed in R13, while the surface temperature is about 10% colder. The fact that the temperature model of R13 provides a significantly worse fit to the observations suggest that the CO emission constrains the gas temperature within about 10%.

As a next step, we introduce gaps in the CO surface density and recalculate the spectrally averaged radial profile of the ^{12}CO, ^{13}CO, and C^{18}O J=2-1 line emission. In this set of models, dust and CO are depleted by the same amount inside the gaps, but we do not change the gas temperature. The results are shown in Figure 5.C.3. We find that the reduction of CO molecules produces a drop in the corresponding emission between about 0.2″ and 2″ from the central star. The emission decrement is the largest for the C^{18}O line due to its lower optical depth compared to the other two lines. These models provide a better match to the ^{13}CO and C^{18}O emission across the middle and outermost gaps, but predict too little line emission at the position of the innermost dust gap. We then compare the observations with models in which the CO density inside the dust gaps is less depleted than the dust itself. We explored a wide range of CO depletion factors for the two extreme dust gaps configurations shown in Figure 5.C.1. In the case in which the gaps are the widest, we find a good match between models and observations for CO depletion factors between 0-2.5 in D1, 3.5-7 in D2, and 1.8-3.6 in D3 (Figure 5.C.4). These values should be compared to the dust depletion factors of 13 in the inner gap, 7 in the middle gap, and 3.6 in outer gap. In the case in which the gaps are the narrowest, we obtain CO depletion factors between 0-2.5 in the inner gap, 30-70 in middle gap, and 3-6 in the outer gap, compared to dust depletion factors > 100, 70, and 6, respectively.

Finally, Figure 5.C.5 shows a comparison between the observed maps of the dust and CO emission and those relative to one of the synthetic disk models that reproduces the observed intensity profiles. Overall, we find that the residuals are small compared to the observed emission. This supports the choice of adopting azimuthally symmetric models for the analysis of the observations. However, some properties of the residual maps are worth a mention. Concerning the continuum, the residuals have amplitudes less than ±10% of the observed flux, but nevertheless higher than 5× the noise level. The residuals are the highest in the north-west part of the disk suggesting that the dusty ring might be eccentric. The residuals of the ^{12}CO emission are also significant compared to the noise, and show that the south west-side of the disk is about 10% fainter than the north-east side. Finally, the ^{13}CO and

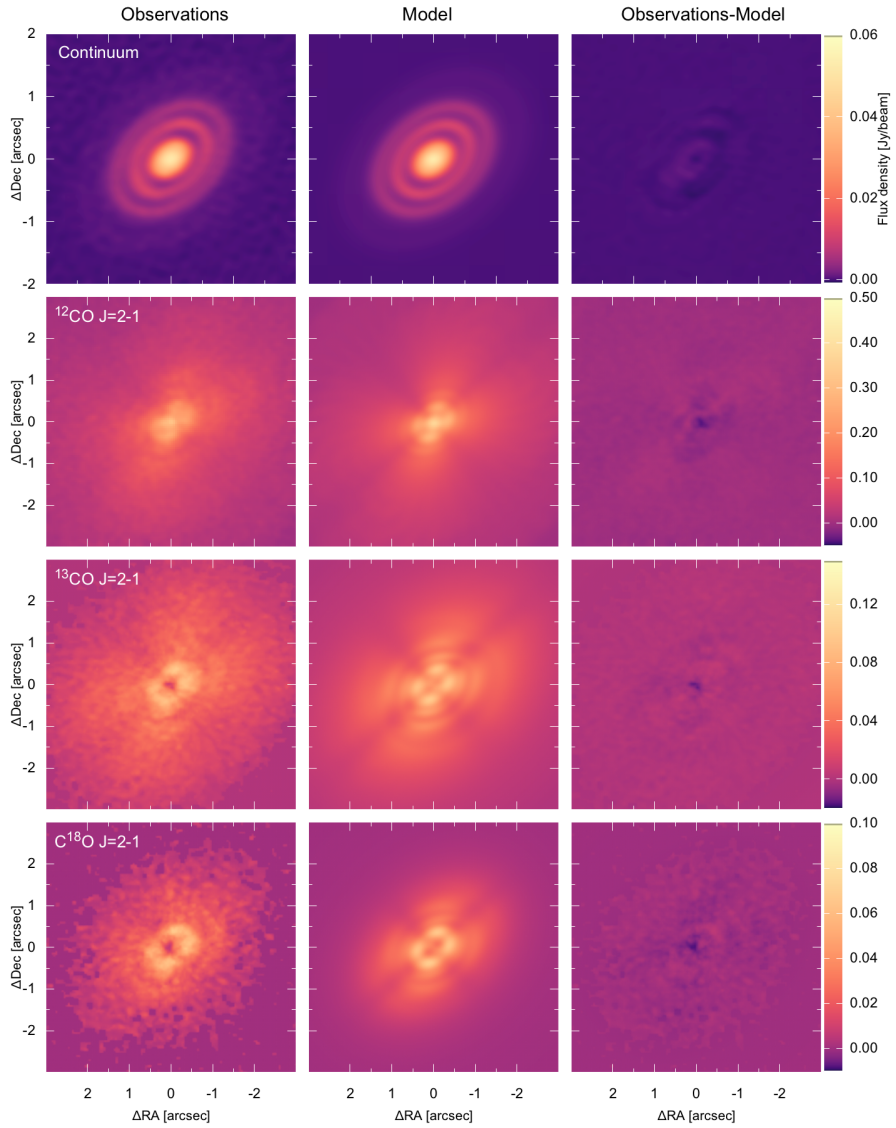

Figure 5.C.5: Comparison between observations and models. The panels in the left column show the continuum image as well as the maps of the integrated line emission. The panels of the central column show maps of the synthetic model emission convolved with the synthesized beam of the observations. Finally, the panels of the right column show the maps of the residual obtained by subtracting models from observations.

C^{18}O residuals are negative on the north-east side of the disk very close to the center, suggesting that an azimuthally symmetric model does not properly reproduce the structure or kinematics of the innermost molecular disk. A detailed investigation of the asymmetries in the HD 163296 disk is beyond the scope of this letter and is left for a future work.

5.D Hydrodynamic simulations of the planet-disk interaction

The effect of the planet gravity on the gas and dust surface density in the HD 163296 disk was calculated by solving the two-fluid equation for the gas+dust+planet disk system surrounding a star, using the LA-COMPASS code (Li et al. 2005, Li and Li 2009, Fu et al. 2014a,b). We initialize the hydrodynamic simulation using the gas surface derived from the ^{12}CO emission ($\gamma = 0.8$, $r_c = 165$ au, $\Sigma_c(^{12}\mathrm{CO}) = 1.6 \times 10^{-3}$ g cm^{-2}) multiplied by a radially constant ratio $H_2/^{12}\mathrm{CO} = 1400$. The temporal evolution of the disk density and kinematics is calculated assuming an isothermal equation of state and the disk temperature discussed in the previous section. We inject fully formed planets in the disk and we keep them at fixed orbital radii for the entire length of the simulation. Initially, the radial profiles of the gas and dust surface density are equal, and we assume a gas-to-dust ratio of 100. Since the ALMA observations of HD 163296 probe the distribution of sub-millimeter grains, we assume a nominal grain size of 0.15 mm, which corresponds to a Stokes number of about 0.015 at 100 AU from the star. The presence of such large grains in the HD 163296 disk has been inferred from multi-wavelength observations (Guidi et al. 2016). For our 2D $\{r, \phi\}$ simulations, we use 3072×1024 grid on $[0.24, 7.92] \times [0, 2\pi]$ in the radial and azimuthal directions, respectively. Radially, the cells are linearly spaced and have a physical size of 0.15 au. Dust is treated as pressureless fluid. Its back-reaction on gas is included. A dust diffusion model in the dust continuity equation to model the turbulent motion is included as well. We typically run our simulations to 2000 orbits at 62 au. This disk is still evolving (especially at large radii) though the lifetime of 7×10^5 yr is a reasonable estimate for the joint planet-disk evolution.

We have carried $\sim$ 100 2D hydrodynamic simulations using various planet masses and disk profiles, including the effects of disk viscosity. We typically find that the joint dust and gas emissions are providing much stronger constraints on the two-fluid evolution of gas+dust in disks. The disk is assumed to have a Shakura-Sunyaev viscosity parameter α that increases with the radius as

$$\alpha(r) = \alpha_2 \left(1 - \frac{(1 - \alpha_1/\alpha_2)(1 - \tanh \frac{r-150}{R_0})}{2} \right), \tag{5.5}$$

where $\alpha_1 = 5 \times 10^{-5}$, $\alpha_2 = 1.5 \times 10^{-2}$, and $R_0 = 60$ AU. The values of these parameters

are chosen so that they give reasonable fits to both observed dust and gas distributions. This generic trend of $\alpha(r)$ is consistent with the results in Bai (2016), though the transition radius of 150 au adopted in our simulations is larger than the estimated value of 100 au. The values of parameters in our simulations are chosen so that they give reasonable fits to both observed dust and gas distributions.

We find that the gas and dust surface density measured across the middle and outer gaps are compatible with the perturbation exerted by two 0.3 M_J planets orbiting at 105 au and 160 au from the central star, respectively, and $10^{-3} < \alpha < 10^{-2}$. A lower value of α in the innermost part of the disk is required to give better fits to the width, the gas depletion, and gas-to-dust ratio measured within the inner dust gap. However, even in this case, we find that the a single planet interaction model does not properly explain the observed characteristics of the inner gap.

6 Hunting for massive protoplanets embedded in the HD 163296 disk

In this Chapter I present the work based on the program set up in the fall of 2016, aimed at searching planetary companions in the disk of HD 13296 making use of the Keck telescope on Mauna Kea (Big Island of Hawai'i). The following sections have been adapted from the paper titled *High-contrast imaging of HD 163296 with the Keck/NIRC2 L′-band vortex coronagraph*. in the process of being submitted to a scientific journal.

6.1 Introduction

Planetary systems form inside disks of gas and dust orbiting around pre-main sequence stars, within the typical disk lifetime of a few million years (e.g. Hernández et al. 2007, Fedele et al. 2010). Thanks to advances in the detection techniques of planets orbiting nearby stars, over the last two decades the available information on extrasolar planets has grown exponentially. Although ~3500 exoplanets have been confirmed to this day[1], only few tens have been directly imaged, as separating the planet from the parent star scattered light represents an arduous technical challenge. Yet, direct imaging of exoplanets is a powerful technique, that allows a full spectroscopic and photometric characterization of the planetary companions, and provides access to a wide range of planet-star separations ($\geq$ 5 AU), compared to other methods (see the review by Fischer et al. 2014). Since newly formed planets have a significant potential gravitational energy available, they are thought to have high temperatures and thus strong emission in the NIR , which make them more easily detectable at these wavelengths. The number of imaged exoplanets has been growing in the last few years, with several companions found in young systems (e.g. Lagrange et al. 2010, Marois et al. 2010, Rameau et al. 2013).

[1] source: Nasa Exoplanets Archive, http://exoplanetarchive.ipac.caltech.edu

Still, the link between planets and the properties of the disks in which they formed remains largely unexplored by observations. Disk-planet interaction plays a major role in shaping the architecture of planetary systems, as well as determining the planets physical properties and orbital elements (Baruteau et al. 2014). Therefore, detecting planets that are still embedded in the disk could provide new and important information on the mechanism of planet formation, but also on the timescales and formation sites. This represents an even harder challenge as the scattered light from the disk can mask the light coming from the planet; the recent development of new infrared detectors combined with advanced adaptive optics mounted on 8-10 meters class telescopes (e.g. VLT/NaCo, Gemini South/GPI, VLT/SPHERE, KeckII/NIRC2, LBT/LUCI) lead to the first discoveries of planet candidates in nearby transitional disks, i.e. systems with inner cavities in the dust/gas (see Espaillat et al. 2014), that are likely to be due to the presence of giant planets. The caveat is that the extensive post-processing required by high contrast observations is known to be prone to the generation of false positives (see Section 3). However, the high sensitivity and contrast achieved by such innovative instruments allowed to put stringent upper limits on the mass of potential planetary candidates in protoplanetary disks.

HD 163296 (MWC 275) is a Herbig Ae star of spectral type A1 (Mora et al. 2001), with stellar mass of $M_* = 2.3 M_\odot$, Luminosity of $L_* = 36 L_\odot$, and effective temperature of $T_{eff} = 9500K$, as computed by Natta et al. (2004). A distance of 122 pc was retrieved from Hipparcos mission (van den Ancker et al. 1998), and the comparison with pre-main sequence evolutionary models indicate an age of 5 Myr (Montesinos et al. 2009). It is surrounded by a gas and dust-rich disk that has been detected in scattered light at large scales in optical (Grady et al. 2000, Wisniewski et al. 2008) and NIR wavelengths (Benisty et al. 2010, Sitko et al. 2008). Its high brightness and spatial extention makes it one of the most well studied protoplanetary disks in the vicinity of the Sun. The dust disk extends to a radius of about 250 au, while the gas has been detected (through CO emission lines, the second most abundant molecule after H_2 in protoplanetary disks) up to 540 au (de Gregorio-Monsalvo et al. 2013). Recently, ALMA observation at high spatial resolution (~0.2″) revealed a morphology of the continuum emission at 1.3 mm characterized by three dark rings with angular radii of 0.5, 0.8, and 1.3 arcsec, corresponding to orbital radii of about 60, 100, and 160 au (Isella et al. 2016). In the same work, hydrodynamical simulation of disk-planet interaction have been compared to the observations, to find that the second and third gap are consistent

with Saturn-like planets (~0.3M_J) partially depleting dust and gas around their orbits.

In this paper we present the results of the observations of the ringed-disk around HD 163296 in the L′ band with the vortex coronograph at KECKII/NIRC2. We detect the scattered light from the inner ring of dust and identify a point-like source near the second dust gap we see in the ALMA image. Finally, the sensitivity of our observations allow us to set upper limits on the mass of giant planets present in this disk.

6.2 Observations and data reduction

HD 163296 was observed with KECKII/NIRC2 and the vortex coronograph (Mawet et al. 2017) for two nights on May 30/31, 2017 in the L′ band (central frequency of 3.7μm), with a pixel scale of 0.01 arcsec/pixel, and angular resolution of ~0.08″. To apply the ADI technique we tracked our target in vertical angle mode, i.e. with the pointing origin Y mantained at a fixed vertical angle relative to the elevation axis. The average seeing was ~0.6″ for both nights, the time on source was 40 minutes each night, and the parallactic rotation (ΔPA) 47° and 40°, respectively. On May 31, the reference star HD 183665 was observed for 30 minutes directly after the primary target. Darks and sky flats were acquired during the same nights of the observations. The raw images were first pre-processed subtracting the sky background, and correcting for flat field and bad pixels, and then registered in a cube using the median speckle pattern for the centering of the frames. The data were processed using the Vortex Image Processing (VIP) package (Gomez Gonzalez et al. 2017), applying Principal Component Analysis (PCA) with ADI.

6.3 Results

Figure 6.1 shows the result of PCA-ADI PSF subtraction using 204 frames from both observing nights. We projected each frame onto 18 principal components (PCs) to build a model of the stellar speckle pattern over an annular region at a distance of 0.″24-1.5″ from the center. There is a clear detection of an elongated structure towards the north-east at a minimum distance of ~0.″35 from the center. The geometry of the emission is consistent with the inclination and position angle of the disk in the sub-millimeter and millimeter continuum, corresponding to 44°and 133°, respectively (see e.g. de Gregorio-Monsalvo et al. 2013). An additional emission, spanning 0.″3-0.″5 in the north-west direction (labeled ‘s’ in

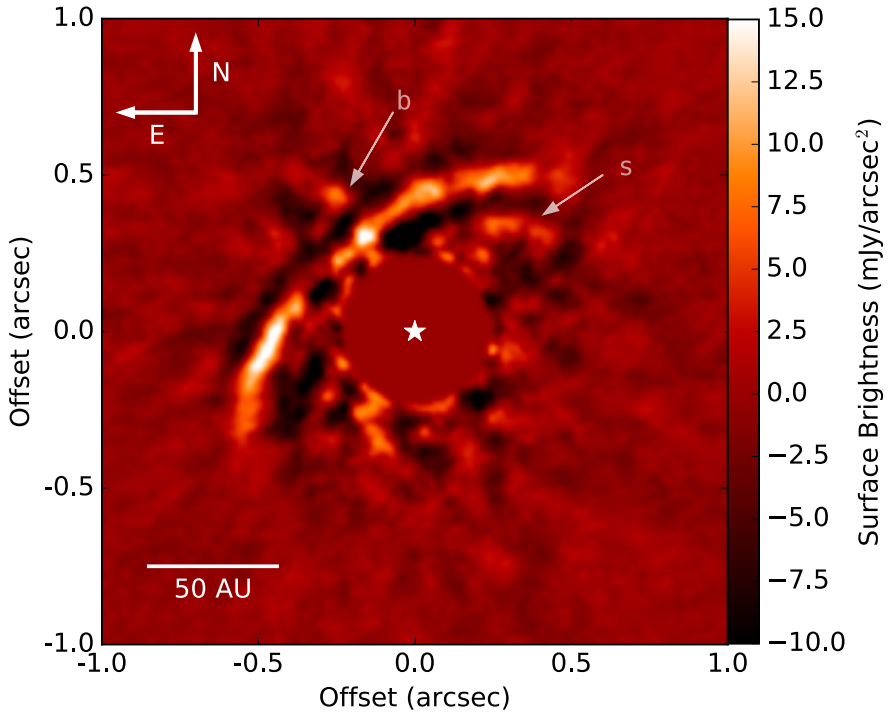

Figure 6.1: Image after two nights observations of HD 163296. The stellar contribution has been subtracted using PCA-ADI with 18 principal components computed from 204 total frames. A inner region with radius of 0.″24 (3*FWHM) was masked. The star symbol marks the position of HD 163296 at the center of the frame.

Fig. 6.1), seems to follow a similar curvature, but the low signal-to-noise ratio (SNR) of this feature make it difficult to claim a reliable detection. Finally, a point-like source (labeled 'b') appears in the north-east direction (PA=30.6° ± 0.7°) at 0.″49 ± 0.″01 from the central star with $\Delta L' = 11.1^{+0.3}_{-0.2}$, corresponding to an SNR of 4.7. The error bars and SNR were calculated by injecting and retrieving a fake companions with the same flux and angular separation over a parallactic angle (PA) range 145°-305°(south-west region). This PA range was chosen to avoid confusing scattered light from the disk and speckle noise. We used the `contrast_curve` method in the VIP package to determine the detection limits of our observations using a similar fake companion inject and retrieval method as described above (Gomez Gonzalez et al. 2017). The noise in the image was computed inside partial rings of λ/D resolution elements over a parallactic angle range 140°-310°. We computed an ensemble of detection limits using PCA-ADI with a varying number of PCs for three overlapping

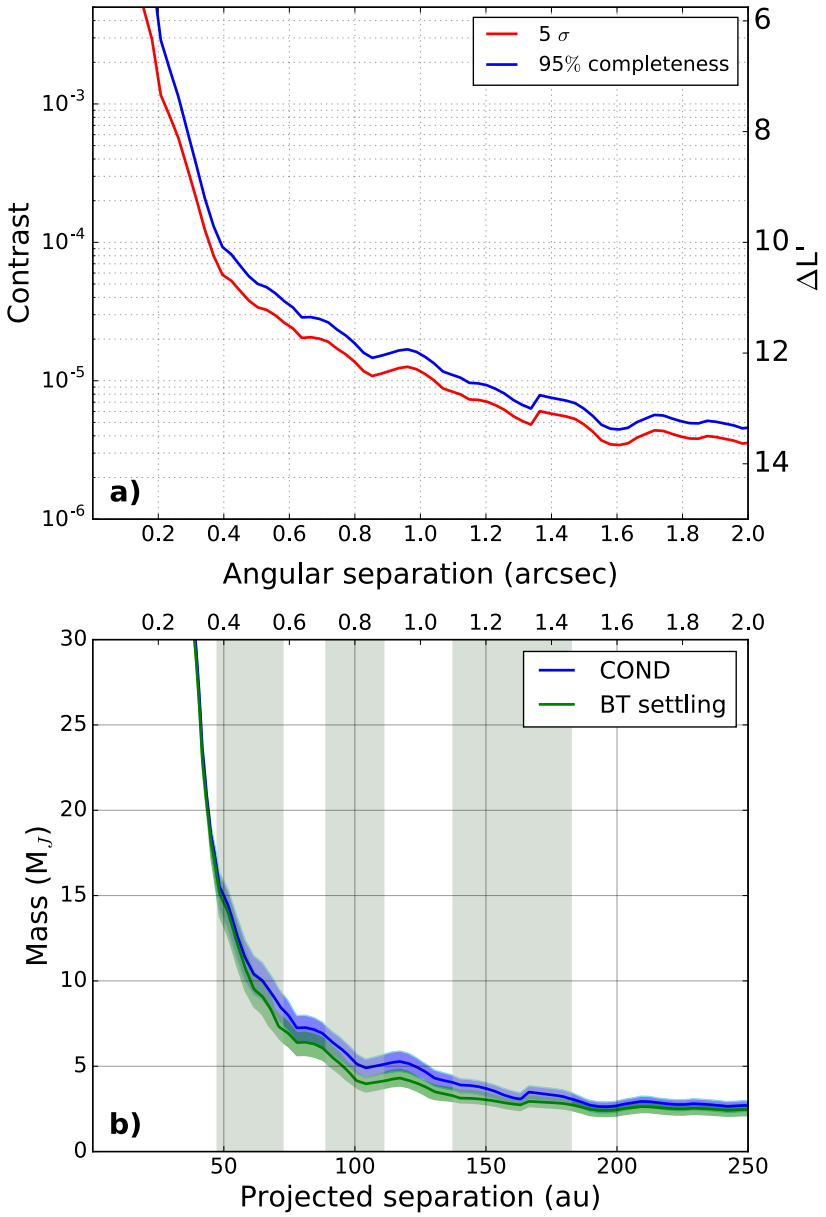

Figure 6.2: *Top panel*: Contrast limit (planet-star flux ratio) after two observation of HD 163296, as a function of the angular separation. Both cases of a 5 σ level (red line) and a 95% completeness (blue line) are shown. *Bottom panel*: planetary masses corresponding to a 95% level of completeness, computed from the COND and BT-Settl models by Baraffe et al. (2003) and assuming an age of 5±1 Myr. The shaded areas are drawn at the location of the gaps in the dust surface density as derived from the modeling of λ =1.3 mm observations (Isella et al. 2016)

annular regions of the image: 0.″2-0.″8, 0.″3-1.″5, and 0.″5-2.″9 (2-9, 3-19, 5-37 λ/D, respectively). We also applied PCA-RDI in inner most region 0.″1-0.″5 (1-6 λ/D). Figure 6.2a shows the resulting detection limits as a function of angular separation using a conventional 5σ "contrast curve" and alternate method proposed by Jensen-Clem et al. (2017). The 5σ contrast curve assumes a Gaussian noise distribution and provides the flux ratio with a true positive fraction (TPF) of 0.5 and a fixed false positive fraction (FPF) of 2.9×10^{-7}. The alternate detection limits assume a Student-t distribution, set a varying threshold that allows a 1% chance of a false positive at evenly distributed within 1″, and provides TPF=0.95; i.e. 95% completeness (see e.g. Jensen-Clem et al. 2017, Ruane et al. 2017). The latter approach accounts for the small number of samples used to estimate the noise in the image, especially at small angular separations (Mawet et al. 2014).

We translate the flux ratio at 95% completeness into upper limits on planetary masses from luminosities computed for non-accreting giant planets by Baraffe et al. (2003). The corresponding masses are shown in Fig. 6.2b. Comparing the computed upper limits found for the planetary masses with the location of the gaps at mm wavelength showed in Isella et al. (2016), we would be sensitive to masses of 11 M_J in the inner most gap (60 au), 5 M_J in the second gap (100 au), and 3 M_J in the third gap (160 au). These planetary masses limits are much higher than the ~0.3 M_J planet expected to be clearing gaps in the dust and gas distribution based on the ALMA image are λ=1.3 mm and hydrodynamical simulations (Isella et al. 2016). However, the flux of point source may also receive a significant contribution from the emission from an accreting circumplanetary disk (see Zhu 2015).

Finally, we note that the derived upper limits for mass and accretion do not take into account the extinction by the disk material, which can be significant in the inner regions of the system, and would result in an attenuation of the emission flux from a planetary companion.

6.4 Discussion

6.4.1 Extended emission

We interpret the bright extended emission on the north-east side of Fig. 6.1 as scattered light from the disk atmosphere at the location of the first bright ring detected at mm wavelengths with ALMA by Isella et al. (2016). The morphology of the structure in our ADI processed image is consistent with the J-band Gemini Planet Imager (GPI) image in polarized light

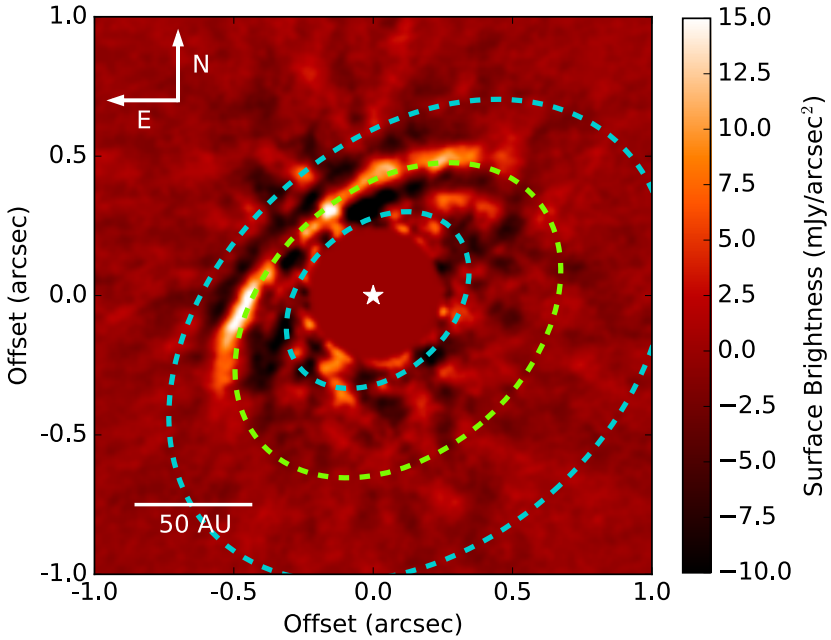

Figure 6.3: Interpretation of the emission in HD 163286 as scattered light from the disk atmosphere: the green dashed curve corresponds to a scale height of 22 au above a location at 81 au on the midplane. The inner light blue curve is drawn for a layer 4 au above a location at 45 au on the midplane. The outer light blue curve corresponds to a scale height of 40 au above the midplane at 123 au.

(Monnier et al. 2017). Based on a visual fit, Monnier et al. (2017) determined the scattered light originates from a scale height of 18 au above the midplane at the location of 77 au.

Following the same approach, we estimate the scale height above the midplane that could reproduce our detections. Unfortunately, the gaps in the dust emission were not resolved in the ALMA images at λ=1.3 mm, and Isella et al. (2016) found a range of width of the gaps in the dust surface density that were consistent with the observations. We therefore adopt the middle radius between the gaps edges for the location of the bright rings on the midplane, taking the average values between the narrowest case and the widest case. Finally, we assume a position angle and inclination of 132°and 44°, respectively. Hence, fixing 81 au for the first bright ring we find that a scattering layer at a scale height of ∼22 au reproduces the extended emission at 3.7 μm coming from the closer side of the disk in the north-east direction (see Figure 6.3, left panel). If we consider instead the inner edge of the first bright ring at 75 au, the corresponding scale height becomes 18 au, which is consistent with the

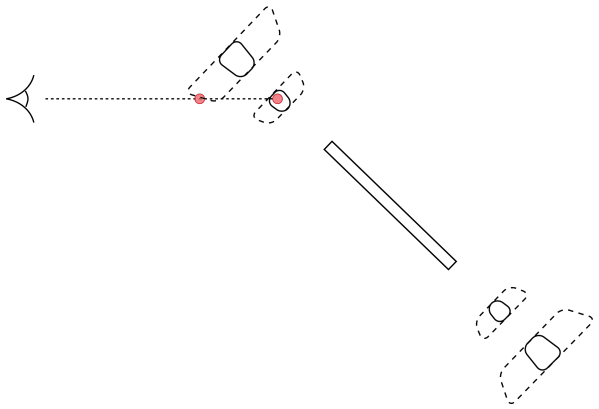

Figure 6.4: Viewing geometry: the cartoon shows the section of HD 163296 disk inclined by 44°with respect to the observer, which is placed on the left of the image. The fist and second ring are drawn with a solid line assuming a "flat" disk with constant h/r=0.08; the dashed contours represent instead a scale height of 22 au above the first ring, and 40 au above the second ring. The blob detected at a projected distance of 0.″49, displayed as a red dot, could either come from a higher layer in the disk atmosphere, in correspondence to the the second bright dust-ring, or at the location of the midplane and close to the first bright ring in the λ1.3 mm continuum.

estimate in Monnier et al. (2017). These values translate to an aspect ratio of $\frac{h}{r} \sim 0.25$, which we note is more than a factor of 3 larger than what found in Guidi et al. (2016), where the disk atmosphere was estimated to have $\frac{h}{r} \sim 0.08$ outside ~50 au, from the modeling of sub-mm ALMA observations, corresponding to 6.5 au at a radial distance of 81 au. de Gregorio-Monsalvo et al. (2013) found a slightly higher scale height fitting the CO channel maps with $\frac{h}{r} \sim 0.07$ at 1 au and flaring power of 1.12, resulting in a scale height of 9.6 au at a distance of 81 au. However, these flaring values were found to overestimate the emission at near and mid infrared wavelengths, which would point to a rather flat disk (see also Tilling et al. 2012). A possible way to reconcile these diskrepancies would be to assumed different flaring for the inner and the outer disk.

Applying the same reasoning to the detection at smaller separation (labeled 's' in Fig. 6.1), and considering the inner edge of the first gap at 45 au we do not find a scale height that can reproduce the observed structure (see Fig. 6.3). The curvature of the detected structure deviates from the ellipse with the adopted inclination and position angle suggesting that the emission could be due to an offset dust ring, a spiral arm, or an artifact of the image processing.

6.4.2 Point source

The reduced image revealed not only the disk emission but also a potential point-like source (labeled 'b' in Fig. 6.1) at 0.″49 ± 0.″01 in the north-east direction (PA=30.6° ± 0.7°). As explained above, we estimate a significance of 4.7σ, which falls just shy of our detection threshold. Assuming Gaussian statistics, we expect ∼10-15% completeness for sources at the estimated flux level and angular separation.

However, the planet is located at a deprojected distance of 83 au and would therefore be close to the inner edge of the second gap in the dust distribution found in Isella et al. (2016), which is a very likely site of planet formation. Assuming an age of 5 Myr and that the detected emission is solely the planet's intrinsic luminosity, the mass of the planet could be as high as 9±1 M_J and 7±1 M_J according to the Ames-COND and BT-Settl models, respectively (Baraffe et al. 2003).

Another possible explanation for the point-like emission is scattered light from dust. Based on the assumed viewing geometry (see Fig. 6.4), there would need a layer ∼40 au above the midplane at a location of the second bright ring (123 au) to reproduce the emission at that location in the image (Fig. 6.3), corresponding to an aspect ratio $\frac{h}{r} \sim 0.33$. Considering the inner wall of the ring at 112 au we find instead a scale height of 30 au, translating to an aspect ratio of $\frac{h}{r}$ ∼0.27. These values are considerably higher than the scale heights found in previous works (see Sect. 6.4.1), and are not in good agreement with the classification of this object as a moderately flat disk (Group II, or more often an intermediate stage between GroupI and GroupII, see Garufi et al. 2017). We note however that the unsuccessful attempts to fit the Spectral Energy Distribution (SED) in the near-IR and mid-IR range using a model with continuous flaring (e.g. Dominik et al. 2003) and the difficulty of reproducing with a unique model the observed emission of this source from IR to millimeter simultaneously (e.g. Tilling et al. 2012, de Gregorio-Monsalvo et al. 2013) suggest a more complex structure of the disk, likely a non constant flaring and variable dust properties with radius. More information on this point source, as well as a more precise characterization of the disk structure, can only be obtained through higher resolution ALMA observations in the millimeter range, that will allow us to resolve the dust gaps and rings and better constrain their location on the midplane, and higher SNR observations in the NIR/mid-IR to rule out the possible artificial nature of the detection.

6.5 Conclusions

The main goal of this program was to search for massive planets embedded in the HD 163296 disk. The observations revealed a clear extended emission that we interpreted as scattered light from the disk atmosphere in the NE region of the system, which corresponds to the closer side of the disk. The contrast of our final frames after the PCA post-processing allowed us to set upper limits on giant planets present in this disk, and in correspondence of the dust gaps found in the millimeter observations.

We also identify a point-like source at $0\farcs49 \pm 0\farcs01$ in the north-east side of the image at a distance of ~83 au when accounting for the disk inclination and position angle. Planetary isochrones suggest that the emission may be explained by the intrinsic luminosity of a 7-9 M_J planet Baraffe et al. (2003). This value is larger by more than a factor of 10 compared to the planetary masses resulting from hydrodynamical simulations as presented in Isella et al. (2016). However, the luminosity may not be entirely from the planet photosphere; the planet's mass could be much smaller if it is surrounded by an actively accreting circumplanetary disk. Follow up observations are needed to confirm the presence of a companion and to determine if a significant contributions is given by a circumplanetary disk.

7 Dust trapping in HD 163296

Based on the results of the multi-wavelength study of HD 163296 described in Chapter 4, we proposed a follow up with ALMA that was accepted for Cycle 3. In Guidi et al. (2016) we detected an excess continuum emission at 850 μm close to the CO snowline at ~90 au on the disk midplane, and we noted that a radial feature in polarized scattered light was found by Garufi et al. (2014) at a similar distance from the star. We hypothesized that such features could be the result of a change in dust properties in the region of the radial CO snowline. The resolution of our mm observations was not sufficient to detect a possible local variation of the maximum grain size at that location. In addition, we measured an opacity spectral index monotonically decreasing towards the inner regions of the disk, with values $\leq$1 inside 90 au, supporting a scenario where the grains outside the snowline have not grown significantly, while the inner disk is populated by large grains. This general distribution would be consistent with an enhanced production of large grains at the CO snowline and subsequent transport to the inner regions. We hence wanted to test the hypothesis that grains grow locally, at the location of the CO snowline, and asked to observe the continuum emission of HD 163296 with ALMA in Band 3 at 90-99 GHz, with an angular resolution within a factor of two of the full disk vertical scale height at the position of the CO snowline, corresponding to a resolution of 0.″3. We also planned to combine these observations with an additional dataset at 1.3 mm from a previously accepted ALMA proposal (PI Andrea Isella, see Chapter 5, Isella et al. 2016), in order to have an additional wavelength to constrain the index at a spatial resolution close to the ones we were proposing.

In this chapter I present the preliminary results of the analysis of ALMA cycle 3 observations of HD 163296 at 3 mm that were delivered in January 2016.

7.1 Observations and data reduction

HD 163296 was observed by ALMA on September 7 and 13, 2016 with an array configuration of 42 antennas covering baselines from 15 m to 3.2 km, resulting in an angular resolution of ∼0.3″ and a maximum recoverable scale of 40″. The correlator was set up with four spectral windows in dual polarization mode: three SPWs for the continuum detection were set to cover the total bandwidth of 1.875 GHz, and were centered at 91.142, 103.006 and 104.694 GHz. One SPW was set to have a higher spectral resolution of 61 kHz (∼0.2km/s after Henning smoothing) and was centered at 93.165 GHz to include the N_2H^+(1 - 0) emission line. J1924-2914, J1733-1304 and J1751-1950 were observed to calibrate for bandpass, flux and phase, respectively. J1753-1934 was additionally observed every 20 minutes as a check source for the complex gains calibration. Data were calibrated with the ALMA pipeline, then self calibration was carried out with two rounds of phase calibration and one round of amplitude and phase calibration, the final continuum map was produced with the CLEAN task in CASA and with robust weighting we achieved a rms of $1.7 \cdot 10^{-5}$ Jy/beam with a beam size of 0.31″x0.22″.

7.2 Preliminary results

7.2.1 Continuum map

In Figure 7.1 we show the continuum map at 3 mm after the cleaning with uniform weighting. The emission is centrally peaked with a maximum of 13.5mJy/beam, we estimate a projected radius of ∼170 au at a 3σ level, with corresponding integrated flux of 61±6 mJy, where a calibration error of 10% has been included. Some signatures of substructures are visible in the image but both the signal-to-noise and the resolution are lower with respect to the 1.3 mm observations, where the rings and gaps were more clearly detected.

7.2.2 Spectral index

In Figure 7.2 (top panel) we show the map of the spectral index α computed from our images at 3 mm and Band 6 continuum at 1.3 mm presented in Isella et al. (2016), smoothed with the same beam of 0.31″x0.22″, as $\alpha = \frac{ln(F_{1.3mm}/F_{3mm})}{3mm/1.3mm}$. The pixels with flux lower

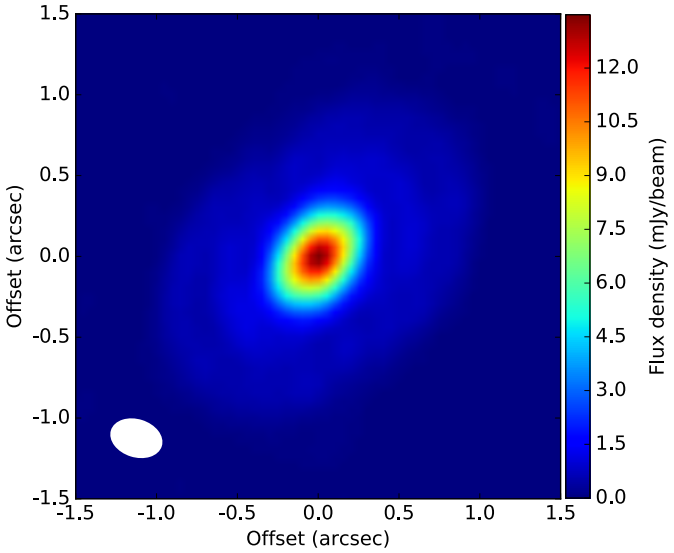

Figure 7.1: Map of the continuum emission at 3 mm in HD163296. The beam of 0.″31x0.″22 and position angle -17°is shown on the bottom left of the image.

than 1 sigma in the continuum maps have been masked. The map displays a local decrease in the spectral index at a projected distance of ∼1″, in the shape of two half rings that seem slightly off-centered. This is better shown in the radial profile computed along the disk major axis (see Figure 7.2, bottom panel), where the values of α seem to diminish between the second and thirds gaps detected in the λ1.3 mm observations (shown as shaded region in the plot). The same effect seems is slightly visible across the first bright ring at ∼0.″65, but the variations are not significant with respect to the errors. Uncertainties are computed as the sum in quadrature of the standard deviation of the averaged pixels in the α map and the errors propagated from the single α measurements, given by $\Delta\alpha = \sqrt{(\Delta F_{1.3mm}/F_{1.3mm})^2 + (\Delta F_{3mm}/F_{3mm})^2}/ln(3mm/1.3mm)$, where the error on the fluxes is given by the rms of the synthesized image and the systematic uncertainty due to calibration set at 10%.

7.3 Discussion

From this preliminary analysis of the continuum emission at 3 mm, we can already derive some interesting results. First, the flux spectral index is in good agreement with the one computed between 870 μm and 9 mm in Guidi et al. (2016), with α monotonically decreasing

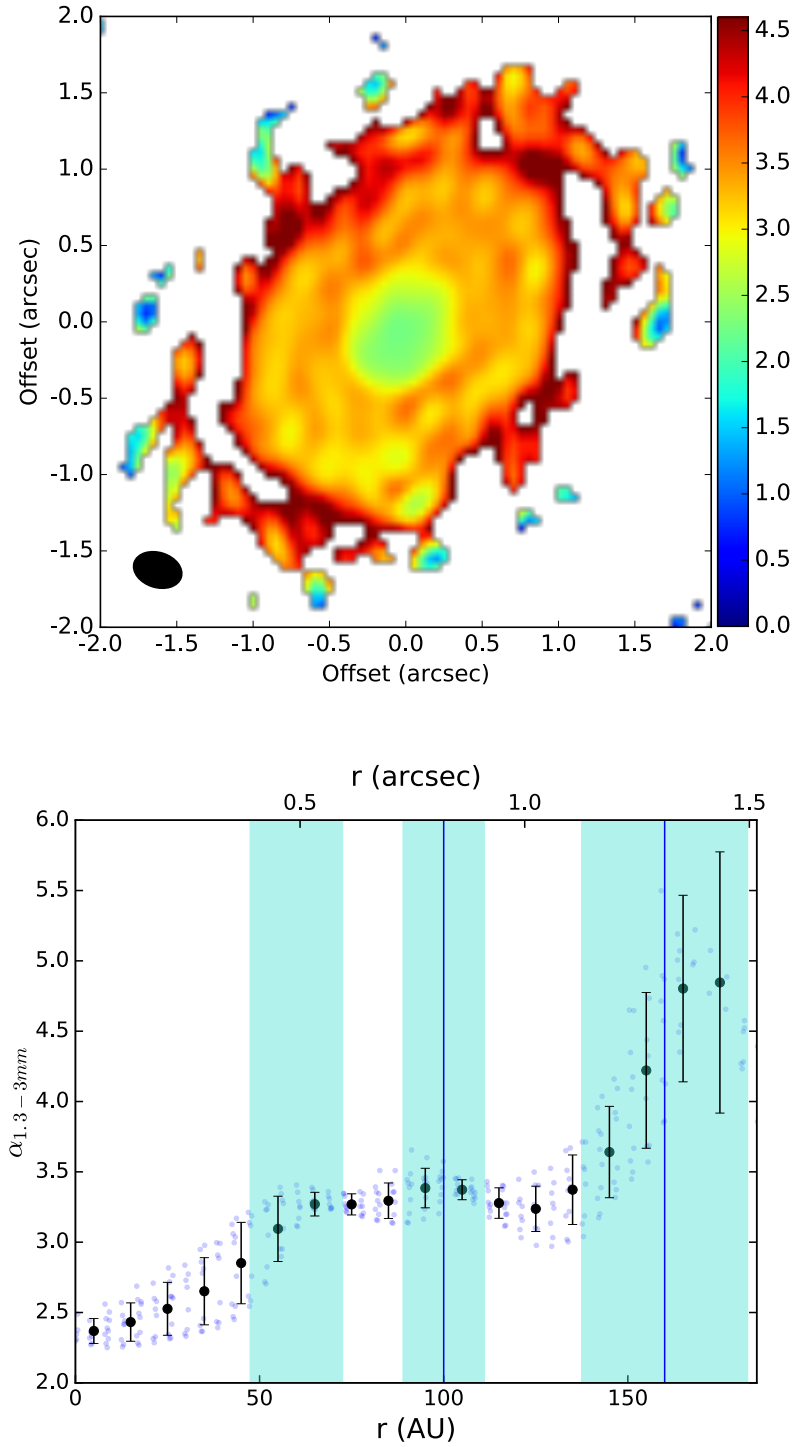

Figure 7.2: *Top panel*: map of the flux spectral index, the matching beam is shown on the bottom left of the image. *Bottom panel*: radial profile of the α index computed along the disk major axis at a position angle of 133°, the black circles represent the average values on bins separate by 10 au and starting from 5 au. The shaded areas and the blue vertical lines are respectively the location of the gaps in the dust surface density, and the location of the putative planets from the modeling of λ1.3 mm observations in (Isella et al. 2016).

towards the inner regions, down to values of ~2.5 at ~25 au (roughly half the resolution of the Science Verification observation). Yet the new measurements highlight a steeper trend inside ~50 au, and in the innermost regions the spectral index approaches the value of 2, suggesting that the emission is becoming optically thick; in Isella et al. (2016) the thermal emission at 1.3 mm was indeed found to be optically thick inside 50 AU, and this could explain the steeper drop in the spectral index inside this radius. The local decrease across the first and second bright dust rings (as computed from the 1.3 mm observations) could be due to confinement of grains outside the gaps, but optical depth effects still cannot be ruled out at this stage: the emission could originate from a radially thin ring, but with high dust densities and thus optically thick and not resolved spatially in our observations.

A significant result of this measurement is also that the spectral index appears to reach values larger that the ISM value of 3.7 beyond 150 AU: these could be explained by the depletion of mm-sized grains that have drifted closer to the star, leaving a grain size distribution corresponding to the resonance on the dust opacity spectral index (see Fig. 1.9). Also, such high values of α give us a precious insight on the grain compactness: in the reasonable assumption that the emission is optically thin at both 1.3mm and 3mm in these outer regions, in the Rayleigh-Jeans regime the dust opacity spectral index β can be computed as $\alpha - 2$, resulting in values ≥ 2 for β beyond 150 AU, which are not compatible with extremely *fluffy* grains (filling factor $\leq 10^{-4} - 10^{-5}$, see Kataoka et al. 2014). We note however that the uncertainties on α at these locations are too large (~40% beyond 160 au) and do not allow a robust constrain.

7.4 Conclusions and future work

The natural prosecution of this work is to obtain higher resolution observations at 3 mm in order to resolve the spectral index across the rings and gaps in this disk: this is currently being done with ALMA as part of a project submitted for cycle 4 (PI Andrea Isella). Furthermore, a higher signal to noise in the outer regions ($\geq$ 150 au) is necessary to obtain a robust measurements of the large values of α (>4) and thus the proof of the depletion of mm-grains at large radii and a direct insight on the porosity level of dust grains in a protoplanetary disk. This measurement is part of a proposal submitted for ALMA cycle 5 (PI Guidi) and accepted with rank C, and will therefore be completed in case the observations are scheduled.

Finally, going to longer wavelength would reduce the optical depth effect at 1.3 mm that prevents us from tracing the dust surface density inside ∼50 AU: VLA observations of HD 163296 in the Ka band ($\lambda \simeq$9 mm) have been carried out in 2016 in the more extended configuration (PI Isella) and are currently being completed in the complementary B configuration (PI Guidi), with the goal of probing the optically thin part of the dust thermal emission at spatial scales comparable with the ALMA datasets. Also, observation in the X band (3.6 cm) have been taken as part of the same project, to allow us to distinguish between dust and ionized gas emission (see 4.3.3, or Pérez et al. 2015), that could be non-negligible at long wavelengths ($\gtrsim$3 mm).

Part III

Conclusions and future prospects

8 Substructures in the dust distribution: a non-imaging data analysis

In this Chapter I describe a method I have used to analyze (sub-)millimeter observations of resolved disks, in order to characterize possible substructures in the dust distribution. I considered a small sample of sources in the Lupus star forming region observed by ALMA, and used them to test this technique and its employment for future analysis of spatially resolved and high s/n observations. In the following section I will introduce the observations as part of a larger collaboration; then I will describe the method and the preliminary results.

8.1 The ALMA Lupus survey

The *ALMA Lupus survey* is a result of an international collaboration with PI Prof. Jonathan Williams (Institute for Astronomy, Honolulu), involving researcher in the field of disk, planets and star formation from different institutes: Juan M. Alcalá (INAF), Megan Ansdell (IfA, Honolulu), John M. Carpenter (ALMA), Greta Guidi (INAF, Universitá di Firenze), Michiel Hogerheide (Leiden Observatory), Carlo Manara (ESA), Geoff Matthews (IfA, Honolulu), Anna Miotello (Leiden Obs.), Antonella Natta (INAF, DIAS), Isa Oliveira (Observatorio National, MCTI), Marco Tazzari (ESO), Leonardo Testi (ESO), Nienke van der Marel (IfA, Honolulu), Sierk van Terwiska (Leiden Obs.) and Ewine van Dishoeck (Leiden Obs.).

The first survey of 90 protoplanetary disks in four main star-forming clouds (Lupus I-IV) was carried out in June 2015 with ALMA in Band 7 (890 μm) as proposed for Cycle 2. Lupus is one of the youngest and closest star forming regions, located at a distance of 150-200 pc from the Sun. The targets were selected on the bases of *Spitzer* infrared surveys and consists of Young Stellar Objects that are more massive than brown dwarfs (i.e. $M \gtrsim 0.08 M_{\odot}$) and host protoplanetary disks (i.e. have Class II or flat IR spectra).

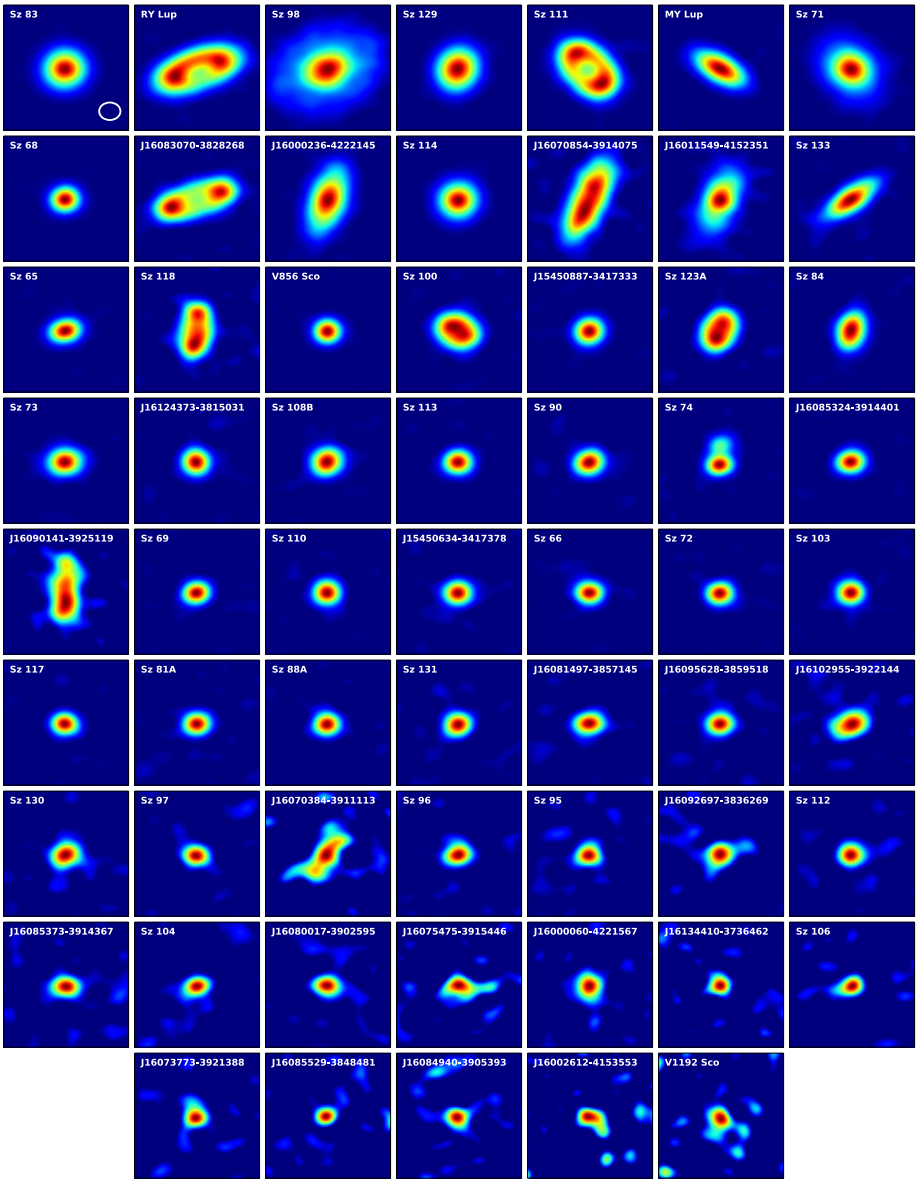

Figure 8.1: From Ansdell et al. (2016): 890 μm continuum images of the Lupus disks detected in our ALMA Cycle 2 program, ordered by decreasing continuum flux density.

A total of 62 sources were detected in the continuum at 890μm with $> 3\sigma$ significance (see Figure 8.1), while 36 were detected in the ^{13}CO and only 11 in the C^{18}O. The first analysis, presented in Ansdell et al. (2016), suggested that the typical disks in Lupus have gas masses much lower than the Minimum Mass Solar Nebula and gas-to-dust ratio lower than the value of 100, typical of the interstellar medium. This could be an indication of rapid disk evolution, and giant planet formation being largely complete within a few Myr. CO-based gas masses were independently calculated by Miotello et al. (2017) through a detailed chemical modeling, and confirmed the CO depletion. However, this could be interpreted either as gas depletion or carbon segregation into more complex molecules or aggregates,

but the available observations still could not distinguish between these two scenarios. An analysis of continuum emission was performed by Tazzari et al. (2017), who measured the dust masses of the Lupus disks through a fitting of the visibilities based on a self-consistent disk model. This work also showed a correlation between the sub-mm flux and the cut-off radius, which can be translated into a disk mass-size correlation, and in particular the Mass/Size slope was found to be less steep with respect to the same relation computed in the younger Taurus-Auriga region (Andrews 2015), with fainter and larger disks in the Lupus sample. This could be interpreted as evidence of viscous evolution, but other processes such as photoevaporation, grain growth, radial drift and planet formation could be also playing a role.

An improved study is currently being carried out using ALMA observations of the Lupus region at 1.3 mm, delivered to the collaboration in winter 2016: the most abundant ^{12}CO will be observed, along with ^{13}CO and C^{18}O, so that it will be possible to derive more accurate information on the level of gas depletion in the Lupus region. Finally, a survey in a third frequency range (Band 3 at 3 mm) was completed in early spring 2017 (PI Tazzari). With the advantage of a more optically thin emission at these longer wavelengths, we aim at constraining the dust properties and the extent of planet formation in this star formation region. The level of grain growth can be constrained with measurement of the dust opacity spectral index between 1.3- 3 mm, and compared with other star forming regions to highlight possible evolutionary trends.

8.2 An alternative approach for detecting substructures: modeling of visibilities

High resolution observations of protoplanetary disks taken with ALMA since the availability of the long-baseline configurations (2014/2015) showed that most of the disks that previously appeared as "smooth" have instead much more complex structures in the dust (and sometimes in the gas) distribution. So far only few observations at $\leq$0.1 arcseconds are available, so that a detailed characterization of these morphologies has been made of less than $\sim$10-15 objects. One of the issues in the analysis of these structures is the fact that the *cleaning* process (see Sect. 2.5.3) performed on interferometric data in order to recover the true images, consisting in a Fourier transform and deconvolution, is a non-linear operation and can result

in the amplification of compact structures, or in general a non-exact representation of the true sky brightness distribution. Viceversa, a more direct analysis can be performed on the visibilities, the true observational measurement provided by an interferometer. Following the methodology presented in Zhang et al. (2016), we analyzed a small sample of disks observed at moderately high resolution, in order to find evidence of substructures that get often smoothed out during the cleaning process and are not clearly detectable in the synthesized images. We selected four sources among the Lupus sample at 890 μm (see previous Section) that showed an extended disk and a higher signal-to-noise ratio. We performed a Marcov Chain Monte Carlo fit using the *emcee* package (Foreman-Mackey et al. 2013), starting from an analytic function in the image plane consisting of a series of Gaussians modulated by a sinusoidal function:

$$I(\theta) = \frac{a_0}{\sqrt{2\pi}\sigma_0} \exp\left(\frac{-\theta^2}{2\sigma_0^2}\right) + \sum_i cos(2\pi\theta\rho_i)\frac{a_i}{\sqrt{2\pi}\sigma_i} exp\left(-\frac{\theta^2}{2\sigma_i^2}\right). \tag{8.1}$$

This representation requires the assumption of circular symmetry of the emission, and the deprojection of the visibilities with a given inclination and position angle, that are typically computed either from the fit of the continuum image, or a keplerian fit of the gas channel maps. Since the chosen brightness distribution is symmetrical, i.e. function of the radial coordinate only, the correspondent visibility function depending on the uv-distance is given by the Hankel transform (Pearson 1999):

$$V(\rho) = 2\pi \int_0^\infty I(\theta)\theta J_0(2\pi\theta\rho)d\theta \tag{8.2}$$

The integral in eq. 8.2 is computed step by step sampling the brightness function I(θ) every 0.1 au in the range 0.1-350 au. According to the number of visible peaks in the visibility profiles we fitted a variable number i of gaussians, i.e. the parameters $a_0, \sigma_0, \rho_i, a_i, \sigma_i$. The χ^2 value between the model and the data was computed as $\chi^2 = \sum_i \mathrm{w}_i(Re_i^{obs} - Re_i^{mod})^2$, where Re_i are the real parts of the complex visibilities and w_i are the weights associated with each visibility. We consider the real part of the visibilities because we are assuming an axisymmetric disk, that translates in a real visibility function coming from Eq. 8.2.

Of the four examined targets Sz 98, Sz 100, J16000236-4222145 and Sz 114, only Sz 98, the most extended and bright, had sufficient S/N to constrain the parameters for at least one peak in the visibility profile (i.e. i=1 in eq. 8.1). In Figure 8.2 the best fit model for Sz 98, corresponding to the median of the marginalized distribution of the 500 chains generated by the MCMC fit. In the top panel the final V(ρ) function is plotted on the binned visibilities;

in the bottom panel we show the intensity model as calculated from eq. 8.1 using the best fit parameters, scaled by the beam solid angle of the synthesized image. As a check we also overplot the azimuthally averaged flux density of the cleaned image and of the axisymmetric model convolved with the 2-dimensional beam: we note that in this procedure we are fitting the visibilities, thus we do not expect an equally good fit in the image plane. We find that the

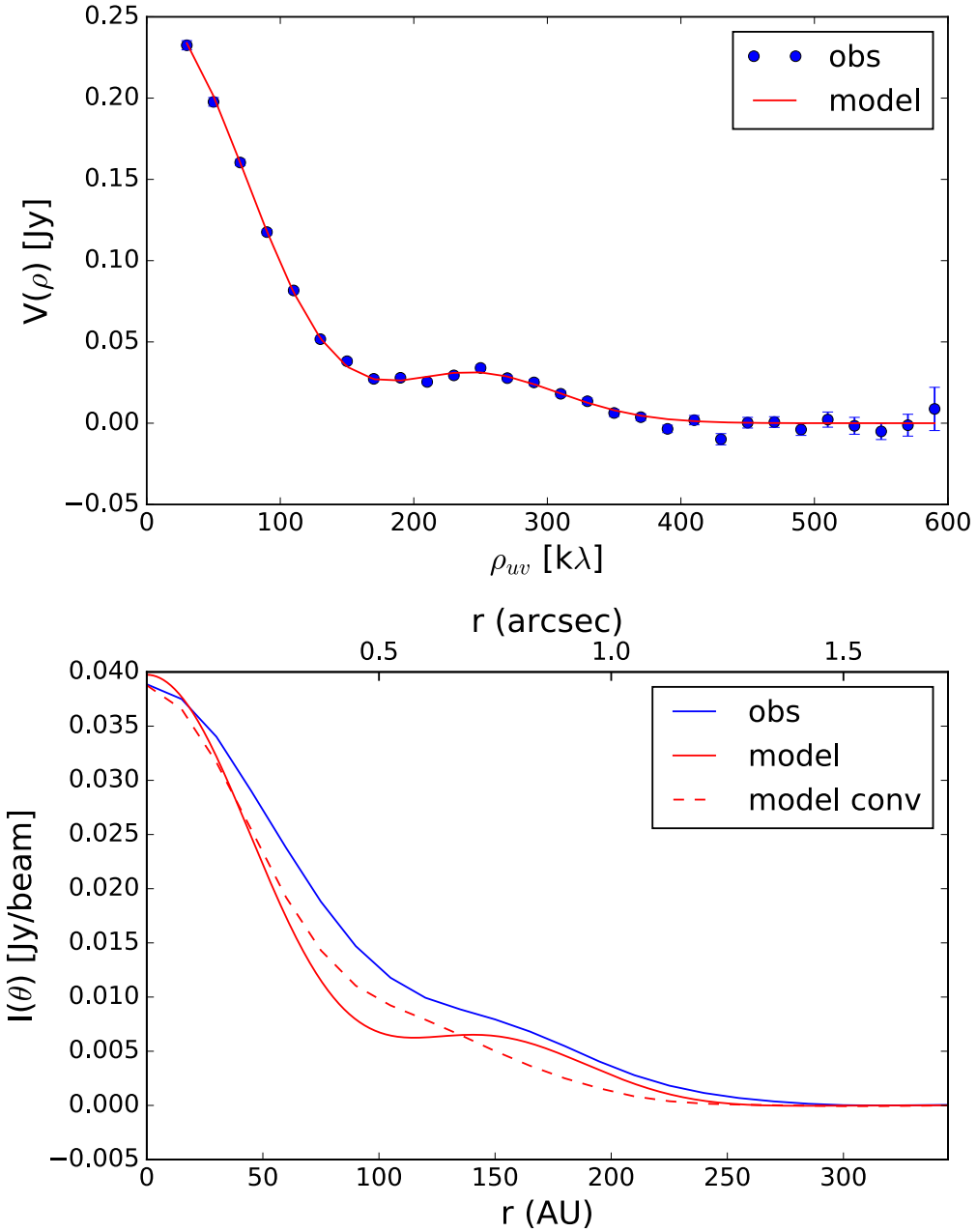

Figure 8.2: *Top panel*: real part of the Sz 98 visibilities binned every 20 kλ (blue dots) with error bars corresponding to the standard deviation of the mean for every bin. The red solid line representing the visibility function of the best fit model. *Bottom panel*: in blue, azymuthally averaged flux density profile from the continuum image at 890μm of Sz 98, the red solid curve represents the best fit model scaled by the beam solid angle, while the red dashed curve is the model convolved with the 2-d gaussian beam.

model is consistent with the image averaged profile, and it shows a much more pronounced feature centered at ∼150 au, that is only marginally visible when smoothing by the beam resolution.

This first experiment, performed on a selected sample of the Lupus survey, appears to be potentially successful, provided a sufficient signal to noise of the data, in detecting small scale structures in the continuum, otherwise barely detectable in the deconvolved images. Note that the Lupus targets were observed by ALMA with a very short integration time (approximately 2 minutes each), so that they are not the ideal dataset for this analysis, as the s/n at long uv-distance is quite low and therefore does not allow to constrain small structures. The principal purpose of this work was to develop a methodology to apply to higher s/n ALMA observations. The information obtained on the possible substructure can be employed to identify possible targets for follow-ups, and to retrieve useful starting points for more detailed modelings, for instance the positions of the rings/gaps to insert in the dust density distribution.

9 Conclusions

This thesis work focused on the study of circumstellar disks and early phases of planet formation. At the beginning of my PhD studies, the general picture of disk evolution was consistent with disks evolving rather quickly with a dispersal time of a few million years, with the timescales and the mechanisms regulating planet formation still remaining poorly constrained. Existing observations at moderately high resolution ($\gtrsim$0.5 arcseconds) indicated a majority of "regular" disks: circularly shaped and well reproduced by models with surface density profiles monotonically declining with the distance from the central star, in both the dust and gas distributions. During the years of my PhD, the development of new facilities operating in the millimeter/submillimeter regime started to unveil with unprecedented detail the structure at small scales of protoplanetary disks, thanks to the improved spatial resolution and sensitivity. It is now becoming clear that, even at early stages, disks present a variety of small scale structures (cavities, rings and spirals), indicating that local processes are playing a major role. Some of the principal mechanisms that are invoked to explain such features are protoplanets, disk instabilities, vortices, disk chemistry; but current observations do not allow, for most cases, to disentangle between these different scenarios.

In this framework I focused on studying disk evolution through high resolution observations, with the purpose of obtaining a better understanding of the mechanisms driving dust growth and ultimately planet formation. The main subject of my work has been the disk around the Herbig Ae star HD 163296, for its properties of being a extremely bright and extrended nearby source, and therefore an excellent prototype for studying dust and gas evolution with great detail.

In the attempt to get an insight on grain growth processes I have been analyzing multi-wavelength observations of HD 163296 at high resolution in the sub-mm and mm regime

with ALMA and VLA, with the aim of measuring the maximum grain size as a function of the distance from the central star (**Chapter 4**, Guidi et al. 2016). The main results of this analysis were: first, the dust opacity spectral index showed a monotonic profile increasing towards larger radii, indicating bigger grains in the inner regions and smaller grains outside, as we would expect as a consequence of radial drift. Second, the dust continuum profile showed an excess of emission at a distance about 100 au, that was interpreted as a local increase of the dust surface density. A possible mechanism that could lead to a piling up of dust was identified in the presence of the CO snowline, already estimated to be at r ~90 au in this disk by Qi et al. (2015).

Following up with observations at higher resolution and sensitivity (**Chapter 5**, Isella et al. 2016), we also analyzed the gas component, showing that not only the dust presented a clear structure of rings and gaps in HD 163296 but also the gas was partially depleted at the same locations. The result of hydrodynamical simulations was that saturn-like planets are compatible with the depletion found in the second and third dust gap, while the first gap remains difficult to explain with the effect of a planet and could be resulting from a different mechanism such as a dead zone due to low ionization. Still, it could not be ruled out the possibility that similar structures might result from other mechanisms such as gravitational instability, vortices, star-disk interaction, or disk chemistry, which do not require the presence of companions.

In order to search directly for protoplanets still embedded in the HD 163296 disk we set up a program to observe this source at infrared wavelengths with Keck/NIRC2 using the vortex coronograph. The analysis, presented in **Chapter 6**, showed a correlation between scattered light in the NIR and ALMA-dust gaps, besides the potential detection of planetary mass candidate close to the second gap, with estimated mass of ~7-9 $M_{Jupiter}$, or a smaller mass planet surrounded by a very active circumplanetary accretion disk.

Finally, we proposed to observe HD 163296 with ALMA at longer wavelength (3 mm) to overcome the effects of the optical depth in the inner regions of the disk and derive a better constrain on the opacity spectral index - and thus attempt to study the grain size distribution in the inner disk midplane. The preliminary analysis of the data is presented in **Chapter 7**, and indicates a spectral index globally consistent with the values found with the previous study, with the higher resolution accentuating local variations at the location of the rings/gaps. In addition, high values of the spectral index ($\gtrsim$4) are found in the outer regions

of the disk (R$\gtrsim$150 au): that could imply the depletion of millimeter grains in the outer disk, and exclude the presence of extremely *fluffy* dust grains (i.e. grains with filling factors $\leq 10^{-4} - 10^{-5}$).

Making use of the extraordinary capabilities of ALMA and VLA I performed a detailed study of a nearby protoplanetary disk and analyzed with unique precision the dust and gas distribution in the disk midplane, unveiling previously hidden substructures that could be due to planet formation taking place, or other local processes at play. In addition, I employed a new generation vortex coronograph at the Keck observatory to search for planetary companions from their thermal emission at infrared wavelengths, and characterized a tentative detection of a candidate protoplanet in this disk. The planned follow-ups on this work are the scheduled observations of HD 163296 at higher resolution and sensitivity at millimeter (ALMA - PI Isella, PI Guidi) and centimeters (VLA - PI Isella, PI Guidi) wavelengths, that will allow a more detailed characterization of the distribution of large grains and constraints on the non-thermal emission potentially affecting millimeter observations. Finally, similar studies are going to be conducted on other sources, where a first characterization of possible small scale structures can be carried out with the method described in **Chapter 8** on resolved sub-mm/mm observations of the dust continuum emission. Regarding the planetary candidate in HD 163296, follow-ups studies in the near-infrared with high contrast imaging have been proposed to confirm the detection.

The work presented in this thesis involves for the most part a single system: given its proximity and the possibility of studying the disk in detail, HD163296 ($M_* \sim 2.3 M_\odot$) is a key benchmark for the study of disk evolution and planet formation around intermediate mass stars. Together with TW Hya (the nearest disk from our Sun, with $M_* \sim 0.8 M_\odot$) for solar mass stars, HD163296 allows us to perform a detailed comparison between observations and models of disk-planet interaction, dust and gas evolution, and chemical differentiation in disks. Both these sources can be considered as evolved systems, with estimates ages of 5 Myr and 10 Myr for HD 163296 and TW Hya respectively, while the majority of disk in nearby star forming regions are on average younger (e.g. Taurus (1-2 Myr), Chamaeleon (2-3 Myr), Lupus (1-3 Myr), σ-Orionis (3-5 Myr), Ophiuchus (1-2 Myr)). Being an individual object, HD 163296 does not allow us to derive information on the demographical properties of disks, which are the subject of less accurate survey programmes (see e.g. Ansdell et al. (2016) for Lupus, Pascucci et al. (2016) for Chamaeleon, Barenfeld et al. (2016) for Upper Sco,

to name a few). Nevertheless, it represents our best prospect of unveiling disk evolution mechanisms that are still not well constrained, involving the interplay between gas and dust, disk chemistry, dust growth. In the future, we expect that it will be possible to extend these detailed studies at larger samples of objects.

References

Adams et al. 1987 F. C. Adams, C. J. Lada and F. H. Shu, 'Spectral evolution of young stellar objects'. *ApJ*, January 1987, volume 312, 788–806, doi:10.1086/164924.

Alexander et al. 2014 R. Alexander, I. Pascucci, S. Andrews, P. Armitage and L. Cieza, 'The Dispersal of Protoplanetary Disks'. *Protostars and Planets VI*, 2014, pages 475–496, doi:10.2458/azu_uapress_9780816531240-ch021, arXiv:1311.1819.

ALMA Partnership et al. 2015 ALMA Partnership, C. L. Brogan, L. M. Pérez, T. R. Hunter, W. R. F. Dent, A. S. Hales, R. E. Hills, S. Corder, E. B. Fomalont, C. Vlahakis, Y. Asaki, D. Barkats, A. Hirota, J. A. Hodge, C. M. V. Impellizzeri et al., 'The 2014 ALMA Long Baseline Campaign: First Results from High Angular Resolution Observations toward the HL Tau Region'. *ApJLett*, July 2015, volume 808, L3, doi:10.1088/2041-8205/808/1/L3, arXiv:1503.02649.

André and Montmerle 1994 P. André and T. Montmerle, 'From T Tauri stars to protostars: Circumstellar material and young stellar objects in the rho Ophiuchi cloud'. *ApJ*, January 1994, volume 420, 837–862, doi:10.1086/173608.

Andrews 2015 S. M. Andrews, 'Observations of Solids in Protoplanetary Disks'. *PASP*, October 2015, volume 127, 961, doi:10.1086/683178, arXiv:1507.04758.

Andrews and Williams 2005 S. M. Andrews and J. P. Williams, 'Circumstellar Dust Disks in Taurus-Auriga: The Submillimeter Perspective'. *ApJ*, October 2005, volume 631, 1134–1160, doi:10.1086/432712, arXiv:astro-ph/0506187.

Andrews et al. 2016 S. M. Andrews, D. J. Wilner, Z. Zhu, T. Birnstiel, J. M. Carpenter, L. M. Pérez, X.-N. Bai, K. I. Öberg, A. M. Hughes, A. Isella and L. Ricci, 'Ringed Substructure and a Gap at 1 au in the Nearest Protoplanetary Disk'. *ApJLett*, April 2016, volume 820, L40, doi:10.3847/2041-8205/820/2/L40, arXiv:1603.09352.

Ansdell et al. 2017 M. Ansdell, J. P. Williams, C. F. Manara, A. Miotello, S. Facchini, N. van der Marel, L. Testi and E. F. van Dishoeck, 'An ALMA Survey of Protoplanetary Disks in the σ Orionis Cluster'. *AJ*, May 2017, volume 153, 240, doi:10.3847/1538-3881/aa69c0, arXiv:1703.08546.

Ansdell et al. 2016 M. Ansdell, J. P. Williams, N. van der Marel, J. M. Carpenter, G. Guidi, M. Hogerheijde, G. S. Mathews, C. F. Manara, A. Miotello, A. Natta, I. Oliveira, M. Tazzari, L. Testi, E. F. van Dishoeck and S. E. van Terwisga, 'ALMA Survey of Lupus Protoplanetary Disks. I. Dust and Gas Masses'. *ApJ*, September 2016, volume 828, 46, doi:10.3847/0004-637X/828/1/46, arXiv:1604.05719.

Armitage 2013 P. J. Armitage, 'Astrophysics of Planet Formation'. *Astrophysics of Planet Formation, Cambridge University Press*, October 2013.

Bai 2016 X.-N. Bai, 'Towards a Global Evolutionary Model of Protoplanetary Disks'. *ApJ*, April 2016, volume 821, 80, doi:10.3847/0004-637X/821/2/80, arXiv:1603.00484.

Bailey et al. 2014 V. Bailey, T. Meshkat, M. Reiter, K. Morzinski, J. Males, K. Y. L. Su, P. M. Hinz, M. Kenworthy, D. Stark, E. Mamajek, R. Briguglio, L. M. Close, K. B. Follette, A. Puglisi, T. Rodigas, A. J. Weinberger and M. Xompero, 'HD 106906 b: A Planetary-mass Companion Outside a Massive Debris Disk'. *ApJLett*, January 2014, volume 780, L4, doi:10.1088/2041-8205/780/1/L4, arXiv:1312.1265.

Balbus and Hawley 1991 S. A. Balbus and J. F. Hawley, 'A powerful local shear instability in weakly magnetized disks. I - Linear analysis. II - Nonlinear evolution'. *ApJ*, July 1991, volume 376, 214–233, doi:10.1086/170270.

Banzatti et al. 2015 A. Banzatti, P. Pinilla, L. Ricci, K. M. Pontoppidan, T. Birnstiel and F. Ciesla, 'Direct Imaging of the Water Snow Line at the Time of Planet Formation using Two ALMA Continuum Bands'. *ApJLett*, December 2015, volume 815, L15, doi:10.1088/2041-8205/815/1/L15, arXiv:1511.06762.

Banzatti et al. 2011 A. Banzatti, L. Testi, A. Isella, A. Natta, R. Neri and D. J. Wilner, 'New constraints on dust grain size and distribution in CQ Tauri'. *A&A*, January 2011, volume 525, A12, doi:10.1051/0004-6361/201015206, arXiv:1009.2697.

Baraffe et al. 2003 I. Baraffe, G. Chabrier, T. S. Barman, F. Allard and P. H. Hauschildt, 'Evolutionary models for cool brown dwarfs and extrasolar giant planets. The case of HD 209458'. *A&A*, May 2003, volume 402, 701–712, doi:10.1051/0004-6361:20030252, arXiv:astro-ph/0302293.

Barenfeld et al. 2016 S. A. Barenfeld, J. M. Carpenter, L. Ricci and A. Isella, 'ALMA Observations of Circumstellar Disks in the Upper Scorpius OB Association'. *ApJ*, August 2016, volume 827, 142, doi:10.3847/0004-637X/827/2/142, arXiv:1605.05772.

Barge and Sommeria 1995 P. Barge and J. Sommeria, 'Did planet formation begin inside persistent gaseous vortices?' *A&A*, March 1995, volume 295, L1–L4, arXiv:arXiv:astro-ph/9501050.

Baruteau et al. 2014 C. Baruteau, A. Crida, S.-J. Paardekooper, F. Masset, J. Guilet, B. Bitsch, R. Nelson, W. Kley and J. Papaloizou, 'Planet-Disk Interactions and Early Evolution of Planetary Systems'. *Protostars and Planets VI*, 2014, pages 667–689, doi:10.2458/azu_uapress_9780816531240-ch029, arXiv:1312.4293.

Batalha 2014 N. M. Batalha, 'Exploring exoplanet populations with NASA's Kepler Mission'. *Proceedings of the National Academy of Science*, September 2014, volume 111, 12647–12654, doi:10.1073/pnas.1304196111, arXiv:1409.1904.

Beckwith et al. 2000 S. V. W. Beckwith, T. Henning and Y. Nakagawa, 'Dust Properties and Assembly of Large Particles in Protoplanetary Disks'. *Protostars and Planets IV*, May 2000, page 533, arXiv:astro-ph/9902241.

Beckwith and Sargent 1991 S. V. W. Beckwith and A. I. Sargent, 'Particle emissivity in circumstellar disks'. *ApJ*, November 1991, volume 381, 250–258, doi:10.1086/170646.

Beckwith et al. 1990 S. V. W. Beckwith, A. I. Sargent, R. S. Chini and R. Guesten, 'A survey for circumstellar disks around young stellar objects'. *AJ*, March 1990, volume 99, 924–945, doi:10.1086/115385.

Bell et al. 1997 K. R. Bell, P. M. Cassen, H. H. Klahr and T. Henning, 'The Structure and Appearance of Protostellar Accretion Disks: Limits on Disk Flaring'. *ApJ*, September 1997, volume 486, 372–387, doi:10.1086/304514.

Benisty et al. 2010 M. Benisty, A. Natta, A. Isella, J.-P. Berger, F. Massi, J.-B. Le Bouquin, A. Mérand, G. Duvert, S. Kraus, F. Malbet, J. Olofsson, S. Robbe-Dubois, L. Testi, M. Vannier and G. Weigelt, 'Strong near-infrared emission in the sub-AU disk of the Herbig Ae star HD 163296: evidence of refractory dust?' *A&A*, February 2010, volume 511, A74, doi:10.1051/0004-6361/200912898, arXiv:0911.4363.

Biller et al. 2014 B. A. Biller, J. Males, T. Rodigas, K. Morzinski, L. M. Close, A. Juhász, K. B. Follette, S. Lacour, M. Benisty, A. Sicilia-Aguilar, P. M. Hinz, A. Weinberger, T. Henning, J.-U. Pott, M. Bonnefoy and R. Köhler, 'An Enigmatic Point-like Feature within the HD 169142 Transitional Disk'. *ApJLett*, September 2014, volume 792, L22, doi:10.1088/2041-8205/792/1/L22, arXiv:1408.0794.

Birnstiel et al. 2012 T. Birnstiel, H. Klahr and B. Ercolano, 'A simple model for the evolution of the dust population in protoplanetary disks'. *A&A*, March 2012, volume 539, A148, doi:10.1051/0004-6361/201118136, arXiv:1201.5781.

Birnstiel et al. 2010 T. Birnstiel, L. Ricci, F. Trotta, C. P. Dullemond, A. Natta, L. Testi, C. Dominik, T. Henning, C. W. Ormel and A. Zsom, 'Testing the theory of grain growth and fragmentation by millimeter observations of protoplanetary disks'. *A&A*, June 2010, volume 516, L14, doi:10.1051/0004-6361/201014893, arXiv:1006.0940.

Borucki et al. 2011 W. J. Borucki, D. G. Koch, G. Basri, N. Batalha, T. M. Brown, S. T. Bryson, D. Caldwell, J. Christensen-Dalsgaard, W. D. Cochran, E. DeVore, E. W. Dunham, T. N. Gautier, III, J. C. Geary, R. Gilliland, A. Gould et al., 'Characteristics of Planetary Candidates Observed by Kepler. II. Analysis of the First Four Months of Data'. *ApJ*, July 2011, volume 736, 19, doi:10.1088/0004-637X/736/1/19, arXiv:1102.0541.

Brauer et al. 2008 F. Brauer, C. P. Dullemond and T. Henning, 'Coagulation, fragmentation and radial motion of solid particles in protoplanetary disks'. *A&A*, March 2008, volume 480, 859–877, doi:10.1051/0004-6361:20077759, arXiv:0711.2192.

Bryden et al. 1999 G. Bryden, X. Chen, D. N. C. Lin, R. P. Nelson and J. C. B. Papaloizou, 'Tidally Induced Gap Formation in Protostellar Disks: Gap Clearing and Suppression of Protoplanetary Growth'. *ApJ*, March 1999, volume 514, 344–367, doi:10.1086/306917.

Chauvin et al. 2005 G. Chauvin, A.-M. Lagrange, C. Dumas, B. Zuckerman, D. Mouillet, I. Song, J.-L. Beuzit and P. Lowrance, 'Giant planet companion to 2MASSW J1207334-393254'. *A&A*, August 2005, volume 438, L25–L28, doi:10.1051/0004-6361:200500116, arXiv:astro-ph/0504659.

Chiang and Murray-Clay 2007 E. Chiang and R. Murray-Clay, 'Inside-out evacuation of transitional protoplanetary discs by the magneto-rotational instability'. *Nature Physics*, September 2007, volume 3, 604–608, doi:10.1038/nphys661, arXiv:0706.1241.

Chiang and Goldreich 1997 E. I. Chiang and P. Goldreich, 'Spectral Energy Distributions of T Tauri Stars with Passive Circumstellar Disks'. *ApJ*, November 1997, volume 490, 368–376, arXiv:astro-ph/9706042.

D'Alessio et al. 1998 P. D'Alessio, J. Cantö, N. Calvet and S. Lizano, 'Accretion Disks around Young Objects. I. The Detailed Vertical Structure'. *ApJ*, June 1998, volume 500, 411–427, doi:10.1086/305702, arXiv:astro-ph/9806060.

de Gregorio-Monsalvo et al. 2013 I. de Gregorio-Monsalvo, F. Ménard, W. Dent, C. Pinte, C. López, P. Klaassen, A. Hales, P. Cortés, M. G. Rawlings, K. Tachihara, L. Testi, S. Takahashi, E. Chapillon, G. Mathews, A. Juhasz, E. Akiyama, A. E. Higuchi, M. Saito, L.-Å. Nyman, N. Phillips, J. Rodón, S. Corder and T. Van Kempen, 'Unveiling the gas-and-dust disk structure in HD 163296 using ALMA observations'. *A&A*, September 2013, volume 557, A133, doi:10.1051/0004-6361/201321603, arXiv:1307.1357.

Dipierro et al. 2015 G. Dipierro, D. Price, G. Laibe, K. Hirsh, A. Cerioli and G. Lodato, 'On planet formation in HL Tau'. *MNRAS*, October 2015, volume 453, L73–L77, doi:10.1093/mnrasl/slv105, arXiv:1507.06719.

Dittrich et al. 2013 K. Dittrich, H. Klahr and A. Johansen, 'Gravoturbulent Planetesimal Formation: The Positive Effect of Long-lived Zonal Flows'. *ApJ*, February 2013, volume 763, 117, doi:10.1088/0004-637X/763/2/117, arXiv:1211.2095.

Dominik et al. 2003 C. Dominik, C. P. Dullemond, L. B. F. M. Waters and S. Walch, 'Understanding the spectra of isolated Herbig stars in the frame of a passive disk model'. *A&A*, February 2003, volume 398, 607–619, doi:10.1051/0004-6361:20021629, arXiv:astro-ph/0212032.

Draine 2006 B. T. Draine, 'On the Submillimeter Opacity of Protoplanetary Disks'. *ApJ*, January 2006, volume 636, 1114–1120, doi:10.1086/498130, arXiv:astro-ph/0507292.

Drążkowska et al. 2014 J. Drążkowska, F. Windmark and C. P. Dullemond, 'Modeling dust growth in protoplanetary disks: The breakthrough case'. *A&A*, July 2014, volume 567, A38, doi:10.1051/0004-6361/201423708, arXiv:1406.0870.

Dullemond 2012 C. P. Dullemond, 'RADMC-3D: A multi-purpose radiative transfer tool'. Astrophysics Source Code Library, February 2012, arXiv:1202.015.

Dullemond et al. 2001 C. P. Dullemond, C. Dominik and A. Natta, 'Passive Irradiated Circumstellar Disks with an Inner Hole'. *ApJ*, October 2001, volume 560, 957–969, doi:10.1086/323057, arXiv:astro-ph/0106470.

Dullemond et al. 2007 C. P. Dullemond, D. Hollenbach, I. Kamp and P. D'Alessio, 'Models of the Structure and Evolution of Protoplanetary Disks'. *Protostars and Planets V*, 2007, pages 555–572, arXiv:astro-ph/0602619.

Ercolano and Pascucci 2017 B. Ercolano and I. Pascucci, 'The dispersal of planet-forming discs: theory confronts observations'. *Royal Society Open Science*, April 2017, volume 4, 170114, doi:10.1098/rsos.170114, arXiv:1704.00214.

Espaillat et al. 2014 C. Espaillat, J. Muzerolle, J. Najita, S. Andrews, Z. Zhu, N. Calvet, S. Kraus, J. Hashimoto, A. Kraus and P. D'Alessio, 'An Observational Perspective of Transitional Disks'. *Protostars and Planets VI*, 2014, pages 497–520, doi:10.2458/azu_uapress_9780816531240-ch022, arXiv:1402.7103.

Fedele et al. 2017 D. Fedele, M. Carney, M. R. Hogerheijde, C. Walsh, A. Miotello, P. Klaassen, S. Bruderer, T. Henning and E. F. van Dishoeck, 'ALMA unveils rings and gaps in the protoplanetary system <ASTROBJ>HD 169142</ASTROBJ>: signatures of two giant protoplanets'. *A&A*, April 2017, volume 600, A72, doi:10.1051/0004-6361/201629860, arXiv:1702.02844.

Fedele et al. 2010 D. Fedele, M. E. van den Ancker, T. Henning, R. Jayawardhana and J. M. Oliveira, 'Timescale of mass accretion in pre-main-sequence stars'. *A&A*, February 2010, volume 510, A72, doi:10.1051/0004-6361/200912810, arXiv:0911.3320.

Fischer et al. 2014 D. A. Fischer, A. W. Howard, G. P. Laughlin, B. Macintosh, S. Mahadevan, J. Sahlmann and J. C. Yee, 'Exoplanet Detection Techniques'. *Protostars and Planets VI*, 2014, pages 715–737, doi:10.2458/azu_uapress_9780816531240-ch031, arXiv:1505.06869.

Fischer and Valenti 2005 D. A. Fischer and J. Valenti, 'The Planet-Metallicity Correlation'. *ApJ*, April 2005, volume 622, 1102–1117, doi:10.1086/428383.

Flock et al. 2015 M. Flock, J. P. Ruge, N. Dzyurkevich, T. Henning, H. Klahr and S. Wolf, 'Gaps, rings, and non-axisymmetric structures in protoplanetary disks. From simulations to ALMA observations'. *A&A*, February 2015, volume 574, A68, doi:10.1051/0004-6361/201424693, arXiv:1411.2736.

Foreman-Mackey et al. 2013 D. Foreman-Mackey, D. W. Hogg, D. Lang and J. Goodman, 'emcee: The MCMC Hammer'. *PASP*, March 2013, volume 125, 306–312, doi:10.1086/670067, arXiv:1202.3665.

Friedjung 1985 M. Friedjung, 'Accretion disks heated by luminous central stars'. *A&A*, May 1985, volume 146, 366–368.

Fu et al. 2014a W. Fu, H. Li, S. Lubow and S. Li, 'Long-term Evolution of Planet-induced Vortices in Protoplanetary Disks'. *ApJLett*, June 2014a, volume 788, L41, doi:10.1088/2041-8205/788/2/L41, arXiv:1405.7379.

Fu et al. 2014b W. Fu, H. Li, S. Lubow, S. Li and E. Liang, 'Effects of Dust Feedback on Vortices in Protoplanetary Disks'. *ApJLett*, November 2014b, volume 795, L39, doi:10.1088/2041-8205/795/2/L39, arXiv:1410.4196.

Fulton et al. 2017 B. J. Fulton, E. A. Petigura, A. W. Howard, H. Isaacson, G. W. Marcy, P. A. Cargile, L. Hebb, L. M. Weiss, J. A. Johnson, T. D. Morton, E. Sinukoff, I. J. M. Crossfield and L. A. Hirsch, 'The California-Kepler Survey. III. A Gap in the Radius Distribution of Small Planets'. *AJ*, September 2017, volume 154, 109, doi:10.3847/1538-3881/aa80eb, arXiv:1703.10375.

Garufi et al. 2017 A. Garufi, G. Meeus, M. Benisty, S. P. Quanz, A. Banzatti, M. Kama, H. Canovas, C. Eiroa, H. M. Schmid, T. Stolker, A. Pohl, E. Rigliaco, F. Ménard, M. R. Meyer, R. van Boekel and C. Dominik, 'Evolution of protoplanetary disks from their taxonomy in scattered light: Group I vs. Group II'. *A&A*, July 2017, volume 603, A21, doi:10.1051/0004-6361/201630320, arXiv:1703.01512.

Garufi et al. 2014 A. Garufi, S. P. Quanz, H. M. Schmid, H. Avenhaus, E. Buenzli and S. Wolf, 'Shadows and cavities in protoplanetary disks: HD 163296, HD 141569A, and HD 150193A in polarized light'. *A&A*, August 2014, volume 568, A40, doi:10.1051/0004-6361/201424262, arXiv:1406.7387.

Gomez Gonzalez et al. 2017 C. A. Gomez Gonzalez, O. Wertz, O. Absil, V. Christiaens, D. Defrère, D. Mawet, J. Milli, P.-A. Absil, M. Van Droogenbroeck, F. Cantalloube, P. M. Hinz, A. J. Skemer, M. Karlsson and J. Surdej, 'VIP: Vortex Image Processing Package for High-contrast Direct Imaging'. *AJ*, July 2017, volume 154, 7, doi:10.3847/1538-3881/aa73d7, arXiv:1705.06184.

Goodman et al. 1993 A. A. Goodman, P. J. Benson, G. A. Fuller and P. C. Myers, 'Dense cores in dark clouds. VIII - Velocity gradients'. *ApJ*, April 1993, volume 406, 528–547, doi:10.1086/172465.

Grady et al. 2000 C. A. Grady, D. Devine, B. Woodgate, R. Kimble, F. C. Bruhweiler, A. Boggess, J. L. Linsky, P. Plait, M. Clampin and P. Kalas, 'STIS Coronagraphic Imaging of the Herbig AE Star: HD 163296'. *ApJ*, December 2000, volume 544, 895–902, doi:10.1086/317222.

Guidi et al. 2016 G. Guidi, M. Tazzari, L. Testi, I. de Gregorio-Monsalvo, C. J. Chandler, L. Pérez, A. Isella, A. Natta, S. Ortolani, T. Henning, S. Corder, H. Linz, S. Andrews, D. Wilner, L. Ricci, J. Carpenter, A. Sargent, L. Mundy, S. Storm, N. Calvet, C. Dullemond, J. Greaves, J. Lazio, A. Deller and W. Kwon, 'Dust properties across the CO snowline in the HD 163296 disk from ALMA and VLA observations'. *A&A*, April 2016, volume 588, A112, doi:10.1051/0004-6361/201527516, arXiv:1601.07542.

Guilloteau et al. 2011 S. Guilloteau, A. Dutrey, V. Piétu and Y. Boehler, 'A dual-frequency sub-arcsecond study of proto-planetary disks at mm wavelengths: first evidence for radial variations of the dust properties'. *A&A*, May 2011, volume 529, A105, doi:10.1051/0004-6361/201015209, arXiv:1103.1296.

Gundlach and Blum 2015 B. Gundlach and J. Blum, 'The Stickiness of Micrometer-sized Water-ice Particles'. *ApJ*, January 2015, volume 798, 34, doi:10.1088/0004-637X/798/1/34, arXiv:1410.7199.

Hayashi 1981 C. Hayashi, 'Structure of the Solar Nebula, Growth and Decay of Magnetic Fields and Effects of Magnetic and Turbulent Viscosities on the Nebula'. *Progress of Theoretical Physics Supplement*, 1981, volume 70, 35–53, doi:10.1143/PTPS.70.35.

Helled et al. 2014 R. Helled, P. Bodenheimer, M. Podolak, A. Boley, F. Meru, S. Nayakshin, J. J. Fortney, L. Mayer, Y. Alibert and A. P. Boss, 'Giant Planet Formation, Evolution, and Internal Structure'. *Protostars and Planets VI*, 2014, pages 643–665, doi:10.2458/azu_uapress_9780816531240-ch028, arXiv:1311.1142.

Hernández et al. 2007 J. Hernández, L. Hartmann, T. Megeath, R. Gutermuth, J. Muzerolle, N. Calvet, A. K. Vivas, C. Briceño, L. Allen, J. Stauffer, E. Young and G. Fazio, 'A Spitzer Space Telescope Study of Disks in the Young σ Orionis Cluster'. *ApJ*, June 2007, volume 662, 1067–1081, doi:10.1086/513735, arXiv:astro-ph/0701476.

Hildebrand 1983 R. H. Hildebrand, 'The Determination of Cloud Masses and Dust Characteristics from Submillimetre Thermal Emission'. *QJRAS*, September 1983, volume 24, 267.

Hillenbrand et al. 1992 L. A. Hillenbrand, S. E. Strom, F. J. Vrba and J. Keene, 'Herbig Ae/Be stars - Intermediate-mass stars surrounded by massive circumstellar accretion disks'. *ApJ*, October 1992, volume 397, 613–643, doi:10.1086/171819.

Howard et al. 2010 A. W. Howard, G. W. Marcy, J. A. Johnson, D. A. Fischer, J. T. Wright, H. Isaacson, J. A. Valenti, J. Anderson, D. N. C. Lin and S. Ida, 'The Occurrence and Mass Distribution of Close-in Super-Earths, Neptunes, and Jupiters'. *Science*, October 2010, volume 330, 653–, doi:10.1126/science.1194854, arXiv:1011.0143.

Ida and Lin 2004 S. Ida and D. N. C. Lin, 'Toward a Deterministic Model of Planetary Formation. II. The Formation and Retention of Gas Giant Planets around Stars with a Range of Metallicities'. *ApJ*, November 2004, volume 616, 567–572, doi:10.1086/424830, arXiv:astro-ph/0408019.

Igea and Glassgold 1999 J. Igea and A. E. Glassgold, 'X-Ray Ionization of the Disks of Young Stellar Objects'. *ApJ*, June 1999, volume 518, 848–858, doi:10.1086/307302.

Isella et al. 2009 A. Isella, J. M. Carpenter and A. I. Sargent, 'Structure and Evolution of Pre-main-sequence Circumstellar Disks'. *ApJ*, August 2009, volume 701, 260–282, doi:10.1088/0004-637X/701/1/260, arXiv:0906.2227.

Isella et al. 2016 A. Isella, G. Guidi, L. Testi, S. Liu, H. Li, S. Li, E. Weaver, Y. Boehler, J. M. Carperter, I. De Gregorio-Monsalvo, C. F. Manara, A. Natta, L. M. Pérez, L. Ricci, A. Sargent, M. Tazzari and N. Turner, 'Ringed Structures of the HD 163296 Protoplanetary Disk Revealed by ALMA'. *Physical Review Letters*, December 2016, volume 117(25), 251101, doi:10.1103/PhysRevLett.117.251101.

Isella and Natta 2005 A. Isella and A. Natta, 'The shape of the inner rim in proto-planetary disks'. *A&A*, August 2005, volume 438, 899–907, doi:10.1051/0004-6361:20052773, arXiv:astro-ph/0503635.

Isella et al. 2007 A. Isella, L. Testi, A. Natta, R. Neri, D. Wilner and C. Qi, 'Millimeter imaging of HD 163296: probing the disk structure and kinematics'. *A&A*, July 2007, volume 469, 213–222, doi:10.1051/0004-6361:20077385, arXiv:0704.0616.

Jensen-Clem et al. 2017 R. Jensen-Clem, D. Mawet, C. A. Gomez Gonzalez, O. Absil, R. Belikov, T. Currie, M. A. Kenworthy, C. Marois, J. Mazoyer, G. Ruane and A. Tanner, 'A New Standard for Assessing the Performance of High Contrast Imaging Systems'. *ArXiv e-prints*, November 2017, arXiv:1711.01215.

Jin et al. 2016 S. Jin, S. Li, A. Isella, H. Li and J. Ji, 'Modeling Dust Emission of HL Tau Disk Based on Planet-Disk Interactions'. *ApJ*, February 2016, volume 818, 76, doi:10.3847/0004-637X/818/1/76, arXiv:1601.00358.

Johansen et al. 2014 A. Johansen, J. Blum, H. Tanaka, C. Ormel, M. Bizzarro and H. Rickman, 'The Multifaceted Planetesimal Formation Process'. *Protostars and Planets VI*, 2014, pages 547–570, doi:10.2458/azu_uapress_9780816531240-ch024, arXiv:1402.1344.

Jørgensen et al. 2009 J. K. Jørgensen, E. F. van Dishoeck, R. Visser, T. L. Bourke, D. J. Wilner, D. Lommen, M. R. Hogerheijde and P. C. Myers, 'PROSAC: a submillimeter array survey of low-mass protostars. II. The mass evolution of envelopes, disks, and stars from the Class 0 through I stages'. *A&A*, November 2009, volume 507, 861–879, doi:10.1051/0004-6361/200912325, arXiv:0909.3386.

Kalas et al. 2008 P. Kalas, J. R. Graham, E. Chiang, M. P. Fitzgerald, M. Clampin, E. S. Kite, K. Stapelfeldt, C. Marois and J. Krist, 'Optical Images of an Exosolar Planet 25 Light-Years from Earth'. *Science*, November 2008, volume 322, 1345, doi:10.1126/science.1166609, arXiv:0811.1994.

Kanagawa et al. 2015 K. D. Kanagawa, T. Muto, H. Tanaka, T. Tanigawa, T. Takeuchi, T. Tsukagoshi and M. Momose, 'Mass Estimates of a Giant Planet in a Protoplanetary Disk from the Gap Structures'. *ApJLett*, June 2015, volume 806, L15, doi:10.1088/2041-8205/806/1/L15, arXiv:1505.04482.

Kanagawa et al. 2016 K. D. Kanagawa, T. Muto, H. Tanaka, T. Tanigawa, T. Takeuchi, T. Tsukagoshi and M. Momose, 'Mass constraint for a planet in a protoplanetary disk from the gap width'. *PASJ*, June 2016, volume 68, 43, doi:10.1093/pasj/psw037, arXiv:1603.03853.

Kataoka et al. 2014 A. Kataoka, S. Okuzumi, H. Tanaka and H. Nomura, 'Opacity of fluffy dust aggregates'. *A&A*, August 2014, volume 568, A42, doi:10.1051/0004-6361/201323199, arXiv:1312.1459.

Kenyon and Hartmann 1987 S. J. Kenyon and L. Hartmann, 'Spectral energy distributions of T Tauri stars - Disk flaring and limits on accretion'. *ApJ*, December 1987, volume 323, 714–733, doi:10.1086/165866.

Klaassen et al. 2013 P. D. Klaassen, A. Juhasz, G. S. Mathews, J. C. Mottram, I. De Gregorio-Monsalvo, E. F. van Dishoeck, S. Takahashi, E. Akiyama, E. Chapillon, D. Espada, A. Hales, M. R. Hogerheijde, M. Rawlings, M. Schmalzl and L. Testi, 'ALMA detection of the rotating molecular disk wind from the young star HD 163296'. *A&A*, July 2013, volume 555, A73, doi:10.1051/0004-6361/201321129, arXiv:1304.5436.

Klahr and Henning 1997 H. H. Klahr and T. Henning, 'Particle-Trapping Eddies in Protoplanetary Accretion Disks'. *Icarus*, July 1997, volume 128, 213–229, doi:10.1006/icar.1997.5720.

Kratter and Lodato 2016 K. Kratter and G. Lodato, 'Gravitational Instabilities in Circumstellar Disks'. *ARA&A*, September 2016, volume 54, 271–311, doi:10.1146/annurev-astro-081915-023307, arXiv:1603.01280.

Kwon et al. 2009 W. Kwon, L. W. Looney, L. G. Mundy, H.-F. Chiang and A. J. Kemball, 'Grain Growth and Density Distribution of the Youngest Protostellar Systems'. *ApJ*, May 2009, volume 696, 841–852, doi:10.1088/0004-637X/696/1/841, arXiv:0902.2008.

Kwon et al. 2015 W. Kwon, L. W. Looney, L. G. Mundy and W. J. Welch, 'Resolving Protoplanetary Disks at Millimeter Wavelengths with CARMA'. *ApJ*, July 2015, volume 808, 102, doi:10.1088/0004-637X/808/1/102, arXiv:1506.03679.

Lada 1987 C. J. Lada, 'Star formation - From OB associations to protostars'. In M. Peimbert and J. Jugaku, editors, *Star Forming Regions*, volume 115 of *IAU Symposium* (1987) pages 1–17.

Lada and Wilking 1984 C. J. Lada and B. A. Wilking, 'The nature of the embedded population in the Rho Ophiuchi dark cloud - Mid-infrared observations'. *ApJ*, December 1984, volume 287, 610–621, doi:10.1086/162719.

Lagrange et al. 2010 A.-M. Lagrange, M. Bonnefoy, G. Chauvin, D. Apai, D. Ehrenreich, A. Boccaletti, D. Gratadour, D. Rouan, D. Mouillet, S. Lacour and M. Kasper, 'A Giant Planet Imaged in the Disk of the Young Star β Pictoris'. *Science*, July 2010, volume 329, 57, doi:10.1126/science.1187187, arXiv:1006.3314.

Laibe 2014 G. Laibe, 'Growing dust grains in protoplanetary discs - II. The radial-drift barrier problem'. *MNRAS*, February 2014, volume 437, 3037–3054, doi:10.1093/mnras/stt1928, arXiv:1310.2637.

Li et al. 2001 H. Li, S. A. Colgate, B. Wendroff and R. Liska, 'Rossby Wave Instability of Thin Accretion Disks. III. Nonlinear Simulations'. *ApJ*, April 2001, volume 551, 874–896, doi:10.1086/320241, arXiv:arXiv:astro-ph/0012479.

Li et al. 2005 H. Li, S. Li, J. Koller, B. B. Wendroff, R. Liska, C. M. Orban, E. P. T. Liang and D. N. C. Lin, 'Potential Vorticity Evolution of a Protoplanetary Disk with an Embedded Protoplanet'. *ApJ*, May 2005, volume 624, 1003–1009, doi:10.1086/429367, arXiv:arXiv:astro-ph/0503404.

Li and Li 2009 S. Li and H. Li, 'A Fast Parallel Simulation Code for Interaction between Proto-Planetary Disk and Embedded Proto-Planets'. *Technical Report, LA-UR-09-2968*, 2009.

Ligi et al. 2017 R. Ligi, A. Vigan, R. Gratton, J. de Boer, M. Benisty, A. Boccaletti, S. P. Quanz, M. Meyer, C. Ginski, E. Sissa, T. Henning, J.-L. Beuzit, B. Biller, M. Bonnefoy, G. Chauvin et al., 'Investigation of the inner structures around HD169142 with VLT/SPHERE'. *ArXiv e-prints*, September 2017, arXiv:1709.01734.

Long et al. 2017 F. Long, G. J. Herczeg, I. Pascucci, E. Drabek-Maunder, S. Mohanty, L. Testi, D. Apai, N. Hendler, T. Henning, C. F. Manara and G. D. Mulders, 'An ALMA Survey of CO Isotopologue Emission from Protoplanetary Disks in Chamaeleon I'. *ApJ*, August 2017, volume 844, 99, doi:10.3847/1538-4357/aa78fc, arXiv:1706.03320.

Lyra et al. 2008 W. Lyra, A. Johansen, H. Klahr and N. Piskunov, 'Embryos grown in the dead zone. Assembling the first protoplanetary cores in low mass self-gravitating circumstellar disks of gas and solids'. *A&A*, December 2008, volume 491, L41–L44, doi:10.1051/0004-6361:200810626, arXiv:0807.2622.

Lyra and Lin 2013 W. Lyra and M.-K. Lin, 'Steady State Dust Distributions in Disk Vortices: Observational Predictions and Applications to Transitional Disks'. *ApJ*, September 2013, volume 775, 17, doi:10.1088/0004-637X/775/1/17, arXiv:1307.3770.

Mamajek 2009 E. E. Mamajek, 'Initial Conditions of Planet Formation: Lifetimes of Primordial Disks'. In T. Usuda, M. Tamura and M. Ishii, editors, *American Institute of Physics Conference Series*, volume 1158 of *American Institute of Physics Conference Series* (2009) pages 3–10, doi:10.1063/1.3215910, arXiv:0906.5011.

Marois et al. 2006 C. Marois, D. Lafrenière, R. Doyon, B. Macintosh and D. Nadeau, 'Angular Differential Imaging: A Powerful High-Contrast Imaging Technique'. *ApJ*, April 2006, volume 641, 556–564, doi:10.1086/500401, arXiv:astro-ph/0512335.

Marois et al. 2008 C. Marois, B. Macintosh, T. Barman, B. Zuckerman, I. Song, J. Patience, D. Lafrenière and R. Doyon, 'Direct Imaging of Multiple Planets Orbiting the Star HR 8799'. *Science*, November 2008, volume 322, 1348, doi:10.1126/science.1166585, arXiv:0811.2606.

Marois et al. 2010 C. Marois, B. Zuckerman, Q. M. Konopacky, B. Macintosh and T. Barman, 'Images of a fourth planet orbiting HR 8799'. *Nature*, December 2010, volume 468, 1080–1083, doi:10.1038/nature09684, arXiv:1011.4918.

Mathews et al. 2013 G. S. Mathews, P. D. Klaassen, A. Juhász, D. Harsono, E. Chapillon, E. F. van Dishoeck, D. Espada, I. de Gregorio-Monsalvo, A. Hales, M. R. Hogerheijde, J. C. Mottram, M. G. Rawlings, S. Takahashi and L. Testi, 'ALMA imaging of the CO snowline of the HD 163296 disk with DCO^+'. *A&A*, September 2013, volume 557, A132, doi:10.1051/0004-6361/201321600, arXiv:1307.3420.

Mawet et al. 2017 D. Mawet, É. Choquet, O. Absil, E. Huby, M. Bottom, E. Serabyn, B. Femenia, J. Lebreton, K. Matthews, C. A. Gomez Gonzalez, O. Wertz, B. Carlomagno, V. Christiaens, D. Defrère, C. Delacroix, P. Forsberg, S. Habraken, A. Jolivet, M. Karlsson, J. Milli, C. Pinte, P. Piron, M. Reggiani, J. Surdej and E. Vargas Catalan, 'Characterization of the Inner Disk around HD 141569 A from Keck/NIRC2 L-Band Vortex Coronagraphy'. *AJ*, January 2017, volume 153, 44, doi:10.3847/1538-3881/153/1/44, arXiv:1612.03091.

Mawet et al. 2014 D. Mawet, J. Milli, Z. Wahhaj, D. Pelat, O. Absil, C. Delacroix, A. Boccaletti, M. Kasper, M. Kenworthy, C. Marois, B. Mennesson and L. Pueyo, 'Fundamental limitations of high contrast imaging set by small sample statistics'. *The Astrophysical Journal*, 2014, volume 792(2), 97, URL http://stacks.iop.org/0004-637X/792/i=2/a=97.

Mawet et al. 2005 D. Mawet, P. Riaud, O. Absil and J. Surdej, 'Annular Groove Phase Mask Coronagraph'. *ApJ*, November 2005, volume 633, 1191–1200, doi:10.1086/462409.

Mayor et al. 2011 M. Mayor, M. Marmier, C. Lovis, S. Udry, D. Ségransan, F. Pepe, W. Benz, J. . Bertaux, F. Bouchy, X. Dumusque, G. Lo Curto, C. Mordasini, D. Queloz and N. C. Santos, 'The HARPS search for southern extra-solar planets XXXIV. Occurrence, mass distribution and orbital properties of super-Earths and Neptune-mass planets'. *ArXiv e-prints*, September 2011, arXiv:1109.2497.

Mayor and Queloz 1995 M. Mayor and D. Queloz, 'A Jupiter-mass companion to a solar-type star'. *Nature*, November 1995, volume 378, 355–359, doi:10.1038/378355a0.

McLean 2008 I. S. McLean, *Electronic Imaging in Astronomy: Detectors and Instrumentation (Second Edition)* (Praxis Publishing 2008).

Menu et al. 2014 J. Menu, R. van Boekel, T. Henning, C. J. Chandler, H. Linz, M. Benisty, S. Lacour, M. Min, C. Waelkens, S. M. Andrews, N. Calvet, J. M. Carpenter, S. A. Corder, A. T. Deller, J. S. Greaves, R. J. Harris, A. Isella, W. Kwon, J. Lazio, J.-B. Le Bouquin, F. Ménard, L. G. Mundy, L. M. Pérez, L. Ricci, A. I. Sargent, S. Storm, L. Testi and D. J. Wilner, 'On the structure of the transition disk around TW Hydrae'. *A&A*, April 2014, volume 564, A93, doi:10.1051/0004-6361/201322961, arXiv:1402.6597.

Miller and Stone 2000 K. A. Miller and J. M. Stone, 'The Formation and Structure of a Strongly Magnetized Corona above a Weakly Magnetized Accretion Disk'. *ApJ*, May 2000, volume 534, 398–419, doi:10.1086/308736, arXiv:astro-ph/9912135.

Miotello et al. 2014 A. Miotello, L. Testi, G. Lodato, L. Ricci, G. Rosotti, K. Brooks, A. Maury and A. Natta, 'Grain growth in the envelopes and disks of Class I protostars'. *A&A*, July 2014, volume 567, A32, doi:10.1051/0004-6361/201322945, arXiv:1405.0821.

Miotello et al. 2017 A. Miotello, E. F. van Dishoeck, J. P. Williams, M. Ansdell, G. Guidi, M. Hogerheijde, C. F. Manara, M. Tazzari, L. Testi, N. van der Marel and S. van Terwisga, 'Lupus disks with faint CO isotopologues: low gas/dust or high carbon depletion?' *A&A*, March 2017, volume 599, A113, doi:10.1051/0004-6361/201629556, arXiv:1612.01538.

Miyake and Nakagawa 1993 K. Miyake and Y. Nakagawa, 'Effects of particle size distribution on opacity curves of protoplanetary disks around T Tauri stars'. *Icarus*, November 1993, volume 106, 20, doi:10.1006/icar.1993.1156.

Monnier et al. 2017 J. D. Monnier, T. J. Harries, A. Aarnio, F. C. Adams, S. Andrews, N. Calvet, C. Espaillat, L. Hartmann, S. Hinkley, S. Kraus, M. McClure, R. Oppenheimer, M. Perrin and D. Wilner, 'Polarized Disk Emission from Herbig Ae/Be Stars Observed Using Gemini Planet Imager: HD 144432, HD 150193, HD 163296, and HD 169142'. *ApJ*, March 2017, volume 838, 20, doi:10.3847/1538-4357/aa6248, arXiv:1702.04780.

Montesinos et al. 2009 B. Montesinos, C. Eiroa, A. Mora and B. Merín, 'Parameters of Herbig Ae/Be and Vega-type stars'. *A&A*, March 2009, volume 495, 901–917, doi:10.1051/0004-6361:200810623, arXiv:0811.3557.

Mora et al. 2001 A. Mora, B. Merín, E. Solano, B. Montesinos, D. de Winter, C. Eiroa, R. Ferlet, C. A. Grady, J. K. Davies, L. F. Miranda, R. D. Oudmaijer, J. Palacios, A. Quirrenbach, A. W. Harris, H. Rauer, A. Collier Cameron, H. J. Deeg, F. Garzón, A. Penny, J. Schneider, Y. Tsapras and P. R. Wesselius, 'EXPORT: Spectral classification and projected rotational velocities of Vega-type and pre-main sequence stars'. *A&A*, October 2001, volume 378, 116–131, doi:10.1051/0004-6361:20011098.

Morton et al. 2016 T. D. Morton, S. T. Bryson, J. L. Coughlin, J. F. Rowe, G. Ravichandran, E. A. Petigura, M. R. Haas and N. M. Batalha, 'False Positive Probabilities for all Kepler Objects of Interest: 1284 Newly Validated Planets and 428 Likely False Positives'. *ApJ*, May 2016, volume 822, 86, doi:10.3847/0004-637X/822/2/86, arXiv:1605.02825.

Myers et al. 1987 P. C. Myers, G. A. Fuller, R. D. Mathieu, C. A. Beichman, P. J. Benson, R. E. Schild and J. P. Emerson, 'Near-infrared and optical observations of IRAS sources in and near dense cores'. *ApJ*, August 1987, volume 319, 340–357, doi:10.1086/165458.

Natta and Testi 2004 A. Natta and L. Testi, 'Grain Growth in Circumstellar Disks'. In D. Johnstone, F. C. Adams, D. N. C. Lin, D. A. Neufeeld and E. C. Ostriker, editors, *Star Formation in the Interstellar Medium: In Honor of David Hollenbach*, volume 323 of *Astronomical Society of the Pacific Conference Series* (2004) page 279.

Natta et al. 2007 A. Natta, L. Testi, N. Calvet, T. Henning, R. Waters and D. Wilner, 'Dust in Protoplanetary Disks: Properties and Evolution'. *Protostars and Planets V*, 2007, pages 767–781, arXiv:astro-ph/0602041.

Natta et al. 2004 A. Natta, L. Testi, R. Neri, D. S. Shepherd and D. J. Wilner, 'A search for evolved dust in Herbig Ae stars'. *A&A*, March 2004, volume 416, 179–186, doi:10.1051/0004-6361:20035620, arXiv:astro-ph/0311624.

Öberg et al. 2011 K. I. Öberg, A. C. A. Boogert, K. M. Pontoppidan, S. van den Broek, E. F. van Dishoeck, S. Bottinelli, G. A. Blake and N. J. Evans, II, 'The Spitzer Ice Legacy: Ice Evolution from Cores to Protostars'. *ApJ*, October 2011, volume 740, 109, doi:10.1088/0004-637X/740/2/109, arXiv:1107.5825.

Okuzumi et al. 2015 S. Okuzumi, M. Momose, S.-i. Sirono, H. Kobayashi and H. Tanaka, 'Sintering-induced Dust Ring Formation in Protoplanetary Disks: Application to the HL Tau Disk'. *ArXiv e-prints*, October 2015, arXiv:1510.03556.

Okuzumi et al. 2016 S. Okuzumi, M. Momose, S.-i. Sirono, H. Kobayashi and H. Tanaka, 'Sintering-induced Dust Ring Formation in Protoplanetary Disks: Application to the HL Tau Disk'. *ApJ*, April 2016, volume 821, 82, doi:10.3847/0004-637X/821/2/82, arXiv:1510.03556.

Okuzumi et al. 2012 S. Okuzumi, H. Tanaka, H. Kobayashi and K. Wada, 'Rapid Coagulation of Porous Dust Aggregates outside the Snow Line: A Pathway to Successful Icy Planetesimal Formation'. *ApJ*, June 2012, volume 752, 106, doi:10.1088/0004-637X/752/2/106, arXiv:1204.5035.

Papaloizou et al. 2007 J. C. B. Papaloizou, R. P. Nelson, W. Kley, F. S. Masset and P. Artymowicz, 'Disk-Planet Interactions During Planet Formation'. *Protostars and Planets V*, 2007, pages 655–668, arXiv:astro-ph/0603196.

Pascucci et al. 2016 I. Pascucci, L. Testi, G. J. Herczeg, F. Long, C. F. Manara, N. Hendler, G. D. Mulders, S. Krijt, F. Ciesla, T. Henning, S. Mohanty, E. Drabek-Maunder, D. Apai, L. Szűcs, G. Sacco and J. Olofsson, 'A Steeper than Linear Disk Mass-Stellar Mass Scaling Relation'. *ApJ*, November 2016, volume 831, 125, doi:10.3847/0004-637X/831/2/125, arXiv:1608.03621.

Pearson 1999 T. J. Pearson, 'Non-Imaging Data Analysis'. In G. B. Taylor, C. L. Carilli and R. A. Perley, editors, *Synthesis Imaging in Radio Astronomy II*, volume 180 of *Astronomical Society of the Pacific Conference Series* (1999) page 335.

Pérez et al. 2016 L. M. Pérez, J. M. Carpenter, S. M. Andrews, L. Ricci, A. Isella, H. Linz, A. I. Sargent, D. J. Wilner, T. Henning, A. T. Deller, C. J. Chandler, C. P. Dullemond, J. Lazio, K. M. Menten, S. A. Corder, S. Storm, L. Testi, M. Tazzari, W. Kwon, N. Calvet, J. S. Greaves, R. J. Harris and L. G. Mundy, 'Spiral density waves in a young protoplanetary disk'. *Science*, September 2016, volume 353, 1519–1521, doi:10.1126/science.aaf8296, arXiv:1610.05139.

Pérez et al. 2012 L. M. Pérez, J. M. Carpenter, C. J. Chandler, A. Isella, S. M. Andrews, L. Ricci, N. Calvet, S. A. Corder, A. T. Deller, C. P. Dullemond, J. S. Greaves, R. J. Harris, T. Henning, W. Kwon, J. Lazio, H. Linz, L. G. Mundy, A. I. Sargent, S. Storm, L. Testi and D. J. Wilner, 'Constraints on the Radial Variation of Grain Growth in the AS 209 Circumstellar Disk'. *ApJLett*, November 2012, volume 760, L17, doi:10.1088/2041-8205/760/1/L17, arXiv:1210.5252.

Pérez et al. 2015 L. M. Pérez, C. J. Chandler, A. Isella, J. M. Carpenter, S. M. Andrews, N. Calvet, S. A. Corder, A. T. Deller, C. P. Dullemond, J. S. Greaves, R. J. Harris, T. Henning, W. Kwon, J. Lazio, H. Linz, L. G. Mundy, L. Ricci, A. I. Sargent, S. Storm, M. Tazzari, L. Testi and D. J. Wilner, 'Grain Growth in the Circumstellar Disks of the Young Stars CY Tau and DoAr 25'. *ApJ*, November 2015, volume 813, 41, doi:10.1088/0004-637X/813/1/41, arXiv:1509.07520.

Pérez et al. 2014 L. M. Pérez, A. Isella, J. M. Carpenter and C. J. Chandler, 'Large-scale Asymmetries in the Transitional Disks of SAO 206462 and SR 21'. *ApJLett*, March 2014, volume 783, L13, doi:10.1088/2041-8205/783/1/L13, arXiv:1402.0832.

Perez-Becker and Chiang 2011 D. Perez-Becker and E. Chiang, 'Surface Layer Accretion in Conventional and Transitional Disks Driven by Far-ultraviolet Ionization'. *ApJ*, July 2011, volume 735, 8, doi:10.1088/0004-637X/735/1/8, arXiv:1104.2320.

Perley and Butler 2013 R. A. Perley and B. J. Butler, 'An Accurate Flux Density Scale from 1 to 50 GHz'. *ApJS*, February 2013, volume 204, 19, doi:10.1088/0067-0049/204/2/19, arXiv:1211.1300.

Perryman et al. 2014 M. Perryman, J. Hartman, G. Á. Bakos and L. Lindegren, 'Astrometric Exoplanet Detection with Gaia'. *ApJ*, December 2014, volume 797, 14, doi:10.1088/0004-637X/797/1/14, arXiv:1411.1173.

Pinilla et al. 2012a P. Pinilla, M. Benisty and T. Birnstiel, 'Ring shaped dust accumulation in transition disks'. *A&A*, September 2012a, volume 545, A81, doi:10.1051/0004-6361/201219315, arXiv:1207.6485.

Pinilla et al. 2012b P. Pinilla, T. Birnstiel, L. Ricci, C. P. Dullemond, A. L. Uribe, L. Testi and A. Natta, 'Trapping dust particles in the outer regions of protoplanetary disks'. *A&A*, February 2012b, volume 538, A114, doi:10.1051/0004-6361/201118204, arXiv:1112.2349.

Pollack et al. 1994 J. B. Pollack, D. Hollenbach, S. Beckwith, D. P. Simonelli, T. Roush and W. Fong, 'Composition and radiative properties of grains in molecular clouds and accretion disks'. *ApJ*, February 1994, volume 421, 615–639, doi:10.1086/173677.

Qi et al. 2011 C. Qi, P. D'Alessio, K. I. Öberg, D. J. Wilner, A. M. Hughes, S. M. Andrews and S. Ayala, 'Resolving the CO Snow Line in the Disk around HD 163296'. *ApJ*, October 2011, volume 740, 84, doi:10.1088/0004-637X/740/2/84, arXiv:1107.5061.

Qi et al. 2015 C. Qi, K. I. Öberg, S. M. Andrews, D. J. Wilner, E. A. Bergin, A. M. Hughes, M. Hogherheijde and P. D'Alessio, 'Chemical Imaging of the CO Snow Line in the HD 163296 Disk'. *ApJ*, November 2015, volume 813, 128, doi:10.1088/0004-637X/813/2/128, arXiv:1510.00968.

Qi et al. 2013 C. Qi, K. I. Öberg, D. J. Wilner, P. D'Alessio, E. Bergin, S. M. Andrews, G. A. Blake, M. R. Hogerheijde and E. F. van Dishoeck, 'Imaging of the CO Snow Line in a Solar Nebula Analog'. *Science*, August 2013, volume 341, 630–632, doi:10.1126/science.1239560, arXiv:1307.7439.

Rameau et al. 2013 J. Rameau, G. Chauvin, A.-M. Lagrange, T. Meshkat, A. Boccaletti, S. P. Quanz, T. Currie, D. Mawet, J. H. Girard, M. Bonnefoy and M. Kenworthy, 'Confirmation of the Planet around HD 95086 by Direct Imaging'. *ApJLett*, December 2013, volume 779, L26, doi:10.1088/2041-8205/779/2/L26, arXiv:1310.7483.

Rameau et al. 2017 J. Rameau, K. B. Follette, L. Pueyo, C. Marois, B. Macintosh, M. Millar-Blanchaer, J. J. Wang, D. Vega, R. Doyon, D. Lafrenière, E. L. Nielsen, V. Bailey, J. K. Chilcote, L. M. Close, T. M. Esposito et al., 'An Optical/Near-infrared Investigation of HD 100546 b with the Gemini Planet Imager and MagAO'. *AJ*, June 2017, volume 153, 244, doi:10.3847/1538-3881/aa6cae, arXiv:1704.06317.

Reggiani et al. 2014 M. Reggiani, S. P. Quanz, M. R. Meyer, L. Pueyo, O. Absil, A. Amara, G. Anglada, H. Avenhaus, J. H. Girard, C. Carrasco Gonzalez, J. Graham, D. Mawet, F. Meru, J. Milli, M. Osorio, S. Wolff and J.-M. Torrelles, 'Discovery of a Companion Candidate in the HD 169142 Transition Disk and the Possibility of Multiple Planet Formation'. *ApJLett*, September 2014, volume 792, L23, doi:10.1088/2041-8205/792/1/L23, arXiv:1408.0813.

Ricci et al. 2010 L. Ricci, L. Testi, A. Natta, R. Neri, S. Cabrit and G. J. Herczeg, 'Dust properties of protoplanetary disks in the Taurus-Auriga star forming region from millimeter wavelengths'. *A&A*, March 2010, volume 512, A15, doi:10.1051/0004-6361/200913403, arXiv:0912.3356.

Ricci et al. 2012 L. Ricci, L. Testi, A. Natta, A. Scholz and I. de Gregorio-Monsalvo, 'ALMA Observations of ρ-Oph 102: Grain Growth and Molecular Gas in the Disk around a Young Brown Dwarf'. *ApJLett*, December 2012, volume 761, L20, doi:10.1088/2041-8205/761/2/L20, arXiv:1211.6743.

Rice et al. 2003 W. K. M. Rice, P. J. Armitage, M. R. Bate and I. A. Bonnell, 'The effect of cooling on the global stability of self-gravitating protoplanetary discs'. *MNRAS*, March 2003, volume 339, 1025–1030, doi:10.1046/j.1365-8711.2003.06253.x, arXiv:astro-ph/0211088.

Rice et al. 2006 W. K. M. Rice, P. J. Armitage, K. Wood and G. Lodato, 'Dust filtration at gap edges: implications for the spectral energy distributions of discs with embedded planets'. *MNRAS*, December 2006, volume 373, 1619–1626, doi:10.1111/j.1365-2966.2006.11113.x, arXiv:astro-ph/0609808.

Rodmann et al. 2006 J. Rodmann, T. Henning, C. J. Chandler, L. G. Mundy and D. J. Wilner, 'Large dust particles in disks around T Tauri stars'. *A&A*, January 2006, volume 446, 211–221, doi:10.1051/0004-6361:20054038, arXiv:astro-ph/0509555.

Ros and Johansen 2013 K. Ros and A. Johansen, 'Ice condensation as a planet formation mechanism'. *A&A*, April 2013, volume 552, A137, doi:10.1051/0004-6361/201220536, arXiv:1302.3755.

Rosenfeld et al. 2013 K. A. Rosenfeld, S. M. Andrews, A. M. Hughes, D. J. Wilner and C. Qi, 'A Spatially Resolved Vertical Temperature Gradient in the HD 163296 Disk'. *ApJ*, September 2013, volume 774, 16, doi:10.1088/0004-637X/774/1/16, arXiv:1306.6475.

Rosotti et al. 2016 G. P. Rosotti, A. Juhasz, R. A. Booth and C. J. Clarke, 'The minimum mass of detectable planets in protoplanetary discs and the derivation of planetary masses from high-resolution observations'. *MNRAS*, July 2016, volume 459, 2790–2805, doi:10.1093/mnras/stw691, arXiv:1603.02141.

Ruane et al. 2017 G. Ruane, D. Mawet, J. Kastner, T. Meshkat, M. Bottom, B. Femenía Castellá, O. Absil, C. Gomez Gonzalez, E. Huby, Z. Zhu, R. Jenson-Clem, É. Choquet and E. Serabyn, 'Deep Imaging Search for Planets Forming in the TW Hya Protoplanetary Disk with the Keck/NIRC2 Vortex Coronagraph'. *AJ*, August 2017, volume 154, 73, doi:10.3847/1538-3881/aa7b81, arXiv:1706.07489.

Sallum et al. 2015 S. Sallum, K. B. Follette, J. A. Eisner, L. M. Close, P. Hinz, K. Kratter, J. Males, A. Skemer, B. Macintosh, P. Tuthill, V. Bailey, D. Defrère, K. Morzinski, T. Rodigas, E. Spalding, A. Vaz and A. J. Weinberger, 'Accreting protoplanets in the LkCa 15 transition disk'. *Nature*, November 2015, volume 527, 342–344, doi:10.1038/nature15761, arXiv:1511.07456.

Serabyn et al. 2017 E. Serabyn, E. Huby, K. Matthews, D. Mawet, O. Absil, B. Femenia, P. Wizinowich, M. Karlsson, M. Bottom, R. Campbell, B. Carlomagno, D. Defrère, C. Delacroix, P. Forsberg, C. Gomez Gonzalez, S. Habraken, A. Jolivet, K. Liewer, S. Lilley, P. Piron, M. Reggiani, J. Surdej, H. Tran, E. Vargas Catalán and O. Wertz, 'The W. M. Keck Observatory Infrared Vortex Coronagraph and a First Image of HIP 79124 B'. *AJ*, January 2017, volume 153, 43, doi:10.3847/1538-3881/153/1/43, arXiv:1612.03093.

Shakura and Sunyaev 1973 N. I. Shakura and R. A. Sunyaev, 'Black holes in binary systems. Observational appearance.' *A&A*, 1973, volume 24, 337–355.

Shu 1977 F. H. Shu, 'Self-similar collapse of isothermal spheres and star formation'. *ApJ*, June 1977, volume 214, 488–497, doi:10.1086/155274.

Simon et al. 2011 J. B. Simon, P. J. Armitage and K. Beckwith, 'Turbulent Linewidths in Protoplanetary Disks: Predictions from Numerical Simulations'. *ApJ*, December 2011, volume 743, 17, doi:10.1088/0004-637X/743/1/17, arXiv:1107.3561.

Sitko et al. 2008 M. L. Sitko, W. J. Carpenter, R. L. Kimes, J. L. Wilde, D. K. Lynch, R. W. Russell, R. J. Rudy, S. M. Mazuk, C. C. Venturini, R. C. Puetter, C. A. Grady, E. F. Polomski, J. P. Wisnewski, S. M. Brafford, H. B. Hammel and R. B. Perry, 'Variability of Disk Emission in Pre-Main-Sequence and Related Stars. I. HD 31648 and HD 163296: Isolated Herbig Ae Stars Driving Herbig-Haro Flows'. *ApJ*, May 2008, volume 678, 1070-1087, doi:10.1086/529003, arXiv:0712.4014.

Stahler and Palla 2005 S. W. Stahler and F. Palla, *The Formation of Stars* (Wiley-VCH 2005).

Stognienko et al. 1995 R. Stognienko, T. Henning and V. Ossenkopf, 'Optical properties of coagulated particles.' *A&A*, April 1995, volume 296, 797.

Strom et al. 1989 K. M. Strom, G. Newton, S. E. Strom, R. L. Seaman, L. Carrasco, I. Cruz-Gonzalez, A. Serrano and G. L. Grasdalen, 'A study of the stellar population in the LYNDS 1641 dark cloud. I - The IRAS catalog sources'. *ApJS*, October 1989, volume 71, 183–217, doi:10.1086/191371.

Supulver and Lin 2000 K. D. Supulver and D. N. C. Lin, 'Formation of Icy Planetesimals in a Turbulent Solar Nebula'. *Icarus*, August 2000, volume 146, 525–540, doi:10.1006/icar.2000.6418.

Tamayo et al. 2015 D. Tamayo, A. H. M. J. Triaud, K. Menou and H. Rein, 'Dynamical Stability of Imaged Planetary Systems in Formation: Application to HL Tau'. *ApJ*, June 2015, volume 805, 100, doi:10.1088/0004-637X/805/2/100, arXiv:1502.05099.

Tazzari et al. 2016 M. Tazzari, L. Testi, B. Ercolano, A. Natta, A. Isella, C. J. Chandler, L. M. Pérez, S. Andrews, D. J. Wilner, L. Ricci, T. Henning, H. Linz, W. Kwon, S. A. Corder, C. P. Dullemond, J. M. Carpenter, A. I. Sargent, L. Mundy, S. Storm, N. Calvet, J. A. Greaves, J. Lazio and A. T. Deller, 'Multiwavelength analysis for interferometric (sub-)mm observations of protoplanetary disks. Radial constraints on the dust properties and the disk structure'. *A&A*, April 2016, volume 588, A53, doi:10.1051/0004-6361/201527423, arXiv:1512.05679.

Tazzari et al. 2017 M. Tazzari, L. Testi, A. Natta, M. Ansdell, J. Carpenter, G. Guidi, M. Hogerheijde, C. F. Manara, A. Miotello, N. van der Marel, E. F. van Dishoeck and J. P. Williams, 'Physical properties of dusty protoplanetary disks in Lupus: evidence for viscous evolution?' *A&A*, October 2017, volume 606, A88, doi:10.1051/0004-6361/201730890, arXiv:1707.01499.

Testi et al. 2014 L. Testi, T. Birnstiel, L. Ricci, S. Andrews, J. Blum, J. Carpenter, C. Dominik, A. Isella, A. Natta, J. P. Williams and D. J. Wilner, 'Dust Evolution in Protoplanetary Disks'. *Protostars and Planets VI*, 2014, pages 339–361, doi:10.2458/azu_uapress_9780816531240-ch015, arXiv:1402.1354.

Testi et al. 2001 L. Testi, A. Natta, D. S. Shepherd and D. J. Wilner, 'Constraints on Properties of the Protoplanetary Disks around UX Orionis and CQ Tauri'. *ApJ*, June 2001, volume 554, 1087–1094, doi:10.1086/321406, arXiv:arXiv:astro-ph/0102473.

Testi et al. 2003 L. Testi, A. Natta, D. S. Shepherd and D. J. Wilner, 'Large grains in the disk of CQ Tau'. *A&A*, May 2003, volume 403, 323–328, doi:10.1051/0004-6361:20030362, arXiv:astro-ph/0303420.

Testi et al. 2015 L. Testi, A. Skemer, T. Henning, V. Bailey, D. Defrère, P. Hinz, J. Leisenring, A. Vaz, S. Esposito, A. Fontana, A. Marconi, M. Skrutskie and C. Veillet, 'Hunting for Planets in the HL Tau Disk'. *ApJLett*, October 2015, volume 812, L38, doi:10.1088/2041-8205/812/2/L38, arXiv:1509.06068.

Thalmann et al. 2009 C. Thalmann, J. Carson, M. Janson, M. Goto, M. McElwain, S. Egner, M. Feldt, J. Hashimoto, Y. Hayano, T. Henning, K. W. Hodapp, R. Kandori, H. Klahr, T. Kudo, N. Kusakabe, C. Mordasini, J.-I. Morino, H. Suto, R. Suzuki and M. Tamura, 'Discovery of the Coldest Imaged Companion of a Sun-like Star'. *ApJLett*, December 2009, volume 707, L123–L127, doi:10.1088/0004-637X/707/2/L123, arXiv:0911.1127.

Thompson et al. 2001 A. R. Thompson, J. M. Moran and G. W. Swenson, Jr., *Interferometry and Synthesis in Radio Astronomy, 2nd Edition* (A Wiley-Interscience publication 2001).

Tielens and Hollenbach 1985 A. G. G. M. Tielens and D. Hollenbach, 'Photodissociation regions. I - Basic model. II - A model for the Orion photodissociation region'. *ApJ*, April 1985, volume 291, 722–754, doi:10.1086/163111.

Tilling et al. 2012 I. Tilling, P. Woitke, G. Meeus, A. Mora, B. Montesinos, P. Riviere-Marichalar, C. Eiroa, W.-F. Thi, A. Isella, A. Roberge, C. Martin-Zaidi, I. Kamp, C. Pinte, G. Sandell, W. D. Vacca, F. Ménard, I. Mendigutía, G. Duchêne, W. R. F. Dent, G. Aresu, R. Meijerink and M. Spaans, 'Gas modelling in the disc of HD 163296'. *A&A*, February 2012, volume 538, A20, doi:10.1051/0004-6361/201116919, arXiv:1111.2549.

Tobin et al. 2012 J. J. Tobin, L. Hartmann, E. Bergin, H.-F. Chiang, L. W. Looney, C. J. Chandler, S. Maret and F. Heitsch, 'Complex Structure in Class 0 Protostellar Envelopes. III. Velocity Gradients in Non-axisymmetric Envelopes, Infall, or Rotation?' *ApJ*, March 2012, volume 748, 16, doi:10.1088/0004-637X/748/1/16, arXiv:1201.2174.

Toomre 1964 A. Toomre, 'On the gravitational stability of a disk of stars'. *ApJ*, May 1964, volume 139, 1217–1238, doi:10.1086/147861.

Trotta et al. 2013 F. Trotta, L. Testi, A. Natta, A. Isella and L. Ricci, 'Constraints on the radial distribution of the dust properties in the CQ Tauri protoplanetary disk'. *A&A*, October 2013, volume 558, A64, doi:10.1051/0004-6361/201321896, arXiv:1308.5070.

Umebayashi and Nakano 1981 T. Umebayashi and T. Nakano, 'Fluxes of Energetic Particles and the Ionization Rate in Very Dense Interstellar Clouds'. *PASJ*, 1981, volume 33, 617.

van den Ancker et al. 1998 M. E. van den Ancker, D. de Winter and H. R. E. Tjin A Djie, 'HIPPARCOS photometry of Herbig Ae/Be stars'. *A&A*, February 1998, volume 330, 145–154.

van den Ancker et al. 1997 M. E. van den Ancker, P. S. The, H. R. E. Tjin A Djie, C. Catala, D. de Winter, P. F. C. Blondel and L. B. F. M. Waters, 'HIPPARCOS data on Herbig Ae/Be stars: an evolutionary scenario.' *A&A*, August 1997, volume 324, L33–L36.

van Leeuwen 2007 F. van Leeuwen, 'Validation of the new Hipparcos reduction'. *A&A*, November 2007, volume 474, 653–664, doi:10.1051/0004-6361:20078357, arXiv:0708.1752.

Vargas Catalán et al. 2016 E. Vargas Catalán, E. Huby, P. Forsberg, A. Jolivet, P. Baudoz, B. Carlomagno, C. Delacroix, S. Habraken, D. Mawet, J. Surdej, O. Absil and M. Karlsson, 'Optimizing the subwavelength grating of L-band annular groove phase masks for high coronagraphic performance'. *A&A*, November 2016, volume 595, A127, doi:10.1051/0004-6361/201628739, arXiv:1610.05065.

Wada et al. 2009 K. Wada, H. Tanaka, T. Suyama, H. Kimura and T. Yamamoto, 'Collisional Growth Conditions for Dust Aggregates'. *ApJ*, September 2009, volume 702, 1490–1501, doi:10.1088/0004-637X/702/2/1490.

Wahhaj et al. 2015 Z. Wahhaj, L. A. Cieza, D. Mawet, B. Yang, H. Canovas, J. de Boer, S. Casassus, F. Ménard, M. R. Schreiber, M. C. Liu, B. A. Biller, E. L. Nielsen and T. L. Hayward, 'Improving signal-to-noise in the direct imaging of exoplanets and circumstellar disks with MLOCI'. *A&A*, September 2015, volume 581, A24, doi:10.1051/0004-6361/201525837, arXiv:1502.03092.

Weidenschilling 1977 S. J. Weidenschilling, 'Aerodynamics of solid bodies in the solar nebula'. *MNRAS*, July 1977, volume 180, 57–70.

Weidenschilling and Cuzzi 1993 S. J. Weidenschilling and J. N. Cuzzi, 'Formation of planetesimals in the solar nebula'. In E. H. Levy and J. I. Lunine, editors, *Protostars and Planets III* (1993) pages 1031–1060.

Weintraub et al. 1989 D. A. Weintraub, G. Sandell and W. D. Duncan, 'Submillimeter measurements of T Tauri and FU Orionis stars'. *ApJLett*, May 1989, volume 340, L69–L72, doi:10.1086/185441.

Wettlaufer 2010 J. S. Wettlaufer, 'Accretion in Protoplanetary Disks by Collisional Fusion'. *ApJ*, August 2010, volume 719, 540–549, doi:10.1088/0004-637X/719/1/540, arXiv:0911.5398.

Williams and Cieza 2011 J. P. Williams and L. A. Cieza, 'Protoplanetary Disks and Their Evolution'. *ARA&A*, September 2011, volume 49, 67–117, doi:10.1146/annurev-astro-081710-102548, arXiv:1103.0556.

Wilner et al. 2000 D. J. Wilner, P. T. P. Ho, J. H. Kastner and L. F. Rodríguez, 'VLA Imaging of the Disk Surrounding the Nearby Young Star TW Hydrae'. *ApJLett*, May 2000, volume 534, L101–L104, doi:10.1086/312642, arXiv:astro-ph/0005019.

Wilson et al. 2013 L. T. Wilson, K. Rohlfs and S. Hüttemeister, *Tools of Radio Astronomy* (Springer 2013), doi:10.1007/978-3-642-39950-3.

Wilson 1999 T. L. Wilson, 'Isotopes in the interstellar medium and circumstellar envelopes'. *Reports on Progress in Physics*, February 1999, volume 62, 143–185, doi:10.1088/0034-4885/62/2/002.

Wisniewski et al. 2008 J. P. Wisniewski, M. Clampin, C. A. Grady, D. R. Ardila, H. C. Ford, D. A. Golimowski, G. D. Illingworth and J. E. Krist, 'The HD 163296 Circumstellar Disk in Scattered Light: Evidence of Time-Variable Self-Shadowing'. *ApJ*, July 2008, volume 682, 548-558, doi:10.1086/589629, arXiv:0807.1766.

Wolf et al. 2007 S. Wolf, A. Moro-Martín and G. D'Angelo, 'Signatures of planets in protoplanetary and debris disks'. *Planet. Space Sci.*, April 2007, volume 55, 569–581, doi:10.1016/j.pss.2006.04.035.

Wolszczan and Frail 1992 A. Wolszczan and D. A. Frail, 'A planetary system around the millisecond pulsar PSR1257 + 12'. *Nature*, January 1992, volume 355, 145–147, doi:10.1038/355145a0.

Yen et al. 2016 H.-W. Yen, H. B. Liu, P.-G. Gu, N. Hirano, C.-F. Lee, E. Puspitaningrum and S. Takakuwa, 'Gas Gaps in the Protoplanetary Disk around the Young Protostar HL Tau'. *ApJLett*, April 2016, volume 820, L25, doi:10.3847/2041-8205/820/2/L25, arXiv:1603.01378.

Zhang et al. 2016 K. Zhang, E. A. Bergin, G. A. Blake, L. I. Cleeves, M. Hogerheijde, V. Salinas and K. R. Schwarz, 'On the Commonality of 10 30 AU Sized Axisymmetric Dust Structures in Protoplanetary Disks'. *ApJL*, February 2016, volume 818, L16, doi:10.3847/2041-8205/818/1/L16, arXiv:1601.05182.

Zhang et al. 2015 K. Zhang, G. A. Blake and E. A. Bergin, 'Evidence of Fast Pebble Growth Near Condensation Fronts in the HL Tau Protoplanetary Disk'. *ApJLett*, June 2015, volume 806, L7, doi:10.1088/2041-8205/806/1/L7, arXiv:1505.00882.

Zhu 2015 Z. Zhu, 'Accreting circumplanetary disks: Observational signatures'. *ApJ*, 2015, volume 799(1), 16, URL http://stacks.iop.org/0004-637X/799/i=1/a=16.

Zhu et al. 2012 Z. Zhu, R. P. Nelson, R. Dong, C. Espaillat and L. Hartmann, 'Dust Filtration by Planet-induced Gap Edges: Implications for Transitional Disks'. *ApJ*, August 2012, volume 755, 6, doi:10.1088/0004-637X/755/1/6, arXiv:1205.5042.